

**New Observational and Modeling Techniques for  
Multistatic Specular Meteor Radar**

by

**Cody Vogel Vaudrin**

Bachelor of Science, Electrical and Computer Engineering

Master of Science, Aerospace Engineering

A thesis submitted to the  
Faculty of the Graduate School of the  
University of Colorado in partial fulfillment  
of the requirements for the degree of  
Doctor of Philosophy  
Department of Aerospace Engineering Sciences

2016

This thesis entitled:  
New Observational and Modeling Techniques for Multistatic Specular Meteor Radar  
written by Cody Vogel Vaudrin  
has been approved for the Department of Aerospace Engineering Sciences

---

Professor Scott E. Palo

---

Dr. Christopher Williams

Date \_\_\_\_\_

The final copy of this thesis has been examined by the signatories, and we find that both the content and the form meet acceptable presentation standards of scholarly work in the above mentioned discipline.

Vaudrin, Cody Vogel (PhD)

New Observational and Modeling Techniques for Multistatic Specular Meteor Radar

Thesis directed by Professor Scott E. Palo

This dissertation presents details of new techniques in specular meteor radar data acquisition, modeling and determining the fundamental specular meteor radar echo signal parameters. One goal of Multistatic Meteor Wind Radar (MMWR) is increasing the spatial and temporal resolution of the upper-atmospheric windfield estimate by distributing a network of synchronized interferometers over large spatial regions on the order of 100's of [km]. Modern theories of meteor trail diffusion are placed in the context of modeling the ground illumination pattern created when an arbitrarily placed meteor trail scatters VHF radio waves originating from an arbitrarily located transmitter. The ground illumination pattern shows how meteor trail scatter can be observed by receivers located over large spatial regions on Earth's surface.

MMWR is enabled with the Colorado Software Radar (CoSRad), a software-defined radar remote sensing transceiver system developed at the University of Colorado's ARSENL laboratory. Various specular meteor trail echoes observed using CoSRad configured to drive existing radars highlight CoSRad's potential for reconfigurability. A set of long-baseline multistatic observations taken using a prototype system deployment in Australia demonstrates the MMWR measurement principle and the ground illumination pattern model.

Unexpected issues encountered when processing the prototype MMWR data using traditional interferometry methods motivated the development of a new technique to solve the parameter estimation problem of specular meteor radar interferometry on the complex plane. One benefit of the complex plane interferometry solution technique is the formation of a parameter covariance matrix, representing the precision of the measured trail location, Doppler and diffusion signal parameters. The determination of fundamental measurement parameter precision is important, as it lays the groundwork for calculating the precision of the derived multistatic windfield. This dissertation presents modern techniques in modeling and observing specular scatter from meteor trails and estimating the fundamental signal parameters of spatial location, Doppler frequency and diffusion coefficient from the specular radar echoes.

# Contents

## Chapter

<b>1</b>	Introduction	1
1.1	Dissertation Overview . . . . .	1
1.2	Background . . . . .	5
1.2.1	Meteor Science . . . . .	10
1.2.2	Software Defined Radio . . . . .	17
1.3	Problem Statement . . . . .	19
1.3.1	Case Study in Reconfigurability . . . . .	20
1.3.2	Scientific Motivations . . . . .	21
<b>2</b>	Meteor Trail Physical Theory and Numerical Modeling	29
2.1	Classical Meteor Trail Scattering . . . . .	29
2.2	Diffusion . . . . .	35
2.2.1	The Meteor Zone Environment . . . . .	38
2.2.2	Jones' Diffusion Solution . . . . .	44
2.2.3	Dimant and Oppenheim's Diffusion Solution . . . . .	49
2.2.4	Discussion of Solutions . . . . .	53
2.3	Numerical Modeling and the Ground Illumination Pattern . . . . .	55
<b>3</b>	The Colorado Software Defined Radar	75
3.1	Design Philosophy . . . . .	75

3.2	Reconfigurability . . . . .	77
3.3	Hardware details . . . . .	80
3.3.1	ADC . . . . .	83
3.3.2	Direct Digital Synthesis and Transmit Pulse Shaping . . . . .	85
3.3.3	FPGA Architecture . . . . .	87
3.3.4	FPGA Development Methodology . . . . .	89
3.3.5	FX2 USB Transceiver . . . . .	91
3.3.6	GPIO and Timing Signals . . . . .	91
3.3.7	Data Format . . . . .	92
3.4	RF Performance and Observing the Analog World . . . . .	93
3.4.1	Direct Convert Noise Theory . . . . .	95
3.4.2	Third Order Intercept . . . . .	101
3.4.3	Second order products . . . . .	101
3.4.4	Third order products . . . . .	101
3.4.5	Simulation of CoSRad RF Characteristics . . . . .	102
3.5	Radar Signal Processing . . . . .	106
3.5.1	I/Q Demodulation . . . . .	107
3.5.2	Matched Filtering . . . . .	110
3.5.3	Synchronization . . . . .	111
3.6	Specular Meteor Trail Scatter Examples and Observational Results . . . . .	113
3.6.1	Signal Extraction . . . . .	118
4	Meteor Radar Interferometry And Measurement Precision . . . . .	125
4.1	Introduction . . . . .	125
4.2	Specular Meteor Trail Signal Model . . . . .	129
4.3	Classical Meteor Radar Interferometry . . . . .	133
4.4	Complex Plane Meteor Radar Interferometry . . . . .	135

4.5	Finding The Least Squares Estimate of $\beta$ . . . . .	138
4.6	Statistical Uncertainty . . . . .	143
4.6.1	Multistatic Wind Vector Retrieval . . . . .	150
4.7	Forward Model and Simulation Results . . . . .	154
4.7.1	Forward Model Range Estimation . . . . .	154
4.7.2	Uncertainty Estimation Performance . . . . .	155
4.8	Complex Plane Phase Calibration . . . . .	160
5	Overview and Future Work . . . . .	168
	<b>Bibliography</b> . . . . .	172
	<b>Appendix</b>	
A	Supplemental Wind Computation and Array Calibration Details . . . . .	180

## Tables

### Table

3.1	Comparison of CoSRad with other receiver technologies . . . . .	77
3.2	Primary Components of the Colorado Software Radar . . . . .	77
3.3	Development Campaign Locations . . . . .	78
3.4	Hardware Specifications . . . . .	79
3.5	Parameters associated with the GPIO and transmit pulse signals depicted in Figure 3.10 . . . . .	91
3.6	CoSRad RF Simulation Parameters . . . . .	103

## Figures

### Figure

1.1	Basic Illustration of Software Defined Radio . . . . .	2
1.2	Reconfigurable Bandwidth Window . . . . .	3
1.3	Conceptual Illustration of Multistatic Meteor Wind Radar . . . . .	8
1.4	First Trail Radial Velocity Measurement . . . . .	11
1.5	Electric Vector Orientation . . . . .	16
1.6	Condition Number of Wind Component Matrix . . . . .	25
1.7	Multistatic System Geometry . . . . .	25
1.8	Total common volume range . . . . .	26
2.1	Classical Scattering Geometries . . . . .	32
2.2	Cornu spiral describing Fresnel oscillations . . . . .	35
2.3	Electron and Ion Diffusion Coefficients . . . . .	37
2.4	Diffusion coefficients . . . . .	37
2.5	Collision Frequencies . . . . .	38
2.6	Chemical Composition of the Upper Atmosphere . . . . .	39
2.7	Diffusion Altitude Parameter . . . . .	40
2.8	Diffusion Coordinate Frame . . . . .	42
2.9	High-altitude Trail Cross-sectional Electron Density When Aligned With $\mathbf{B}$ . . . . .	46
2.10	High-altitude Trail Cross-sectional Electron Density When Unaligned with $\mathbf{B}$ . . . . .	47

2.11 High-altitude Trail Cross-sectional Electron Density When Significantly Unaligned With $\mathbf{B}$ . . . . .	47
2.12 Low-altitude Trail Cross-sectional Electron Density . . . . .	48
2.13 Background Ionosphere Electron Depletion . . . . .	50
2.14 PDE solution and Jones' Solution . . . . .	51
2.15 Instantaneous Increase in Specular Echo Diffusion Coefficient . . . . .	52
2.16 Geometry of the Ground Illumination Pattern . . . . .	56
2.17 Ground Illumination Pattern Example 1 . . . . .	61
2.18 Ground Illumination Pattern Example 2 . . . . .	62
2.19 Ground Illumination Pattern Example 3 . . . . .	63
2.20 Ground Illumination Pattern Example 4 . . . . .	64
2.21 Gaussian Approximations Vs. Fully Integrated Illumination Patterns . . . . .	66
2.22 Ground Illumination Pattern Dependence on Trail Azimuthal Orientation . . . . .	69
2.23 Ground Illumination Pattern Dependence on Trail Orientation in Elevation $\alpha$ . . . . .	70
2.24 Multistatic Detection Region . . . . .	71
2.25 Temporal Progression of Trail Detection Probability Over the Quadrantid Meteor Shower . . . . .	72
2.26 Change in Meteor Trail Detection Rates over the Quadrantid Meteor Stream Simulation . . . . .	73
3.1 CoSRad System Block Diagram . . . . .	78
3.2 Monostatic Specular Observation using CoSRad . . . . .	81
3.3 Sample Rate Conversion . . . . .	82
3.4 LFMCW Boundary Layer Winds . . . . .	82
3.5 The CoSRad Receiver . . . . .	84
3.6 Pulse Shaping RF Technique . . . . .	86
3.7 FPGA Block Diagram . . . . .	88
3.8 FPGA Filtering . . . . .	90
3.9 FPGA Filter Frequency Response . . . . .	90
3.10 Radar Timing Signals . . . . .	92

3.11 Low-Level Data Format . . . . .	94
3.12 Data Organization . . . . .	94
3.13 RF Front End for the Direct Convert Receiver Architecture . . . . .	95
3.14 CoSRad noise simulation: DR Vs. Gain . . . . .	104
3.15 CoSRad noise simulation: MDS Vs. Gain . . . . .	104
3.16 Noise Figure Vs. Environmental Noise . . . . .	105
3.17 Results from the Oscillator Phase Mismatch Experiment . . . . .	112
3.18 Multistatic Experimental Setup . . . . .	114
3.19 Forward-scatter Observation . . . . .	115
3.20 Trail Height Distribution . . . . .	115
3.21 Trail Diffusion Vs. Height . . . . .	116
3.22 CoSRad observation from the Jicamarca All-sky Specular Meteor Radar . . . . .	116
3.23 CoSRad observation from the Platteville All-sky Specular Meteor Radar . . . . .	117
3.24 Individual Pulse Interferometry Solutions . . . . .	121
3.25 Time-dependent Doppler Drift . . . . .	122
3.26 CoSRad Multistatic Experimental Data Visualization Example 1 . . . . .	122
3.27 CoSRad Multistatic Experimental Data Visualization Example 2 . . . . .	123
4.1 Classical Jones Meteor Radar Antenna Array . . . . .	126
4.2 Nonlinear Least Squares Minimization Core . . . . .	136
4.3 NLS Fit Example . . . . .	140
4.4 Inverse of the Jones Array Objective Function . . . . .	142
4.5 Modeled Specular Meteor Trail Echo . . . . .	143
4.6 Global Vs. Local Minimization Techniques . . . . .	144
4.7 Most Advanced Wind Inversion Currently Available . . . . .	153
4.8 Qualitative Residual Distributions . . . . .	155
4.9 Elevation Vs. Height Uncertainty . . . . .	156

4.10	Estimated Doppler Uncertainty Vs. True Error Vs. SNR . . . . .	157
4.11	Estimated Diffusion Uncertainty Vs. True Error Vs. SNR . . . . .	158
4.12	CDFs of true a-priori parameter errors with respect to the estimated parameter uncertainties	159
4.13	Phase Calibration Illustration . . . . .	161
4.14	Geometric Spatial Bias Terms Used in Phase Calibration . . . . .	163
4.15	Calibrated Vs. Uncalibrated Echoes . . . . .	164
4.16	Histograms of $\eta_x$ and $\eta_y$ . . . . .	165
4.17	Phase Calibration Map . . . . .	166
4.18	Effect of Phase Biases on Echo Height Determination . . . . .	167
A.1	Supplemental Wind Computation and Array Calibration Details . . . . .	181

# Chapter 1

## Introduction

“Enter here the timeless fellowship of the human spirit” - Dr. George Norlin, former president of the University of Colorado

### 1.1 Dissertation Overview

The field of Remote Sensing is broadly defined as the science of determining properties of an object or diffuse medium at a some distance by measuring aspects of its interactions with the electromagnetic spectrum. The interacting field may be supplied actively by an illuminating device, as is the case with radar and lidar, or its origin may be external in nature, such as a star. The following discussions concern the radar class of remote sensing instrumentation. All modern radar systems may be divided into two subsystems, the illumination hardware of which the primary devices are the antennas and a transmitter, and the data acquisition and signal processing systems which record and analyze the scattered field. Multistatic Meteor Wind Radar (MMWR) represents one class of modern radar remote sensing system. This dissertation covers topics concerning multistatic specular meteor wind radar, and specifically addresses the state-of-the-art in receiver hardware design, specular meteor trail scatter modeling and processing of the received specular meteor trail signal in a rigorous statistical sense for quantification of instrumentally-driven uncertainty in the fundamental measurement parameters. Aspiring radar engineers and scientists may use this dissertation as a reference for the current state of specular meteor radar observational techniques and meteor trail modeling.

Recent advances in electronics technology have enabled the development of a new class of radio transceiver known as ‘Software Defined Radio’ (SDR). Traditional radio receivers isolate frequencies of interest from a broad band of frequencies presented to the input using banks of analog filters. As a result, traditional receivers are limited to predefined applications by static analog and digital signal processing hardware. The SDR concept relies on moving the analog-to-digital converter (ADC) closer to the antenna along the receiving chain, thus enabling reconfigurable software-defined signal processing as shown in Figure 1.1. A software defined receiver implements signal processing in the digital domain and consequently is limited in bandwidth by the sampling frequency as depicted in Figure 1.2. For example, a wideband digital receiver can record a large band of frequencies, and process information contained over smaller bands of interest during later processing. A universal software defined radar transceiver designed for use with a wide range of radar remote sensing systems has been developed at the University of Colorado’s Active Remote Sensing Laboratory (ARSENL). The Colorado Software Radar (CoSRad) described in Chapter 3 is capable of data acquisition over an expansive range of applications, however, the receiver has been primarily developed for use as a multistatic specular meteor radar controller and data acquisition system. Consistent with the goals outlined by both the National Science Foundation’s Coupling and Energetic Dynamics of Atmospheric Regions (CEDAR) strategic vision of 2011 [16] and the Distributed Arrays of Small Instruments (DASI) initiative [29], CoSRad represents the current state-of-the-art in multistatic scientific radar remote sensing data acquisition, a claim supported in detail throughout this dissertation.

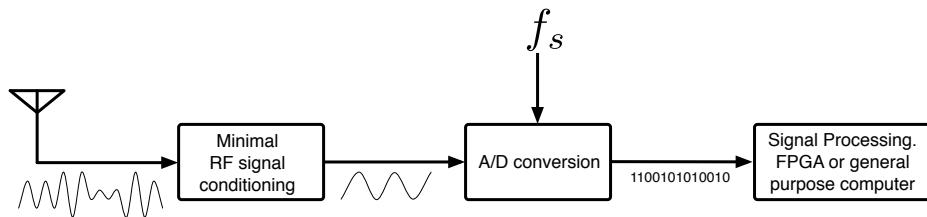


Figure 1.1: Basic illustration of SDR where the ADC is placed closer to the antennas along the receiver chain as compared to traditional analog receivers. SDR-based data acquisition captures a band defined by the sampling frequency  $f_s$  where all subsequent signal processing is performed using digital devices.

Before diving into the technical details of CoSRad, the reader is encouraged to explore the compelling field of meteor trail physics and modeling described in Chapter 2. Chapter 2 describes the physics governing

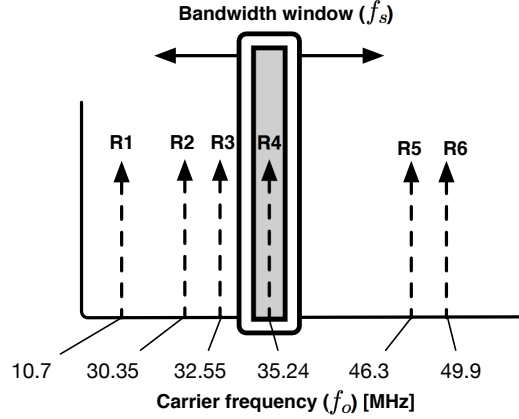


Figure 1.2: The software configurable digital bandwidth window can slide along the analog input bandwidth to select regions of interest. Both the bandwidth window width  $f_s$  and center frequency  $f_o$  are software configurable. The vertical arrows in the figure are labeled with  $Rx$  indicating the center frequencies listed in Table 3.3 where CoSRad has been successfully configured for specular meteor trail radar observations.

classical meteor trail formation from the perspective of specular meteor radar remote sensing. In Chapter 2, diffusion of the charged meteor trail into the neutral atmosphere is explored and a first-principles model of trail diffusion formulated by Dimant and Oppenheim [26] is discussed. Numerical simulations of specular meteor trail scatter based on Tinin’s formulations [126] are presented and provide deep insight into the observation of specular meteor trail scattering from Earth’s surface. Technical details of CoSRad are discussed in Chapter 3 and placed in the context of observing the modeled specular scatter discussed in Chapter 2. Chapter 4 describes the most modern work in voltage-level specular meteor radar signal processing. In Chapter 4, an elegant solution to the problem of meteor radar interferometry is presented and cast on the complex plane. The entire set of fundamental meteor radar parameters are solved under an arbitrary antenna geometry using statistical nonlinear least-squares estimation of the physical model parameters described in Chapter 2. Finally, the statistical precision of all the estimated parameters is characterized by calculation of the full covariance matrix. Similar techniques have been used for Incoherent Scatter Radar (ISR) parameter estimation [83, 66] and in satellite orbit determination [116], however, Chapter 4 describes a first application of these statistical signal processing techniques to the field of specular meteor radar. The dissertation reaches a denouement in Chapter 4 with a new approach for specular meteor radar low-level signal processing and statistical array calibration.

This work aims to reduce uncertainties in specular meteor radar remote sensing measurements by providing a universal data acquisition and radar control platform in addition to developing the MMWR technique enabled by CoSRad's multistatic phase synchronous capabilities. Three primary advancements in the field of specular meteor radar are described in this dissertation:

- (1) **Numerical modeling of the ground illumination pattern generated by specular scatter of radar pulses from meteor trails with arbitrary receiver/transmitter geometry strongly motivates the development and deployment of multistatic specular meteor radar.**
- (2) **A universal software-defined radar transceiver, the Colorado Software Radar (CoSRad) has proven the fundamental viability of the multistatic specular meteor radar measurement technique. First of their kind specular meteor trail observations are presented in Chapter 3.**
- (3) **In Chapter 4, the problem of meteor radar interferometry and statistical uncertainty is elegantly solved by casting the relevant equations onto the complex plane and performing a global search for the objective function minimum using a nonlinear least squares (NLS) iterative technique.**

## 1.2 Background

“If I have seen further than others, it is by standing upon the shoulders of giants” -Isaac Newton

Earth’s middle atmosphere at a height range of 80-110 [km] has historically been a challenging measurement domain as the region’s altitude is too high for sounding balloons and too low for satellite measurements. Observations [112] and modeling [45] suggest that anthropogenic climate change will cause large observable changes in the mesospheric region, motivating the development of better observational tools for this region of the atmosphere. Various rocket campaigns [85] have measured the wind and chemistry with limited spatial and temporal coverage, whereas passive optical measurements are limited to specific emission layers only visible at night. Specular meteor radars transmit in the lower-VHF band (typically 20-60 [MHz]) and have been used for many years to measure mesospheric winds. Since 1929, meteors have been a serious topic of study in radio science when Nagaoka [99] first suggested that meteors entering Earth’s atmosphere caused disturbances in atmospheric ionization capable of modifying the propagation of radio waves. Since that time, radar remote sensing has developed into an expansive field concerning the study of Earth’s various atmospheric regions through their interactions with radio waves, of which the study of meteors and related phenomenon is one component. Meteoric studies encompass a wide range of topics including meteoric origins, ablation, plasma processes and upper atmospheric winds. During ablation in Earth’s atmosphere, meteors deposit trails of temporary ionization which are advected with the background flow [123, 95]. When probed with a Meteor Wind Radar (MWR) measurement system, the trail can reveal details in the structure of the upper atmospheric wind field. The canonical all-sky MWR statistically combines a number of individual meteor trail position and velocity measurements over some height window producing a vector estimate of the windfield spatially and temporally averaged over some time period, typically 30-60 [minutes] [23].

The Colorado Software Radar (CoSRad) addresses a number of issues with traditional meteor wind radar systems, in addition to enabling new types of measurements based on the multistatic radar topology outlined in Chapter 2. Capable of direct-convert sampling over the VHF band, CoSRad has the ability to

replace the large variety of currently operating systems with a single common data acquisition and control solution. CoSRad is fundamentally a data acquisition system with extensive timing and control capabilities specifically designed for integration with existing specular meteor radar remote sensing systems. After data acquisition, any latency tolerant signal processing algorithms may be implemented. When configured for VHF data acquisition, no intermediate frequencies are necessary thereby solving the problem of imbalances between the  $I$  and  $Q$  channels of traditional receivers, and when configured for phase-synchronous multistatic operation, a geographically distributed network of CoSRad receivers has the capability to measure common-volume winds solving the problem of windfield homogeneity endemic to all monostatic MWR systems [122]. Furthermore, a multistatic network of inexpensive receivers enables mesoscale windfield monitoring systems capable of covering large geographical areas. Most directly applicable to this dissertation, the CoSRad multistatic radar facilitates implementation of common volume meteor wind experiments by exploiting the forward-scatter specular meteor trail signal.

Primarily studied in the context of long distance communication links, meteor trail forward-scatter has received little attention from the radar remote sensing scientific community until recently. Primarily due to complex system designs, the Doppler information contained in the forward-scatter specular meteor trail echo has not been incorporated into any statistical wind estimation procedures. Older specular meteor radar systems did not have the phase coherence capability to extract reasonable Doppler information, however, accurate GPS-synchronous receivers such as CoSRad have removed this limitation. One comprehensive theory on oblique meteor trail scattering has been formulated by Jones [76]. Jones' theory is an extension of Poulter and Baggaley's full-wave backscatter case [107] of which considerable experimental evidence does exist, however, little experimental work has been done in support of the full-wave forward-scatter theory. Using the "classical" forward-scatter theory, one can calculate the power from a trail with constraints on the geometry (see Section 2.1), however, the calculation of a ground illumination footprint using the classic forward-scatter radar equation as given by McKinley [95] is troublesome because the formulation assumes the trail is tangent to an ellipse with foci at the receiver and transmitter locations. Recently, Tinin [126] has combined the classic theory with first-order perturbation analysis containing a term for arbitrary cross-

sectional electron density profiles enabling straightforward ground illumination pattern calculations from meteors having arbitrary geometry with respect to the receiver and transmitter. The numerical Ground Illumination Pattern (GIP) simulations in Chapter 2 based on this work suggest that specular scatter from meteor trails using a single transmitter should be detectable by receivers distributed over a large geographical area. In Chapter 3, the first phase-synchronous forward-scatter observations of their kind using two geographically separated CoSRad receivers configured for multistatic specular meteor trail observations are presented.

In addition to enabling new insights into meteor physics, a multistatic network of receivers has the potential to measure winds in a common volume using a larger angular measurement diversity, eliminating the need for the homogeneous windfield assumption which is commonly used in monostatic meteor wind inversion techniques. Current monostatic MWR systems measure the radial component of the wind velocity using two nearly orthogonal look angles from a single point on the earth, and fit the observed radial velocities to the meridional and zonal wind components assuming wind homogeneity over the radar’s field of view. Geographically distributed interferometric receivers enable the identification of a common volume as seen by both antenna arrays, where the wind is assumed constant in the volume thereby increasing the spatial resolution as compared to the monostatic MWR as is illustrated in Figure 1.3. With traditional monostatic specular meteor radar, a single wind vector estimate  $\hat{\mathbf{u}}(\mathbf{r}_i)$  is generated which represents the spatially averaged wind in some height and time window. In the general multistatic case, a vector field representing the windfield is generated which represents the wind with an arbitrary spatial and temporal resolution  $\hat{\mathbf{u}}(\mathbf{r}_i)$  over some desired height and time window. The general form of the multistatic specular meteor wind radar vector field equation including the instrument precision terms of Chapter 4 is described in Section 4.6.1.

A universal software defined data acquisition system brings a number of technical and scientific advances to the field of radar remote sensing. A lack of ground-based instrumentation enabling mesoscale and common-volume, multifrequency studies is identified by the DASI initiative [29] and Mathews [93] as current challenges in providing experimental evidence for various aspects of meteor physics and for continued char-

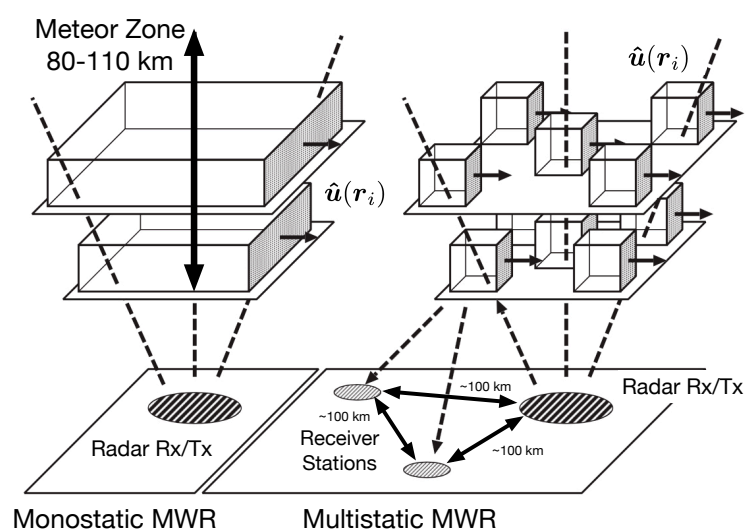


Figure 1.3: Conceptual illustration adapted from [101] of how multistatic meteor wind radar can increase the spatial resolution and spatial extent of the mesospheric wind estimate. Temporal resolution is improved through increased trail detection rates. For multistatic meteor wind radar, the receiver stations are distributed over length scales of 100's of km as opposed to 10's of km for meteor orbit determination radars such as SAAMER-OS [69] or AMOR [92].

acterization of the overall geospace environment. Furthermore, CEDAR’s strategic vision of 2011 identifies the “development of observational and instrumental strategies for geospace systems studies” as a strategic impetus for the coming decade. With respect to radar remote sensing, these needs are directly addressed with CoSRad, a phase synchronous, multistatic and reconfigurable data acquisition system and radar controller. Efforts to configure the Advanced Meteor Orbit Radar (AMOR) as a MWR [92] (see Section 1.3.1) provides an interesting case study in the potential benefits of implementing CoSRad-based data acquisition and demonstrate how straightforward implementation of mesoscale and macroscale networks of MWR are enabled through the deployment of CoSRad with existing radar facilities. Capable of direct-convert sampling over the VHF band, CoSRad could replace nearly every currently operating specular meteor radar receiver with a well-characterized, common data acquisition and control system. Assorted and often proprietary algorithms used to interpret observations from different systems has historically been a source of measurement uncertainty as is currently the case with the Jicamarca All Sky Meteor Radar (JASMET) located at the Jicamarca Radio Observatory (JRO) [48] near Lima, Peru. Additionally, CoSRad has the capability to operate as a universal radar receiver over many radar topologies as demonstrated by collaborations with Dr. Christopher Williams [136] in the development of a Linear Frequency Modulation Continuous Wave (LFMCW) tropospheric boundary layer radar. From a scientific standpoint, CoSRad enables straightforward phase-synchronous, multistatic, multifrequency studies of meteor phenomenology. Common-volume wind measurements enabled by multistatic MWR can remove the assumption of all-sky wind homogeneity (see Section 1.3.2) thereby increasing the spatial resolution and enabling the study of gradients within the windfield [122].

A number of measurement campaigns demonstrate CoSRad’s capabilities. Specular meteor trail echoes observed by configuring CoSRad for use with both the JASMET array and the Colorado Obninsk Radar (COBRA) [38] array located in Platteville, CO exemplify CoSRad’s potential for reconfigurability. A multistatic observation campaign conducted in Dec, 2014 in South Australia showcase the first major results of their kind using software defined remote sensing radar configured for multistatic meteor wind radar observations. Specular meteor trail scatter originating from a transmitter located in Delamere, Australia was

observed at a co-located Jones [74] interferometer and at a phase-synchronous forward-scatter station located 86 [km] away in Adelaide, Australia.

### 1.2.1 Meteor Science

The early experimentation in meteor radar science is interesting and provides a valuable historical perspective on the current state of meteor wind radar. The casual observer may consult Buderer [14] for a general historical overview of radar. Perhaps the first suggestion that E-region disturbances caused by meteors could modify the propagation of radio waves was provided by Nagaoka in 1929 [99]. By this time, the existence of the ionized E and F layers was known along with their predictable solar-induced ionization cycles. During the International Polar Year of 1932, various observations of irregularities in nighttime E-region ionization led to Appleton and Naismith's conclusion that "Either the recombination of ions is prevented or there is some ionizing agent present which can influence the dark side of the earth" [2]. Only a few years later in 1935, the first conclusive experimental evidence that sudden transient increases in E-region ionization were caused by ablating meteors was presented by Skellett [120] who correlated radio meteor echoes from the Leonid shower using a primitive ranging radar with visual meteors. Humorously, his first attempt at such a measurement campaign was unsuccessful due to a mysterious "magnetic disturbance," with no additional information provided. By this time, the existence of the ionospheric E and F regions was well established [1] placing a rough lower bound on the electron density of meteoric ionization. Daytime E-region electron number density is on the order of  $10^5$  [cm<sup>-3</sup>] having a critical frequency of 3 [MHz] as given by Eq 2.4. Only waves with frequencies below the critical frequency are reflected by a plasma, therefore observed meteoric ionization must have an electron density above that of the E-layer to be observed at frequencies higher than the known E-layer critical frequency thereby placing a lower limit on the ionization. At this time, the idea of a meteor trail as an 'elongated plasma inhomogeneity' was still forming, and the available observations did not support conclusions on ionization geometry beyond that of transient, spatially diffuse cloud-like irregularities in E-region ionization coincident with meteor showers. At this time, meteoric

ionization had only been directly associated with visible showers, however, a constant background of sporadic “ionization-bursts,” similar to those recorded from visible meteors had been observed with a diurnal and seasonal variability. The “ionization-bursts” were suspected to be meteoric in origin, and the first compelling evidence supporting a constant influx of meteoric dust into Earth’s atmosphere was provided by Appleton [3]. After the existence of E-region ionization of meteoric origin was confirmed, [53], controversy in attempts to mathematically describe the phenomenon began to emerge.

The first measurement suggesting bulk motion of transient E layer ionization shown in Figure 1.4 was recorded by Eckersley and Farmer [33] who observed phase changes in the scattered wave using a primitive interferometer thereby suggesting motions of a coherent scattering center. In an extraordinary example of how interpretations of observations in the absence of developed theory can lead to erroneous conclusions, the authors used the result in Figure 1.4 as an argument **against** ionization of meteoric origin. They reasoned “that the scattered echoes could not be due to single clouds but to a number of centers distributed widely in the E region or to a shower of particles entering the atmosphere-and hence that their origin could not arise from meteoric ionization.” Incredibly, the authors go on to identify the mechanism of motion (wind): “with some certainty that the echoes are of such a nature as to be inexplicable in terms of single clouds in the ionosphere, unless these are assumed to move during their lifetime with enormous and random velocities; and other considerations make this supposition very unlikely.”

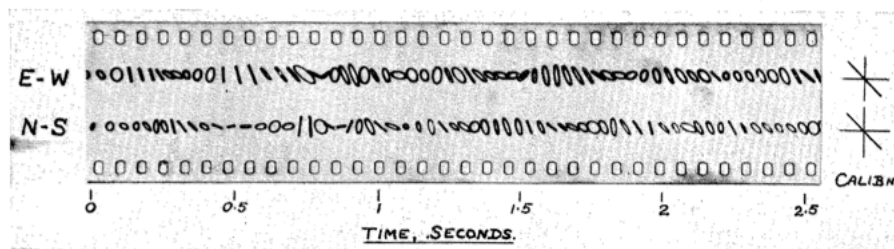


Figure 1.4: First measurement of the phase changes in a meteor trail echo at  $f_o = 7.6$  MHz suggesting motion of the scattering center. Originally reasoned as evidence against meteoric ionization, this may be the first Doppler measurement of the radial velocity component of a drifting meteor trail.

By 1948 the idea of meteor trails consisting of elongated clouds of ionization had been gaining popularity through antenna aspect sensitivity studies. Prentice and Lovell observed the vast majority of echoes

from showers when the antenna beam was pointed normal to the meteor trajectory [109], a phenomenon explained by the idea that meteors deposit long columns of ionization. Meteor observations had now reached the level of sophistication needed to test the three theories of meteor trail scattering at the time. Built on work done by Blackett [13], theories proposed by Eckersley [32], Pierce [106] and Lovell [89] were tested using observations interpreted under with Herlofson's [88] theory suggesting that electron diffusion, and not recombination was the primary factor in determining echo duration, an assumption recently called into question under some circumstances [139]. Evidence at the time supported Herlofson's two primary claims that a diffusion dominated echo duration should strongly depend on the radar wavelength by a factor of  $\lambda^2$ , and that the orientation of the antenna pattern with respect to the earth's magnetic field should have a measurable effect on echo duration under certain circumstances. Meteor trails experience anisotropic diffusion, where the parallel component of the diffusion velocity with respect to the earth's magnetic field will be larger than the perpendicular component. This was predicted to shorten the specular echo duration for trails oriented perpendicular to the earth's magnetic field. The first claim was experimentally verified by observing the same trails using multiple frequencies [89], and the second by observing trails from the same shower at the same time from multiple antenna angles and locations [88]. Eckersley's theory of scattering from ionization having a cloud-like geometry fails to predict the observed aspect sensitivity. Pierce's theory assumes a highly ionized trail having a radius **larger** than the radar wavelength where the majority of the meteor's kinetic energy is converted into ionization, essentially a large, dense cylinder of ionization. Both Eckersley's and Pierce's theories predicted electron densities in large disagreement with Herlofson's accepted values as determined through coincident measurements with visual meteors. Lovell and Clegg's theory of scattering from an ionization column with a radius **small** compared to the radar wavelength explained the majority of observations, and their measurements of electron density were in decent agreement with Herlofson's theory. One of the earliest experiments based on Lovell's radar equation was to measure the velocity of meteors using the diffraction fringes or **Fresnel intervals** that form as the meteor deposits an ionization trail with a sharply defined edge [21]. More recent work on Fresnel diffraction from meteor trails has introduced the "Fresnel Transform" [34] as a promising technique for the study of meteoric velocity and fragmentation through the identification of superimposed Fresnel oscillations suggesting parallel trails.

Lovell’s meteor radar equation accurately predicted the electron density, frequency dependence and Fresnel oscillations associated with a trail assuming the electron density is sufficiently low so each electron radiates independently of all others. Herlofson saw the inability of Lovell’s theory to predict a defined boundary between the single and multiple scattering regimes, and in 1951 refined his earlier work to address this problem [52]. Herlofson’s revised work was the first formulation of a “full-wave” theory where the entire scattered EM field is solved using Maxwell’s equations under a set assumptions of which the low-density, backscatter formulation of Lovell is a special case. Herlofson’s more general scattering theory led to the work of Kaiser and Closs [77] where, unlike Herlofson’s theory, the solution is derived without limits on the electron line density or trail radius. Like Lovell’s work, these two theories were formulated under the assumption of normal incidence meaning that  $\hat{\mathbf{E}} \times \hat{\mathbf{z}} = 1$  (See Figure 1.5). Kaiser and Closs’s theory patches together reflection coefficients, making no assumptions for initial electron density or trail radius and solving Maxwell’s equations for a long cylinder. One primary result of this work was that the decay in meteor echoes is not due to recombination of the ions and a subsequent reduction in electron density, but rather destructive interference resulting from the ambipolar diffusive expansion of the trail. Today the literature refers to two primary types of specular echoes based on Kaiser’s work, **overdense** and **underdense** where a transition region of electron line density exists between the two from  $10^{12}$  to  $10^{14}$  [electrons/meter]. When the electron line number density exceeds  $10^{14}$  [ $\text{m}^{-1}$ ], the dielectric constant becomes negative and the trail scatters like a metallic cylinder. As the trail expands, the dielectric constant increases as a function of trail radius, becoming positive during the transition region. When the dielectric constant becomes significantly larger than one, the column is considered to be a dilute plasma where the single-scattering assumptions apply. Using the Fresnel Transform Elford [34] has claimed a remarkable capability to measure the diffusion velocity of a slightly overdense trail to a precision of  $\pm 1$  [cm], an assertion which should be reexamined in light of the instrument precision analysis of Chapter 4.6.

Kaiser’s theory also outlines the idea of ambipolar diffusion as the primary mechanism governing a trail’s radial expansion. This type of diffusion occurs in a plasma when the electron thermal velocity is much greater than the ion thermal velocity, which is usually the case as the electrons are much less massive

then the ions. When a newly formed meteor trail begins to diffuse into the surrounding neutral region, the electrons initially diffuse more quickly (because of their lower mass) resulting in a charge separation giving rise to a radially directed electric field. Coulomb forces acting on the electrons and ions by the naturally emergent electric field slows the outward radial motion of the electrons, and increases the radial velocity of the ions, creating a net radial motion referred to as ambipolar diffusion [49]; a topic of much study in the recent literature [27, 26]. Major advances in the backscatter theory came to an end with Poulter and Baggaley's full-wave theory [107], and artfully summarized a year later by Poulter [108].

During the same time that Herlofson and Kaiser were constructing their full-wave solutions for specular radar, Eshleman published his initial theory on forward (oblique) scatter from meteor trails [36], which is essentially identical to that found in McKinley's seminal book, *Meteor Science and Engineering* [95]. Primarily studied in the context of long-distance communication links, oblique scatter has received little attention as a tool for meteor and atmospheric studies due to a lack of theories with which to test experimental data, and the complicated geometries and systems necessary to perform scientific measurements in the oblique scatter case. For thirty years, only two sources seemed to have attempted serious formulation of oblique meteor trail scatter. Eshleman's theory is an extension of Lovell's backscatter radar equation, showing that in the forward scatter geometry, echo amplitudes can increase by a factor of  $\sec \phi$  where  $2\phi$  is the forward scattering angle between the transmitter and receiver due to the relative lengthening of the first Fresnel interval at the receiver (see Figure 2.1). Furthermore, echo decay rates would decrease as if a wavelength of  $\lambda \sec \phi$  were used at the transmitter. This effect is actually caused because the Bragg wavelengths are different in the forward and backscatter cases [122]. Similar to the backscatter case, a condition of specularity where the trail lies tangent to an ellipse with foci at the transmitter and receiver is assumed. Building on Eshleman's initial formulation of forward scatter, Hines and Forsyth [55] placed an upper limit on the received echo power assuming overdense trails. Following Hines, no thoughtful work on the theory of oblique trail scattering was conducted until 1990 with a series of three papers by Jones and Jones [73] outlining the full-wave calculations for oblique scatter. The full-wave theory assumes a Gaussian plasma distribution and solves Maxwell's equations using numerical techniques. Most recently, Tinin [126, 125] has provided an

expression for the calculation of the oblique scatter ground illumination pattern based on first approximation plasma perturbation theory (see Figures 2.17, 2.18 and 2.19). Apparently, very little work has been done in providing robust experimental evidence supporting the full wave theories of Jones or Tinin.

A first understanding of meteor trail formation and scattering is aided through the identification of some interesting physical properties of the processes. When the trail reaches a radius larger than  $\lambda/2\pi$ , the reflection coefficients decrease rapidly. This critical radius leads to the idea of a wavelength dependent height ceiling because the initial trail radius  $r_o$  varies as a function of the atmospheric molecular mean free path which is in turn related to the density  $\rho$  and meteor velocity  $V$  through the parametric approximation  $r_o \approx \rho^{-0.3} V^{0.6}$  [98]. Meteors with increasing ablation height produce trails with larger initial radii eventually exceeding the critical radius of the probing wavelength resulting in a biased trail height distribution [121]. A similar effect is also observed concerning the meteor head echo [134]. Two additional interesting properties naturally arise from the ambipolar diffusion of the plasma trail. The first is a polarization dependent resonance in the underdense trail, and the second is a trail decay constant depending only on the trail height and wavelength of the incident wave assuming an underdense trail. Ambipolar diffusion theory predicts the trail will expand through a region meeting the geometrical condition for a plasma resonance causing a temporary increase in the perpendicular scattering coefficient thereby enhancing the scattered wave, a phenomenon which may enable direct experimental evidence in support of the current full-wave theory [72] [9]. Figure 1.5 depicts the electric vector oriented perpendicular to a meteor trail. Finally, the rate at which ambipolar diffusion causes a decrease in the echo amplitude of an underdense trail is constant at a given height, dependent only on the radar wavelength. This is not to be confused with the total time the echo is observable with a given receiver, but rather the rate at which the echo amplitude decays (the decay time constant). Crude estimates of meteor heights have been calculated using the echo decay [42], however, this technique only applies to trails firmly in the underdense regime  $N_e \ll 10^{14}$  [elec/m]. Ambipolar diffusion leads to one important reason justifying the use of full-wave theories for interpretation of meteor trail echos. During the transition region as a trail diffuses from overdense to underdense, the mechanism by which a Doppler shift is imposed upon the radiated wave transitions from that of an expanding metallic cylinder to

the bulk motion of a cylinder of electrons moving with the neutral wind. Clearly, wind estimates based on echos from such transitional trails could produce observational biases because a Doppler velocity measured from an expanding metallic cylinder does not represent the neutral windfield. This point has been discussed by Poulter [108] and briefly mentioned by Nechitailenko [100]. The field of meteor trail scatter is extensive, and many thesis can be found on the obscure details of the above topics. This discussion is intended to provide the reader with an overview of the primary ideas and physical mechanisms involved with the basic physical processes of meteor trail formation and scattering.

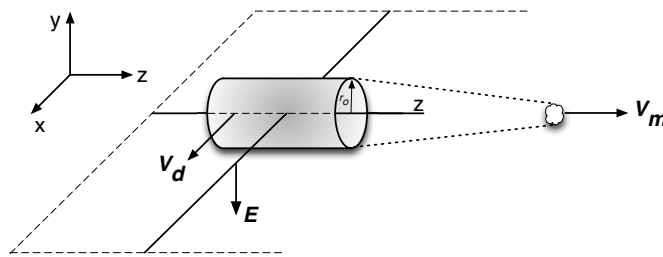


Figure 1.5: Under the traditional ‘backscatter’ meteor trail scattering theory, the electric vector of the incident wave  $\mathbf{E}$  is oriented perpendicular to the axis of the trail oriented along  $\hat{z}$ . The trail is assumed to diffuse into the neutral atmosphere along the radial coordinate in the  $xy$  plane.

In addition to the study of meteor, ionospheric and plasma physics, another important application involves the measurement of the upper atmospheric wind structure. Meteor wind radar (MWR) infers the horizontal wind by measuring the range and Doppler shift of the VHF radio pulses scattered from meteor trails sharing the neutral wind motion [5]. Through interferometric techniques [74], the elevation and azimuth of the trail is subsequently determined. A new interferometric technique for meteor radar is described in Chapter 4.4. The first measurements using this technique were accomplished in 1950 by Manning [91], and later Robertson [113]. Combining many height and Doppler measurements using statistical estimation theory [44] yields a measure of the windfield primarily used for atmospheric tidal analysis [97, 87] and recently for gravity wave observations [56, 96]. For an excellent history of early meteor observations using radio and radar, see Valentic’s PhD thesis [129].

A fundamental question naturally arises. How do we know that the ionized column shares the wind motion? The first analytical answer to this question was provided by Kaiser, Pickering and Watkins in 1969

[105] who showed that below 95 km, an ionized column should move with the ambient gasses unless closely aligned with the earth’s magnetic field. The answer to this question boils down to one fundamental idea: if the electron cyclotron frequency of a trail immersed in Earth’s magnetic field is much less than its collisional frequency with the neutrals, its motion is dominated by collisional processes (wind). Over the past 20 years there have been numerous meteor/lidar [39] and meteor/satellite wind comparisons [50, 30]. See Section 2.2 for a more detailed discussion of this topic.

Three case studies are helpful in providing a general overview of canonical MWR. The Georgia Tech Radio Meteor Wind Facility [114], the University of Illinois Meteor Radar System [43] and a number of related systems operating at Buckland Park in Adelaide Australia [130] all measure mesospheric winds using interferometric echo location. This basic measurement technique has undergone few significant changes over the last thirty years, aside from technological advances in data acquisition (a primary topic of this dissertation) and improvements in meteor diffusion modeling enabling more discriminatory wind measurements. For example, as more advanced models for meteor diffusion become available, earlier assumptions may prove to influence the derived winds. One such assumption is that of a negligible magnetohydrodynamic effect on trail motion and diffusion, which has come into question [100]. Another problem identified concerns the assorted and sometimes proprietary algorithms used to estimate and interpret the winds from different systems, which is directly addressed through CoSRad’s transparent signal processing chain for MWR.

### 1.2.2 Software Defined Radio

Software Defined Radio (SDR) is based on the idea that most radio signal processing tasks can be accomplished digitally assuming the use of a fast analog to digital converter (ADC). The feasibility of SDR has been enabled with the advent of high-speed ADCs and fast, reconfigurable signal processing hardware. With SDR methodology, the ADC is placed as close to the signal source as possible in the processing chain with a minimum amount of analog signal conditioning. Typically, only preselection filtering and

gain are applied to the signal before sampling. A number of textbooks are available on the topic of SDR, with Reed [111] being a comprehensive introduction. SDR brings two important improvements to radar remote sensing. By definition, SDR systems capture an entire band of the EM spectrum as defined by the sampling frequency, rather than isolating a narrow band of interest and recording only the signals of assumed importance. Most importantly, SDR systems are highly reconfigurable, a characteristic ideally suited for use in radar remote sensing. An appropriately designed SDR with integrated radar and timing control is capable of acquiring the data necessary for later calculation of atmospheric parameters using nearly all Mesosphere Lower Thermosphere (MLT) radars in existence today [60]. A common data acquisition platform capable of implementing the signal processing techniques described in Chapters 3 and 4 for all radar remote sensing systems would increase confidence within the MLT community that instrumentation errors are not affecting measurement results.

Along with the University of Colorado's active development of CoSRad, various groups are currently developing SDR systems for use with radar remote sensing. Most projects started with system prototypes based on commercial digital receiver cards such as those available from Pentek, Echotek or the Universal Software Radio Peripheral (USRP) project, and are now transitioning to custom hardware. The most active being groups at the University of Illinois [117], The Jicamarca Radio Observatory, [67] MIT's Millstone Hill Observatory [133, 46], the Institute for Atmospheric Physics in Germany [122] and Genesis Software [58], a scientific radar company based in Australia. A number of problems have been encountered with commercial systems when applied to remote sensing SDR. Viable SDR systems for radar remote sensing require a significant level of synchronization, including GPS time tagging, RF pulse generation and a minimum of five channels for MWR systems based on the canonical Jones [74] antenna geometry. Commercial receivers with this combination of hardware resources have historically been unavailable at reasonable price points, however the newly available Nutaq systems [137] show much promise. Various groups involved with SDR have anecdotally reported significant problems with the proprietary drivers and firmware included with the commercial systems. Designing custom hardware ensures maximum possible control and knowledge over the experimental apparatus, reducing the possibility of instrumental errors affecting scientific measurements.

These points underpin the potential benefit of a common radar remote sensing data acquisition and control architecture.

### 1.3 Problem Statement

The primary focus of this research has been the development of a new class of software defined radar transceiver system for use in radar remote sensing applications. This effort has culminated in the development of a prototype receiver architecture referred to throughout this dissertation as the Colorado Software Defined Radar or by the stylish acronym ‘CoSRad.’ More specifically, we have developed a software defined radar transceiver capable of multistatic, multi-frequency phase synchronous operation including software defined bandwidth and sampling techniques enabling integration with most existing remote sensing radars. Few radar remote sensing systems are immune to the benefits of the software defined model. Both those employing high power, large aperture antennas like many ionospheric remote sensing radars, and smaller systems such as Meteor Wind Radar (MWR) and MF/HF radars can benefit from a common data acquisition system architecture thereby reducing instrumental uncertainty through well-understood common hardware. A software defined reconfigurable and inexpensive remote sensing radar receiver is the ideal measurement tool permitting common data acquisition and analysis using currently deployed systems in addition to enabling the development of new systems. Ultimately, the CoSRad hardware/software platform endeavors to deploy a worldwide network of MLT radars based on a common hardware platform and non-proprietary data processing techniques. Enabling a reconfigurable, mobile and scalable platform having common data attributes and extensive reconfigurability supporting yet to be imagined experiments [46]. Within the geospace community, this work aspires to enable cost effective ground-based mesoscale radar remote sensing experimentation and system deployments.

### 1.3.1 Case Study in Reconfigurability

At the highest level, CoSRad is software configurable over the two fundamental parameters depicted in Figure 1.2. Both the sampling bandwidth  $f_s/2$  and carrier frequency  $f_o$  are independently programmable for each of the available 8 channels. Furthermore,  $f_s$  is dynamically configurable during operation and  $f_o$  is capable of various frequency sweep profiles enabling multi-frequency and LFM CW operation (see Figure 3.4). Higher carrier frequencies are implemented by the use of external up and down conversion hardware, while the sampling bandwidth is fixed at a maximum of 25 [MHz] (see Table 3.4). At this point, a brief case study is helpful in illustrating the benefits of reconfigurable multistatic software defined radar. Similar to SAAMER-OS [69], the Advanced Meteor Orbit Radar (AMOR) located near Christchurch, New Zealand is one of the more advanced radars employing multi-station capabilities [7]. AMOR measures range offsets through the time differences between detections at two remote stations (named Nutt and Spit) and combines this with an interferometric elevation measurement made at the primary station to spatially locate a specular trail and calculate the meteor trajectory and velocity. Originally designed as a meteor orbit determination radar, AMOR suffers from a number of synchronization problems when configured for wind measurements, requiring the implementation of complex reference oscillator schemes to measure the phase drifts between the receiver and transmit oscillators required for wind measurements [92]. While the results from the AMOR wind experiment do contain the expected meridional component of the semidiurnal tide, relying on a complex set of oscillators is not ideal. Furthermore, the remote stations only serve to spatially locate the specular meteor echo, and are not involved in the calculation of the radial wind component. As a result, the remote stations are not capable of measuring the phase of the received signal necessary for a Doppler (and therefore wind) determination. The primary challenge in using AMOR as a close-station MWR (10's of [km] receiver spacing) is lack of synchronization requiring a complex oscillator arrangement for determination of the Doppler velocity. CoSRad would completely eliminate AMOR's oscillator synchronization problem, providing a straightforward MWR implementation.

### 1.3.2 Scientific Motivations

CoSRad brings reconfigurable multistatic, multi-frequency, phase-synchronous, networked and common volume radar measurements to the field of radar remote sensing. Without drowning in the technical details of how these feats of engineering are accomplished, the following projects are of immediate interest. Building on work done by Malhotra [94], a project at the Jicamarca Radio Observatory (JRO) [41], proposes a multistatic interferometer configuration for the coincident study of various meteor radio echo phenomenon. Observing specular meteor trail backscatter is possible when a meteor trail formation geometry meets the backscatter specularity condition depicted in Figure 2.1. High Power Large Aperture (HPLA) radar, such as JRO’s primary array [65], will observe scatter from the head echo and non-specular trail. Using HPLA radar, coincident measurements of all meteor echo phenomenology is usually not possible as a trail meeting the specular scattering condition will not produce a head echo, of which the reverse is also generally true, however, some new results show that specular meteor radar systems are capable of observing head echoes under certain conditions [70]. Using a phase-synchronous interferometer located 10’s - 100’s of [km] away from the HPLA transmitter enables Doppler resolved coincident measurement of all primary meteor scatter processes. Various investigators have also proposed a common-volume comparison between non-specular winds derived using JRO’s primary array and those measured through the specular meteor radar technique [94, 102]. Mathews [93] identifies a number of specific scenarios in which multi-frequency measurements would alleviate identified issues surrounding VHF meteor radar. Specifically, because of the variation of a trail’s scattering cross-section as a function of frequency, a calibrated frequency-multiplexed radar could infer the initial radius of the trail, a parameter presented with some variability throughout the literature. Furthermore, Mathews makes a case for multi-frequency common-volume studies of so called “anomalous trail-echo formations” or “long-lived range-spread trail-echoes” as a function of the angle of the radar  $\mathbf{k}$  vector to the earth’s geomagnetic field. These observations should yield new insights into the plasma processes governing these events. These configurations based on the CoSRad architecture are intended to qualitatively describe the system’s intended operational capabilities. Clearly, the atmospheric and space physics communities would benefit from a universal receiver architecture specifically designed for radar remote sensing

systems.

Thus far, the primary application for this new class of receiver is the Meteor Wind Radar (MWR). Traditional MWR infers the horizontal wind by measuring the range and Doppler shift of the VHF radio pulses scattered from meteor trails sharing the neutral wind motion. Trail motion with the neutral wind is itself an assumption, not immune to the critical eye of review. Some work suggests that basis in wind measurements arise from the plasma's motion due to the earth's magnetic field [100]. The canonical MWR system consists of an array of transmit antennas illuminating the entire azimuthal sky with a 3 dB pattern usually from about  $30^\circ$  in elevation and losing gain approaching zenith. Specular meteor trail echoes are received with an interferometric array of antennas used to determine the echo's angle-of-arrival (AOA). The AOA combined with the radar range calculation allows for the determination of the 3D trail locations. Doppler shifts and echo location are sequentially processed to calculate the trail's radial velocity and fit a vector to the windfield. After a number of radial velocity measurements are averaged, a component-resolved wind measurement is said to represent the mean wind over some time interval, usually 30-60 minutes [23], where the variances associated with the calculated parameters are related to the final measurement error [78]. One of the primary difficulties identified in the analysis of MLT tidal phenomenon and wind measurements is the limited spatial coverage inherent with ground-based instrumentation. Developing a software reconfigurable data acquisition system capable of controlling both new multistatic systems and recording science data using existing systems in a "piggy back" configuration are benefits of the universal receiver solution. SDR is the ideal technological model in moving toward the creation of inexpensive and scalable systems capable of continuous multistatic mesoscale windfield observations. A number of groups have published results from various forward-scatter bistatic experiments, of which those associated with the European Bologna-Lecee-Modra system seem to be the most developed [19, 140]. The current literature contains few references concerning multistatic, common-volume MWR measurements of which the only serious historical consideration seems to be a report to the US Air Force from the Smithsonian Astrophysical Observatory [24]. Two very recent related publications indicate a new interest in the multistatic meteor radar topic, one using pseudorandom CW meteor radar from MIT in collaboration with IAP [133] and the

other describing an experiment currently being conducted at IAP [122].

As was mentioned in Section 1.2.1, little experimental evidence has been provided supporting the full-wave theory from the standpoint of the ground illumination pattern. A natural question arises: can we experimentally verify aspects of the illumination pattern predicted by the full-wave theory? The ground illumination patterns presented in Chapter 2 calculated using Tinin's formulation [126] suggest that a signal could be observed over a large geographic area given an appropriately configured network of receivers. Assuming Tinin's equations are a reasonable approximation of reality, one could envision a network of receivers spaced so as to sample the ground pattern and compare the measured illumination pattern with one calculated using various full-wave approximations. Simulation parameters include the transmitted power  $P_t$ , the angle between the  $x$  and  $x'$  axis  $\alpha$ , gain of the receiver  $G_r$  and transmitter  $G_t$  antennas, the radar frequency  $f_o$ , electron number density which has a Gaussian distribution along both dimensions of the trail  $N_e$  and the geometric dimensions of the trail with  $l_{\parallel}$  being the trail characteristic length, and  $l_{\perp}$  the characteristic trail radius. The electron number density has a Gaussian profile so that  $\sigma = l_{\parallel}$  and  $\sigma = l_{\perp}$  are the first standard deviations of the electron density profile along the primary and secondary axes of the trail. Calculations are performed over two reference frames. The  $(x, y, z)$  frame has an origin on the earth's surface where the center of the trail is placed on the  $x$ -axis at the desired height  $x_m$ . The  $(x', y', z')$  frame has an origin at the center of the trail, with the trail axes along the  $\hat{z}'$  direction lying in the  $\hat{x}\hat{z}$  plane. The two frames are related by a rotation matrix, Eq 1.1. The ground illumination patterns of Chapter 2 suggest that trails will produce forward-scatter echoes covering a significant geographical area. In Chapter 2, a multistatic experiment is proposed where a known distribution of meteor trails is observed over some temporal period. This amounts to observing a meteor stream as the radiant transits across the sky. Observation of the temporal evolution of the spatial asymmetry of the modeled aggregate illumination pattern would strongly support Tinin's formulation and the forward-scatter model.

$$\begin{bmatrix} x' \\ y' \\ z' \end{bmatrix} = \begin{bmatrix} \cos \alpha & 0 & \sin \alpha \\ 0 & 1 & 0 \\ -\sin \alpha & 0 & \cos \alpha \end{bmatrix} \begin{bmatrix} x \\ y \\ z \end{bmatrix} + \begin{bmatrix} -x_m \cos \alpha \\ 0 \\ -x_m \sin \alpha \end{bmatrix} \quad (1.1)$$

$$\begin{bmatrix} V_{ra} \\ V_{rb} \end{bmatrix} = \begin{bmatrix} \cos \phi_a \cos \theta_a & \cos \phi_a \sin \theta_a \\ \cos \phi_b \cos \theta_b & \cos \phi_b \sin \theta_b \end{bmatrix} \begin{bmatrix} V_x \\ V_y \end{bmatrix} = \mathbf{A} \mathbf{V}_w \quad (1.2)$$

Perhaps the most dramatic motivation for multistatic MWR is the possibility of reducing the assumption of windfield homogeneity. Eq 1.2 gives the zonal and meridional components of the windfield at some height as a function of the angle-of-arrival (AOA) and trail radial velocity neglecting the Bragg effect:  $(V_x, V_y) = f(V_r, \phi, \theta)$  which is acceptable for this qualitative example. The subscripts  $a$  and  $b$  refer to the specific receiver which measured the radial velocity and AOA of the echo. First, consider the case of two radial velocity measurements taken at a monostatic MWR, both having similar AOA coordinates to within a few degrees. Assuming the windfield changes slowly with respect to the time difference between detections, we could solve the system for the wind velocity components. But alas, the world does not allow such simplicity. The issue with this scenario is the ill-condition of matrix  $\mathbf{A}$ . In this scenario,  $\mathbf{A}$  will have a very large “condition number” ( $\kappa$ ) defined by Eq 1.3, qualitatively meaning that large changes in the solution  $\mathbf{V}_w$  will result from very small changes in the AOA matrix,  $\mathbf{A}$ . In the monostatic configuration,  $\phi$  and  $\theta$  are of similar values for detections from a common volume, therefore  $\mathbf{A}$  is nearly singular and errors in the AOA measurement will amplify, causing huge (in fact catastrophic) changes in the solution for the wind vector. Alleviating this obnoxious fact of reality requires assuming a homogeneous windfield over the radar’s field of view allowing the use of orthogonal AOA measurements to solve for  $\mathbf{V}_w$ . Next, consider the multistatic radar as depicted in Figures 1.3 and 1.7. With this configuration, one may define a volume in the field of view of both radars. Both receivers will measure different radial velocities  $V_r$  and AOA values from trails moving with a constant wind through the volume. Depending on the geometry of the multistatic system, we can now solve for the wind using the well-conditioned matrix  $\mathbf{A}$  whose elements are derived from more

nearly orthogonal AOA measurements. There is no need to assume a homogeneous windfield.

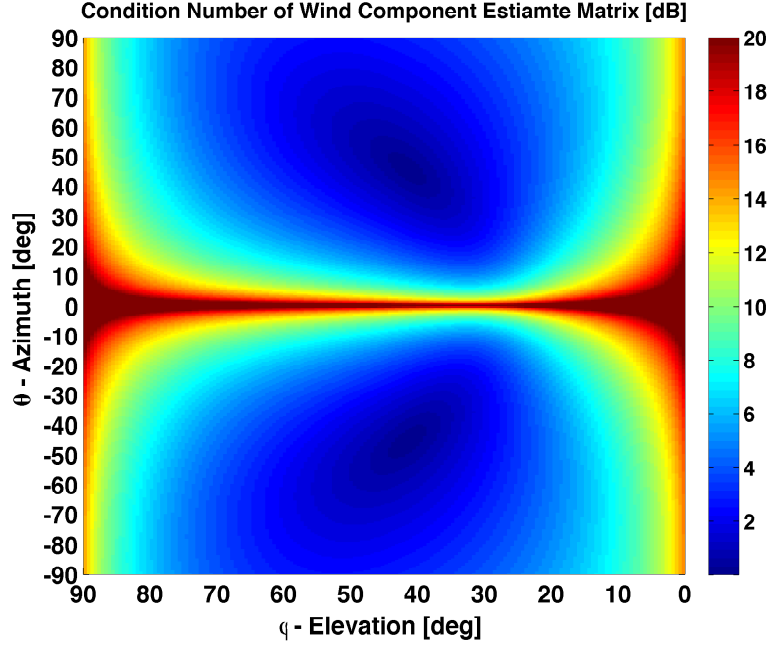


Figure 1.6: Condition Number of  $\mathbf{A}$  in Eq 1.2 using a common volume location specified by  $\phi$  and  $\theta$  with  $R_d = 150$  [km] and  $h = 95$  [km]. In the case of a monostatic radar,  $\mathbf{A}$  is ill-conditioned over the entire space requiring the homogeneous windfield assumption. with the multistatic system depicted in Figure 1.7,  $\mathbf{A}$  is well-conditioned for common volumes from approximately  $\pm(20^\circ$  to  $90^\circ)$  in azimuth and  $20^\circ$  to  $70^\circ$  in elevation.

$$\kappa(\mathbf{A}) = \|\mathbf{A}\| \cdot \|\mathbf{A}^{-1}\| \quad (1.3)$$

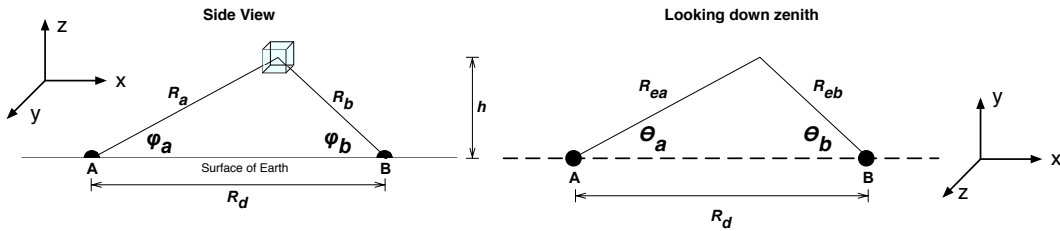


Figure 1.7: Multistatic system illustration. Receivers  $\mathbf{A}$  and  $\mathbf{B}$  are separated by a distance  $R_d$  on the order of 100's of [km]. A common volume is defined with elevation and azimuth positions defined by  $\phi_a$ ,  $\phi_b$  and  $\theta_a$ ,  $\theta_b$ . The range to the volume from each receiver is  $R_a$  and  $R_b$  and the magnitude of the projection of the range vectors on the surface of the earth are  $R_{ea}$  and  $R_{eb}$ .

Performing a common volume wind measurement requires the determination of three fundamental parameters. Figure 1.8 suggests that for each elevation and azimuth angle measured at a remote interfer-

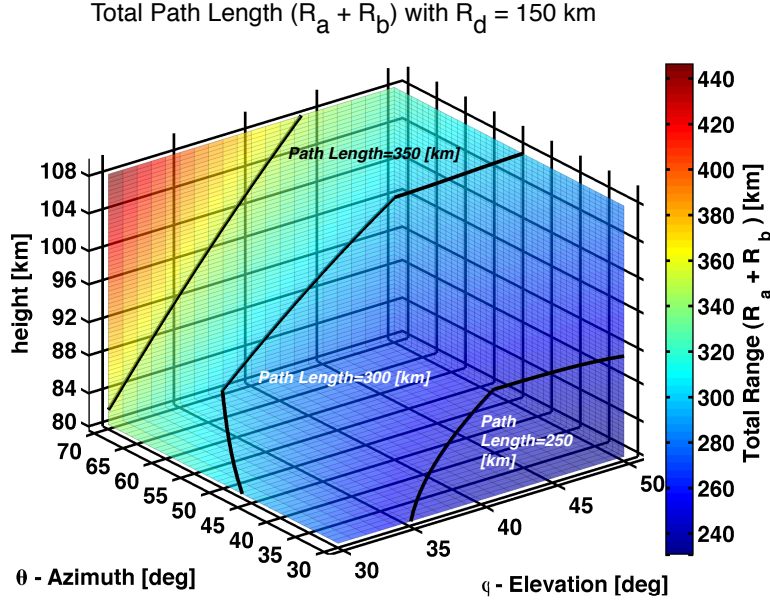


Figure 1.8: Using the quantities defined in Figure 1.7, a common volume is defined between the azimuth angles of  $\theta_a = 30^\circ$  to  $70^\circ$ , elevation angles of  $\phi_a = 30^\circ$  to  $50^\circ$  and over a height of 80-110 [km]. Within the volume, the total range from a scatterer ( $R_a + R_b$ ) is calculated between two receivers **A** and **B** separated by a distance  $R_d = 150$  [km]. Contours of three surfaces of constant path length at 350 [km], 300 [km] and 250 [km] within the volume are indicated.

ometer **A**, there exists a unique range. Therefore, the three pieces of information measured at the remote receiving interferometer ( $R_a + R_b$ ,  $\theta_a$ , and  $\phi_a$ ) define a unique position within a common observation volume of two interferometric specular meteor radar arrays. If two surfaces were to intersect within the volume, this would indicate that a given AOA and range measurement could occur at multiple locations within the volume, a situation requiring careful treatment. All receivers involved in a common-volume multistatic configuration must have ranging, Doppler and interferometric AOA measurement capabilities. Of these three measurements, range and Doppler require an inter-station synchronization mechanism to ensure phase coherence and measurement accuracy. For example, free-running oscillators on two geographically separated systems will experience a relative, random frequency drift. Assuming the transmitter is synchronous with its collocated receiver, a random drifting frequency at the remote receiver introduces a significant frequency error in Doppler. Furthermore, accurate determination of the range requires knowledge of the time of the transmit pulse to within the desired range resolution of the measurement. Past systems have accomplished this through an analyses of the transmit pulse observed at the remote receiver.

The meteor radar literature is sparse on the topics of interferometry solution techniques, instrument precision and calibration. Indeed, many past investigators have simply ignored measurements of meteor trails lying outside the expected meteor zone heights and labeled them as “outliers” to be removed from the subsequent wind analysis. Unsurprisingly, there are no compelling citations for this dubious tradition, however, in my many conversations with various experts in the field, I have concluded that the practice is more widespread than the literature suggests. Jacobi speaks of “outlier rejection” in his wind fitting but offers no additional details [68]. Hocking writes about outlier rejection in [58]: “This procedure tends to ‘clean up’ the data.” If measurements which do not fit an investigator’s assumed physical model are labeled “outliers” and ignored, then the resulting data will tend to have good agreement with the assumed model! The known (but unquantified) precision degradation of the Jones interferometer at lower elevations is a motivating factor behind the dismissal of echoes originating from below  $\sim 40^\circ$  in elevation in many studies [56]. Ignoring low-elevation echoes is not wholly unreasonable if we impose field-of-view restrictions on the array, however, the ultimate goal should be to quantify the measurement precision of every observed echo, and select echoes for processing based on this metric.

The problem of ignoring ‘outlying’ observations must be addressed if the meteor radar community is to deploy multistatic meteor wind radar relying on lower-elevation forward-scatter echoes. Various authors have attempted to address the problem of meteor radar interferometry using odd mathematical schemes. Three papers are often cited in the literature [74, 63, 64] as the current standard for meteor radar interferometry and calibration. The standard Jones array is a simple antenna configuration for sparsely sampling the spatial wavefield generated by a single source (meteor trail). Unfortunately, solutions to the interferometry problem using the Jones array described in Holdsworth’s papers are mathematically inelegant and overly complex, resulting in an enormous degradation of the potential interferometry results, especially for echoes below  $50^\circ$  in elevation and at low SNR. Cervera [18] explicitly states the use of Holdsworth’s calibration and angle-of-arrival techniques for echoes at 10 dB SNR, which the simulations of Chapter 4 suggest have poor solution quality. The principle of Holdsworth’s statistical calibration technique has a solid conceptual foundation, but his approach must be reformulated onto the complex-plane and put into a functional form for practical

application (as was partially accomplished by Dr. Chau in Appendix A). Chapter 4 presents the first self-consistent and mathematically elegant solution to the related problems of meteor radar interferometry, instrument precision and calibration.

## Chapter 2

### Meteor Trail Physical Theory and Numerical Modeling

“All of physics is either impossible or trivial. It is impossible until you understand it, and then it becomes trivial.” – Ernest Rutherford

#### 2.1 Classical Meteor Trail Scattering

Every day, billions of particles enter Earth’s atmosphere and mostly evaporate due to atmospheric friction starting in the lower E region of the ionosphere corresponding to the mesospheric region of Earth’s atmosphere. Ablating meteors deposit a strongly elongated plasma inhomogeneity in Earth’s upper atmosphere along their trajectory. The meteor trail is almost entirely composed of ionic vaporized meteoric material [123]. Trails form with an initial radius on the order of 0.5 [m] at 80 [km] and increase with height to 2 [m] at 100 [km] [6] with a linear extent of 10-30 [km] and mean length of 25 [km] [35]. As with all fields of science, the classical theory is usually the simplest description. From the classical meteor trail scattering Eqs of 2.1, decreasing levels of physical assumptions and approximations lead to the more advanced and comprehensive theories based on Maxwell’s equations culminating in the full-wave theories of [76] and implemented by [126]. The more advanced theories provide insight into the fundamental plasma processes at the expense of added complexity, and are useful in interpreting radar echoes in the context of meteor and

plasma physics.

The theory of radio scattering by plasmas is a scientific field in itself, developed by those masochistic souls having the serendipitous combination of freakish intelligence and dogged determination. The simple treatment given here is an attempt to define the basic geometries and properties of scattering by meteor trails without drowning in the ocean of plasma physics. Specifically, the theory is outlined at a sufficient level to justify application of the phase synchronous multistatic receiver to the field of specular meteor radar. In the design of any remote sensing system, the signals of interest must be defined to such a level so as to make appropriate engineering decisions. Straightforward results of the multistatic configuration are an increase in the Bragg wave vector [122] which directly translates into an increase in the detectable trail height ceiling [95] and an increase in trail echo duration, and an increase in the number of detected echoes per unit common volume of the geographically distributed receiving array [133].

A number of important assumptions are made in the case of meteor scattering from electron trails. First, we assume that upon formation, the initial radius of the plasma trail is small compared to the wavelength ( $r_o \ll \lambda$ ). When the electron line density of the trail is below  $\sim 10^{14}$  [electrons/meter] [98] as is the case with most micro-meteors [72, 17], the trail behaves according to the ‘underdense’ scattering regime. When a trail is ‘underdense’, an incident electric field vector perpendicular to the axis of the trail fully penetrates the plasma column with negligible attenuation causing the electrons in a small segment the trail (ds) to oscillate and reradiate in-phase, allowing for the single-scatterer ‘Thomson’ approximation where the net reradiated field is the superposition of the fields created by each individually radiating electron which radiates as if no others are present. As the trail radius increases to a significant fraction of  $\lambda$ , scatter from different sections of trail’s radial cross-section can constructively interfere, causing an attenuation of the scattered field in the direction of the receiver. Because trails which form at higher altitudes will tend to have larger initial radii, a frequency dependent height ceiling is observed as reported by [95] and [122]. Some additional definitions for an underdense trail are sometimes employed. If the trail’s plasma frequency is below that of the incident wave, or if the dielectric function is positive [77] the trail may be modeled as un-

derdense. Typically, only echoes obtained from underdense trails are used for determination of the windfield [15]. The characteristic time scales of the trail's post-formation diffusion rate are assumed small compared to the time scales of the trail's initial formation. This implies we neglect the initial diffusion effects on the trail formation. The trail is assumed to have a Gaussian cross-sectional electron distribution satisfying the condition of quasi-neutrality so that any dimension of the trail is large compared to the Debye length of the plasma and volumetric parcels of the plasma larger than the Debye length are charge-neutral. Also, we assume that only free electrons contribute to the reradiated field because the mass of an electron is much less than the mass of a proton ( $m_e \ll m_p$ ).

Three primary classes of meteor radar echoes exist. Specular echoes occur when a column of ionization deposited by an ablating meteor scatters VHF frequencies having a wavelength larger than the trail radius [123]. Non-Specular echoes originate from ionized structures meeting the Bragg condition within the meteor trail [31] and head echoes result from the plasma ball surrounding the high-velocity ablating meteor [70]. Typically, only high power large aperture type radars are capable of observing non-specular echoes as their radar cross-sections are smaller than those of specular echoes. Specular echoes are routinely observed with lower power meteor wind radar systems [40]. Diffusion of the trail into the meteoric zone of Earth's atmosphere is of key importance in specular trail observations. A number of studies have attempted to infer temperature from the measured diffusion coefficients [84], and meteor wind radar measurements rely on the assumption that momentum is completely transferred from the neutral wind to the trail's electrons on timescales below the diffusion timescale. The accuracy of both temperature measurements based on trail diffusion and wind measurements based on neutral atmosphere momentum transfer rely on realistic physics-based descriptions of the trail diffusion process. This Chapter explores two modern theories of trail diffusion in the context of specular trail observations, and suggests a possible experimental technique to provide evidence for Dimant and Oppenheim's modern theory [27].

In the classical sense, specular scattering geometry is defined by a meteor trail forming tangent to the surface of an ellipsoid whose foci are the receiver and transmitter locations as shown in Figure 2.1. When the

receiver and transmitter are collocated as is the case with monostatic meteor radar, the ellipse has coincident foci and the surface becomes a sphere. The theory developed by McKinley [95] assumes all trails lie tangent to the elliptical surface mentioned above. This assumption, while mathematically convenient, fails to capture most trail geometries (in particular, those trail geometries not normal to the ellipse which accounts for most trail formations). If the trail has an elevation angle relative to the ellipse (the parameter not included in the basic forward scatter model) the classical form of the meteor radar equation does not apply. The more comprehensive treatment of scattering from cold collisionless cylindrical plasmas (a meteor trail) developed by Jones [76] and Tinin [126] are necessary to interpret and predict scattering from trails having arbitrary geometries with respect to the transmitter and receiver.

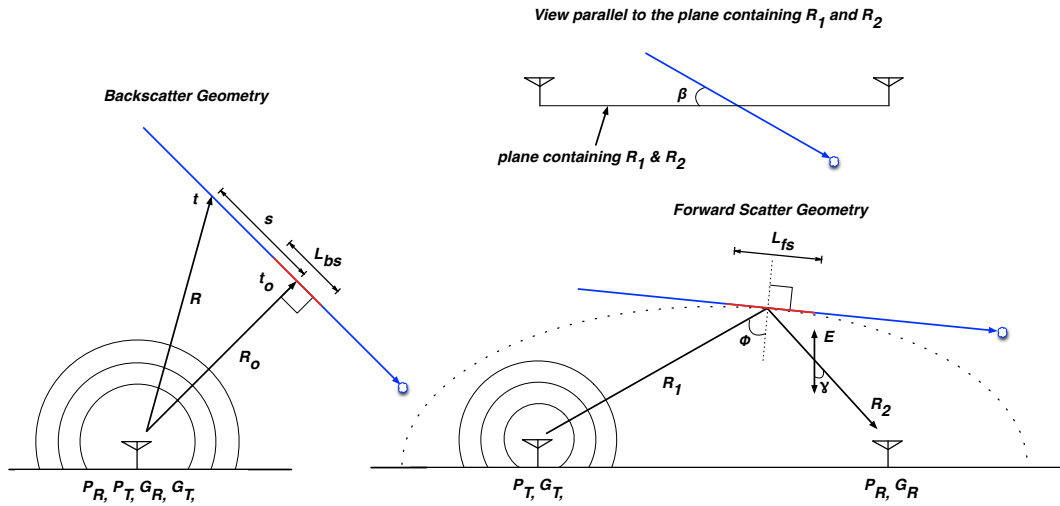


Figure 2.1: Classical scattering geometries defining the parameters in Eq 2.1.  $L_{bs}$  and  $L_{fs}$  are the lengths of the first Fresnel intervals in the backscatter and forward-scatter geometries. The Fresnel zone is the segment of the trail contributing most of the scattered power to the receiver [17].  $\gamma$  is the angle between the electric vector  $\mathbf{E}$  and the line of site to the receiver.  $\beta$  defines the trail's orientation in the plane tangent to an ellipse with foci at the receiver and transmitter.  $\phi$  is the classical 'forward-scatter' angle. Traditionally, monostatic specular radars have assumed  $\phi = 0$ .

Some interesting scattering features are observed from the classical meteor trail scattering Eqs of 2.1. An increase in both detection rates and improvement of Doppler frequency estimates due to longer decay times are possible with the multistatic, common-volume configuration. Because of the  $\sec^2 \phi$  term

introduced in the forward-scatter geometry, the power available at a remote receiver increases as can be seen by comparison with the backscatter case as is illustrated by the GIP visualizations later in this chapter. Furthermore, the diffusive time constant  $\tau$  increases (see Eq 2.6), leading to a slower decay of the forward-scattered echo. Finally, the attenuation due to the trail's initial finite radius given by Eq 2.1c decreases thereby raising the effective detection height ceiling [95].

The forward scatter meteor radar equation given by Eq 2.1a describes the power delivered to the receiver after trail formation [95]. Eq 2.1a reduces to the traditional specular meteor radar backscatter equation when  $R_1 = R_2$ ,  $\phi = 0^\circ$ ,  $\beta = 90^\circ$  and  $\gamma = 90^\circ$ . This suggests that the phase of the received wave changes with range as expected. Intuitively, this concept explains why Fresnel zones are formed along the trail. The Fresnel zone is the segment of the trail contributing most of the scattered power to the receiver. Electrons from each differential segment of the trail ( $ds$ ) are located at different ranges from the receiver and oscillate with incidence of the spherical radar wavefront, therefore the net scatter from each differential trail segment forms regions of interference in the reradiated electric field. Eq 2.1f gives the an apparent increase in  $\lambda$  for the case of non-zero specular scatter angle which is more accurately classified as an increase in the Bragg wavelength [122] and the corresponding radial trail velocity with respect to the remote station is then found using  $v_r = f_d \lambda_B$ . See Section 4.6.1 for a more detailed description of this phenomenon. This increase is also observed in the numerical simulations of Section 2.3. Notice that Eqs 2.1d and 2.1e also define the minimum spatial sampling along the meteor trail because the Fresnel interval contributes most of the scattered power to the receiver.

$$P_R = \frac{P_T G_T G_R \lambda^3 \sigma_e}{64\pi^3} \frac{N_e^2 \sin^2 \gamma}{(R_1 R_2)(R_1 + R_2)(1 - \sin^2 \phi \cos^2 \beta)} T_d A_e F_t \quad [\text{W}] \quad (2.1a)$$

$$T_d = \exp \left[ \frac{-16\pi^2 D t}{\lambda^2 \sec^2 \phi} \right] \quad (2.1b)$$

$$A_e = \exp \left[ \frac{-8\pi^2 r_o^2}{\lambda^2 \sec^2 \phi} \right] \quad (2.1c)$$

$$L_{bs} = \sqrt{2R_o \lambda} \quad [\text{m}] \quad (2.1d)$$

$$L_{fs} = 2 \sqrt{\frac{\lambda R_1 R_2}{(R_1 + R_2)(1 - \sin^2 \phi \cos^2 \beta)}} \quad [\text{m}] \quad (2.1e)$$

$$\lambda_B = \frac{\lambda}{2 \cos \phi} \quad (2.1f)$$

An additional product term given by Eq 2.2 and visualized in Figure 2.2 can be multiplied by Eq 2.1a to describe the time-evolution of the return power as a meteor deposits a trail of ionization within the radar beam. First given by Blackett and Lovell [13], this additional term describes the Fresnel oscillations observed during trail formation as the scattered wave fronts interfere as a result of the trail's abrupt edge within the radar beam during formation. In Figure 2.2,  $x$  is directly related to the meteor's location along its trajectory by Eq 2.3 where  $s$  is distance from the point of orthogonality  $t_o$ . The full scattering model of Eq of 2.1a including Fresnel oscillations is taken into account when forming simulated echoes using the meteor radar forward model like that shown in Figure 4.5.

$$F_t = \left( \frac{C^2 + S^2}{2} \right) \quad \text{where:} \quad (2.2)$$

$$C = \int_{-\infty}^x \cos \left( \frac{\pi x^2}{2} \right) dx$$

$$S = \int_{-\infty}^x \sin \left( \frac{\pi x^2}{2} \right) dx$$

$$x = \frac{2s}{\sqrt{R_o \lambda}} \quad (2.3)$$

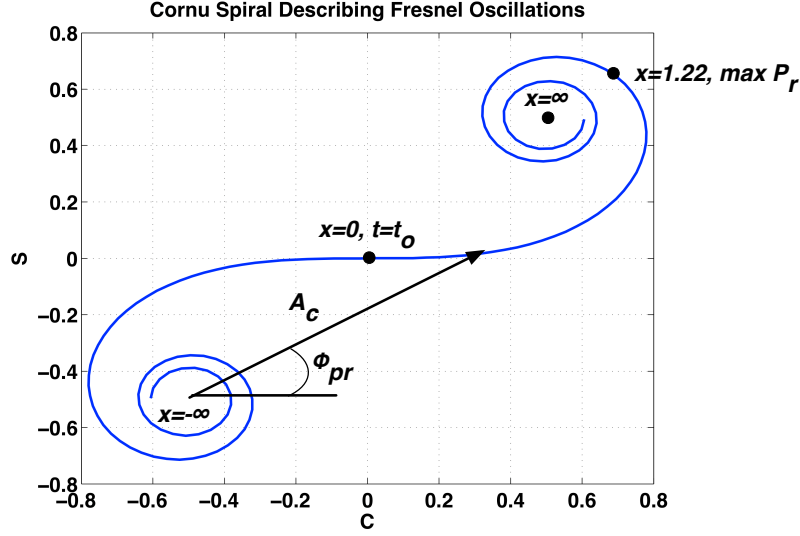


Figure 2.2: Cornu spiral describing Fresnel oscillations [98] present during underdense trail formation. In the classical backscatter case, Eq 2.1a is multiplied by the length of the vector  $\mathbf{A}_c$ . During trail formation, the vector  $\mathbf{A}_c$  remains anchored at  $x = -\infty$  and tracks the curve as the parameter  $x$  increases reaching a maximum at  $x = 1.217$ .

## 2.2 Diffusion

Various waves naturally exist in a cold, unmagnetized plasma. Consider the Langmuir wave [49, 110], which one can visualize by considering a plasma with a small electron displacement with respect to the ions away from an equilibrium position. The electrons will experience an electrostatic restoring force driving their return to the equilibrium position thereby restoring charge neutrality. When the electron positions spatially satisfy charge neutrality they will have acquired kinetic energy due to the restoring forces, causing them to overshoot their spatial equilibrium positions. The process repeats and is termed a Langmuir oscillation with a frequency given by Eq 2.4. In principle, both the ions and electrons are involved in Langmuir oscillations (there is also an ion plasma frequency), however, because the electron mass is much smaller than the ion mass, ( $m_e \ll m_i$ ) the ions respond far more slowly. With this assumption, the ions are considered stationary and Eq 2.4 is termed the ‘plasma frequency.’ Radio waves incident on a plasma having a frequency higher than the plasma frequency will penetrate the plasma, while waves with a frequency lower than the plasma frequency are reflected by the plasma.

$$\omega = \sqrt{\frac{N_e e^2}{\epsilon_0 m_e}} \quad (2.4)$$

The term  $A_e$  in equation 2.1a arises because the finite initial radius of the trail  $r_o$  has an attenuating affect given by Eq 2.1c. As the trail diffuses into the neutral atmospheric gas, the return power decreases by  $T_d$  given by Eq 2.1b and the trail's electron number density  $N_e$  in Eq 2.4 also decreases thereby lowering the plasma's critical frequency (which is the primary mechanism by which a trail transitions from the overdense to underdense regime). The physical interpretation of Eq 2.1b is fairly straightforward. If the cross sectional electron density is assumed to have an initial Gaussian distribution, and if we ignore the forces on the electrons caused by Earth's magnetic field below 90 km, then the rate at which the trail diffuses is based on the linear differential equation describing the diffusion of a gas. Under these circumstances, Eq 2.5 can be analytically solved for  $N_e(r, t)$  producing an exponential with a decay time constant given by Eq 2.6 [139] where  $D$  is an ion diffusion coefficient given as a function of height in Figures 2.4 and 2.3. Figure 2.3 shows that ion diffusion in the meteor zone is unaffected by the geomagnetic field as  $D_{i\parallel} \simeq D_{i\perp}$  below 115 [km] and  $\Omega_i < \nu_{in}$ . Well above 97 [km],  $\Psi \ll 1$  and  $D_{e\perp} \ll D_{e\parallel}$ , therefore the electrons of trails closely aligned with the geomagnetic field will experience inhibited diffusion in the  $\mathbf{B}_\perp$  direction as  $D_{e\perp} \ll D_i$ . Electrons of high-altitude trails ( $\Psi < 1$ ) forming with a misalignment with respect to  $\mathbf{B}$  experience significant asymmetric diffusive components out of the trail's cross-sectional plane as components of their gyromotion are parallel to  $\mathbf{B}$ , and  $D_{e\parallel}$  is the dominant diffusive term when the gyrofrequency terms dominate over the neutral collisional terms ( $\Omega_e \Omega_i > \nu_{en} \nu_{in}$ ) of  $\Psi$  as is shown in Figure 2.7.

$$\frac{\partial N_e(r, t)}{\partial t} = D \nabla^2 N_e(r, t) \quad (2.5)$$

$$\tau = \frac{\lambda^2 \sec(\phi)^2}{16\pi^2 D} \quad (2.6)$$

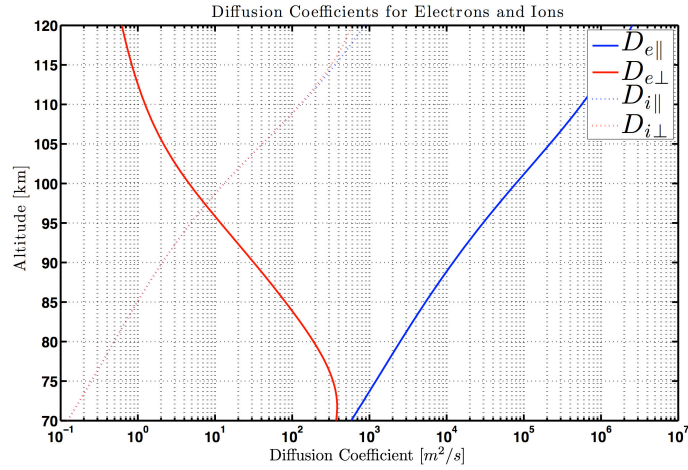


Figure 2.3: Electron and ion diffusion coefficients given by Eqs 2.10-2.13.

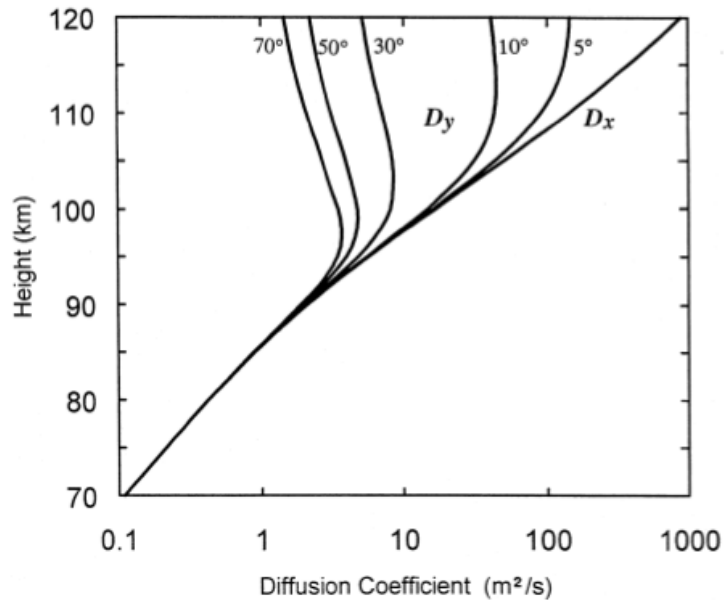


Figure 2.4: Figure 6 from Cepelcha [17] gives the diffusion coefficients  $D$  in Eq 2.5 as a function of trail height.  $D_x$  refers to diffusion in the plane containing both the trail and Earth's magnetic field, and  $D_y$  is the orthogonal direction. At heights above 90 [km], the diffusion becomes anisotropic as indicated by the divergence of the diffusion coefficients. Various values for  $D_y$  are indicated as a function of the trail's angle to the earth's magnetic field. A more thorough approach to the diffusion coefficients is given by Figure 2.3.

### 2.2.1 The Meteor Zone Environment

This section will explore the basic principles underlying the physics of meteor trail diffusion. All figures regarding collision frequencies or atmospheric composition were created using daytime MSIS on Jan 1st, 2000. The vast majority of material entering Earth’s atmosphere ablates in the lower E and upper D regions of the ionosphere. The dominant ionic species of the daytime ablation-zone ionosphere from the International Reference Ionosphere (IRI) is  $O_2^+$  and  $NO^+$  [12, 110].

The atomic masses of  $N$  and  $O$  are 14 and 16, therefore  $m_i \approx 30m_p$ , where  $m_i$  and  $m_p$  are the mass of an ion and proton. The following inequalities hold throughout the meteor region and indicate that most particle collisions are between the neutrals and ions:  $\Omega_i < \nu_{in}$  and  $\nu_{en} < \Omega_e$  where  $\Omega_{e,i}$  [110] are the electron and ion gyro-frequencies given by Eq 2.8 where  $m_e$  is the electron mass,  $B = |\mathbf{B}|$  is the geomagnetic field and  $e$  is the elementary charge. These meteoric zone quantities are calculated using  $B = 0.25 \times 10^{-4}$  T representing the equatorial geomagnetic field. The electron/ion neutral collision frequencies,  $\nu_{en, in}$  for the meteor region are shown in Figure 2.5.

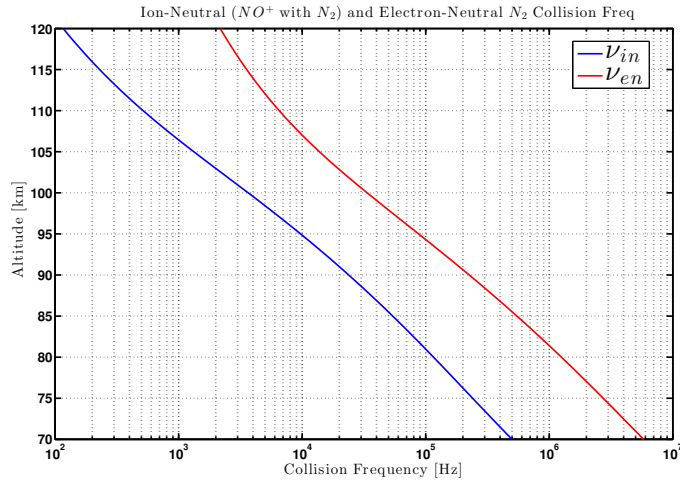


Figure 2.5: Ion-neutral and electron-neutral collision frequencies. Only the major ion and neutral species ( $NO^+$  and  $N_2$ ) are used in the calculation. Note that  $\nu_{en} \approx 10\nu_{in}$  throughout the indicated altitudes. Throughout the meteor region, the ion-neutral  $\nu_{in}$  collision frequency always exceeds the ion gyro-frequency  $\Omega_i$  effectively demagnetizing the ions, and the electron-neutral collision frequency  $\nu_{en}$  is less than the electron gyro-frequency  $\Omega_e$  allowing for geomagnetic influences on trail diffusion when  $\Psi < 1$ .

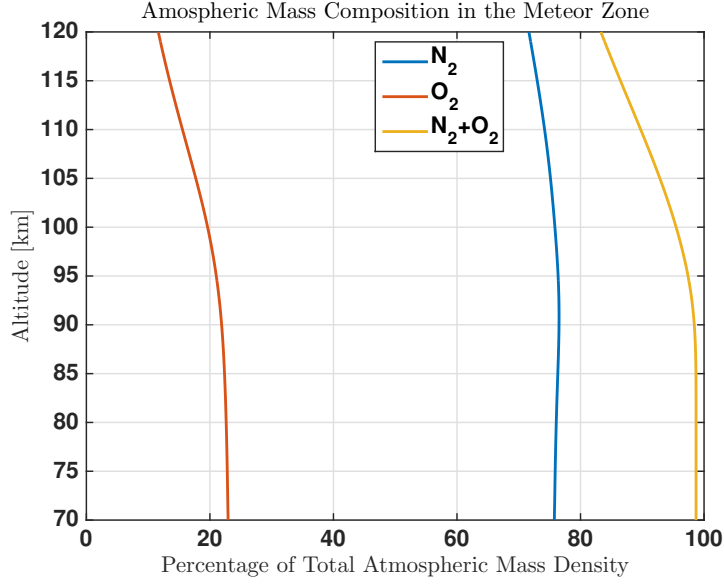


Figure 2.6: Percentages of neutral  $N_2$  and  $O_2$  of the total atmospheric mass density from MSIS.  $N_2$  is clearly the dominant neutral species followed by  $O_2$  which comprises  $\sim 20\%$  of the total mass density. As their molecular masses are similar, using only  $N_2$  when calculating collision frequencies will yield reasonable results.

Using the dominant species of  $NO^+$  and  $N_2$  for calculation of the collision frequencies in Figure 2.5 is justified by inspection of Figure 2.6 and by noting that  $NO^+$  contributes the majority of the charged atmospheric mass in the ablation region [11]. Inclusion of the minor species in these calculations has only small effects on diffusion coefficients calculated using the major species. Due to frequent electron-neutral and ion-neutral collisions (as compared with the higher ionosphere), the region is assumed isothermal with  $T_e = T_i = T_n = T$ . Dimant does point out that upon trail formation, the ions cool faster than the electrons creating an initial divergence of temperatures which may influence early-trail diffusion; a phenomenon currently open to investigation [9].

An important quantity used in describing the meteor zone diffusion is the Altitude Parameter [37] listed in Eq 2.7 and shown in Figure 2.7. The altitude parameter indicates if the trail diffusion is governed by ambipolar diffusion ( $\Psi \gg 1$  and  $\nu_{en}\nu_{in} \gg \Omega_e\Omega_i$ ), or if geomagnetic effects play some roll in the plasma motion ( $\Psi < 1$ ). By inspection of Figure 2.7, it is apparent that geomagnetic effects can influence trail diffusion above  $\sim 97$  [km]. Furthermore, we assume that diffusion begins nearly simultaneously along the

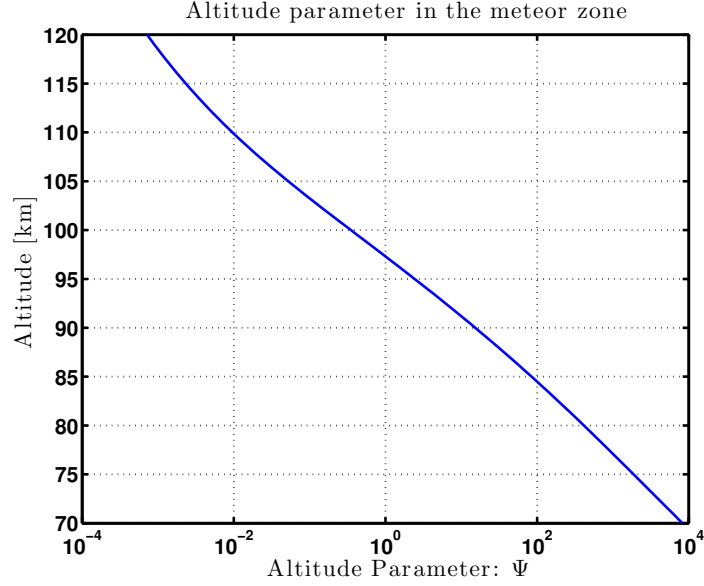


Figure 2.7: Altitude parameter [37] in the meteor zone. Note the change from  $\Psi > 1$  to  $\Psi < 1$  at  $\sim 97$  [km] indicating a change from strictly collisional ambipolar diffusion to geomagnetically-influenced diffusion. For trails below  $\sim 97$  [km] in altitude, the atmosphere is collisionally dominated as  $\Psi > 1$  and  $\Omega_i < \nu_{in}$ . In this region, the trail shares the motion of the neutral wind. At higher altitudes when  $\Psi < 1$ , the geomagnetic field can influence electron motion (because  $\Omega_e > \nu_{en}$  and  $\Omega_e \Omega_i > \nu_{en} \nu_{in}$ ).

meteoric trajectory as its velocity is much larger than the diffusion velocities and the plasma is assumed to be deposited homogeneously along the trail axis. Finally, total electron line density of the meteor trail is assumed conserved as the time constant for recombination is much greater than the diffusion time constants in the meteoric region [72]. As the gyrofrequency terms of the altitude parameter given by Eq 2.7 and shown in Figure 2.7 become dominant over the collisional terms with increasing altitude, the electron diffusion coefficients in Figure 2.3 can influence electron diffusion thereby causing spatially divergent motion between the electrons and neutrals. The specular meteor radar measures the motion of the electrons to infer the motion of the neutral wind, and therefore the Doppler measurement may not reflect the true motion of the neutral atmosphere at higher altitudes when  $\Psi < 1$ .

$$\Psi = \frac{\nu_{en}\nu_{in}}{\Omega_e\Omega_i} \quad (2.7)$$

$$\Omega_{e,i} = \frac{eB}{m_{e,i}} \quad (2.8)$$

$$\Omega_e \approx 6.5 \times 10^6 \text{ [Hz]}$$

$$\Omega_i \approx 80 \text{ [Hz]}$$

These assumptions have a number of interesting consequences. Because the meteor region is ion-neutral collisional (because  $\Omega_i \ll \nu_{in}$ ), the ions are **demagnetized** through frequent collisions with the neutral particles (primarily  $N_2$ ), and the geomagnetic field has little effect on ion dynamics as supported by Figure 2.3. At higher altitudes (when  $\Psi \ll 1$  indicating geomagnetically influenced diffusion), trail diffusion is strictly ambipolar only when the trail axis is closely aligned with the geomagnetic field. Above 97 [km] the altitude parameter (Figure 2.7) indicates that the geomagnetic field will exert some degree of influence on electron motion. Electrons gyrating at an angle greater than the critical angle of Eq 2.9 with respect to  $\mathbf{B}$  will undertake highly-mobile motion along  $\mathbf{B}$  outside of the trail's transverse cross-section and will diffuse along the geomagnetic field in accordance with  $D_{e\parallel}$  shown in Figure 2.3. Trails formed in atmospheric regions where  $\Psi < 1$  at an angle greater than  $\Theta_o$  will experience a faster depletion of their cross-sectional electron density over trails closely aligned with the geomagnetic field (when  $\theta < \Theta_o$ ). Furthermore, when  $\Psi < 1$  electron motion is not guaranteed to track the neutral motion. As the radar measures scattering from the electrons, this situation has the potential to bias the Doppler measurements.

$$\Theta_o \equiv \sqrt{\frac{m_e \nu_{en}}{m_i \nu_{in}}} \simeq 0.8^\circ \text{ in the meteor region} \quad (2.9)$$

$$D_{i\parallel} = \frac{k_b T}{m_i \nu_{in}} \quad (2.10)$$

$$D_{e\parallel} = \frac{k_b T}{m_e \nu_{en}} \quad (2.11)$$

$$D_{i\perp} = \frac{\nu_{in}^2 D_{i\parallel}}{\nu_{in}^2 + \Omega_i^2} \quad (2.12)$$

$$D_{e\perp} = \frac{\nu_{en}^2 D_{e\parallel}}{\nu_{en}^2 + \Omega_e^2} \quad (2.13)$$

Derivation of the basic meteor trail diffusion equation begins with the two coupled nonlinear PDEs for the plasma density and electric potential given by Eq 2.14 [27]. These two equations describe the assumptions of continuity and quasi-neutrality where the divergence of the ion and electron fluxes are equal. By defining the total force on an electron as the residual potential given by Eq 2.15 which is a combination of the electric potential ( $\Phi$ ) and the electron pressure gradient, and by defining the electron and ion fluxes as straightforward but cumbersome functions of the residual potential  $\phi_{res}$  and total electron density  $n_e$ , (see Eq 2.16) [27], we may write Eq 2.14 as Eq 2.17 where  $n_{e_0}$  is the constant background ionospheric plasma density. This is the fundamental meteor trail diffusion equation in two spatial dimensions representing the meteor trail cross-section with the coordinates defined in Figure 2.8.

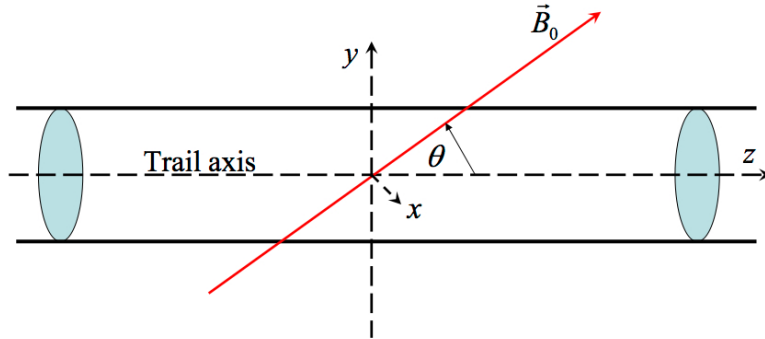


Figure 2.8: Figure 2 from [27]. Coordinate system used in meteor trail diffusion equations.  $\hat{x}$  is perpendicular to  $\hat{y}$  and  $\mathbf{B}$  such that  $\mathbf{B}$  has components in the  $\hat{z}$  and  $\hat{y}$  directions.  $\mathbf{B}$  lies in the  $\hat{y}\hat{z}$  plane such that  $x$  is always normal to the plane. The trail makes an angle of  $\theta$  with  $\mathbf{B}$ .

$$\partial_t n_e + \nabla \cdot \mathbf{\Gamma}_i = 0 : \text{Continuity} \quad (2.14a)$$

$$\nabla \cdot \mathbf{\Gamma}_i - \nabla \cdot \mathbf{\Gamma}_e = 0 : \text{Quasineutrality} \quad (2.14b)$$

$$\phi_{res} \equiv \frac{e\Phi - T_e \ln(n_e/n_{oe})}{k_b(T_e + T_i)} \quad (2.15)$$

$$\Gamma_{e,i} = f(\phi_{res}, n_e) \quad (2.16)$$

$$\partial_t n_e - D [\nabla^2 n_e + \nabla \cdot (n_e \nabla \phi_{res})] = 0 \quad (2.17a)$$

$$(1 + \psi) \partial_x (n_e \partial_x \phi_{res}) + (1 + Q) \partial_y (n_e \partial_y \phi_{res}) + \nabla^2 n_e +$$

$$\mu (\partial_x \phi_{res} \partial_y n_e - \partial_x n_e \partial_y \phi_{res}) = 0 \quad (2.17b)$$

Eq 2.17 describes the electron density and residual potential (and therefore electrical potential through Eq 2.15) along the two spatial coordinates ( $x$  and  $y$ ) and describes how these two dependent variables evolve with time. Before considering solutions to Eq 2.17, we should explore the fundamental assumption allowing us to describe trail diffusion using the magnetized two-fluid magneto hydrodynamic equations (MHD). In addition to Eq 2.17, the electrical potential  $\Phi$  and electron density  $n_e$  are linked by Poisson's Equation 2.18, which must also have a valid solution in the same temporal and spatial domain as Eq 2.17. Solving Poisson's equation highlights the fundamental assumption of the meteor trail diffusion equation, and in fact any attempt to describe a plasma using MHD requires the following assumption. Solving Poisson's equation requires the assumption listed in Eq 2.19 (see pages 7-9 in [49] for a detailed mathematical justification). The assumption implies that the number of charged particles in a Debye sphere is large ( $\gg 1$ ) so that electrical neutrality is maintained over the spatial scales in question which implies that the physical dimensions of a system described using MHD must be large compared to the Debye length.

$$\nabla^2 \Phi = -\frac{e}{\epsilon_o} (n_i - n_e) \quad (2.18)$$

$$\frac{e\Phi}{k_b T_e} \ll 1 \implies \frac{4}{3} \pi \left( \frac{\epsilon_o k T}{n_e^{1/3} e^2} \right) \gg 1 \quad (2.19)$$

A number of solutions for Eq 2.14 exist in the literature, however, solutions proposed by Jones [75] and Dimant and Oppenheim [26] are most instructive in the study meter trail diffusion.

### 2.2.2 Jones' Diffusion Solution

Jones solves Eq 2.17 for  $n_e(x, y, t)$  and  $\phi_{res}(x, y, t)$  under the boundary conditions  $n_e \rightarrow 0$  as  $x, y \rightarrow \infty$  and  $\Phi \rightarrow \infty$  as  $x, y \rightarrow \infty$  given by Eqs 2.20 and 2.21 [75].  $D$  is the ambipolar diffusion coefficient assuming  $m_i \nu_{in} \gg m_e \nu_{en}$  given by Eq 2.22.  $Q$  and  $\mu$  are the electron mobility parameter and the electron Hall parameter given by Eqs 2.23 and 2.24 and  $N_e$  is the conserved electron line density of the trail. By allowing the ambipolar electric field to approach infinity, Jones was able to find an analytic solution to Eq 2.17. The clearly non-physical boundary condition of infinite electric potential has the effect of neglecting the background ionosphere by allowing current closure ( $\nabla \cdot \mathbf{j} = 0$ ) at infinite spatial coordinates. Jones' approach accurately describes trail diffusion when the trail plasma density is many orders of magnitude above the background plasma density  $n_{e_o}$ , however his solution shows significant deviation from Dimant's at the later stages of trail diffusion as Jones' solution inaccurately describes the polarization electric field which provides current closure and significantly effects late-stage trail diffusion (when  $n_e$  is only slightly larger than  $n_{e_o}$ ).

$$n_e(x, y, t) = \frac{C}{t} \exp\left(-\frac{A_{xx}x^2 + A_{yy}y^2 + A_{xy}xy}{4Dt}\right) \quad (2.20)$$

$$\phi_{res}(x, y, t) = \frac{B_{xx}x^2 + B_{yy}y^2 + B_{xy}xy}{4Dt} \quad (2.21)$$

where:

$$B_{xx} = \frac{Q(2 + Q + \Psi)^2 + 2\mu^2(Q + \Psi)}{Q\Psi(2 + Q + \Psi)^2 + \mu^2(Q + \Psi)^2}$$

$$B_{yy} = \frac{\Psi(2 + Q + \Psi)^2 + 2\mu^2(Q + \Psi)}{Q\Psi(2 + Q + \Psi)^2 + \mu^2(Q + \Psi)^2}$$

$$B_{xy} = \frac{2\mu(2 + Q + \Psi)(\Psi - Q)}{Q\Psi(2 + Q + \Psi)^2 + \mu^2(Q + \Psi)^2}$$

$$A_{xx} = 1 + B_{xx}$$

$$A_{yy} = 1 + B_{yy}$$

$$A_{xy} = B_{xy}$$

$$C = \frac{(4A_{xx}A_{yy} - A_{xy}^2)^{1/2}}{8\pi D} N_e$$

$$D \equiv \frac{2k_b T}{m_i \nu_{in}} \quad (2.22)$$

$$Q \equiv \Psi \cos^2 \theta + \frac{\sin^2 \theta}{\Theta_o^2} \quad (2.23)$$

$$\mu \equiv \frac{\sqrt{\Psi}}{\Theta_o} \cos \theta \quad (2.24)$$

By numerically calculating Jones' solutions for  $n_e$  and  $\phi_{res}$  we may investigate a number of interesting features of early-stage trail diffusion. As discussed in Section 2.2.1, trail diffusion at higher altitudes ( $\Psi < 1$ ) can be influenced by the geomagnetic field  $\mathbf{B}$  based on the electron and ion diffusion coefficients depicted in Figure 2.3, which is confirmed in the solutions to the Jones meteor diffusion equation by inspection of Figures 2.9 and 2.10. The only difference between the two trail cross-sections is the angle  $\theta$ , which changes from  $\theta < \Theta_o$  in Figure 2.9 to  $\theta > \Theta_o$  in Figure 2.10 where  $\Theta_o$  is defined by Eq 2.9. The trail closely aligned with  $\mathbf{B}$  experiences inhibited electron diffusion in the cross-sectional plane of the trail thereby slowing the cross-sectional electron depletion. The slight asymmetry of the cross-sections in Figures 2.9 and 2.10 is due to the  $A_{xy}$  Hall term of Eq 2.20. At lower altitudes where  $\Psi \gg 1$ , the geomagnetic field has little effect as

seen in by inspection of the altitude parameter (Eq 2.7) and Figures 2.12 and 2.7. Small deviations away from  $\mathbf{B}$  have dramatic effects on the character of the electron diffusion because of the high electron mobility along the geomagnetic field lines, which is the dominant diffusive term by  $\sim 4$  orders of magnitude at higher altitudes as is seen in Figure 2.3. When  $\theta > \Theta_o$ , the electrons experience significant  $D_{e\parallel}$  diffusion away from the cross-sectional plane of the trail, causing a faster reduction in the cross-sectional electron density. Study of Doppler biases introduced by geomagnetic effects on high-altitude meteor trail electron motion is currently an active field of research, but many investigators anecdotally believe the effect to be small as the structure of the wind inversion usually remains coherent throughout the higher altitudes as is shown in Figure 4.7. Study of the ground illumination pattern described in Section 2.3 generated by scatter from high-altitude meteor trails using an electron density function given by Dimant & Oppenheim's geomagnetic diffusion theory described in section 2.2.3 could reveal new aspects of geomagnetically influenced electron motion.

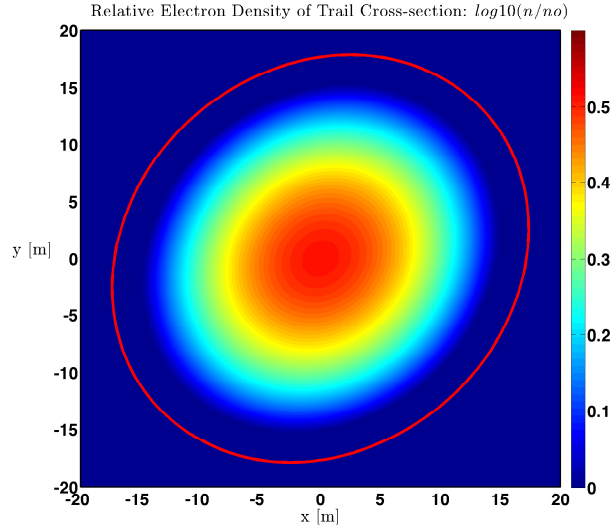


Figure 2.9: Cross-section of relative trail electron density  $\Delta n_e = n_e/n_{e_o}$  of a trail aligned with  $\mathbf{B}$  ( $\theta = 0.6^\circ < \Theta_o$ ) at  $t = 0.3$  [s] at an altitude of 110 [km] based on Jones' solution. The cross-sectional radial component of the electron diffusion is inhibited due to the trail's close alignment with  $\mathbf{B}$ . The dominant component of electron diffusion occurs normal to the trail cross-section, therefore the electron density exhibits slower cross-sectional depletion compared to Figures 2.10 and 2.11. The inequality of Eq. 2.19 is met inside the red ellipse

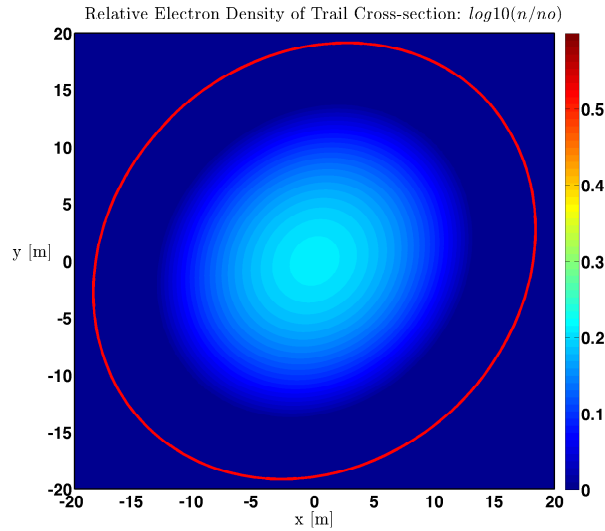


Figure 2.10: Cross-section of relative trail electron density  $\Delta n_e = n_e/n_{e_0}$  of a trail not aligned with  $\mathbf{B}$  ( $\theta = 1^\circ > \Theta_o$ ) at  $t = 0.3$  [s] at an altitude of 110 [km] based on Jones' diffusion solution. Because of the high altitude where  $\Psi < 1$ , electron motion is influenced by the geomagnetic field and they experience high mobility along  $\mathbf{B}$  described by  $D_{e\parallel}$ . More pronounced geomagnetic effects are observed in this trail's diffusion along  $\mathbf{B}$  by comparison with Figure 2.9. The inequality of Eq. 2.19 is met inside the red ellipse

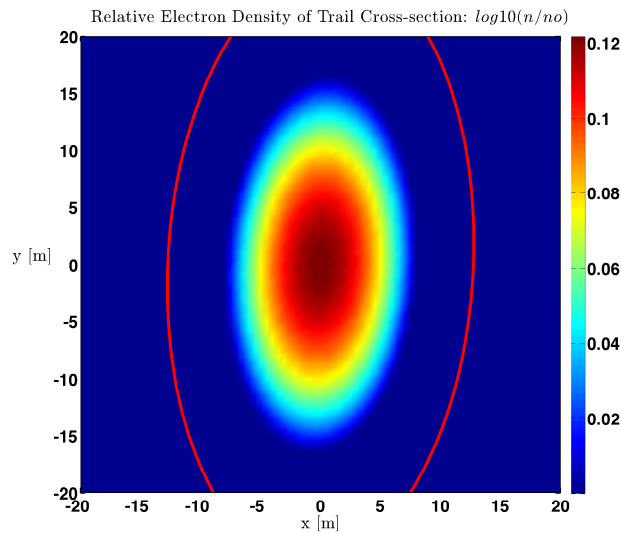


Figure 2.11: Cross-section of relative trail electron density  $\Delta n_e = n_e/n_{e_0}$  of a trail significantly unaligned with  $\mathbf{B}$  ( $\theta = 10^\circ > \Theta_o$ ) at  $t = 0.3$  [s] at an altitude of 110 [km] based on Jones' solution. The trail is elongated along  $\mathbf{B}$  and has a lower cross-sectional electron density at the same time as the trail in Figure 2.10. This results from the larger angle  $\theta = 10^\circ$  causing more significant diffusion along  $\mathbf{B}$ . Note the different colorbar scale from Figure 2.10.

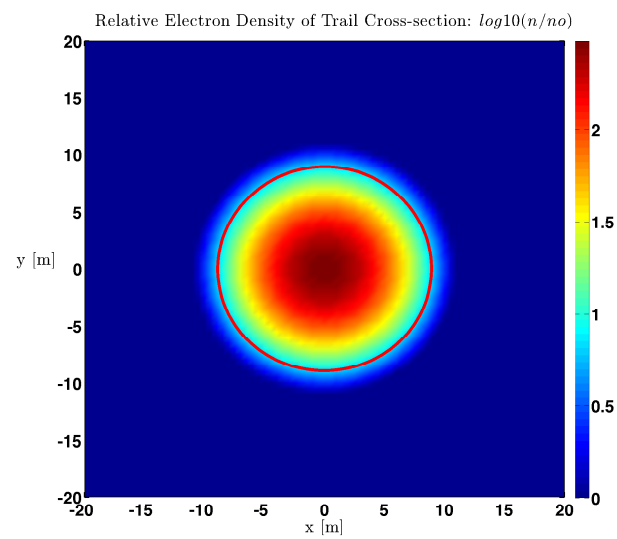


Figure 2.12: Cross-section of relative trail electron density  $\Delta n_e = n_e/n_{e_o}$  of a trail significantly unaligned with  $\mathbf{B}$  ( $\theta = 10^\circ > \Theta_o$ ) at  $t = 0.3$  [s] at an altitude of 90 [km] based on Jones' solution. By comparison with Figure 2.11, observe that at lower altitudes where  $\Psi > 1$  the geomagnetic field has little effect on diffusion as the cross-sectional density distribution is diagonally-symmetric and the trail experiences strict ambipolar diffusion.

### 2.2.3 Dimant and Oppenheim's Diffusion Solution

Dimant and Oppenheim have written a series of advanced papers exploring the solutions and implications of Eq 2.17 under the boundary conditions  $n_e \rightarrow 0$  as  $x, y \rightarrow \infty$  and  $\Phi \rightarrow 0$  as  $x, y \rightarrow \infty$  which ultimately has the effect of forcing current closure through the background ionosphere ( $\nabla \cdot \mathbf{j} = 0$ ) at finite distances from the trail. Under these boundary conditions, analytic solutions under arbitrary  $\theta$  to Eq 2.17 do not exist, and the authors present a series of analytic approximations valid under specific trail geometries and conditions. Specifically, their analytic theory applies when  $\theta$  is large compared with  $\Theta_o$  as is shown by Eq 2.25. When the inequality of Eq 2.19 is maintained, Dimant's solution follows Jones' while the trail density exceeds the background ionosphere by at least a few hundred times. Dimant and Oppenheim's most modern meteor trail diffusion simulation results are presented in [28] and the reader is encouraged to explore the beautiful supercomputer animations included in this paper.

$$Q \approx \frac{\sin^2 \theta}{\Theta_o^2} \gg 1 \quad (2.25)$$

Interestingly, Eq 2.17 can be solved numerically under Dimant's boundary conditions using a finite-element PDE solver. Dimant found the numerically generated solutions to reasonably approximate the exact solutions [27], and capture the major ambipolar electric field and electron density features [27]. By forcing the electric potential to zero at the spatial limits, the background ionospheric plasma is permitted to participate in maintaining quasineutrality **in addition** to the trail electrons. In other words, both electrons originating from the meteor trail **and** electrons already present in the ionospheric background can comprise  $\Gamma_e$  in Eq 2.14. In Jones' solution, both  $\Gamma_e$  and  $\Gamma_i$  arise only from particles originating from the trail. Qualitatively, currents are established along  $\mathbf{B}$  when  $\theta > \Theta_o$  because  $D_{e\parallel} \gg D_{e\perp}$ . The currents close in complex ways through the background ionosphere (because  $\Phi \rightarrow 0$  as  $x, y \rightarrow \infty$  and  $\nabla \cdot \mathbf{j} = 0$ ) and create a number of interesting features in electron density. The analytic solution formulated by Dimant and Oppenheim is somewhat bulky, and the reader is referred to the actual paper [26] for mathematical details. By imposing

current closure, depletions in the background ionosphere can appear at considerable distances from trails that are not aligned with  $\mathbf{B}$  as can be seen in Figure 2.13 as the ionospheric electrons participate in trail diffusion. Observation of either the ionospheric electron depletion shown in Figure 2.13 or the diffusive critical time shown in Figure 2.15 and described by Eq 2.26 could provide compelling evidence for Dimant and Oppenheim’s theory from the perspective of specular meteor radar.

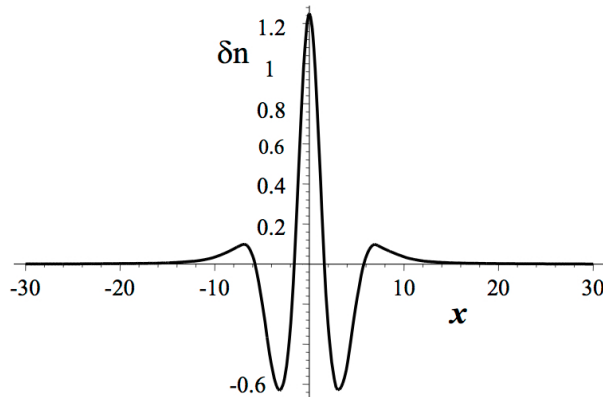


Figure 2.13: Figure 6 from [27]. Disturbance of the **background** electron density  $\delta n_{e_o} = n_o/n_{e_o}$  for  $\Psi = 0.2$  (higher altitude) at  $t = 3.5$  sec and  $\Delta n_e = n_e/n_{e_o} = 10^4$ .  $n_{e_o}$  is the constant background density,  $n_o$  is the instantaneous background density ( $n_o$  is a function of time) and  $n_e$  is the quasineutral total plasma density. The coordinate system is given in Figure 2.8. The  $y$ -coordinate is located at 20 [m], far from the trail where the trail density is much less than the background plasma density ( $\Delta n_e = n_e/n_{e_o} \approx 1$ ).

One consequence of Dimant and Oppenheim’s theory for the observation of specular meteor trails is the prediction of the diffusion ‘Critical Time’  $t_{cr}$  given by Eq 2.26 (see Eq 21 in [27]) where  $N_{lin}$  is the meteor trail electron line density,  $e$  is the elementary electron charge,  $\mathcal{K}(\Psi)$  is a dimensionless parameter related to the altitude parameter,  $T_e$  and  $T_i$  are the electron and ion temperatures,  $\mathbf{B}$  is the magnetic field strength and  $n_o$  is the background ionosphere electron density. The critical time  $t_{cr}$  describes the time of a nearly instantaneous transition (with respect to the total trail observation time) of the trail’s diffusion from sharply anisotropic to largely isotropic. This transition is a consequence of the complex current closures in the background ionosphere. Figure 2.14 shows how the trail diffusion becomes more isotropic in nature at the later stage of diffusion as compared to Jones’ solution. Confirmation of the critical time would provide strong evidence in support of Dimant and Oppenheim’s diffusion theory, of which little exists from

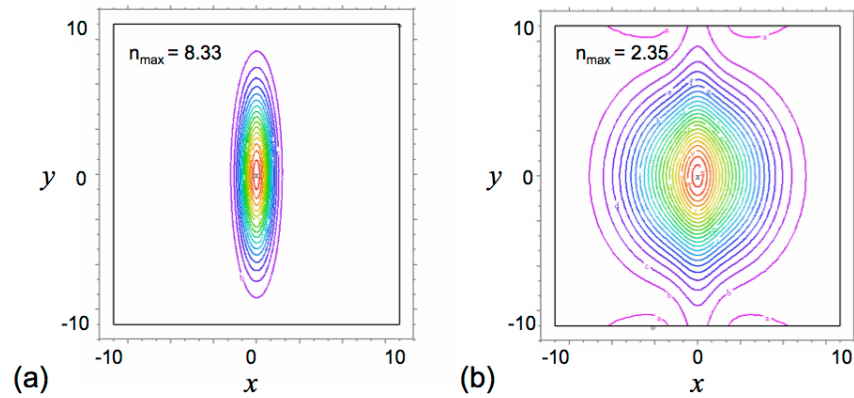


Figure 2.14: Figure 4 from [27]. Numerical PDE solution from Dimant and Oppenheim **(b)** and Jones' solution **(a)** for  $\Psi = 0.2$  (higher altitude) at  $t = 6$  [s]. and  $\Delta n_e = n_e/n_{e_0} = 50$ .  $n_{e_0}$  is the constant background density and  $n_e$  is the quasineutral total plasma electron density. Diffusion is faster and more isotropic when including the background plasma and current closure. The maximum relative electron density,  $n_{\max}$  is shown in the contour plots. High altitude trails are predicted to experience a sharp transition from anisotropic to nearly isotropic diffusion at the critical time  $t_{cr}$  as given by Eq 2.26. This figure has been generated when  $t > t_{cr}$  and therefore the change in diffusion coefficient has already occurred as is shown by the more nearly isotropic electron density distribution in the PDE simulation of panel **(b)**.

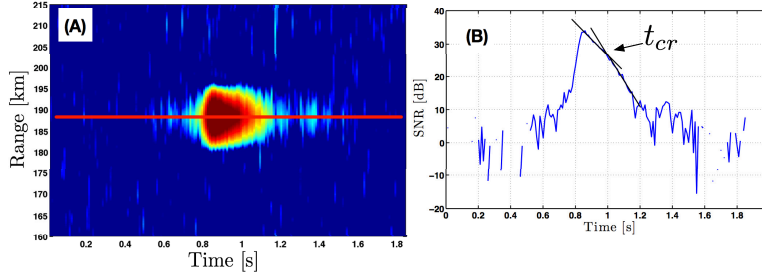


Figure 2.15: Example specular meteor trail echo observed by CoSRad using the Platteville meteor radar system displaying an instantaneous increase in the diffusion constant consistent with the critical time hypothesis given by Eq 2.26 and shown in Figure 2.14.

the perspective of specular meteor trail echoes. The critical time would be present in the measurements from high-altitude trails which are not closely aligned with  $B$  as an instantaneous increase in the diffusion constant. Figure 2.15 shows a CoSRad specular meteor trail observation from the Platteville meteor radar displaying an instantaneous change in diffusion coefficient. Because the trail's orientation with respect to  $B$  is unknown, no meaningful conclusions can be drawn using a single observation so Figure 2.15 only serves as an example of the expected diffusion behavior under a critical time hypothesis. Without coincident LIDAR or ISR measurements of  $T_e$ ,  $T_i$  and  $n_o$  of Eq 2.26 cannot be directly measured. Furthermore, without meteor trajectory information, the trail's orientation with respect to  $B$  is unknown, however,  $t_{cr}$  is a function of the background E-region electron density  $n_o$  which can fluctuate by three orders of magnitude between day and night [110]. Finding a correlation between the critical time of trail diffusion and the time of day would provide evidence in support of Dimant and Oppenheim's theory from the perspective of specular meteor radar. The model of the least-squares fitting procedure in Chapter 4 could be modified to include two decaying exponentials which would automate the process of finding echoes with strong, nearly instantaneous changes in diffusion coefficient.

$$t_{cr} = \frac{N_{in} e B K(\Psi)}{2\pi(T_e + T_i)n_o} \quad (2.26)$$

### 2.2.4 Discussion of Solutions

Both Jones' and Dimant's solutions similarly describe trail diffusion when the trail is aligned with the magnetic field, however significant differences surface in the meteor zone as  $\theta > \Theta_o$  when  $\Psi < 1$ . To describe a plasma using the MHD equations from which Eq 2.17 is derived, the number of charged particles within a Debye sphere must be large which is the case throughout the meteor region at VHF length-scales [75]. Another, more qualitative approach is to realize that the spatial lengths of a plasma phenomenon under consideration must be large compared with the Debye length. Inclusion of the background plasma increases the diffusion rate as the electric potential created during current closure reinforces the ambipolar electric field and accelerates diffusion.

In light of Dimant's and Oppenheim's work, studies inferring atmospheric parameters such as  $T_n$  when  $\Psi < 1$  by measuring diffusion coefficients may consider revisiting results as accelerated diffusion may introduced a bias as was partially done by [9]. Structures in the background ionospheric electron density are predicted to occur during high-altitude trail formation as illustrated in Figure 2.13. The ionospheric electron density depletion is predicted to form at distances from the trail where  $\Delta n_e = n_e/n_{e_o} \approx 1$  and may prove to be a useful feature in providing evidence for Dimant's theory, however, no feasible remote sensing experiment has been proposed with the potential to observe this predicted depletion structure. This predicted feature of high-altitude meteor trail diffusion has proved difficult to observe as LIDAR does not directly measure the background electron density, and observation of this short-lived feature using ISR would require very high power due to the short incoherent integration time. Nonetheless, this predicted background electron depletion region is a significant consequence of Dimant and Oppenheim's modern diffusion theory. For beautifully rendered meteor trail diffusion supercomputer simulations, see the modern paper [28]. Limited evidence exists in providing experimental evidence for this theory [102]. Moving forward, a measurement campaign aimed at providing evidence of Dimant and Oppenheim's diffusion theory using specular echoes is the logical next step.

Two modern theories of meteor trail diffusion are presented for the meteoric region of Earth's ionosphere. Both theories solve the fundamental equation for meteor trail diffusion in two dimensions (Eq 2.17) but under different boundary conditions. Both theories force the trail electron density to zero at the spatial limit ( $n_e \rightarrow 0$  as  $x, y \rightarrow \infty$ ), but Jones allows the electric potential to approach infinity ( $\Phi \rightarrow \infty$  as  $x, y \rightarrow \infty$ ) while Dimant and Oppenheim provide an analytical approximation to solve Eq 2.17 under the more geophysically realistic boundary condition of forcing the electric potential to zero at the spatial limit ( $\Phi \rightarrow 0$  as  $x, y \rightarrow \infty$ ). Both theories describe trail diffusion at the early stage similarly, but deviate significantly at the later stages of trail diffusion, identified in Dimant's theory by a transition from primarily anisotropic to isotropic diffusion. While Jones' theory captures the major altitude and  $\theta$ -dependent features of trail diffusion as is shown in Figures 2.9-2.12, it fails to account for current closure in the background plasma. Dimant's theory includes the background plasma, and allows for complex current closure structures which influence the trail electron density's temporal and spatial evolution. Two consequences of accounting for current closure through the background plasma is the creation of electron depletion regions in the background ionosphere at large distances from the trail (see Figure 2.13) where the trail density is well below that of the background plasma ( $\Delta n_e = n_e/n_{e_0} \approx 1$ ), and the instantaneous increase in the specular echo decay coefficient at the 'critical time'  $t_{cr}$  given by Eq 2.26.

## 2.3 Numerical Modeling and the Ground Illumination Pattern

A number of primary assumptions are used in the formulation of the Ground Illumination Pattern (GIP) equations. The GIP equations were derived by Tinin using a modified single-scattering theory, which is based on solving Maxwell's equations in their first perturbed (linearized) approximation [126]. The trail is also assumed to be in the Fraunhofer zone described by Eq 2.27 where  $W$  is the size of some trail dimension,  $\lambda$  is the radar operating wavelength and  $L$  is the distance from the trail to the receiver. The scattering volume is assumed smaller than the first Fresnel radius which is on the order of 1 [km] for meteor radar frequencies assuming mesospheric scatterers with the transmitter and receiver located on the earth's surface. The transverse radius of the trail is on the order of several meters, which clearly falls within the Fresnel assumption, however, trails are typically tens of kilometers in length, much larger than the Fresnel radius. Because of the strong spatial anisotropy of meteor trails, the single-scattering theory only directly applies when analyzing scattering along the transverse (cross-sectional) spatial components of the trail. Scattering along the primary axis of the trail (longitudinal direction) is described using a stationary-phase technique where the majority of the longitudinal scattering is assumed to originate from a point of stationary phase along the trail (with respect to the transmitter and receiver locations) as determined by the conditions of Eq. 2.28a and explicitly calculated by Eq. 2.29c.  $\Psi$  is the phase change along the path from the transmitter  $\mathbf{r}_o$  to a point in the scattering volume (trail)  $\mathbf{r}_s$  and continuing to the receiver  $\mathbf{r}$  assuming the coordinate system depicted in Figure 2.16. Throughout this section, the following notation is used, and all scattering equations are based on the work of Tinin [126] with some minor notation changes for clarity. Other than the fully integrated GIPs in Figure 2.21, all GIPs in this chapter are calculated by evaluating Eq 2.31 over a set of candidate receiver locations  $\mathbf{r}$  with fixed transmitter  $\mathbf{r}_o$  and trail locations. In the formulations of Eqs 2.31 and 2.29, the transmitter and receiver locations are given with respect to the trail. In some of the GIP figures, the axis are adjusted to show the trail and receivers with respect to the transmitter.



- $\mathbf{r}_o$  : Location of transmitter with respect to the trail,  $\mathbf{r}_o = (x_o, y_o, z_o)$  [m]
- $\mathbf{r}_s$  : Scattering section along the trail [m]
- $\rho$  :  $(y, z)$  coordinates of Rx location,  $(x, \rho) = (x, y, z)$  [m],  $\rho$  and  $\rho'$  are related through Eq 2.30
- $\rho_o$  :  $(y_o, z_o)$  coordinates of Tx location,  $(x_o, \rho_o) = (y_o, z_o)$  [m],  $\rho_o$  and  $\rho'_o$  are related through Eq 2.30
- $z'_s$  :  $z'$  component of  $\mathbf{r}_s$  [m]
- $x_m$  : Height of meteor trail [m]
- $z'_c$  : Point of stationary phase along trail axis [m]. Defined by Eq 2.28a
- $\gamma(z'_c)$  : Angle between electric vector of incident wave  $\mathbf{E}$  and the vector connecting  $z'_c$  to  $\mathbf{r}$
- $l_{\parallel}$  : Characteristic length of meteor trail [m]
- $l_{\perp}$  : Characteristic transverse radius of meteor trail [m]
- $\alpha$  : Angle between  $x$  and  $x'$  (Angle between zenith and meteor trail primary axis)
- $\mathbf{E}$  : Electric vector of incident wave [ $\text{V m}^{-1}$ ]
- $\Psi(\mathbf{r}, \mathbf{r}_s, \mathbf{r}_o)$  : Phase of radar wave as a function of Tx and Rx locations ( $\mathbf{r}_o, \mathbf{r}$ ) and the point of scattering  $\mathbf{r}_s$

Throughout this section, a boldface symbol indicates a vector-valued quantity, and its norm is indicated by the standard typeface. For example:  $r = |\mathbf{r}|$ .

$$\frac{\partial \Psi(z'_s)}{\partial z'_s} = 0 \quad (2.28a)$$

where

$$\Psi(\mathbf{r}, \mathbf{r}_s, \mathbf{r}_o) = |\mathbf{r}_s - \mathbf{r}_o| + |\mathbf{r} - \mathbf{r}_s| \quad (2.28b)$$

and

$$\mathbf{r}' = \{\rho', z'\} = \{x', y', z'\} \text{ and } \mathbf{r}'_o = \{\rho'_o, z'_o\} = \{x'_o, y'_o, z'_o\} \quad (2.28c)$$

$$(2.28d)$$

The primed coordinate system has an origin at the center of the meteor trail, and the unprimed coordinates are centered on the surface of the earth as depicted in Figure 2.17. The meteor is at a height  $x_m$  above the earth's surface and at an angle  $\alpha$  with respect to the unprimed coordinates. The two coordinate systems are related by Eq. 2.30

$$I(\mathbf{r}) = \left(\frac{80.6\pi^2}{c^2}\right)^2 \frac{\lambda^3 |F_N|^2}{\rho' \rho'_o \sqrt{(\rho' + \rho'_o)^2 + (z' - z'_o)^2}} \quad (2.29a)$$

$$\frac{1}{L_{eff}} = \left(\frac{1}{\rho'_o} + \frac{1}{\rho'}\right) \left[1 + \left(\frac{z' - z'_o}{\rho' + \rho'_o}\right)^2\right]^{3/2} \quad (2.29b)$$

$$z'_c = \frac{z'_o \rho'_o + z' \rho'}{\rho' + \rho'_o} \quad (2.29c)$$

$$z'_a = z'_c + \frac{\xi}{\sqrt{\frac{k}{L_{eff}}}} \quad (2.29d)$$

$$|F_N| = \frac{1}{\sqrt{2\pi}} \int_{-\infty}^{\infty} \exp\left[\frac{j\xi^2}{2}\right] \Phi\left(\mathbf{Q}, z'_c + \frac{\xi}{\sqrt{\frac{k}{L_{eff}}}}\right) d\xi \quad (2.29e)$$

$$\mathbf{Q}(\mathbf{r}') = k \left[ 1 + \left( \frac{z' - z'_o}{\rho' + \rho'_o} \right)^2 \right]^{-\frac{1}{2}} \left[ \frac{\rho'}{\rho'} + \frac{\rho'_o}{\rho'_o} \right] \quad (2.29f)$$

$$\Phi(\mathbf{Q}, z'_a) = \frac{1}{\sqrt{2\pi}} \iint_{-\infty}^{\infty} N(\boldsymbol{\rho}'_s, z'_a) \exp[-i\boldsymbol{\rho}'_s \mathbf{Q}] d^2 \boldsymbol{\rho}'_s \quad (2.29g)$$

$$N(\boldsymbol{\rho}'_s, z'_a) = \frac{q(z'_a)}{\pi l_{\perp}^2} \exp\left[-\frac{\rho_s'^2}{l_{\perp}^2}\right] \quad (2.29h)$$

$$q(z'_a) = q_m \exp\left[-\frac{z_a'^2}{2l_{\parallel}^2}\right] \quad (2.29i)$$

$$\gamma(z'_c) = \frac{\mathbf{E} \cdot [x' \ y' \ z' - z'_c]}{E|[x' \ y' \ z' - z'_c]|} \quad (2.29j)$$

$$P_r(\mathbf{r}) = P_t G_t G_r I(\mathbf{r}) \sin^2(\gamma(z'_c)) \quad (2.29k)$$

$$x' = (x - x_m) \cos \alpha + z \sin \alpha \quad (2.30a)$$

$$z' = z \cos \alpha - (x - x_m) \sin \alpha \quad (2.30b)$$

$$y' = y \quad (2.30c)$$

The ground pattern created when radar-illuminating an elongated electron cloud is calculated using the series of Eqs 2.29 where the arbitrary cross-sectional electron density is used in place of the Gaussian distribution of Eq 2.29h. Eqs 2.29 require the time-consuming numerical evaluation of a triple integral expression. Under the assumptions of Gaussian electron density distribution along both the trail length  $l_{\parallel}$  and trail radius  $l_{\perp}$  Eqs 2.29 reduce to Eqs 2.31 where  $\mathbf{Q}(\mathbf{r}')$  is given by Eq 2.29f and  $z'_c$  is found using Eq 2.29c. The power received at a candidate receiver location is a function of the transmitted electric vector polarization  $\gamma$  and the radar system parameters both included in Eq 2.29k. It can be shown that Eq 2.31 reduces to the classical meteor radar equation given by 2.1a (see Section 4 of [126]). The procedure for finding the numerically integrated illumination pattern is a 6-stage process outlined below:

$$I_g(\mathbf{r}) = D \frac{\lambda^3 q_m^2}{\rho' \rho'_o \sqrt{(\rho' + \rho'_o)^2 + (z' - z'_o)^2}} \exp\left(\frac{-z'_c}{2l_{\parallel}^2} - \frac{Q(\mathbf{r}')^2 l_{\perp}^2}{2}\right) \quad (2.31)$$

where  $D = \left(\frac{20.15}{c^2}\right)^2 \approx 5.027 \times 10^{-32}$  [unitless]

- (1) Choose a candidate receiver location  $\mathbf{r}$  in the  $\hat{z}\hat{y}$  plane.
- (2) Transform receiver and transmitter into the trail coordinate frame using Eq 2.30.
- (3) Find the point of stationary phase with respect to the receiver using Eq 2.29c.  $z'_c$  represents the point along the trail where the derivative of the phase with respect to changes in the receiver location is zero as is indicated by Eq 2.28a. This point is assumed to lie in the first Fresnel zone contributing most of the scattered power at any given receiver location.
- (4) Evaluate Eq 2.29e by integrating over  $\xi$ . In principle the limits of integration are at infinity, however, we may set the limits of integration to an order of magnitude greater than the trail's effective length given by Eq 2.29b. The effective length is related to the length of the first Fresnel zone and contributes most of the scattered power at the chosen receiver location.
- (5) In step (4) the trail is sliced into cross-sectional pieces. Each cross-sectional section is integrated

over the 2D electron density profile using Eq 2.29g.

- (6) Move the receiver to a new candidate location and repeat the process to form the ground illumination pattern.

Studying the full numerical solution is helpful for understanding the technique and assumptions, however, Tinin has also provided a closed-form expression of Eq 2.29 assuming a Gaussian electron density which can be directly evaluated without the need for extensive numerical integrations. The closed-form expression is shown by Eq 2.31.

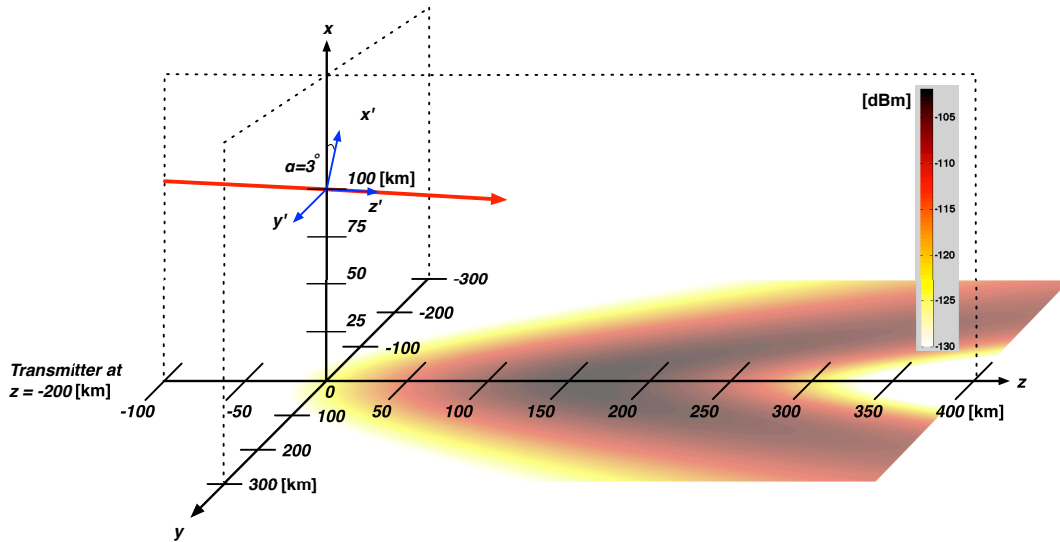


Figure 2.17: Power available at antenna terminals from Eqs 2.31 and 2.29k. The transmitter is located on the  $z$ -axis at  $-200$  [km]. Simulation parameters:  $\alpha = 3^\circ$ , trail height  $x_m = 100$  [km], Transmit power =  $10e3$  [W], Gain of receive and transmit antennas  $G_r = G_t = 3$  [dB]. Carrier frequency  $f_o = 30$  [MHz], Max electron line density  $N_e = 10^{13}$  [m $^{-1}$ ], Gaussian trail distribution  $l_{||} = 30$  [km],  $l_{\perp} = 1$  [m], Transmitter location  $Tx = -200\hat{z}$  [km], Electric vector polarization  $\mathbf{E} \times \hat{x} = 0$

The widely cited scattering theory proposed by McKinley [95] was formulated in such a way as to make the calculation of GIPs difficult, as the equations were not explicit functions of positions on the ground with respect to arbitrary transmitter and receiver locations. Tinin has reformulated McKinley's original theory for the calculation of GIPs by creating a set of equations as a function of the position of transmitter and receiver. A final set of equations describing the ground illumination as an **explicit function** of the transverse (cross-sectional) electron density  $N(\rho'_s, z'_a)$  is described by Eqs 2.29 and under the Gaussian electron density

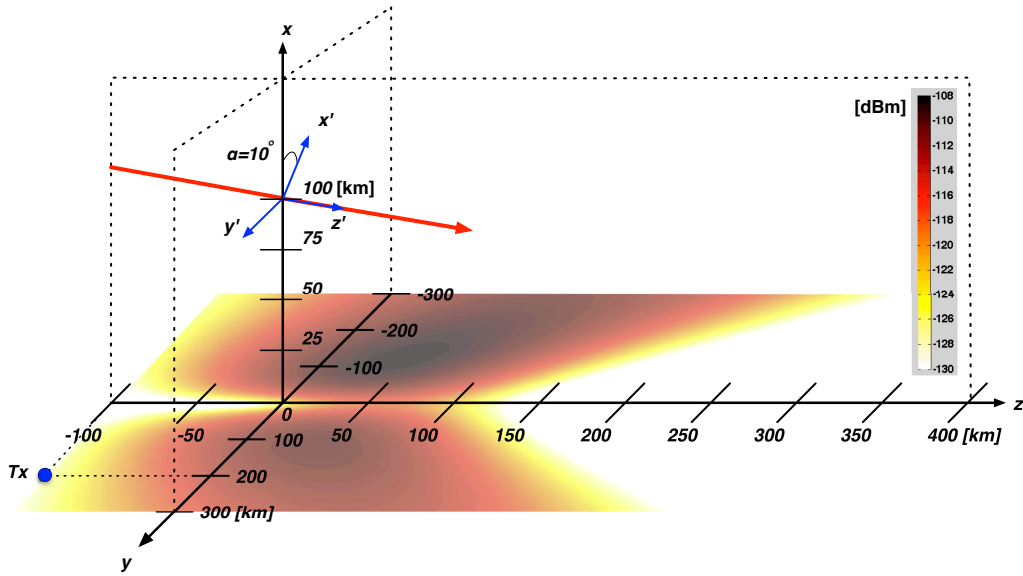


Figure 2.18: Power available at antenna terminals from Eqs 2.31 and 2.29k. Simulation parameters:  $\alpha = 10^\circ$ ,  $x_m = 100$  [km],  $P_t = 10e3$  [W],  $G_r = G_t = 3$  [dB].  $f_o = 30$  [MHz],  $\text{Max } N_e = 10^{13}$  [m $^{-3}$ ],  $l_{\parallel} = 20$  [km],  $l_{\perp} = 1$  [m], transmitter location:  $\text{Tx} = (300\hat{y} - 100\hat{z})$  [km],  $\mathbf{E} \times \hat{z}' = 0$ . The trail does not meet the classical backscatter geometry as can be seen by a lack of scattered power at the transmitter, however, a multistatic system could observe this echo.

distribution assumption by Eq 2.31. The explicit dependence on electron density is important because this allows for calculation of the GIP for any arbitrary electron density distribution function assuming the function meets the single-scattering assumptions. Historically, Gaussian distribution functions such as Eqs 2.29h and 2.29i have been used to describe both the transverse and along-trail electron density, an assumption which allows considerable simplifications to Eq 2.29 and results in the analytic solution of Eq 2.31 for the GIP. While the assumption of a radial Gaussian electron density distribution describes the early evolution of the meteor trail [76], it fails to accurately capture the later-stage radial distribution when the trail electron density has diffused to only a few orders of magnitude above that of the background ionospheric plasma. Furthermore, the Gaussian electron distribution assumption neglects the known temporal effects of earth's magnetic field in addition to the background ionosphere on trail diffusion [102], and the assumption of a Gaussian electron density distribution along the primary axis of the trail is a notable geophysical simplification.

Dimant and Oppenheim's modern theory of diffusion discussed in Section 2.2.3 [27, 26] includes the effects of Earth's geomagnetic field and the motion of the background ionosphere on the spatial and temporal

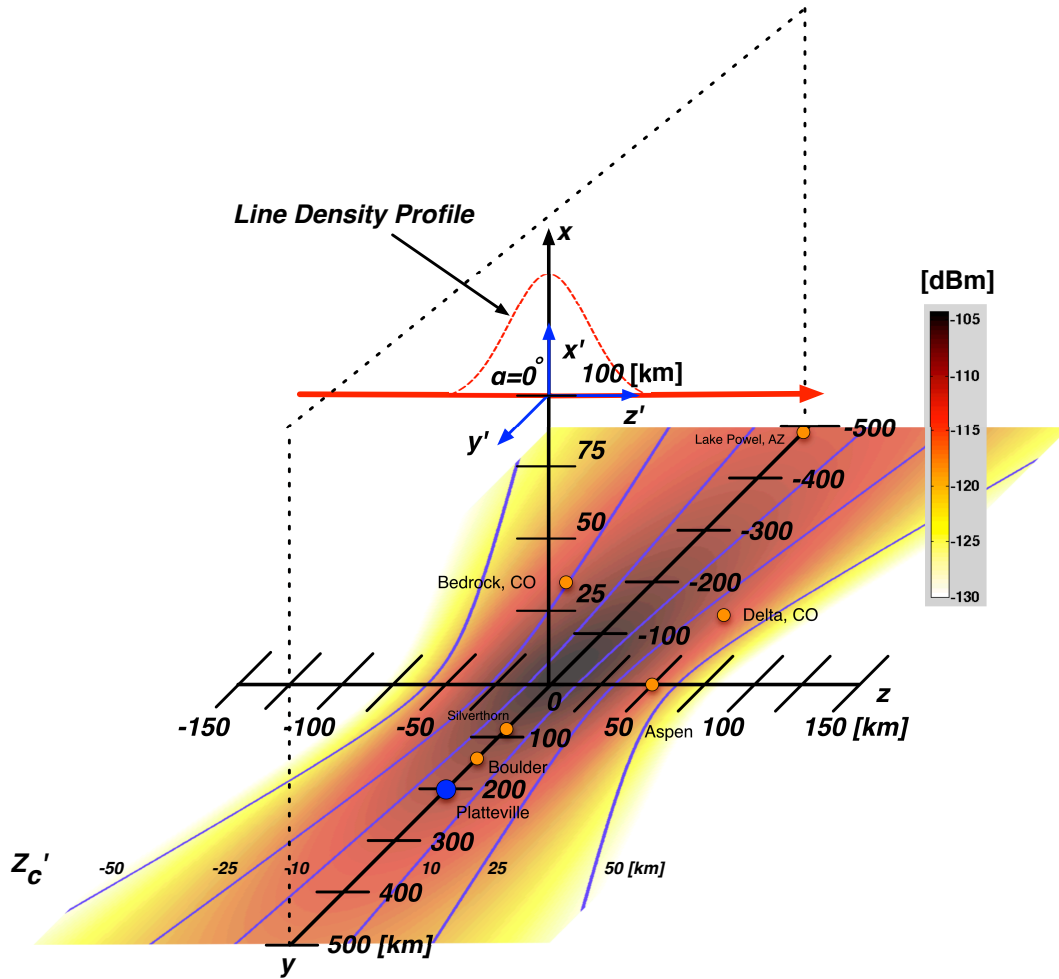


Figure 2.19: Power available at antenna terminals with geographical landmarks in Colorado (USA) from Eqs 2.31 and 2.29k. Simulation parameters:  $\alpha = 0^\circ$ ,  $x_m = 100$  [km],  $P_t = 10$  [kW],  $G_r = G_t = 3$  [dB].  $f_o = 30$  [MHz],  $\text{Max } N_e = 10^{13}$  [elec/m],  $l_{\parallel} = 20$  [km],  $l_{\perp} = 1$  [m], transmitter location:  $\text{Tx} = 200\hat{y}$  [km],  $\mathbf{E} \times \hat{z} = 0$  (electric vector is parallel to  $\hat{z}$ ). The trail lies normal to the  $\hat{x}\hat{y}$  plane connecting Platteville and Boulder. An increase in power at the forward-scatter location is due to the effective increase in Bragg wavelength by  $\sec \phi$  where  $\phi$  is half the forward-scatter angle (see Figure 2.1). The  $z'_c$  coordinate is the location on the trail (shown projected onto the  $\hat{y}\hat{z}$  plane) in the primed coordinate frame (Eq 2.30) of the center of the first Fresnel zone contributing to 90% [17] of the scattered power at any given point on the  $\hat{y}\hat{z}$  plane (receiver location). Receivers located along contours of constant  $z'_c$  will observe scatter from the same location along the trail.

evolution of a meteor trail. Eq 2.17 is solved for the plasma density distribution and the residual potential as a function of the spatial and temporal coordinates. Fundamentally, Eq 2.17 governs the spatial evolution of the meteor trail plasma  $N(x, y, z, t)$ . The constant terms  $D$ ,  $Q$ ,  $\psi$  and  $\mu$  are a function of various plasma and environmental parameters including the electron and ion temperatures, collision frequencies and the trail's orientation with respect to the geomagnetic field  $\mathbf{B}$ . The initial electron distribution is actually assumed

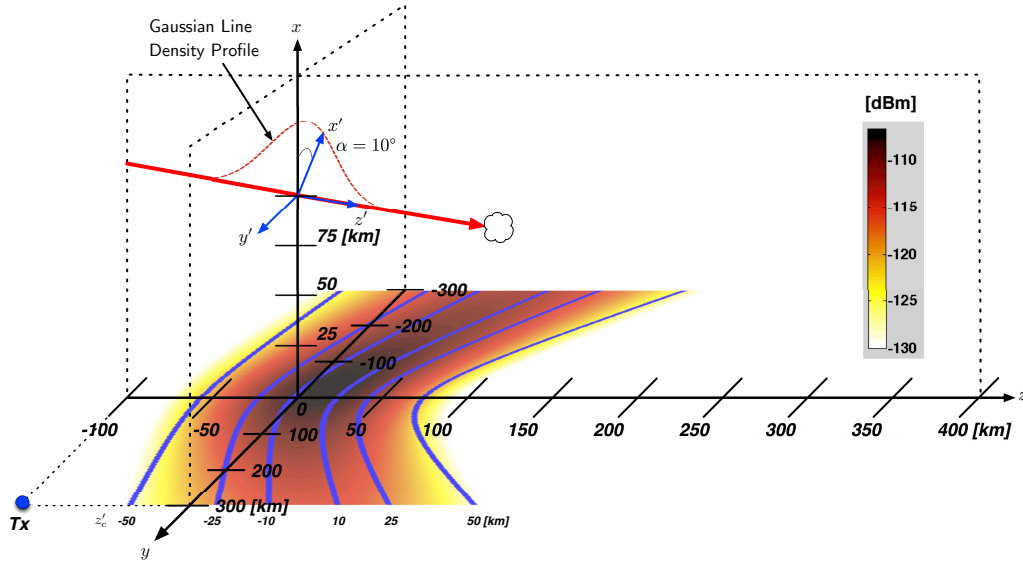


Figure 2.20: Power available at antenna terminals from Eqs 2.31 and 2.29k. Model parameters:  $\alpha = 10^\circ$ ,  $x_m = 100$  [km],  $P_t = 10$  [kW],  $G_r = G_t = 3$  [dB],  $f_o = 30$  [MHz],  $q_m = 10^{13}$  [m $^{-3}$ ],  $l_{\parallel} = 20$  [km],  $l_{\perp} = 1$  [m], transmitter location: Tx =  $(300\hat{y}, -100\hat{z})$ , [km]  $\mathbf{E} \times \hat{x}' = 0$ . The trail does not meet the condition for classical ‘backscatter’ as can be seen by a lack of scattered power at the transmitter location, however, a multistatic system could observe this echo. The  $z'_c$  coordinate is the location on the trail (shown projected onto the  $\hat{y}\hat{z}$  plane) in the primed coordinate frame of the center of the first Fresnel zone. Receivers located along contours of constant  $z'_c$  will observe scatter from the same location on the trail.

to be Gaussian [76], and subsequently diffuses according to Eq 2.17. By using the solution for the electron density distribution  $N(x, y, z, t)$  in Eq 2.17 in place of Eq 2.29h in the full formulation, the temporal evolution and spatial distribution of the scattered field under the modern diffusion theory could be determined. Note that Eq 2.29g relates the scattering intensity to the Fourier transform of the spatial distribution of the trail’s cross-sectional electron distribution. This would suggest (consistent with antenna theory) that a larger trail radius will produce a more spatially localized GIP. General analytical solutions to Eq 2.17 do not exist and  $N(x, y, z, t)$  must either be solved numerically, or under some limiting assumptions on trail geometry which enable analytic descriptions. The ultimate goal is the calculation of GIPs under arbitrary trail, transmitter and receiver geometry assuming an electron density distribution described by Eq 2.17. In Figure 2.21 the full numerical GIP model (Eqs 2.29 represent a nontrivial problem in computational electromagnetics) is compared with the closed-form analytical model described by Eq 2.31 under an identically Gaussian electron density distribution. New spatial structures of the scattered field are observed in the fully integrated model, suggesting that the classical scattering equations do not capture all structures present in the scattered field.

Including the electron density described by Eq 2.17 and presented by [28] into Eq 2.29h would undoubtedly reveal a new and rich tempo-spatial structure in the scattered field not captured under the classical theory described by Eq 2.1a and assumed in the formulation of Eq 2.31. In both models of Figure 2.21, the electron density profile is identically Gaussian. The general structure of the numerically integrated GIP is consistent with that of Figure 2.19 using similar system and physical parameters. The fully integrated models show spatial structures which are not present when the equations are evaluated using the closed-form analytical equation (Eq 2.31) which implicitly assumes a Gaussian electron density profile. These results should be taken with a dose of skepticism as I have not performed an extensive study of the GIPs produced through evaluating the fully integrated set of equations in Eq 2.29, which is an excellent starting point for future investigations. As a first step, expressions containing explicit Fourier transforms in Eqs 2.29 should be reformulated using the FFT for the purpose of sane execution times.

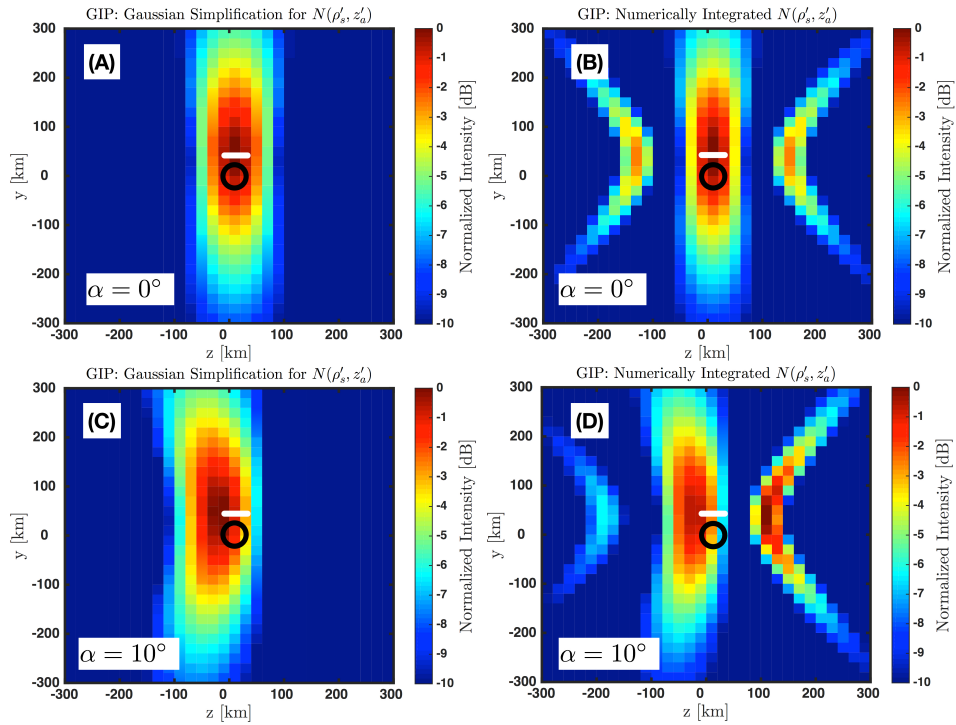


Figure 2.21: Evaluating the 3D Fourier transform described by Eqs 2.29 and finding the resultant electric field over an arbitrarily oriented plane (in this case Earth's surface) is a nontrivial problem in computational electromagnetics. The illumination patterns in panels (A) and (C) were calculated using Tinin's analytic expression which assumes a Gaussian electron density profile along each axis of the trail (Eqs 2.31 and 2.29k). Panels (B) and (D) show the integrated solution generated by evaluating the full set of GIP equations in 2.29 which allows for an arbitrary electron density profile  $N(\rho'_s, z'_a)$  in Eq 2.29h.

The simplified GIP formulation of Eq 2.31 was evaluated over a variety of trail orientations. Figure 2.17 shows the GIP for a transmitter oriented along the axis of the trail. The transmitter is located at  $x = -200$  [km] and the meteor trail electron density is described by the Gaussian distribution centered at  $x = y = 0$  [km]. Figures 2.18 and 2.20 show GIPs with similar transmitter and trail geometries, but different transmit electric vector orientations. Figure 2.19 shows the GIP of a trail having the classical ‘backscatter’ geometry with some familiar Colorado landmarks. These Figures clearly show that power scattered from meteor trails with typical physical parameters is available over large spatial regions on Earth’s surface. In fact, the terms ‘backscatter’ and ‘forward-scatter’ used throughout the meteor radar literature seem misleading under these results. The meteor trail need not lie nearly perpendicular to the radar’s wavevector for specular scatter to occur as the modern literature often suggests [25]. This model suggests that all meteor trails will exhibit specular scatter over large spatial regions when illuminated by a low-VHF meteor radar. Furthermore, these results show that power from specular scatter is available from any given trail on spatial scales of 100’s of km, which strongly supports the fundamental assumption of multistatic meteor wind radar.

Figure 2.22 shows how the GIP changes when sweeping through the trail’s azimuthal orientation by rotating the trail in the  $\hat{y}\hat{z}$  plane about the  $\hat{x}$  axis. Figure 2.23 shows how the GIP changes when rotating the trail about the  $\hat{y}$  axis in the  $\hat{x}\hat{z}$  plane by sweeping through  $\alpha$ . The radar system parameters are included for completeness but only serve as a scaling factor as seen by Eq 2.29k. One conclusion of the illumination pattern simulations is that the spatial structure of the scattered field is a complex function of the trail and transmitter geometry, and that specular scatter from meteor trails under arbitrary Tx/Rx and trail geometries is always available to properly located receiver stations.

Figures 2.25 and 2.26 suggest an experiment with the potential to provide evidence in support of Tinin’s trail scatter theory by observing a meteor shower having a known problem geometry. In addition to observing the spatial detection rate asymmetry of a meteor shower, Figure 2.24 shows the probability of detecting a trail out of a large spatially uniform population at any geographic location with respect to the transmitter. Each receiver added to the network will increase the total number of detections  $N$  according

to Eq 2.32 [133] where  $N_o$  is the number of meteors detected by a monostatic system ( $(z,y)=(0,0)$  in Figure 2.24),  $N_{tx}$  and  $N_{rx}$  are the number of transmitters and receivers and  $c(d)$  is a scaling factor related to the transmitter/receiver spacing which decreases with longer station baselines. As the shower radiant propagates across the sky from panels **(A)** to **(E)** in Figure 2.25, the distribution of detection rates on the ground exhibits clear spatial asymmetry. Each receiver in a spatially distributed grid over the region would observe different rates of trail detection as the shower radiant passed over the observer. Figure 2.26 shows the normalized detection rates that would be expected at the receiver locations shown in panel **(E)** over the course of the radiant transit. This experiment would enable direct experimental evidence for Tinin's theory of meteor trail scatter [126]. A multistatic meteor radar could observe the spatially asymmetric trail detection rates of a meteor shower. For multistatic meteor radar networks with stations spacing in the low 100's of [km], this value is usually between 0.3 and 0.8.

$$N \approx c(d)N_oN_{tx}N_{rx} \tag{2.32}$$

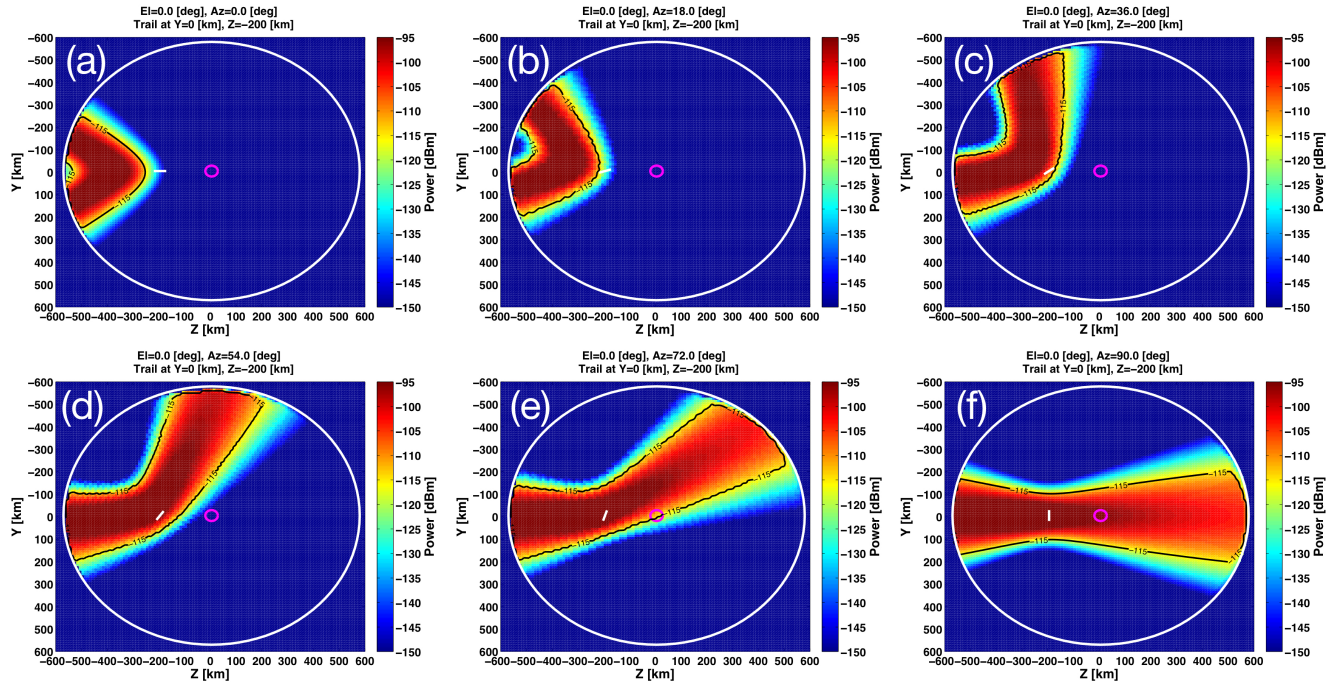


Figure 2.22: Effect of the trail's azimuth angle on the GIP using Eqs 2.31 and 2.29k. The azimuth angle is varied from  $0^\circ$  to  $90^\circ$  as the trail is rotated in the  $\hat{y}\hat{z}$  plane about the  $\hat{x}$  axis. The trail's height is  $x_m = 100$  [km]. The trail is represented by the white line centered at  $(z, y) = (-200, 0)$  [km], and the transmitter is located at  $(z, y) = (0, 0)$  [km] which is represented by the magenta circle. GIPs are calculated under the same system parameters as used in Figure 2.23. A monostatic system would only observe the trail in panel (f) under realistic environmental noise conditions ( $T_e \approx 100,000[K]$ ).

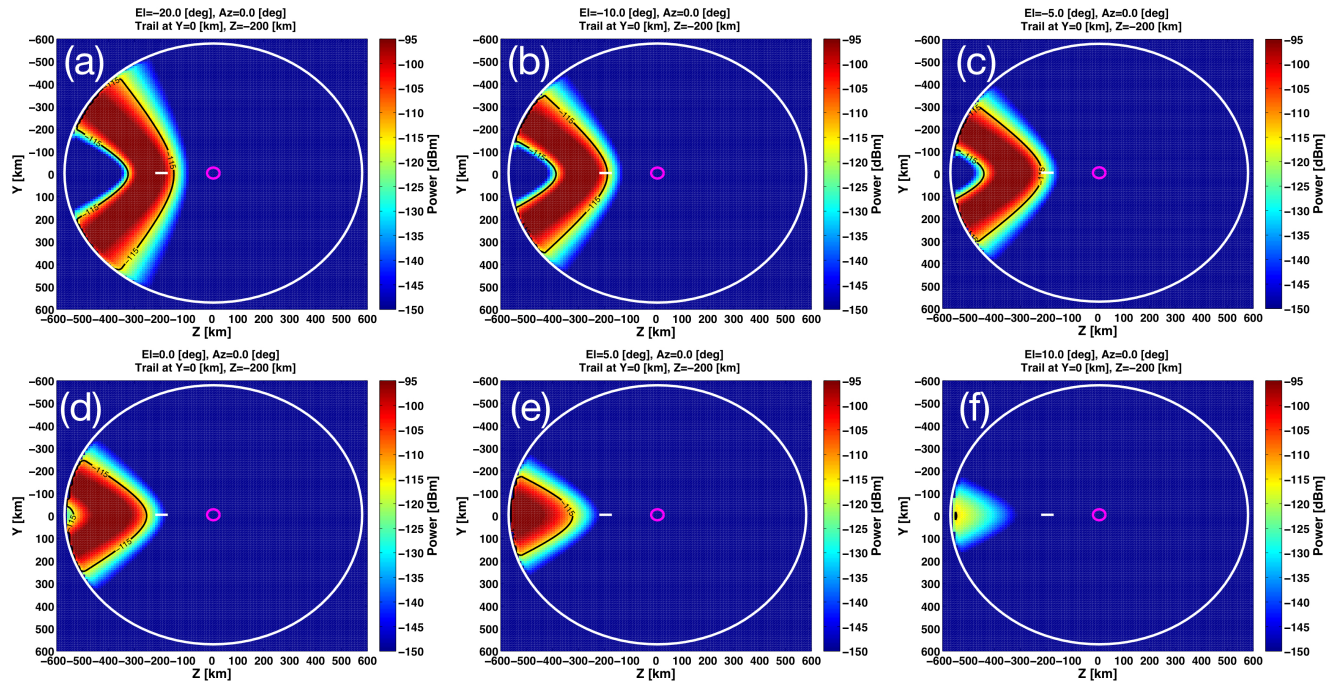


Figure 2.23: Effect the trail's elevation angle  $\alpha$  on the GIP using Eqs 2.31 and 2.29k. The elevation angle is varied from  $-20^\circ$  to  $10^\circ$  as the trail is rotated about the  $\hat{y}$  axis in the  $\hat{x}\hat{z}$  plane by sweeping through  $\alpha$ . The trail's height is  $x_m = 100$  [km]. Note that panel (d) is identical to panel (a) in Figure 2.22. The trail is represented by the white line centered at  $(z, y) = (-200, 0)$  [km], and the transmitter is located at  $(z, y) = (0, 0)$  [km] which is represented by the magenta circle. See Figure 2.16 for the definition of trail elevation angle. As the elevation angle is increased, the effective size of the Fresnel zone with respect to the transmitter location causes a decrease in scattered power. These GIPs were calculated under the system parameters of:  $G_r = 15$  [dB],  $G_t = 15$  [dB],  $P_t = 10$  [kW]. A classical monostatic MWR system would observe none of these trails.

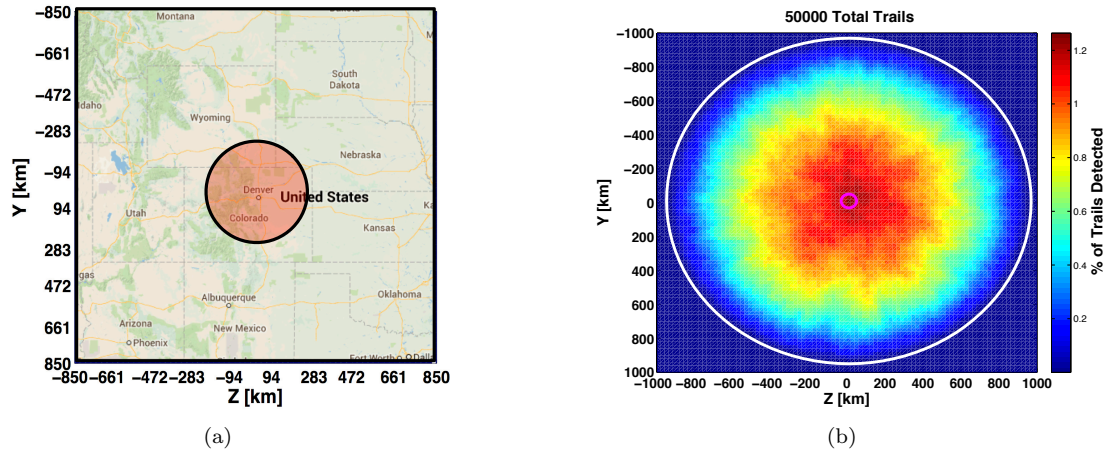


Figure 2.24: Panel (b) shows the percentage of trails detected out of a total population of 50,000 simulated trails uniformly distributed over a geographic region of  $2000 \text{ [km}^2\text{]}$  as a function of the receiver's geographical location. Trail heights were generated using the Gaussian parameters:  $\mu = 95 \text{ [km]}$ ,  $\sigma = 5 \text{ [km]}$ . Azimuth and elevation angles are realized from the uniform distribution. The region containing the largest number of detections is bounded by an approximate  $400 \text{ [km]}$  radius ring centered at the transmitter location, which is shown on a geographic map centered at the Platteville, Colorado radar site (a). The simulation is consistent with Eq 2.32 which describes how the number of additional meteor trail detections increases for each additional receiver and transmitter added to the geographically distributed multistatic network.

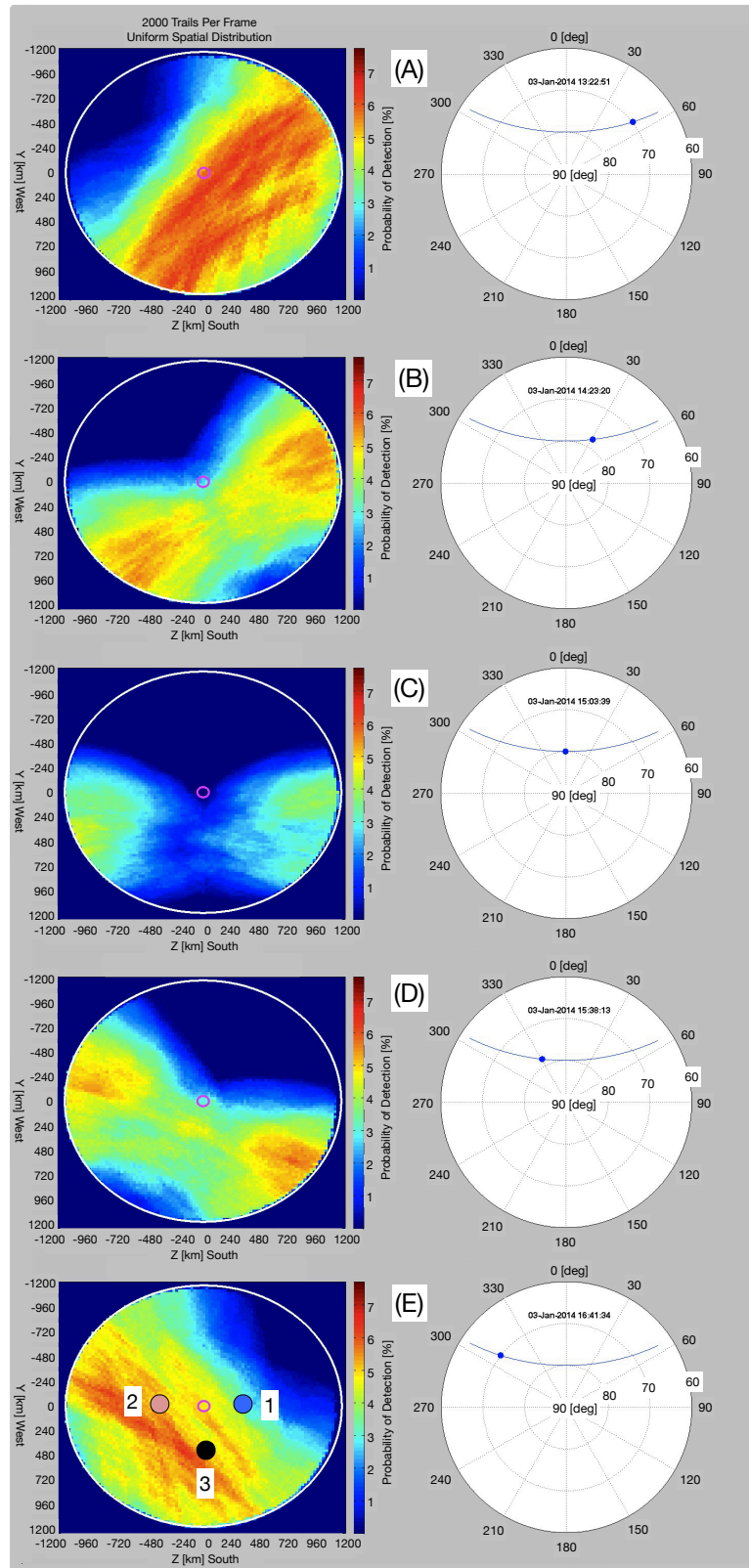


Figure 2.25: This figure shows the simulated temporal evolution of the integrated ground illumination pattern over the course of the Quadrantid meteor shower as observed from Boulder, Colorado on 3-Jan-2014. The right panel shows the position of the radiant in the sky where 0 [deg] is true north. The left panel shows the percentage of meteor trails detected at any given location over a region of 2400 [km<sup>2</sup>] where the 40 [kW] transmitter is located at (Y,Z)=(0,0) [km] and represented by the magenta circle.

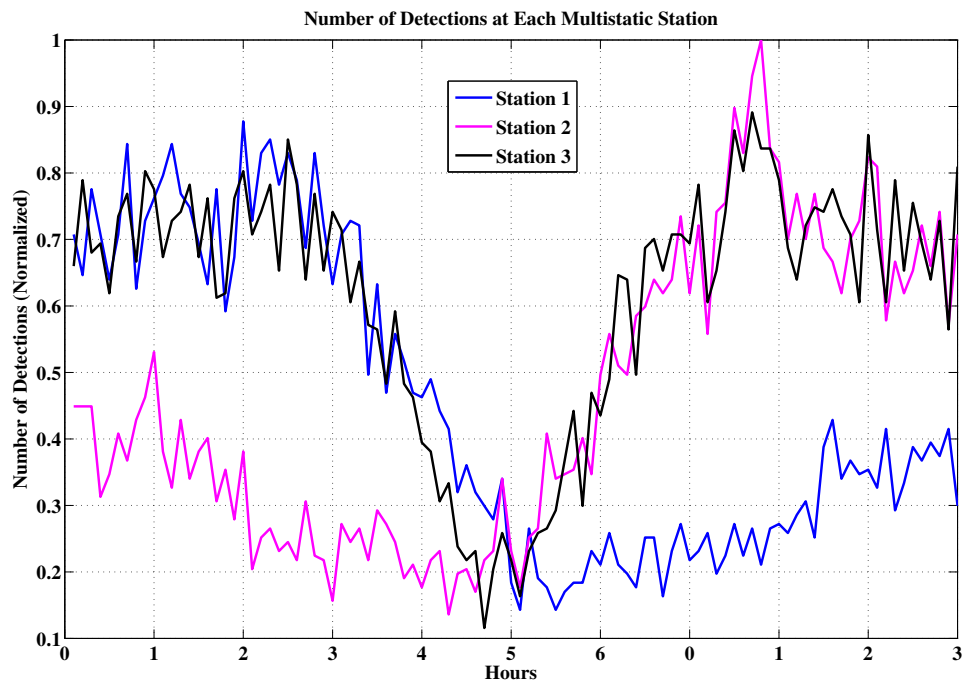


Figure 2.26: Normalized meteor trail detection rates over the course of the Quadrantid radiant transit at the receiver locations shown in panel (E) of Figure 2.25. Observation of this predicted spatial asymmetry using a multistatic meteor radar network could provide direct experimental evidence for the Ground Illumination Pattern model described in this Chapter.

This section described the numeral GIP formulation as formulated by Tinin, and presents a limited comparison of the numerically calculated GIP with the analytical solution under the Gaussian electron density assumption. The GIP simulations presented in this chapter are the first numerical results which clearly show the expected meteor trail radar response under an arbitrary receiver, transmitter and trail geometry. The large spatial distribution of scattered power on Earth's surface supports the fundamental viability of multistatic meteor wind radar. The numerically integrated formulation allows for an arbitrary electron density distribution in Eq 2.29h. The numerical and analytic GIP solutions are consistent in their structure and the ratio of the magnitudes of the intensity. The magnitudes of the calculated intensities are slightly different, an inconsistency which has yet to be resolved. See Chapter 5 for suggested future work related to the GIP and diffusion topics. Possible future research topics include parallelizing the numerical GIP calculation and implementing a full electrodynamic description for electron density distribution (use Eq 2.17 for Eq 2.29h) in addition to implementing a time-dependent numerical simulation to study the time-evolution of the radar return under Dimant and Oppenheim's full electrodynamic diffusion.

## Chapter 3

### The Colorado Software Defined Radar

“Machines take me by surprise with great frequency.” – Alan Turing

#### 3.1 Design Philosophy

Problems inherent with traditional analog radar remote sensing receiver systems are suboptimal in meeting the scientific goals of mesoscale, MMWR observations. Long-term stability of analog receiver systems are difficult to quantify. For example, free-running transmit oscillators radiating at the carrier frequency of the radar easily leak into the receive chain of an analog receiver, resulting in DC offsets at baseband and degraded SNR. Furthermore, fixed-frequency operation and geographically distributed synchronization issues inherent in the analog receiver systems are all roadblocks in the deployment of coherent, MMWR systems. CoSRad address these problems by enabling direct-convert data acquisition with straightforward geographically distributed array synchronization.

CoSRad began as a project funded under Prof. Palo’s NSF-CAREER award ATM0449985 with a goal of replacing the analog receiver used in the Colorado Obninsk Radar (COBRA) [38] series of meteor radars with a software defined radio (SDR) based receiver solution, and has evolved into a highly-reconfigurable

data acquisition and radar transceiver system well suited for use in nearly all radar remote sensing topologies. At the beginning of this project in 2008, no commercially available products met the requirements needed for deploying a SDR based receiver in the existing COBRA radar configuration. The primary requirements driving our SDR based receiver development are summarized below. First, a minimum of six synchronously sampled channels were required to deploy a software radar solution in the existing COBRA topology. Five channels are required for the canonical all-sky receive antenna array described in [74] and used with many meteor radar systems including those described in [48, 86] in addition to the COBRA-specific yagi-based detection antennas. Secondly, each system must be fully synchronous with itself (synchronous  $f_s$ ,  $f_o$  and  $f_p$ ), capable of synchronizing with other collocated receivers, and be capable of synchronizing with any number of geographically distributed receivers.  $f_s$  is the DDS-generated receiver sampling frequency (see Eq 3.1),  $f_o$  is the DDS-generated carrier frequency, and  $f_p$  is the pulse repetition frequency defined by a FPGA counter. Thirdly, the system should be based on open source hardware and software, and make use of well-specified interfaces and protocols whenever possible. Similar to the SuperDARN Auroral Radar Network model [8], this could enable anyone to build and innovate upon the CoSRad hardware [47].

A number of secondary requirements are derived from the primary design drivers listed above. For example, avoiding expensive and time consuming board-level hardware design was desirable. The use of well supported open-source development tools and software packages was instrumental in cost reduction as was the use of USB 2.0 or gigabit ethernet as the receiver's interface protocol. Having a long support lifetime, Red Hat Linux was the natural choice for the General Purpose Computer (GPC) operating system. Use of a Field Programable Gate Array (FPGA) device was the most straightforward way to integrate the various development boards and interfaces necessary to build a MMWR system meeting our primary design goals. At the most abstract hardware level, CoSRad consists of an 8-channel data acquisition system where a stream of real-valued voltage samples from an interferometric antenna array are transferred over a serial interface and stored on a GPC where the traditional radar signal processing tasks such as I/Q demodulation, matched filtering and signal detection are preformed.

Table 3.1: Comparison of CoSRad with other popular software defined receiver technologies

	<b>CoSRad</b>	<b>USRP N210</b>	<b>Pentek</b>	<b>Nutaq</b>
Approximate cost (USD) $\pm$ 20%	5k	11k	30k	30k
Number of channels	8	2	4	16
Native $f_o$ and $f_s$ generation	✓			✓
Native GPS disciplined timing	✓			✓
Integrated radar controller	✓			
Open source drivers	✓	✓		✓
Extensive multistatic synchronization capabilities	✓		✓	✓

Our current approach utilizes the development boards listed in Table 3.2 to build the CoSRad receiver depicted in Figures 3.1 and 3.5. In Table 3.1, the complete receiver system cost is calculated based on all hardware necessary to meet technical specifications approaching those of the CoSRad system. For example, implementation of a system based on the USRP N210 would require the integration of four separate USRP N210 units to provide an aggregated eight channels which are natively available on a single CoSRad system. Since the beginning of this project, the Nutaq digitizer system has become commercially available which shows promise in providing a complete hardware solution, but will not be further discussed.

### 3.2 Reconfigurability

CoSRad is a software configurable data acquisition system, timing pulse generation engine and software defined radar signal processor designed to operate over a wide range of radar remote sensing topologies. A defining characteristic of the SDR approach to data acquisition and radar receiver design is the location of the ADC in the signal processing chain. In accordance with maximizing flexibility in frequency selection

Table 3.2: Primary commercial components used to build the CoSRad receiver depicted in Figures 3.1 and 3.5

<b>Description</b>	<b>Manufacturer</b>	<b>Part Number</b>
Virtex 5 Eval Board	Avnet	AES-XLX-V5LX-EVL50-G
ADC Eval Board	Analog Devices	AD9252-50EBZ
Interface Board	Avnet	AES-EXP-ADI-ADPT-G
DDS Eval Board	Analog Devices	AD9954/PCBZ
DAC Eval Board	Analog Devices	EVAL-AD5440EBZ
GPS Disciplined Oscillator	Trimble	53110-45

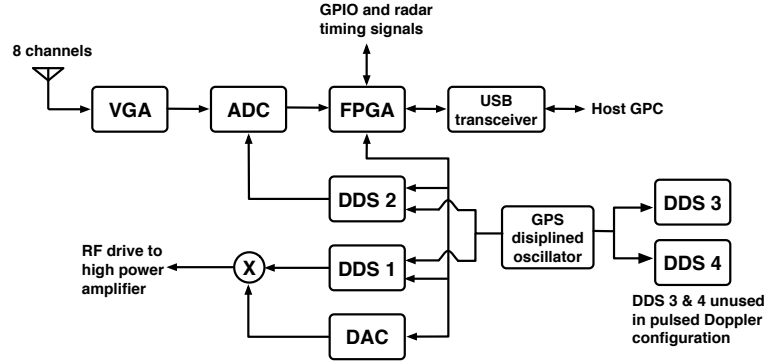


Figure 3.1: CoSRad hardware block diagram when configured for pulsed Doppler operation. For LMFCW operation, two additional DDS devices are utilized. Both the carrier frequency  $f_o$  and sampling frequency  $f_s$  are defined using the programmable frequency tuning words associated with each DDS.

Table 3.3: CoSRad was successfully configured for measurement campaigns with the following existing radar systems. See Figure 1.2 for a graphical depiction of the carrier frequencies listed in this table. Reconfigurability for use with a wide range of existing antenna and transmitter systems is a characteristic of the software-defined approach to radar remote sensing. The LFMFCW system has an  $f_o=926$  [MHz] (via up conversion) and an IF at 10.7 [MHz] with 2 [MHz] Bandwidth

Symbol	System Description	Frequency [MHz]
R1	LFMCW	10.7
R2	Platteville (COBRA)	30.355
R3	SAAMER	32.55
R4	DEL-ADL Multistatic Configuration	35.24
R5	South Pole (COBRA)	46.3
R6	Jicamarca (JASMET)	49.9

Table 3.4: Fundamental Hardware Specifications

Symbol	Description	Value	Unit
$f_s$	Sampling Frequency Range	5 - 50	MSPS
$N_{ch}$	Available Number of Channels	8	
$f_o$	DDS Carrier Frequency Range	0.5 - 200	MHz
$B_{sys}$	Analog Bandwidth of AD9252-50EBZ	0.01 - 325	MHz
$B_d$	Max Digital Bandwidth (USB 2.0)	480	Mbps
$f_{dac}$	DAC Update Rate	21	MHz
$V_{in}$	ADC Input Voltage Range	2	V <sub>pp</sub>
$ADC_{res}$	ADC Resolution	14	bits
$G_{VGA}$	Built-in VGA gain	-4.5 - 55.5	dB

and system reconfigurability, the ADC is placed as close as possible to the antenna terminals in the RF processing chain. Typically, the antenna output will only be subjected to gain and anti-alias filtering before sampling. Transmit waveform structure and processing of the received radar echoes are software defined. Their characteristics fall within the fundamental hardware parameters listed in Table 3.4. For VHF carrier frequencies with a bandwidth below the receiver’s Nyquist frequency ( $f_s/2$ ) and carrier below the receiver’s analog bandwidth ( $B_{sys}$ ), traditional analog receiver components such as IF mixers are absent from the high level architecture outlined in Figure 3.1.

Both  $f_s/2$  (sampling bandwidth) and  $f_o$  (carrier frequency) are programmable within the ranges specified in Table 3.4. Furthermore,  $f_s$  is dynamically configurable during operation and  $f_o$  is capable of various frequency sweep profiles enabling multi-frequency and LFM CW operation. Carrier frequencies ( $f_o$ ) greater than  $B_{sys}$  are implemented through the use of external up and down conversion hardware, while the sampling bandwidth is fixed at a maximum of 25 [MHz]. See the datasheets associated with the components listed in Table 3.2 for additional hardware details. While we have described a specific set of hardware components used to implement CoSRad, the software defined design philosophy depicted in Figure 3.1 can be applied to all SDR radar remote sensing receivers using a range of available hardware.

CoSRad includes an integrated data acquisition timing controller which can be configured as a radar controller. See [117] for an overview of configurable FPGA-based timing control. When configured for meteor radar observations, CoSRad functions as a radar controller, VHF direct-sampling data acquisition system and

software-defined pulsed Doppler radar. In this configuration, the channels of an interferometric array similar to that depicted in Figure 4.1 [74, 57] are sampled at the output of an RF front-end. The resulting time series of real-valued samples are transferred over USB 2.0 to a GPC where the signal detection and pulsed Doppler processor components of CoSRad are implemented (see Section 3.5). Figure 3.2 shows a specular meteor trail echo visualized using the software pulsed Doppler component of CoSRad. Configuring CoSRad for integration into existing meteor radar systems typically involves setup of the integrated radar timing controller to interface with external hardware (usually a transmitter and RF switches) and modification of  $f_o$  and  $f_s$  unique to each radar site (see Figure 3.3). Table 3.3 in combination with Figure 1.2 detail the CoSRad configurations which resulted in successful specular radar observations of meteor trails.

In collaboration with Dr. Christopher Williams [136], the CoSRad receiver was configured for LFMCW observation of boundary-layer winds. A thorough exploration of the LFMCW technique is beyond the scope of this thesis, however, this campaign showcases the potential for extensive reconfigurability inherent in software defined radar observations. Two additional DDSs (DDS3 and DDS4 in Figure 3.1) were employed to generate the necessary frequency swept waveforms and when coupled with an up-converting RF front end at  $f_o = 926$  [MHz] and a software defined linear frequency modulation radar software component, we successfully observed the line-of-sight boundary layer wind velocities depicted in Figure 3.4. The data was acquired on a gusty day at NOAA’s Boulder Atmospheric Observatory. These LFMCW observations represent an important aspect of the software defined approach to radar remote sensing. As was discussed in section 3.2, CoSRad can be configured for use in a wide range of radar remote sensing regimes through modifying the software configuration and incorporating an appropriate RF front end.

### 3.3 Hardware details

The core components comprising the CoSRad receiver are listed in Table 3.2. These components are packaged with supporting power distribution and RF front-end blocks (gain and anti-aliasing filters

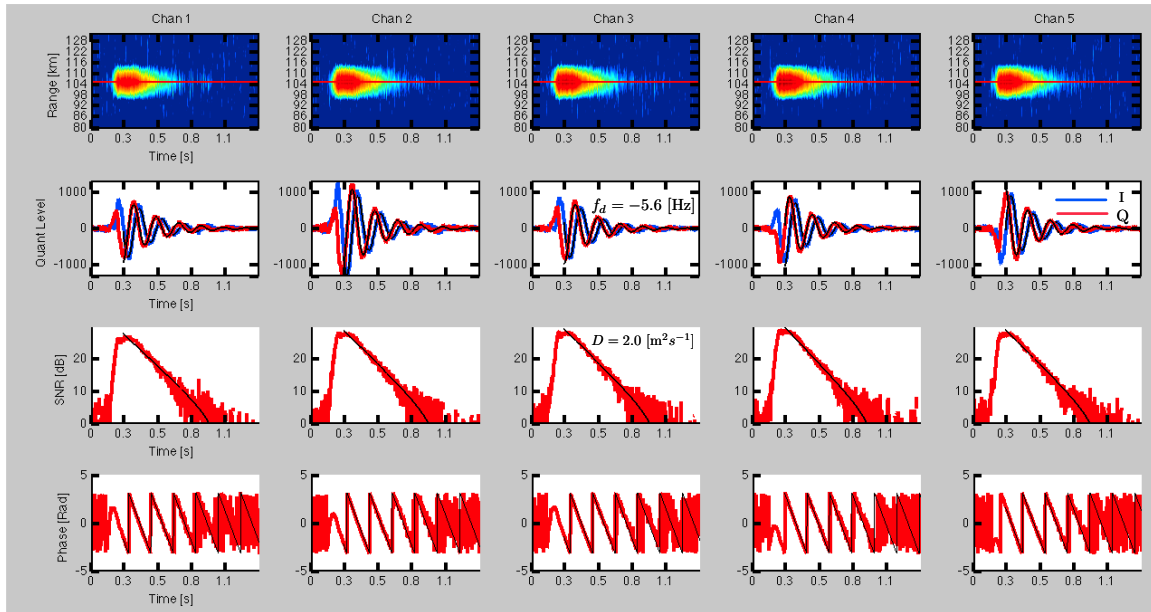


Figure 3.2: A specular meteor trail echo observed by CoSRad configured for monostatic meteor radar. Each column is a separate receiver channel, one for each antenna of the interferometric antenna array depicted in Figure 4.1. The radar was operating with  $f_p = 500$  [Hz],  $PW = 80$  [us],  $f_o = [35.24]$  MHz and  $f_s = [10.843]$  MHz. The echo was processed and visualized with latest pulsed Doppler processor CoSRad software module. Row 1 shows the SNR of the processed radar pulse at the output of the matched filter (see Section 3.5.2). The range of maximum SNR (indicated by the horizontal red line in row 1) is shown in row 3. The ADC quantization level of the  $I$  and  $Q$  components at the range of maximum SNR are shown in row 2 and are directly related to the ADC input voltage by a scale factor of  $2/2^{14}$ . The phase and Doppler at maximum SNR are shown in row 4. The  $I$  and  $Q$  components (row 2) is the row of  $\tilde{\mathbf{V}}_q$  corresponding to the row of  $\mathbf{E}$  which exceeds an SNR threshold in the Doppler bandwidth (columns of  $\mathbf{E}$ ). The black trace is the functional form of the least-squares estimate of the signal model parameters  $\hat{\beta}$  found using Eq 4.21 which represents the basic analytic model of radar echoes from an underdense specular meteor trail [98]. The Doppler frequency estimate  $\hat{f}_d$  and the diffusion coefficient estimate  $\hat{D}$  are also shown.

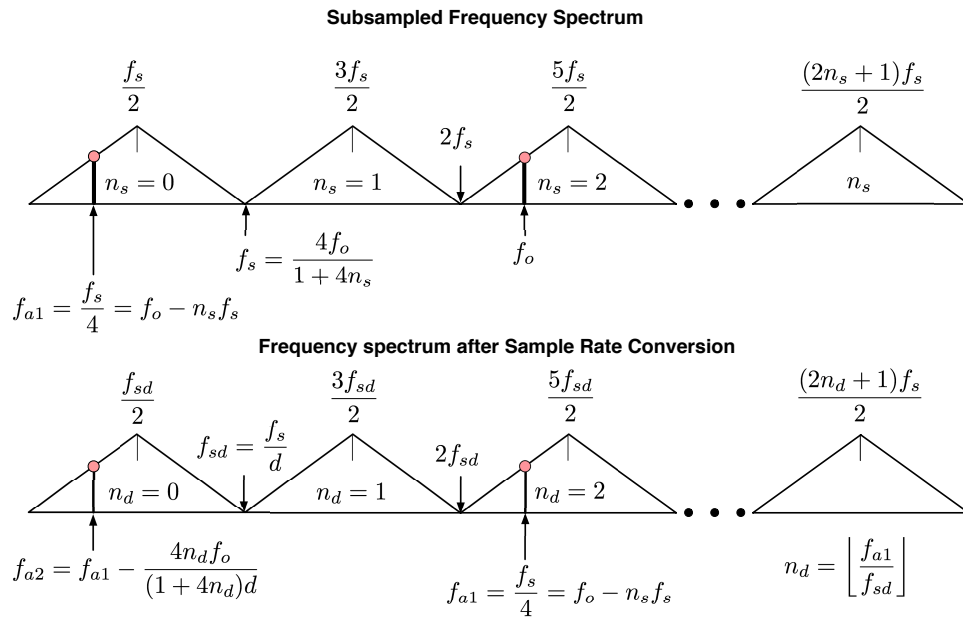


Figure 3.3: Graphical depiction of CoSRad’s sample rate conversion scheme when configured for meteor radar applications. Bandpass sampling shifts the carrier from  $f_o$  to  $f_{a1}$  when sampled at  $\frac{4f_o}{1+4n}$ . Programmable integer decimation further transforms  $f_{a1}$  to  $f_{a2}$  where  $d$  is the integer decimation factor (i.e.  $d=3$  implies every 3rd sample is retained for further processing).  $n_s$  and  $n_d$  are the number of spectral folds introduced by bandpass sampling and decimation. The frequency tuning words of DDS1 and DDS2 (see Figure 3.1) are chosen such that each carrier cycle  $f_o$  always contains exactly 4 samples.

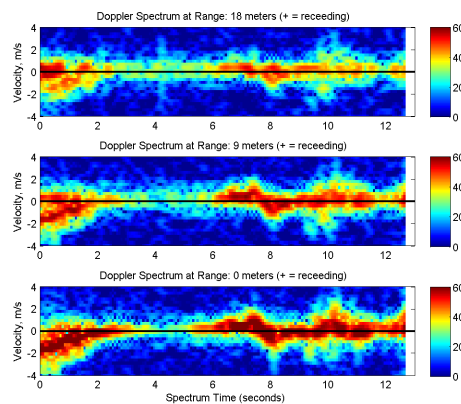


Figure 3.4: Boundary-Layer wind velocities observed by CoSRad configured for LFM CW operation [135]. A component of the problem statement for this dissertation is the development of a universal radar remote sensing receiver, exemplified by our successful observation of boundary layer winds

for typical meteor radar applications) to create a CoSRad receiver shown in Figure 3.5. CoSRad consists of a set of integrated development boards housing the main receiver components such as analog-to-digital converters (ADC) and direct digital synthesizers (DDS). The electrical interface between the ADC and FPGA development boards consists of a low voltage differential signaling interface running at a maximum of 350 [MHz] requiring careful board-to-board interconnect design. The ADC and FPGA boards are connected via a commercially produced, impedance controlled high-speed interface board. As the radar remote sensing community moves toward large-scale MMWR observations, it is our expectation that many groups will implement software defined architectures meeting their specific requirements using a variety of hardware realizations. Hardware specifications for the CoSRad-based receiver realization shown in Figure 3.5 using the components listed in Table 3.2 are given in Table 3.4.

### 3.3.1 ADC

In accordance with software defined radar design methodology, the ADC is placed at the closest point in the analog receive chain which does not exceed the ADC's maximum analog input bandwidth of 325 [MHz] or maximum digital bandwidth of 25 [MHz]. The ADC listed in Table 3.2 has a maximum input voltage specification of 2 [Vpp] and outputs a stream of 14-bit samples via eight separate serial bit streams (one for each channel) controlled by the FPGA. The samples are transmitted synchronous to edge transitions on the ADC's DCO output which are derived from the DDS-generated sampling clock ( $f_s$ ). Upon system initialization, the ADC device is configured via a standard two-wire serial programmable interface. The gain applied to the analog signal before sampling should be set such that the effects of quantization noise are minimized (gain too low) while the environmental noise is clearly observed by the ADC's least significant bits. In other words, the gain should be set as high as possible while staying within the expected dynamic range of the input signal, in this case specular meteor trail echoes. At higher gain levels, nonlinearities introduced by quantization become less significant. Practically, this corresponds to around 80 [dB] of gain for a 14-bit ADC with the environmental noise present in the lower-VHF band of around 100e3 [K].

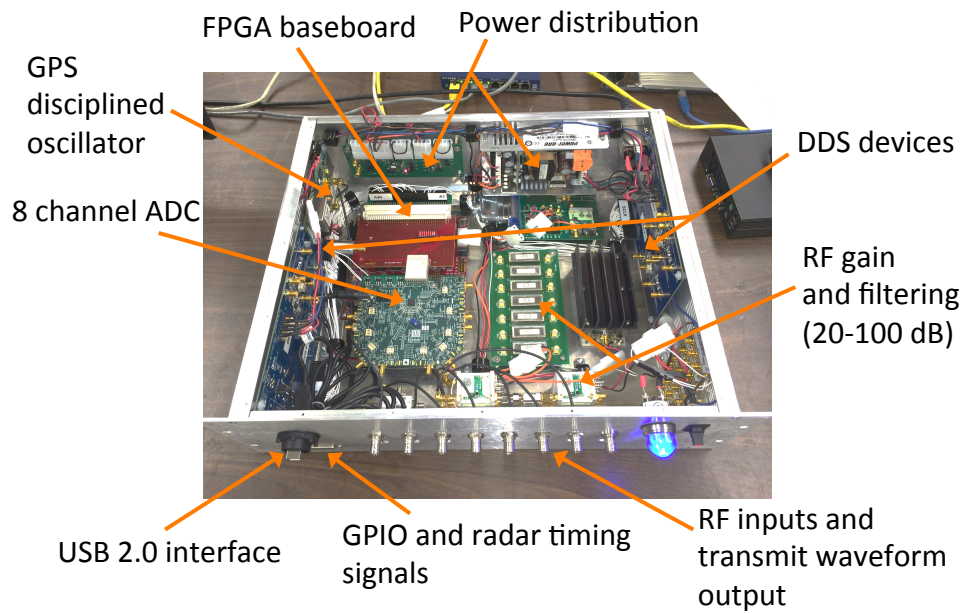


Figure 3.5: Major hardware components are identified in the CoSRad receiver when configured for multistatic meteor wind radar applications. The receiver is housed in a standard 4U, 19-inch enclosure and weighs approximately 10 kg.

For meteor wind radar applications, CoSRad is configured for bandpass sampling of the amplified and band-limited received signal. See Figure 3.3 for definitions of the quantities used in the following discussion. Bandpass sampling intentionally aliases the carrier ( $f_o$ ) into the Nyquist region ( $f_s/2$ ) of the sampled signal [54, 132].  $f_o$  and  $f_s$  are chosen such that Equation 3.1 is satisfied. For any given  $f_o$  there exist an ensemble of sampling frequencies  $f_s$  that satisfy Eq 3.1. For meteor radar applications with  $f_o$  in the lower VHF band, choosing  $f_s$  such all CoSRad hardware specifications are met restricts  $n_s$  to low-valued integers and places  $f_s$  in the range of 6-15 [MHz].  $n_s$  is the number of spectral folds introduced when band-pass sampling  $f_o$ .

$$f_s = \frac{4f_o}{1 + 4n_s} \text{ where } n_s \in \mathbb{Z} \quad (3.1)$$

This requirement intentionally aliases  $f_o$  to  $f_s/4 = f_{a1}$ . For pulsed Doppler configuration,  $f_o$  is constant which leads directly the requirement that  $FTW_{f_s} = 4FTW_{f_o}/1 + 4n_s$  where  $FTW_{f_s}$  and  $FTW_{f_o}$  are the 32 bit frequency tuning words defining the DDS output frequencies. Further reduction in the data rate is accomplished through downsampling  $f_{a1}$  by an integer ratio  $d$  where  $n_d$  is the number of spectral folds introduced by decimation by  $d$ . Equation 3.2 is the total data production rate of CoSRad where  $N_{ch}$  is the number of active channels. For best performance,  $d_o$  should be kept below 40 [MBytes/s] when using USB 2.0.

$$d_o = \frac{2f_s N_{ch}}{d} \text{ [Bytes/s]} \quad (3.2)$$

### 3.3.2 Direct Digital Synthesis and Transmit Pulse Shaping

Measurement of the Doppler frequency associated with specular forward scatter from meteor trails requires a phase coherent, geographically distributed receiver array. When CoSRad is configured for pulsed Doppler mode, two DDS devices generate the RF transmit waveform and ADC sampling clock ( $f_s$ ). Both

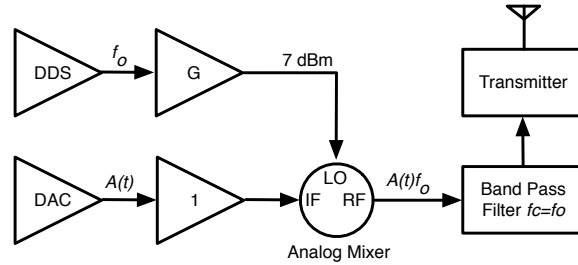


Figure 3.6: the DDS-generated carrier frequency  $f_o$  is mixed with the ADC-generated pulse shaping envelope  $A(t)$ . The low DDS output power is boosted to 7 [dBm] using a simple linear amplifier which is necessary for driving a standard 7 [dBm] mixer. The high DAC output impedance is lowered using a unity-gain BUF634P IC for driving the 50 [Ohm] IF analog mixer input. An optional bandpass filter with center frequency at  $f_o$  may be necessary at the mixer's RF output to condition the transmit pulse for presentation to a high-power amplifier.

DDS devices are driven using a 10 MHz GPS disciplined clock source ensuring synchronous outputs. DDS devices typically provide only crude amplitude modulation capabilities. Precise amplitude modulation of the RF transmit pulse is achieved by mixing the output of the digital-to-analog converter,  $A(t)$  with the DDS-generated RF carrier,  $f_o$  as shown in Figure 3.6. Samples representing points on the transmit pulse waveform envelope ( $A(t)$  in Figure 3.10) are calculated from an analytic function (i.e. Gaussian or trapezoidal envelope). During receiver configuration, samples representing the transmit waveform envelope are loaded into a FPGA block RAM primitive where they are used to drive the digital-to-analog converter and mixed with the DDS  $f_o$  output to shape each individual transmit pulse. Imposing a constant pulse-to-pulse carrier phase on each transmit pulse simplifies debug and signal processing and is usually straightforward to implement. Choosing the frequency tuning words such that Equation 3.3 is satisfied ensures that an exact integer number of carrier ( $f_o$ ) cycles are contained within a single inter-pulse period.  $R_s$  is the *IPP* counter value discussed in section 3.3.7.  $R_s + 1$  is equal to the number of samples per pulse  $n$  discussed in section 3.5.1.

$$\text{mod} \left( \frac{dR_s FTW_{f_o}}{FTW_{f_s}}, 1 \right) = 0 \quad (3.3)$$

Care should be taken when calculating this modulus because values exist for  $FTW_{f_o}$  and  $FTW_{f_s}$

which can satisfy Equation 3.3 within the numerical precision of standard computational software such as Matlab. Practically, choosing  $FTW_{f_o}/FTW_{f_s}$  such that the resultant is clearly rational (repeating pattern in the decimal) will prevent numerical errors and ensure the modulus is precisely met.

### 3.3.3 FPGA Architecture

The FPGA depicted in Figure 3.7 controls the receiver. Bold face text indicates reference to a FPGA logic block. FPGA register initialization, system control and transmission of status information is achieved through custom USB vendor requests (see USB specification). An 8051 uProcessor monitors USB activity over endpoint zero and transmits configuration data and status request commands directly to the **Command Transceiver** block on external device pins. The **Command Transceiver** and **Reset Unit** perform configuration and initialization of all FPGA logic. After FPGA initialization, ADC configuration commands sent by the host are received by the **Command Transceiver** and passed to the **ADC SPI Core** for transmission to the ADC. After full system initialization, individual channels are enabled over USB via the **Command Transceiver**. When a channel is enabled, serial samples originating from the ADC are parallelized into 16-bit words (the two most significant bits are unused) by the **LVDS Deserializer** and processed by the **DSP Core**. Processed data is finally packetized and buffered in the **Data Packetizer** for transmission to the host GPC via the **USB Controller**. Data packets originating from enabled channels are multiplexed into a single stream and transferred to the USB FX2 transceiver chip by the **USB Controller** block. See Section 3.3.7 for a more through discussion of the data format. A **Timing Synchronization** block creates logic signals used to control the various external timing requirements. See Section 3.3.6 for more details on the radar controller block and timing signals. All timing signals are synchronous to  $f_s$  and therefore also  $f_{gps}$ .

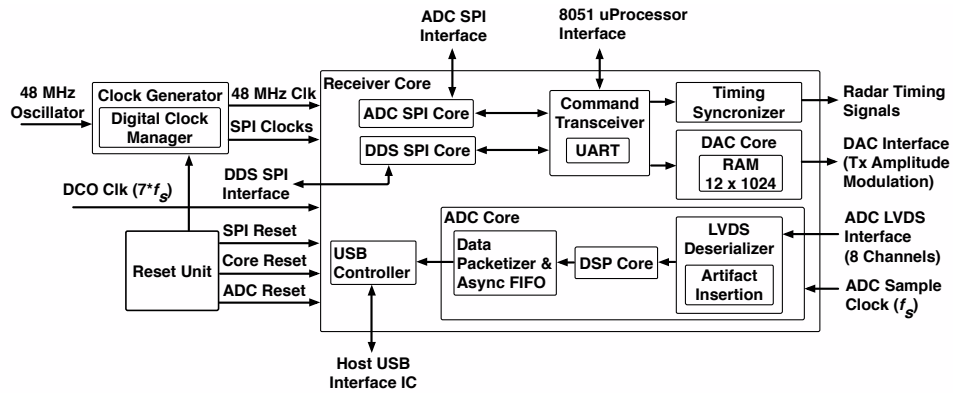


Figure 3.7: Block diagram of the CoSRad FPGA. The radar timing signals and transmit pulse amplitude modulation are both synchronous to the ADC sample clock ( $f_s$ ). DDS devices synthesizes the sampling clock  $f_s$  and transmit pulse frequency  $f_o$ . Both DDS devices are driven by a GPS disciplined oscillator (see Figure 3.1), therefore the FPGA's **ADC Core** processing chain is GPS synchronous. Each block in this diagram represents a VHDL module. Note that the **ADC Core** is replicated 8 times in parallel, one core for each available channel.

### 3.3.4 FPGA Development Methodology

A suite of industry standard tools were used to create the FPGA architecture. The FPGA is described in VHDL (with the exception of the **DSP Core**), while some vendor-supplied models are written in Verilog. ModelSim SE, the Xilinx ISE development suite and Matlab are the primary tools used in FPGA development. FPGA development enjoys a long and thriving reputation of frustration inducing cryptic errors and excruciatingly complex development tools. One design goal of the CoSRad system is to provide reconfigurable software defined data acquisition to users who lack extensive FPGA programming experience. After device configuration, the FPGA appears to the user as a bank of registers accessed via USB custom vendor requests to endpoint zero. Registers control which channels are active, timing characteristics of the radar control signals, configuration parameters of the ADC and DDS along with various aspects of the signal processing performed by the FPGA. For example, programmable registers define the data artifact format (see Section 3.3.7) and **DSP Core** sample rate conversion factor. Adhering to software defined radar design methodology, CoSRad provides flexibility in sampling rate and FPGA-based signal processing. Interestingly, the FPGA's **DSP Core** functionality is defined in Matlab and synthesized into HDL primitives using the Matlab HDL Coder toolbox. For narrow-band specular meteor radar applications, the filter structure shown in Figure 3.8 with frequency response shown in Figure 3.9 is implemented on a per-channel basis. Algorithms used to synthesize code described by a highly abstracted language like Matlab into a set of FPGA hardware primitives comes at the price of speed and efficiency, however, considering the gains in simplicity of implementation, the tradeoff is acceptable for most meteor radar receiver applications. Receiver configurations requiring signal processing speeds approaching the physical timing limitations of the FPGA will require a less abstracted (but more time consuming and complex) implementation strategy. The **DSP Core** is individually configurable on each of CoSRad's eight receive channels, implying another tradeoff between the number of active channels and the FPGA-based signal processing complexity. For example, applications requiring fewer channels could implement higher order filter structures on each of the active channels and still use the abstracted Matlab based design flow.

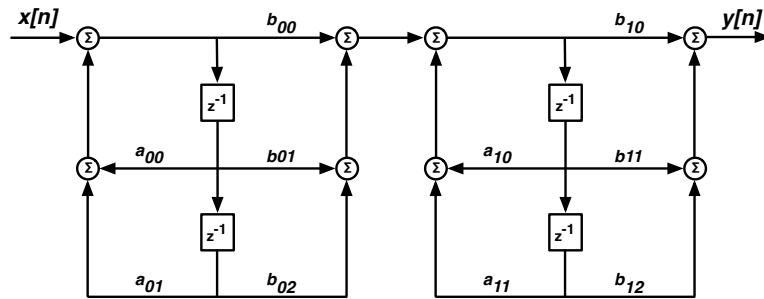


Figure 3.8: A fourth-order direct form II second order section structure used to implement the bandpass filter for the purpose of reducing the bandwidth of  $f_{a1}$  before decimation (see Figure 3.3). For the observations presented in the following sections, the coefficients are configured to implement a band-pass filter with a center frequency at  $f_{a2}$  and bandwidth  $f_{sd}$ . Energy outside the bandwidth is attenuated by a minimum of 40 dB as shown in Figure 3.9. For typical MWR applications, each of the 8 **DSP Core** blocks in Figure 3.7 would contain the same filter, however, each filter could be individually configured.

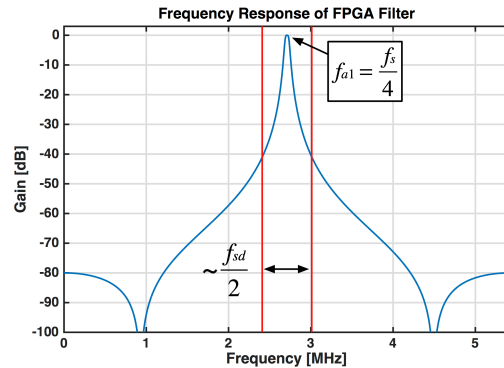


Figure 3.9: Frequency response of the filter structure depicted in Figure 3.8 as configured for use with the Delamere antenna array and transmitter at  $f_o = 35.24$  [MHz] and  $f_s = 10.843$  [MHz].  $f_{a1}$  is the subsampled carrier (see Figure 3.3) and  $f_{sd}$  is the final per-channel receiver bandwidth at the USB port. The frequency response for this filter was specifically configured for each radar site in Table 3.3, and is replicated for each active channel in the **DSP Core** FPGA block of Figure 3.7.

Table 3.5: Parameters associated with the GPIO and transmit pulse signals depicted in Figure 3.10

Symbol	Description
$t_{IPP}$	Inter-pulse period
$t_{PW}$	Pulsewidth
$t_{DLY}$	Pulse delay
$A(t)$	Pulse shaping envelope
$\Delta t$	Timing resolution

### 3.3.5 FX2 USB Transceiver

Samples are requested from the host general purpose computer (GPC) over a USB 2.0 link with a maximum throughput of 480 [Mbps] aggregate over all channels. A Cypress Semiconductor FX2 USB transceiver arbitrates USB bus transactions. The FPGA clocks data packets into the slave FIFO interface of the USB transceiver, where a host PC subsequently reads the data using the open source LibUSB libraries. Architecture of the FX2 slave FIFOs is optimized for 1024 byte data transfers, hence, the FPGA transfers data to the FX2 slave FIFOs in multiples of the optimal transfer size. Exhaustive documentation describing USB, the FX2 device and LibUSB libraries are available online. Two freeware Linux tools, the Small Device C Compiler (SDCC) and CycFX2Prog provided useful for development and debug of the USB and 8051 microprocessor-to-FPGA interface.

### 3.3.6 GPIO and Timing Signals

CoSRad includes a programmable controller capable of modifying the timing parameters depicted in Figure 3.10 and Table 3.5 based on a GPS synchronous oscillator and are therefore synchronous to  $f_s$ . The inter-pulse period  $t_{IPP}$ , pulse width  $t_{PW}$ , pulse delay  $t_{DLY}$ , carrier frequency  $f_o$  and pulse shaping envelope  $A(t)$  are all modified by configuring various FPGA registers. In this way, CoSRad functions as a GPS synchronous programmable radar controller. When configured to generate the radar control signals needed to drive a typical transmitter, 32 GPS-synchronous GPIO signals are also available. All timing signals have a maximum time resolution of  $\Delta t = 1/7f_s$ .

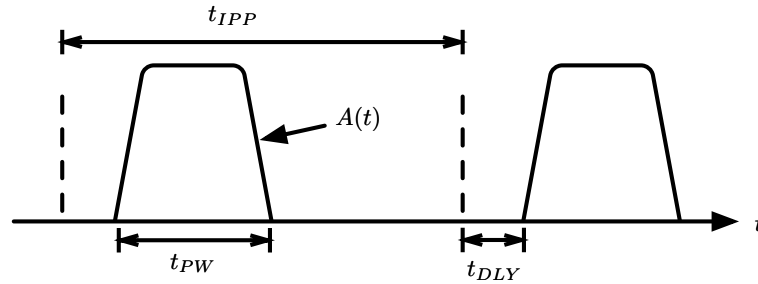


Figure 3.10: Properties of the radar timing signals generated by the CoSRad **Timing Synchronizer** FPGA core. The properties defined in Table 3.5 are defined through various FPGA registers for each signal. This allows CoSRad to function as a programmable GPS-synchronous pulse engine, capable of driving external radar hardware components such as transmitters and switches.

### 3.3.7 Data Format

CoSRad is a real-time system generating a constant stream of real-valued samples transferred to a host computer through an asynchronous USB interface. All low-level USB bus transactions are handled by the FX2 USB transceiver and LibUSB library. Data samples are written by the FPGA into the FX2 and at some nondeterministic time later are read by the GPC. Bulk transfer mode USB does not guarantee time of delivery; therefore, the instantaneous USB interface throughput may temporarily drop below the data generation rate of the receiver (see Equation 3.2). Buffering in the **Data Packetizer** FPGA block provides some tolerance to this scenario, however, in the event of a buffer overflow in the FPGA's FIFOs, the host GPC must identify the quantity of dropped data. This functionality is provided through a transmission protocol imposed on the USB data stream. Consider the data protocol depicted in Figure 3.11 as abstracted from the low-level USB layers, implementable over any serial interface. The serial stream of data contains two features of interest. Packet headers containing metadata information and artifacts identifying the start of each radar pulse are artificially inserted into the data stream. All data is read by the GPC in 2040 byte chunks with an 8 byte header forming a stream of 2048 byte packets. Packets generated from data received on identical channels have sequentially numbered packet counter fields assuming the absence of a receiver buffer overflow. Any non-sequential packet counter values received by the host indicate a dropped data event. Data is associated with a specific channel through a 'Channel ID' field in the packet header. The

**USB Controller** interleaves packets from sequential channels for transmission to the GPC. For example, if channels 1, 4 and 5 are enabled, packets containing data from those channels are sequentially and circularly queued for transmission to the GPC.

An optional data artifact comprised of a geophysically improbable numerical sequence is written over the data stream at the start of each transmit pulse. Note that the packet headers are inserted into the data stream in addition to the data samples while the data artifact replaces a section of data. When configured for pulsed Doppler meteor radar, replacement of the lower range-gate data by the artifact does not influence science results because samples directly following the transmit pulse are blanked by the host processing software. The data artifact allows software on the GPC to identify the start of each pulse and quickly identify samples from identical range gates acquired on different channels within the stream. Furthermore, by changing the format of the artifact on a pulse-wise basis, specific information about each pulse is encoded. For example, if multiple antenna feeds are multiplexed onto a single receiver channel (as they are in the COBRA configuration), pulses are associated with specific transmit antennas by defining a unique artifact for each antenna. Data artifacts are written into the stream at the beginning of each pulse, and are separated by the number of samples per pulse  $n = R_s + 1$  where  $R_s$  is the counter value determining  $f_p$ . The CoSRad GPC software presents received data in the format of Figure 3.12 and mathematically by Equation 3.20 for subsequent signal processing tasks.

### 3.4 RF Performance and Observing the Analog World

Characterizing the interface between the actual analog world and the digital world of computer systems requires an understanding of the boundary between the two. While attempting to analytically characterize the noise of a direct convert receiver, I found a number of poorly written and incomplete sources, with none directly dealing with the following topics in a comprehensive, general and straightforward manner. The best of the worst texts that I did encounter was probably James Tsui's book on Digital Wideband Receivers [127],

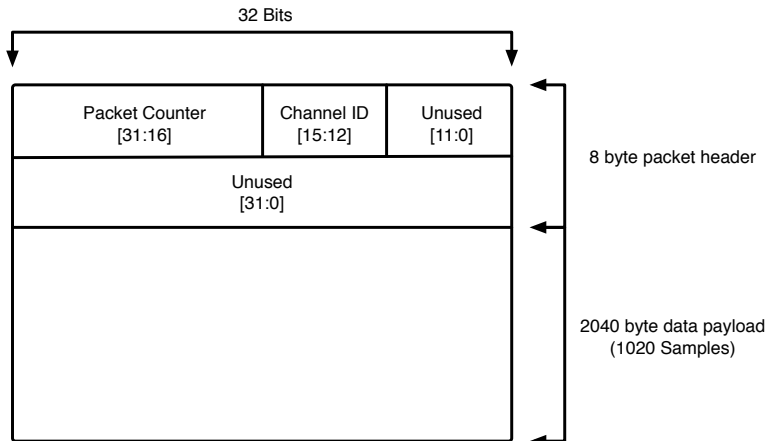


Figure 3.11: Data is received over the USB 2.0 interface in the depicted format. All data is received in 2048 byte packets where the first 8 bytes contain header information and the remaining 2040 bytes contain the actual samples. The header contains a 16 bit sequentially incrementing packet counter and a 4 bit channel ID indicating the channel associated with data payload of each packet. The remaining 44 bits of header space are user configurable. Packets of this format are sequentially written to the GPC storage device during operation.

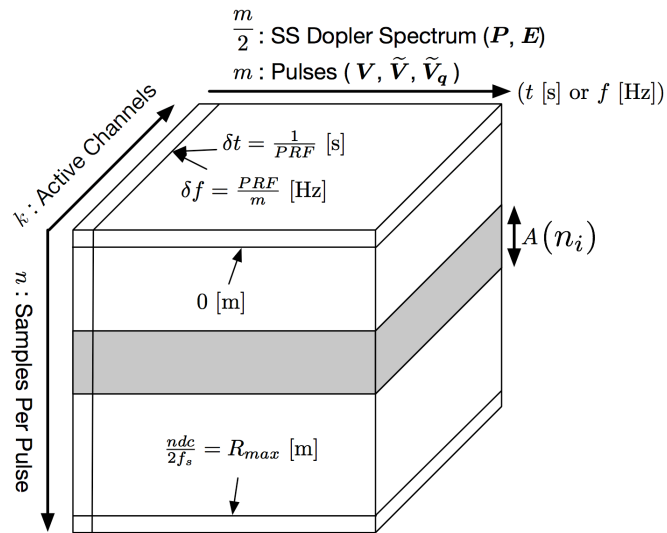


Figure 3.12: Data is stored in GPC memory in the depicted format.  $\mathbf{V}$ ,  $\tilde{\mathbf{V}}$  and  $\tilde{\mathbf{V}}_q$  are time-domain signals while  $\mathbf{P}$  and  $\mathbf{E}$  are frequency-domain signals. The GPC requests  $m$  pulses on  $k$  channels with  $n$  samples-per-pulse over USB 2.0 from the CoSRad receiver.

and it goes downhill from there. My intension with this section is to provide a general treatment of noise characteristics in direct-convert receiver architectures for future SDR engineers. General concepts concerning the observation of analog signals is followed by a numerical simulation of the CoSRad noise characteristics in section 3.4.5.

### 3.4.1 Direct Convert Noise Theory

This section deals with the fundamental limits on the detection of signals in direct RF sampling receiver systems. In this analysis, only signals at the output of the ADC are considered. This arrangement allows for the definition of fundamental limits on the parameters describing signals sampled using the direct convert receiver. After analog-to-digital conversion, a colossal variety of processing techniques may increase the signal to noise ratio or isolate various bands of interest, but if the fundamental limits of the input signal are not met, subsequent processing will be of little use. Figure 3.13 depicts the hardware setup used in the following description.

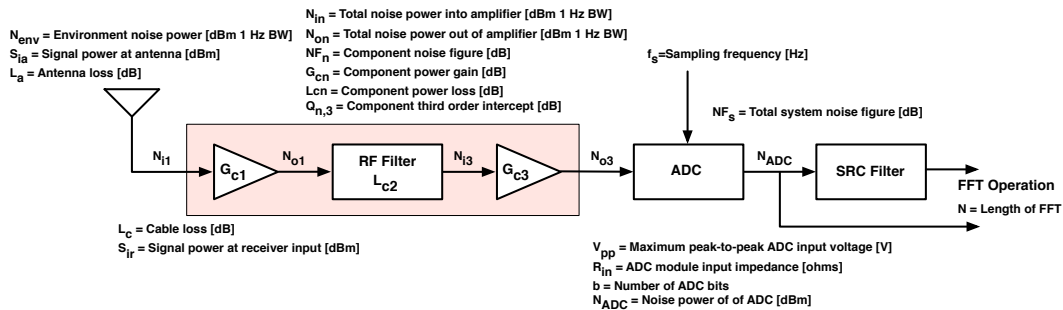


Figure 3.13: General layout of the direct-convert receiver RF front end

First, consider an antenna with loss  $L_a$  connected to a low noise amplifier with gain  $G_{c1}$  by a segment of cable with loss  $L_c$ . The noise power at the antenna is  $N_{env}$  and the noise power out of an amplifier with gain  $G_{cn}$  and noise figure  $NF_n$  is  $N_{on}$  where  $n$  is the component number in the chain (See Figure 3.13). Equation 3.4 relates the environmental noise temperature  $T_{env}$  to the sky and galactic noise temperatures for the various environments listed in ITU-R P.372 [4] to the average noise power in a 1 [Hz] bandwidth where

$k$  is Boltzman's constant. We can approximate the thermal noise power spectral density by  $S_n(\omega) \approx kT$  if  $|\omega| \ll 2\pi kT/h$  where  $h$  is Plank's constant, and  $\omega$  is in radians, a condition clearly satisfied in the VHF band. Equation 3.5 is used to calculate the average noise power in a 1 [Hz] bandwidth at the input to the first amplifier  $G_{c1}$ . Being a physical object at a temperature above absolute zero, the antenna and cable generate a thermal noise power ( $kT_o$ ) when connected to a matched load where  $T_o$  is the physical temperature of the antenna. Usually, a room temperature of  $T_o=290$  [K] is used to calculate the thermal noise power. In the VHF band, terrestrial noise power  $T_{env}$  based on sky and galactic noise temperatures  $T_{sky}$  is much greater than the thermal noise power generated in the receiver system and  $T_o$  has little influence on the noise power into the LNA. In other situations, (for example if the receiver were operating in the gigahertz band) this may not be the case and the thermal system noise could significantly contribute to the noise power into the LNA  $N_{i1}$ . When an equation produces a value in logarithmic units, it is followed by a [dBm] or [dB] to indicate decibels relative to 1 [mW] or decibels expressed as a ratio between two values. Power in [dBm] and [Watts] is related by  $P_{dBm} = 10\log_{10}P_W + 30$

$$N_{env} = kT_{env} = k(T_{sky} + T_{galactic}) \quad \left[ \frac{\text{W}}{\text{Hz}} \right] \quad (3.4)$$

$$N_{i1} = 10\log_{10}(kT_{env} + kT_o) + 30 - L_c - L_a \quad \left[ \frac{\text{dBm}}{\text{Hz}} \right] \quad (3.5)$$

Knowledge of the noise figures for each component of the system allows one to calculate the total system noise factor of a cascade of components using the well-known Friis' Formula [82] as  $F_T$  in linear units. Finally, calculate the noise power at the output of the final amplifier  $N_{o3}$  where  $NF_T$  is the total noise figure (or "noise factor" in linear units) of the pre-ADC RF chain. The noise figure is a measure of the amount of additional noise the amplifier introduces to the input signal as referenced to matched load at the reference temperature. In an amplifier with  $NF = 0$  dB, the input signal would be amplified by  $G$  dB and the noise power at the output is completely defined by the noise power at the input and the gain. Of course, this ideal situation does not exist and all amplifiers at temperatures above absolute zero add some

amount of additional noise to the input signal.

$$\text{Noise Factor} = \frac{\text{actual output noise power}}{\text{ideal output noise power}} = \frac{\text{actual output noise power}}{kBT_o \times G} \quad (3.6)$$

Using the input noise power and total noise figure of the RF chain, the noise power in a 1 [Hz] band into the ADC is calculated as  $N_{o3}$ .

$$\begin{aligned} G_T &= G_{c1} + G_{c2} + G_{c3} & (3.7) \\ N_{o3} &= N_{i1} + G_T + NF_T \quad \left[ \frac{\text{dBm}}{\text{Hz}} \right] \\ \text{where } G_{c2} &= \frac{1}{L_{c2}} \end{aligned}$$

We are now in a position to define the noise power at  $N_{ADC}$  in Figure 3.13. The ADC measures an input voltage in discrete steps at specified times defined by the quantization level  $Q$  defined in Equation 3.8 where  $V_{pp}$  is the maximum peak-peak voltage level of the ADC and  $b$  is the number of bits used to represent the ADC's analog input.

$$Q = \frac{V_{pp}}{2^b} \quad [V] \quad (3.8)$$

An arbitrary analog input signal may fall anywhere within a quantization level at the time of voltage measurement causing errors in the digital representation of the analog signal. When the input signal is large compared to  $Q$  and is uncorrelated to the sampling frequency  $f_s$ , this error in the ADC's measurement of the input voltage is represented by an additive noise power defined by Equation 3.9 [10]. The quantization noise power is only valid for signals that are uncorrelated to the sampling frequency. In a configuration where the

carrier may be correlated with the sampling frequency, dither may be added to decorrelate the input signal [81].  $P_s$  is the RMS power delivered to the ADC at the maximum peak-to-peak voltage level  $V_{pp}$  assuming a zero-biased sinusoidal input. The ADC has an input impedance of  $R_{in}$ . Unlike the environment noise  $N_{env}$  which was defined as the noise power in a 1 Hz band, quantization noise power as defined by Equation 3.9 is the total noise power in the sampling bandwidth  $f_s/2$ .

$$N_b = P_s - 6b - 1.76 \quad [\text{dBm}] \quad (3.9)$$

$$P_s = \frac{V_{pp}^2}{8R_{in}} \quad [\text{W}] \quad (3.10)$$

The total noise power out of the ADC is the sum of the RF chain output noise power from Equation 3.7 and quantization noise power  $N_b$ . Recall that the output noise power from the RF chain given by Equation 3.7 is defined in a 1 [Hz] bandwidth while the quantization noise power  $N_b$  is defined over the entire sampling bandwidth. Therefore we must multiply  $N_{o3}$  by the filter bandwidth  $B_f$  to calculate the total noise power at the output of the ADC.  $B_f$  is the bandwidth of the RF filter measured in [Hz]. A number of different definitions may be used to calculate  $B_f$ . Often, the 6 [dB] power bandwidth is used as an approximation to the true filter bandwidth. In other applications, one may require a more accurate measure of bandwidth and various correction factors and strategies exist for the calculation of accurate values of  $B_f$ .

$$N_{ADC} = 10\log_{10}(N_b + N_{o3}B_f) + 30 \quad [\text{dBm}] \quad (3.11)$$

where  $N_b$ ,  $B_f$  and  $N_{o3}$  are in linear units

The value of  $N_{ADC}$  is the noise power one would expect to calculate using a sequence of samples acquired from the ADC. At first glance, we may be tempted to conclude that because  $N_b$  is constant, the ADC will have an output even in the absence of amplifier noise power ( $N_{o3} = 0$ ). In this case, a sequence

of samples will indeed indicate zero-valued ADC voltage input, but this simply represents an analog input noise power of  $N_{o3} \leq N_b$ . The ADC will produce a zero-valued voltage measurement until  $N_{o3} \geq N_b$ . In other words, an ADC output indicating no voltage fluctuations higher than the lowest quantization level  $Q$  does not imply zero system noise power.

With the total noise power at the output of the ADC of Equation 3.11 we may calculate the noise figure  $NF_s$  at the ADC output and the ratio of input noise to quantization noise  $N_r$

$$NF_s = N_{ADC} - N_{i1} - G_T - B_f \quad [\text{dB}] \quad (3.12)$$

$$N_r = N_{o3} + B_f - N_b \quad (3.13)$$

Equations 3.11 and 3.12 provide a description of the direct-sampling receiver in terms of gain and noise power. The task now becomes selecting appropriate values for the system gains  $G_{cn}$  based on the receiver parameters and characteristics of the expected input signals. Accomplishing this task requires the definition of two additional quantities, receiver sensitivity  $S_e$  and dynamic range  $DR$ . Various definitions of sensitivity exist in the technical literature, but the most straightforward and insightful definition of Equation 3.14 provides the minimum input signal  $S_e$  power necessary at the receiver input to produce an FFT output at a specified  $SNR$  assuming a rectangular FFT window.

$$S_e = N_{i1} + NF_s + B_f + SNR - 10\log_{10}\left(\frac{N}{2}\right) \quad [\text{dBm}] \quad (3.14)$$

Given a desired  $SNR$  at the FFT output, the dynamic range of the signal power at the receiver input is defined by Equation 3.16. Together, the dynamic range  $DR$  and sensitivity  $S_e$  describe the minimum signal power and the maximum variations of the signal power that the receiver can process at a minimum

specified  $SNR$  using a rectangular windowed FFT length of  $N$ .  $S_{iMax}$  is the necessary signal power at the input to  $G_{c1}$  to drive the ADC to its full-scale voltage level  $V_{pp}$  given the RF chain, and represents the maximum input power of the receiver. This formulation assumes perfect amplifier linearity (i.e. the amplifier produces an output  $S_o = S_i G$  with no spectral contamination under all circumstances). This assumption will be discussed in a later section.

When calculating the dynamic range, it is convenient to define the noise floor at the output of the FFT operation as  $P3$ . Conceptually, the dynamic range is the difference between the receivers maximum input power as seen on the FFT and the FFT noise floor. The factor of ‘3’ in Eq 3.16 results from using a single-sided FFT.

$$P3 = N_{i1} + G_T + NF_s + B_f - 10\log_{10}(N) \quad [\text{dBm}] \quad (3.15)$$

$$DR = S_{iMax} + G_T + P3 - SNR - 3 \quad [\text{dB}] \quad (3.16)$$

$$S_{iMax} = P_s - G_T \quad [\text{dBm}] \quad (3.17)$$

In a conventional analog receiver, the gain is usually set so that when the input is connected to an antenna, the external environmental noise dominates the receiver noise. In a digital receiver, the nonlinearities introduced by the sampling processes and radiated noise from the digital lines both cause spurs to appear in the sampling bandwidth. These spurs are independent of the power of the input signal, and as such are easily masked by raising the noise floor. Contrary to analog receiver gain, in a digital receiver the gain should be set as high as possible while not saturating the ADC when a signal of maximum expected power is present at the receiver input. In other words, under ideal situations, the gain of the digital receiver should be tuned to exercise the maximum full-scale ADC voltage ( $V_{pp}$ ) without saturation. The challenge with the specular meteor radar receiver is maximizing the number of observed echoes. As most echoes occur at a lower SNR, the gain may be tuned such that the small population of high-SNR echoes (above 25 [dB])

will cause receiver saturation.

### 3.4.2 Third Order Intercept

### 3.4.3 Second order products

When driven with a single tone, non-linearities present in all amplifiers will cause harmonics of the fundamental to appear at the output. Assuming the radar's carrier frequency is related to the sampling frequency by  $f_o = f_s/4$  (see Figure 3.3) then the second-order harmonics produced by the single tone will appear at 0 and  $f_s$  [Hz].  $f_s$  is aliased into 0 [Hz] so with a single tone at located at  $f_s/4$  the harmonics will appear at DC. Using two tones ( $f_1$  and  $f_2$ ), the second order intermodulation products will appear at  $f_2 + f_1$  and  $f_2 - f_1$ . Again, assuming  $f_1$  and  $f_2$  are close to the carrier frequency  $f_o = f_s/4$  then the second order intermodulation products will appear near DC at  $f_s$ . The second-order intercept products appear at places in the receiver bandwidth which are far from the carrier  $f_o$  and are easily removed by appropriate filtering. In general, second order products of carriers near  $f_s/4$  will appear near DC and  $f_s$  at the output of the ADC.

### 3.4.4 Third order products

The Third Order Intercept (TOI) point of an amplifier is a measure of device linearity and therefore of interest. The TOI point can be defined in terms of the input power (IP3) or output power (OP3). Two different definitions exist for the IP3 based on driving an amplifier with a single tone, or two closely spaced tones. Third order products generated with a single tone input into the amplifier appear at integer multiples of the input tone which when sampled will alias to the same frequency as the carrier. For this reason, it may be advantageous to insert a filter at the output of the LNA depending on the strength of the IP3. If the amplifiers are chosen such that their aggregate IP3 at the maximum expected signal input level  $S_{iMax}$

is below the FFT noise floor given by Equation 3.15, then an RF filter is not needed.

The more conventional definition for the third order intercept involves inputting two tones close in frequency, and measuring the output of the third order intermodulation products with respect to the power of one of the input tones. The input power level which produces third order intermodulation products equal to the output power of the fundamental is called the third order intercept (TOI). This specification is the output power at which the third order intermodulation products will be equal to the amplitude of the fundamental. This is a purely theoretical specification and has no physical manifestation, as the TOI power level is most likely beyond the maximum power output of the device in question. The primary point of concern is to choose a set of amplifiers whose combined second and third order products are below that of the FFT noise floor  $P_3$  given by Equation 3.15.

### 3.4.5 Simulation of CoSRad RF Characteristics

Using the theory formulated in Section 3.4.1, the minimum detectible signal and dynamic range were calculated over a range of gain values for  $G_{c1}$  and  $G_{c3}$  with the simulation parameters given in Table 3.6. Contours of constant quantization noise ratio and noise figure are indicated. To ensure that the system is dominated by external noise, gain values should be chosen so that  $N_r$  is large and  $NF_s$  is small. The plots also indicate one of the primary tradeoffs with receiver design, that between gain and sensitivity. Introducing additional gain to a system will increase its sensitivity, but decrease the dynamic range of the input. Another consequence is that the sensitivity will reach an asymptote as additional gain is added to the system, indicating that the output of the receiver is dominated by external noise. When this limit is reached, additional gain will not improve sensitivity, but will continue to deteriorate the dynamic range, therefore we must design the RF front end to have sufficient gain necessary to meet a MDS specification without unnecessarily degrading the dynamic range. Various investigators have suggested adding amplifiers at the output of the antennas (before the feed cables) to boost the system SNR. A simulation of the total SNR

degradation caused by the feed cables based on the concepts outlined in this section was performed and the results are presented in Figure 3.16. Figure 3.16 clearly shows that under typical low-VHF environmental noise conditions ( $T_e \approx 100,000[K]$ ), adding LNAs at the antenna terminals will produce a nearly negligible improvement in system SNR.

Table 3.6: Parameters used to generate Figures 3.14 and 3.15 using the theory described in Section 3.4.1

Symbol	Parameter Description	Value
$NF_1$	Noise Figure of $G_{c1}$	1.3 [dB]
$NF_2$	Noise Figure of $G_{c2}$ ( $= L_{c2}$ )	3.35 [dB]
$NF_3$	Noise Figure of $G_{c3}$	5 [dB]
$f_s$	Sampling Frequency	9.34e6 [Hz]
$B_f$	RF Filter Bandwidth	2.6e6 [Hz]
$b$	Number of ADC bits	14
$V_{pp}$	Max peak-peak ADC voltage	2 [V]
$R_{in}$	ADC input impedance	50 [ohms]
$N$	FFT length	256
$SNR$	Desired SNR at FFT output	13 [dB]
$L_c$	Cable loss	0 [dB]
$T_o$	Thermal noise reference temp	290 [K]
$T_{env}$	Environmental noise	100e3 [K]

Throughout the following discussions, we will assume that the instantaneous noise amplitude at any antenna of the array  $w(t)$  is a realization of a zero-mean Gaussian white noise signal  $W(\sigma^2, 0)$  with variance  $\sigma^2$ .  $\sigma^2$  is related to the antenna noise temperature  $\sigma^2 = k_b B_a (T_e + T_a) \simeq k_b B_a T_e$  where  $k_b$  is the Boltzmann constant,  $B_a$  is the antenna bandwidth and  $T_e$  is the external noise temperature ( $T_e > 100,000[K] \gg T_a$  [K] for meteor radar applications). This implies that the Fourier transform of the noise is constant across all frequencies. The input noise bandwidth  $B_a$  is shaped by the RF front-end, the FPGA IIR filter (Figure 3.9) and the matched filter (Eq 3.28). The noise bandwidth at each processing stage is less than the system bandwidth, ensuring optimal SNR of the power spectrum. Equation 3.18 gives the 3 [dB] noise bandwidth at each stage in the processing chain. Because the signal detection described in section 3.6.1 is based on the power spectrum, the input noise bandwidth to any section must only be less than the digital bandwidth for optimal detector performance.

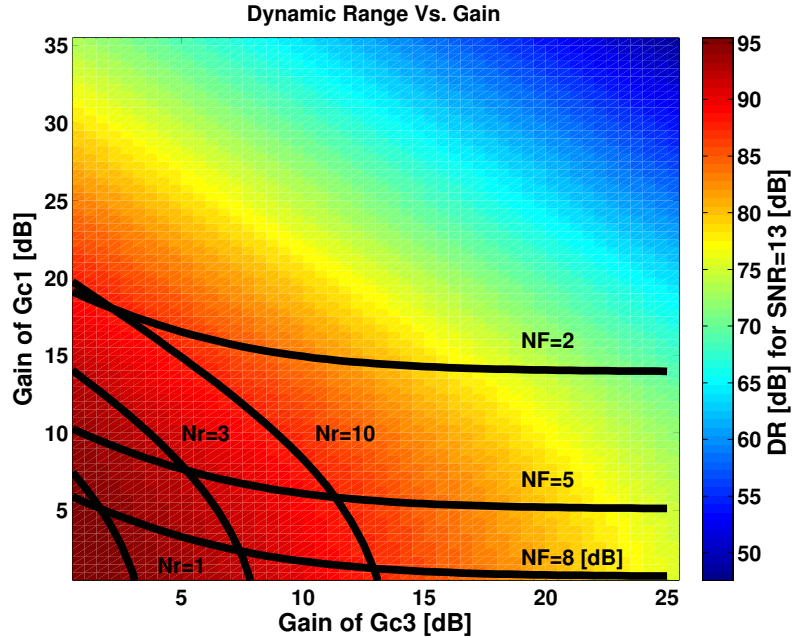


Figure 3.14: Dynamic range Vs. gain for  $G_{c1} = G1$  and  $G_{c3} = G2$  at the receiver input. Higher gain results in higher MDS at the expense of dynamic range. For a digital receiver, the gain should be set as high as possible while staying within the expected dynamic range of the input signal. At higher gain levels, nonlinearities introduced by quantization become less significant

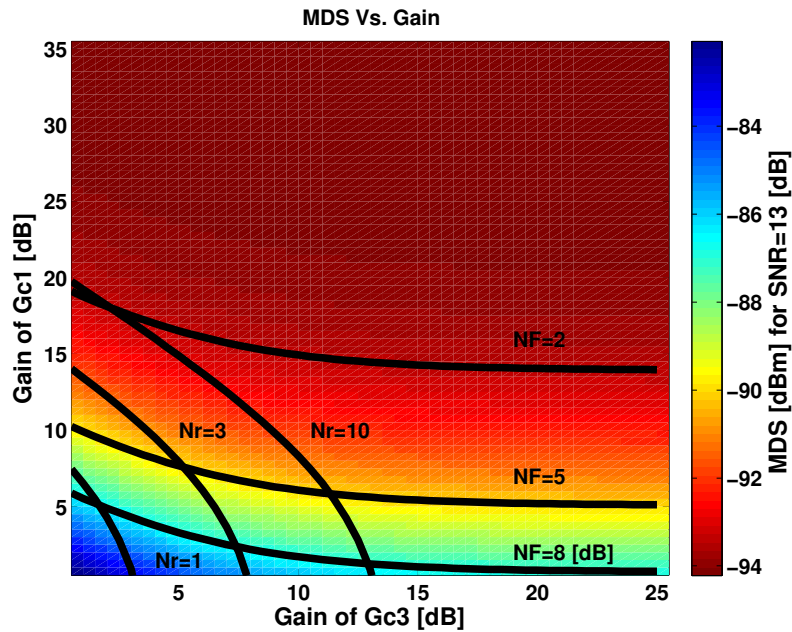


Figure 3.15: Minimum detectable signal (MDS) Vs. gain for  $G_{c1} = G1$  and  $G_{c3} = G2$  at the receiver necessary to produce a  $SNR = 13$  [dB] at the FFT output. Contours of constant noise figure at the ADC  $NF_s$  and quantization noise ratio  $N_r$  are shown. At gain values producing low  $N_r$  or high  $NF_s$ , the noise characteristics become non-linear and signal dependent.

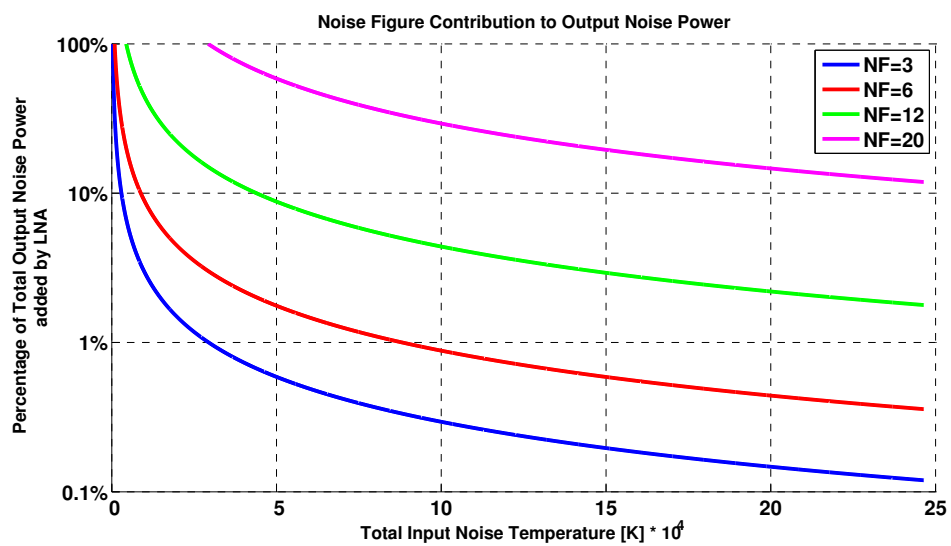


Figure 3.16: Various investigators have suggested the placement of low-noise amplifiers at the antennas of specular meteor radar systems operating in the lower VHF band. Assuming antenna feed cables of rational length (a few  $\lambda$ ), this simulation suggests that such a modification would result in limited system performance improvements. The use of high-performance LNA's at the antennas would only result in an appreciable SNR increase in very low environmental noise conditions or with very long antenna feed cables.

$$\begin{aligned}
B_1 &= H_{RF}(3\text{dB}) < \frac{f_s}{2} \text{ [Hz]} \\
B_2 &= H_{RF}(3\text{dB})H_{IIR}(3\text{dB}) < \frac{f_s}{2d} \text{ [Hz]} \\
B_3 &= H_{RF}(3\text{dB})H_{IIR}(3\text{dB})H_{MF}(3\text{dB}) < \frac{1}{t_{PW}} \text{ [Hz]}
\end{aligned} \tag{3.18}$$

$H_{RF}$ ,  $H_{IIR}$  and  $H_{MF}$  are the frequency responses of the RF front-end, the FPGA IIR bandpass filter and the matched filter (Eq 3.28). The notation ‘3dB’ in eq 3.18 indicates the 3dB bandwidth of the resulting frequency response. The notation  $w_1(t)$ ,  $w_2(t)$  and  $w_3(t)$  refers to the spectrally shaped (real or complex valued) time-domain noise signal at the input to each processing stage with bandwidths defined by  $B_1$ ,  $B_2$  and  $B_3$  and  $t$  defined by Eq 3.22.

### 3.5 Radar Signal Processing

The Doppler shifts imposed on the carrier by the radial velocity of the drifting meteor trail is given by Equation 3.19 where  $f_d$  is the Doppler frequency, or the deviation of the carrier frequency  $f_o$  due to a Doppler shift.  $v_r$  is the radial velocity of the trail,  $f_o$  is the carrier frequency and  $c$  is the speed of light. For an absolute maximum radial wind velocity of 200 [m/s] at VHF, the Doppler frequency imposed on the carrier is  $f_d=40\text{-}400$  [Hz] for  $f_o=30\text{-}300$  [MHz]. CoSRad’s sampling scheme intentionally aliases the radar’s carrier frequency into the ADC’s sampling bandwidth [51]. Figure 3.3 graphically depicts the process of subsampling and decimation. Rather than directly sampling the carrier, bandpass sampling captures the information ( $f_d$ ) bandwidth.

$$v_r = \frac{cf_d}{-2f_o} \tag{3.19}$$

After the amplified, band-limited signal is sampled by an ADC channel and received by the FPGA,

the samples are passed through the **DSP Core** block where integer multiple sample rate conversion further reduces the data rate to a value below that of the USB bandwidth. CoSRad implements sample rate conversion as a two-stage process consisting of bandpass filtering using the second-order-section structure in Figure 3.8 with a frequency response shown in Figure 3.9 followed by a decimation stage. Fundamentally, sample rate conversion reduces the bandwidth of the sampled signal to a value below the USB 2.0 bandwidth of 60 [MB/s] and amounts to a maximum data rate of 7 [MB/channel] when CoSRad is configured for 8 active channels. A wider per-channel bandwidth is possible using fewer channels, but the combined data rate defined by Equation 3.2 over all channels should not exceed the maximum possible USB 2.0 throughput. One straightforward upgrade for future versions of CoSRad is the use of gigabit ethernet, implemented by substituting an **Ethernet Controller** block for the **USB Controller** block in Figure 3.7.

### 3.5.1 I/Q Demodulation

The CoSRad GPC software component formats the stream of real-valued samples received over USB 2.0 in the manner depicted in Figure 3.12 and mathematically described by Equation 3.20 with a bandwidth shown by Figures 3.9 and 3.3. When sampling a Jones array,  $k = 5$ .  $n$  is the number of samples-per-pulse, and  $m$  is the programmable number of pulses to process on each iteration of the pulsed Doppler processor.  $v_{(1,*)}$  is the first sample along each pulse corresponding to zero range, and  $v_{(n,*)}$  is the last sample corresponding to the maximum unambiguous range defined by  $R_{max} = c/2f_p = ndc/2f_s$  [m]. Equation 3.20 represents the most basic data structure generated and formatted by the receiver. Throughout the following discussion, all operations are identical for each active channel, so the subscript  $k$  is not always explicitly listed. The notation  $m_i$ ,  $n_i$ , and  $k_i$  refer to specific rows, columns and channels.

$$\mathbf{V} = \begin{bmatrix} v_{(1,1)} & \cdots & v_{(1,m)} \\ \vdots & \ddots & \vdots \\ v_{(n,1)} & \cdots & v_{(n,m)} \end{bmatrix} \in \mathbb{R}^{n \times m \times k} \quad (3.20)$$

After bandpass sampling by the ADC, sample rate conversion and bandpass filtering in the FPGA, the carrier  $f_o$  is placed at  $f_{a2} = f_s/4d$  with a bandwidth of  $f_s/2d$ . Any meteor trail radar echo present in the real-valued stream of samples represented by Eq 3.20 will be embedded in noise  $w_2(t)$  at the subsampled carrier frequency  $f_{a2}$  with an additive Doppler deviation  $f_d$  as shows in Eq 3.21. Eqs 3.21, 3.25, 3.26 and 3.29 all use  $t$  as it is defined by Eq 3.22. The goal of the CoSRad signal processing chain is detection of time-coherent signals (across the rows of  $\mathbf{V}$ ) occurring at a frequency of  $f_s/4d + f_d$ . A time-domain specular meteor trail radar echo observed by each CoSRad receiver channel is represented by Eq 3.20 where each element of  $\mathbf{V}$  can be calculated using Eq 3.21. A square transmit pulse envelope  $A(n_i)$  with pulsewidth  $t_{PW}$  [s] can be placed at an arbitrary range  $R$  within  $\mathbf{V}$  by defining  $A(n_i)$  using Eq 3.23. A constant phase offset  $\phi(k_i)$  is associated with each channel. Note the dependence of  $t$  on  $m_i$  and  $n_i$  through Eq 3.22. This explicitly notated dependence has been notationally dropped after Eq 3.21 for convenience.

$$v(n_i, m_i, k_i) = A(n_i) \sin \left( \left( \frac{f_s}{4d} + f_d \right) 2\pi t(n_i, m_i) + \phi(k_i) \right) + w_2(t(n_i, m_i)) \quad (3.21)$$

In the data block format of Figure 3.12,  $t$  is a function of  $n_i$  and  $m_i$  identically over each channel  $k$  as shown in Eq 3.22.

$$t(n_i, m_i) = (m_i n - n + n_i) \frac{d}{f_s} \quad (3.22)$$

$$A(n_i) = \begin{cases} 1 & \text{if } \left( \frac{2R}{c} + \frac{t_{PW}}{2} \right) \frac{f_s}{d} > n_i > \left( \frac{2R}{c} - \frac{t_{PW}}{2} \right) \frac{f_s}{d} \\ 0 & \text{otherwise} \end{cases} \quad (3.23)$$

Both signals represented by Eqs 3.21 and 3.23 are embedded in a sampled bandwidth defined by  $B_2$

which far exceeds that necessary for the observation of the narrow-band meteor trail radar echoes (see section 3.5). The detector of Section 3.6.1 is sensitive to coherent signals at equal ranges across sequential radar pulses, therefore our goal becomes minimizing the noise bandwidth without degrading the amplitude of the narrow-band radar echo approximated by Eq 3.21. A number of methods exist for this purpose, but we will focus on the traditional technique of I/Q demodulation and matched filtering.

Placing the subsampled carrier  $f_{a2} = f_s/4d$  at  $f_b$  in addition to moving Eq 3.20 into the complex domain for determination of the Doppler sign (negative or positive frequencies) is accomplished by performing the element-wise matrix multiplication (Hadamard product) of Eq 3.24.

$$\tilde{\mathbf{V}} = \mathbf{Y} \circ \mathbf{V} = \mathbf{Y} \circ \begin{bmatrix} v_{(1,1)} & \cdots & v_{(1,m)} \\ \vdots & \ddots & \vdots \\ v_{(n,1)} & \cdots & v_{(n,m)} \end{bmatrix} \in \mathbb{C}^{n \times m \times k} \quad (3.24)$$

The elements of  $\mathbf{Y}$  are calculated using Eq 3.25 where  $t$  is defined by Eq 3.22 and  $f_b$  is a tuning frequency offset discussed in section 3.6.1.  $\mathbf{Y}$  can be conceptualized as a synthesized local oscillator generated by the GPC, typically having zero phase.

$$y(n_i, m_i, k_i) = \exp\left[j\left(\frac{f_s}{4d} + f_b\right)2\pi t\right] \in \mathbb{C}^{n \times m \times k} \quad (3.25)$$

Each element  $y(n_i, m_i, *)$  is equal across all channels  $k$ . After performing the element-wise matrix multiplication in Eq 3.24, each element  $\tilde{v}_{(n_i, m_i, k_i)}$  of the complex-valued time-domain signal  $\tilde{\mathbf{V}}$  is now represented by Eq 3.26.

$$\begin{aligned}
\tilde{v}(n_i, m_i, k_i) &= A(n_i) \exp^{j[(\frac{f_s}{4d} + f_d)2\pi t + \phi(k_i)]} \exp^{j[(\frac{f_s}{4d} + f_b)2\pi t]} + w_2(t) \\
&= A(n_i) \exp^{j[(\frac{f_s}{2d} + f_d + f_b)2\pi t + \phi(k_i)]} + w_2(t) \in \mathbb{C}^{n \times m \times k} \quad (3.26)
\end{aligned}$$

The real and imaginary parts of  $\tilde{\mathbf{V}}$  represent the  $I$  and  $Q$  components of  $\mathbf{V}$ .

### 3.5.2 Matched Filtering

The frequency of interest in Eq 3.26 is the Doppler shift  $f_d$ . By low-pass filtering the columns of Eq 3.26, the higher-frequency carrier  $f_s/2d$  is removed resulting in a time-domain signal with frequency  $f_d + f_b$  at the maximum possible SNR. This is accomplished using a filter with a frequency response matched to that of the transmit pulse along each column of  $\tilde{\mathbf{V}}$  to form  $\tilde{\mathbf{V}}_q$ . In the case of a square-envelope transmit pulse  $A(n_i)$ , the matched filter bandwidth is defined by  $B_{PW} = t_{PW}^{-1}$  and implemented using the moving average of Eq 3.28. A trapezoidal transmit pulse where the rise and fall times of the pulse are small compared to the pulsewidth can be approximated by a square pulse. The number of samples  $s$  to include in the moving average ‘boxcar’ filter for a square transmit pulse is given by Eq 3.27.

$$s = \left\lceil \frac{t_{PW} f_s}{d} \right\rceil \quad (3.27)$$

The matched filter is applied to the columns of  $\tilde{\mathbf{V}}$  by Eq 3.28.

$$\tilde{v}_{q(n_i, m_i)} = \sum_{p=l}^{l+s} \tilde{v}_{(p, m_i)} \text{ where } l : [1 \dots (n_i - s)] \quad (3.28)$$

$\tilde{\mathbf{V}}_q$  has the functional form given by Eq 3.29.

$$\tilde{v}_{q(n_i, m_i, k_i)} = A(n_i) \exp^{j[(f_d + f_b)2\pi t + \phi_\delta(k_i)]} + w_3(t) \quad (3.29)$$

Where  $\phi_\delta(k_i)$  is the phase offset of each channel after matched filtering. The phase delay introduced by the matched filter is constant across all channels and therefore will not affect the interferometry results.  $\tilde{\mathbf{V}}_q$  represents the final output of CoSRad's signal processing chain and is used in section 3.6.1 to extract meteor trail echoes from the data stream. Any correlation across the rows of  $\tilde{\mathbf{V}}_q$  within the Doppler bandwidth indicate a radar return at a range given by Eq 3.31.

### 3.5.3 Synchronization

The multistatic meteor wind radar architecture relies on phase synchronization of all the remote stations. This is accomplished using a GPS locked oscillator with a frequency stability of  $S = 10^{-10}$  [Hz] over 1 [sec] to drive the DDSs on each receiver. This implies a maximum error in the radial velocity determination of  $V_{err} = f_o S \lambda / 2$ . At  $f_o = 35.24$  [MHz],  $V_{err} = 15$  [cm/s]. Range synchronization is accomplished by starting each receiver on a specific GPS-PPS determined by reading the GPS week number and time of week from the GPS oscillator's serial port. GPS specifies that the PPS will be synchronized to  $\sigma = \pm 15$  [ns] across the entire network, which drives the absolute range error of 2.25 [m]. Rubidium-based GPS oscillators are also available which could improve the frequency stability to  $S = 10^{-11}$  [Hz] over 1 [sec], however, the forward-scatter Doppler error introduced using the GPS disciplined oscillator listed in Table 3.2 is acceptable for multistatic meteor wind radar applications. By sampling the transmit pulse at both the Delamere and Adelaide stations, the oscillator stability can be quantified. The DFT of the transmit pulse is taken over both one second and 200 [ms] data segments for two hours and zero-padded to produce a sufficiently interpolated spectrum. The Doppler frequency at the maximum of the interpolated spectra are counted and shown in Figure 3.17 at both receiver locations. As expected, the observed forward-scatter signal is less stable in Doppler at the receive-only Adelaide station, but still consistent with the specified oscillator stability.

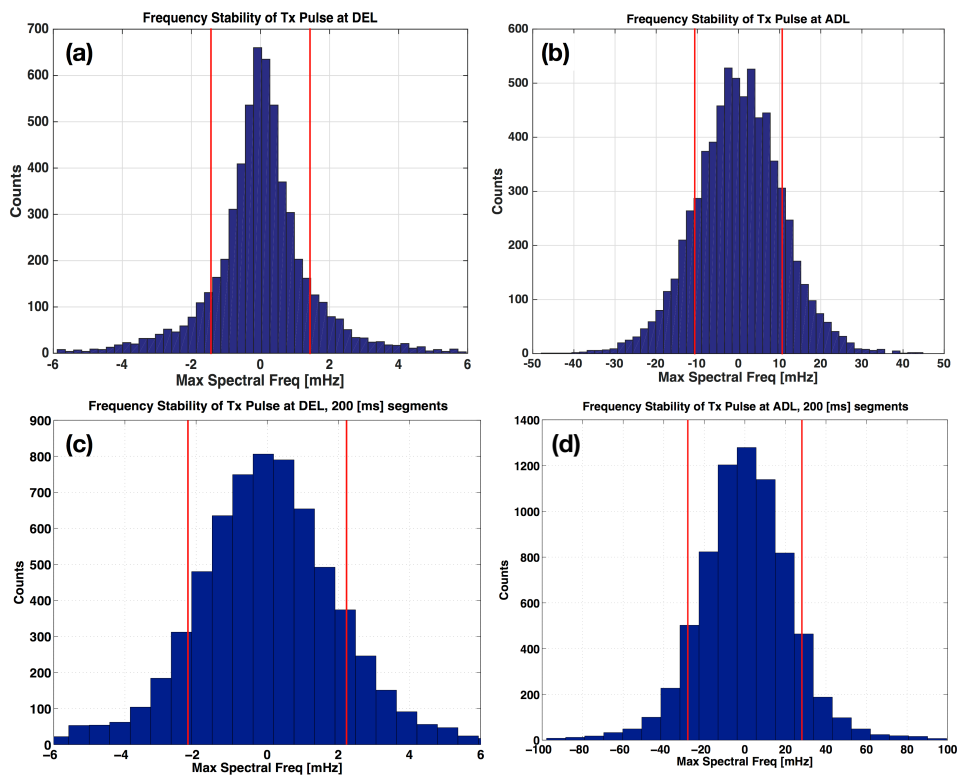


Figure 3.17: Maximum of interpolated Doppler spectrum over 1 [sec] and 200 [ms] data segments during pulse transmission for two hours at both the Delamere backscatter (**a** & **c**) and Adelaide forward-scatter (**b** & **d**) sites. The transmit pulse was sampled at zero range at DEL and at 86 [km] in propagation path length at ADL (see Figures 3.26 and 3.27). Both signals are at  $\sim 10$  [dB SNR]. Using Eq 3.19 applied to the identified standard deviations in frequency, these figures suggest the bounds in radial wind velocity error due to oscillator synchronization mismatches as  $\sigma_{DEL} = \pm 0.6 - 1.1$  [cm/s] and  $\sigma_{ADL} = \pm 4.5 - 16.2$  [cm/s] associated with the typical duration of meteor trail echoes. This technique for experimentally measuring the Doppler error due to oscillator phase mismatches can be continuously applied throughout an observation campaign by configuring CoSRad to persistently record the transmit pulse at all stations.

### 3.6 Specular Meteor Trail Scatter Examples and Observational Results

Figure 3.2 depicts an example meteor trail echo as observed by CoSRad at the Delamere interferometer under the experimental setup shown in Figure 3.18. The 80 [us] transmit square pulse is sampled at  $f_s = 1.2$  [MHz] leading to a range resolution of 12 [km] which can be seen by inspecting the SNR RTI plots on Figures 3.2 and 3.19.

Figure 3.19 shows a strong specular echo observed at the Adelaide forward-scatter site. The detection rates at the Adelaide site are rather low due to its location in an urban noise environment ( $T_e = 450$  [K] noise power) and the use of a low-efficacy single-dipole receive antenna. Observation of specular meteor trail scatter at a long-baseline phase synchronous multistatic station strongly supports the fundamental viability of future large-scale MMWR installations. Both Figures 3.20 and 3.21 show the height distribution of one week of high-SNR echoes at the Delamere monostatic station and the expected increase in ambipolar diffusion as a function of echo height. Figures 3.22 and 3.23 present echoes observed by CoSRad at the Jicamarca All-sky Specular Meteor Radar [48] and at the Platteville COBRA meteor radar (similar to [23] but with  $f_o = 30.355$  [MHz]). Both campaigns were conducted for system development purposes and serve as important examples of CoSRad's potential for extensive reconfigurability. Both sites require separate configurations for  $f_o$ ,  $f_s$ , and FPGA filters (Figure 3.9). Each site also requires a different  $f_p$  ensuring an integer number of samples-per-pulse and distinct timing signal configurations are necessary to drive external hardware (see Figure 3.10). Figures 3.26 and 3.27 show SNR-RTI plots observed during the Geminids meteor shower at both the Delamere and Adelaide sites with interesting features identified.

While the approach taken with CoSRad of varying the sampling frequency dependent on the carrier frequency is simple and effective, it does have some drawbacks. Primarily, the FPGA must be re-compiled for every new deployment. Fixing the sampling rate at the maximum specified by the ADC would require more complex FPGA-based polyphase filtering without the need for re-compiling the FPGA.

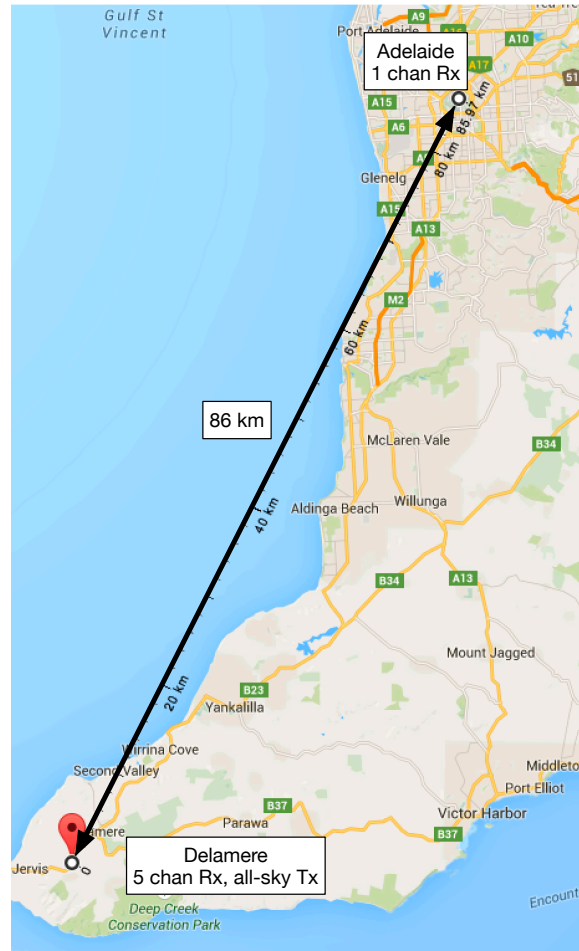


Figure 3.18: Experimental setup for the multistatic observation campaign of the Geminids meteor shower in December, 2014. A 5-channel Jones receive interferometer (see Figure 4.1) and 7.5 [kW] all-sky transmitter are located at the Delamere site (DEL). A single channel receive antenna is located at the multistatic remote site in central Adelaide (ADL). The two stations are separated by a distance of 86 [km]. Note that in Figures 3.26 and 3.27, the transmit pulse is observed at ADL at the expected one-way ground propagation path length of 86 [km].

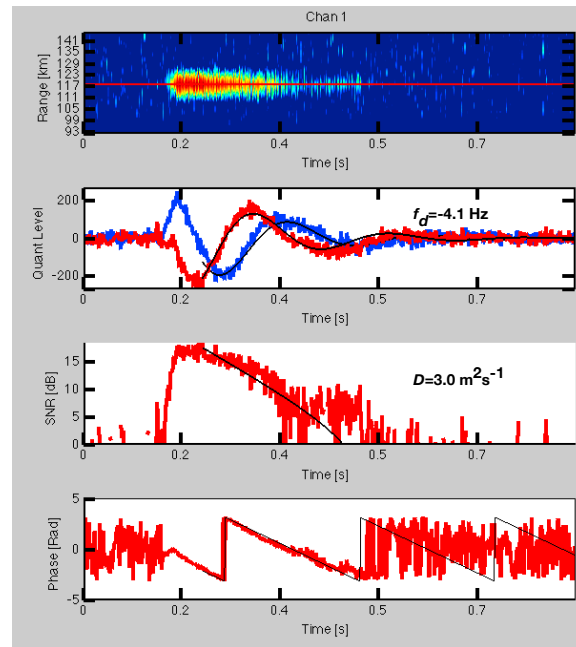


Figure 3.19: Specular meteor trail scatter observed at the Adelaide single channel forward-scatter site. In most cases, the Delamere and Adelaide sites will observe specular scatter from different trails. If an interferometer is located at the forward-scatter site (instead of a single dipole as was used in this experiment), both the multistatic and monostatic sites can observe common volumes of atmosphere as depicted in Figure 1.3. Observation and accurate estimation of the Doppler signal at multistatic remote sites is the fundamental mechanism enabling multistatic meteor wind radar.

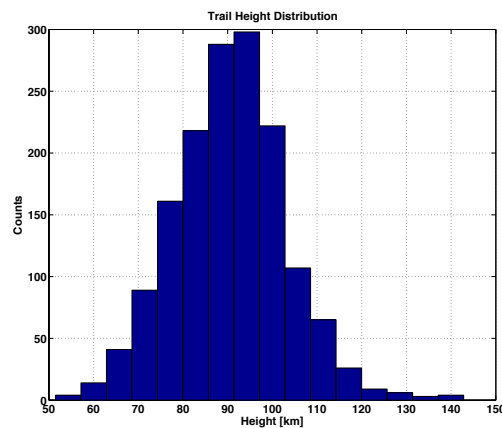


Figure 3.20: Trail height distribution for one week of data starting Dec 13, 2014 observed at the DEL monostatic site. Only echoes above 17 [dB SNR], above 30 [deg] in elevation and between 70-160 [km] in range are counted. The array was calibrated by determining the phase offsets associated with each antenna with the maximization technique of Chapter 4.8, however, only the imprecise  $0.5\lambda$  baseline was used to find the height (See [63] and Chapter 4.3). The structure of the height distribution is generally consistent with that found by other investigators [40], however, the distribution is wider than expected due to use of only the imprecise  $0.5\lambda$  phase offsets. Efforts to calibrate the Jones array without using the traditional real-valued solution methods without discarding ‘outlying observations’ was met with limited success, and served as the catalyst behind the complex plane interferometry and calibration approach presented in Chapter 4.

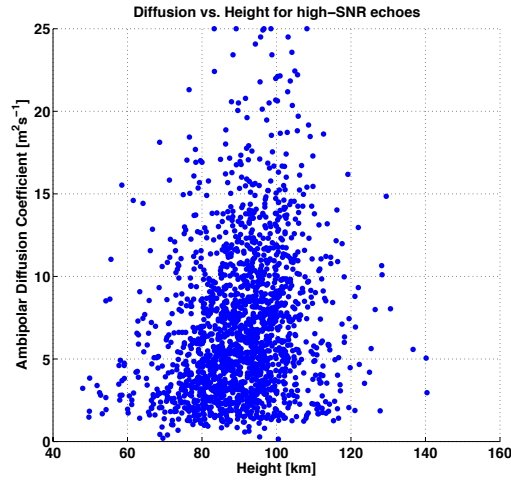


Figure 3.21: Ambipolar diffusion Vs. height for a population of high SNR echoes (>17 [dB SNR]) counted in Figure 3.20. The expected trend towards higher diffusion at higher altitudes is clearly observed.

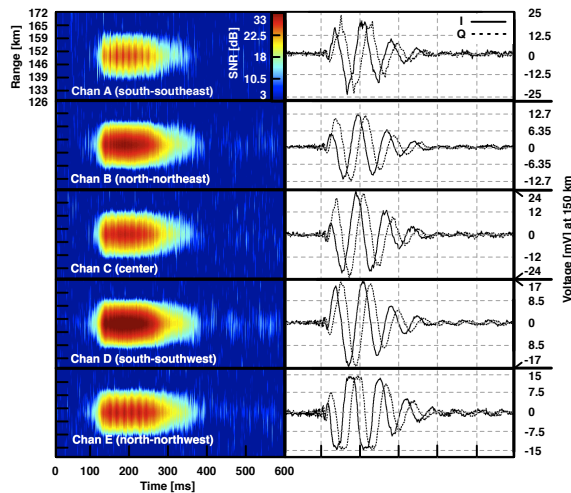


Figure 3.22: Specular meteor trail echo observed by CoSRad configured for 5-channel observations using the Jones antenna array and driving a Tomco transmitter at the Jicamarca Radio Observatory in Sep of 2012. An uncoded square 80 [us] pulse was generated by the receiver with a  $f_p = 499.65$  [Hz],  $f_o = 49.9$  [MHz] and  $f_s = 1.305$  [MHz]. This echo was processed and visualized using an earlier version of the pulsed Doppler processor software. This observation highlights CoSRad’s potential for extensive reconfigurability

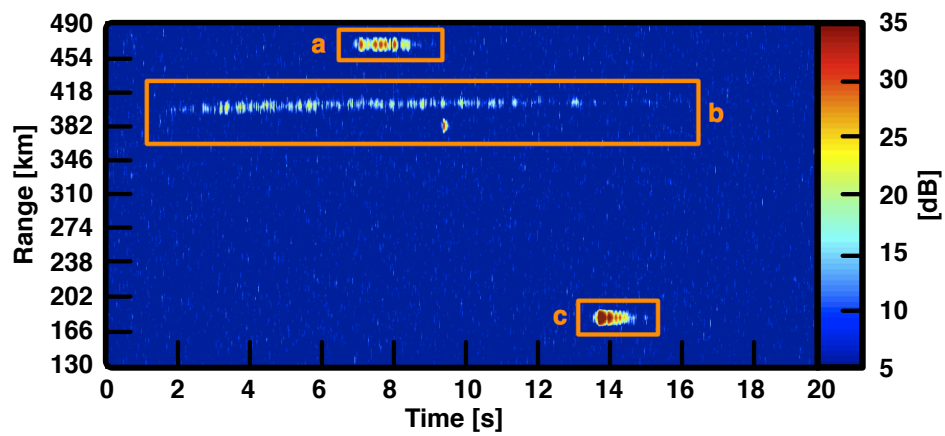


Figure 3.23: Specular meteor trail echoes observed by CoSRad configured for use on a Yagi channel of the Plateville meteor radar and driving the COBRA transmitter in August, 2012. An uncoded square 60 [us] pulse was generated with a  $f_p = 305$  [Hz],  $f_o = 30.355$  [MHz] and  $f_s = 9.34$  [MHz]. This observation shows 4 simultaneous distinct echoes at four different ranges, one of CoSRad's advantages over traditional meteor radar. Echo (c) appears as a possibly underdense echo, whereas the echoes in region (a) and (b) seem to be overdense and range-spread. Note that two distinct echoes appear in region (b)

### 3.6.1 Signal Extraction

Figure 3.26 and 3.27 shows blocks of data acquired under the multistatic configuration depicted in Figure 3.18. The data was acquired during the Geminids meteor stream on 14 Dec, 2014 at 4:53AM and 4:39AM, Adelaide time. The top panels shows data acquired at the Delamere 5-channel interferometer from Figure 4.1 and the bottom panels shows the phase and pulse synchronous forward scatter data acquired at the Adelaide single-channel forward scatter site. Data from all 5 channels of the interferometer is summed to form the top panel. A signal detection algorithm is used to identify both forward and backscatter coherent signals within the RT-SNR data block identified by the white outlines around the visible echoes. The detection algorithm performs a short-time Fourier transform (STFT) over a 128-pulse block with a 32-pulse overlap. Begin the analysis by forming a complex-valued magnitude (voltage) block of radar pulses as depicted in Equation 3.30 and Figure 3.12. Eq 3.30 is the end result of the matched filtering stage of sec 3.5.2.

$$\tilde{\mathbf{V}}_q = \begin{bmatrix} [I + jQ]_{(1 \times 1)} & \cdots & [I + jQ]_{(1 \times m)} \\ \vdots & \ddots & \vdots \\ [I + jQ]_{(n \times 1)} & \cdots & [I + jQ]_{(n \times m)} \end{bmatrix} \in \mathbb{C}^{n \times m \times k} \quad (3.30)$$

Take the single-sided DFT along each row (range) of each channel of  $k$  to form  $\mathbf{X}_{ss}$ . Each row of  $\mathbf{X}_{ss}$  now represents the Doppler amplitude spectrum observed on each antenna at a range  $R$  defined by Eq 3.31 where  $n_i$  is the sample number in the pulse starting from zero range. Because the DFT in Eq 3.32 is real-valued, only the columns  $m_i = [1 : \frac{m}{2}]$  are unique along each row  $n_i$ .

$$R = \frac{n_i dc}{2f_s} \text{ [m]} \quad (3.31)$$

$$\mathbf{X}_{ss} = \left| DFT_{\text{row}} \left( \begin{bmatrix} \tilde{v}_{q(1 \times 1)} & \cdots & \tilde{v}_{q(1 \times m)} \\ \vdots & \ddots & \vdots \\ \tilde{v}_{q(n \times 1)} & \cdots & \tilde{v}_{q(n \times m)} \end{bmatrix} \right) \right| \in \mathbb{R}^{n \times \frac{m}{2} \times k} \quad (3.32)$$

Detection could be performed on each channel  $k_i$  of  $\mathbf{X}_{ss}$ , however we can combine the amplitudes in each DFT bin to improve the overall SNR. Form  $\mathbf{X} \in \mathbb{R}^{n \times \frac{m}{2}}$  by summing  $\mathbf{X}_{ss}$  over each channel  $k_i$  as shown in Eq 3.33.  $\mathbf{X}$  now represents the amplitude spectrum as a function of range as observed by the entire array.

$$\mathbf{X} = \sum_{k_i=1}^k \mathbf{X}_{ss_{(*,*,k_i)}} \quad (3.33)$$

Form the real-valued power spectrum by taking the Hadamard product of  $\mathbf{X}$  (element-wise multiplication) as shown in Eq 3.34. At this point, each column of  $\mathbf{P}$  represents a power spectral bin as a function of range ( $n_i$ ). The frequency axis of the DFT is defined by the Doppler bandwidth ( $f_p/2$ ). The synthesized local oscillator of Eq 3.25 forming the  $I$  and  $Q$  components of Eq 3.30 can be intentionally de-tuned so that echoes with zero Doppler will appear at  $f_b = f_p/4$  in the Doppler spectrum.

$$\mathbf{P} = \mathbf{X} \circ \mathbf{X} \in \mathbb{R}^{n \times \frac{m}{2}} \quad (3.34)$$

$\mathbf{E}$  is the ratio of signal power to noise power (SNR) in each DFT bin. Calculate  $\mathbf{E}$  by first forming the diagonal matrix  $\mathbf{M}$  by squaring the median ( $\mathbb{E}_M$ ) of each column of the amplitude spectrum  $\mathbf{X}$  as shown in Eq 3.35.

$$\mathbf{M} = \begin{bmatrix} \mathbb{E}_{\mathbf{M}} [\mathbf{X}_{(*,1)}]^2 & \dots & 0 \\ \vdots & \ddots & \vdots \\ 0 & \dots & \mathbb{E}_{\mathbf{M}} [\mathbf{X}_{(*,\frac{m}{2})}]^2 \end{bmatrix} \quad (3.35)$$

$\mathbf{M}$  now represents an estimate of the median noise power in each spectral bin along range. We use the median to avoid heavily biasing the noise estimate in the presence of strong signals (meteor trail echoes). Subtract the average noise power from the total power in each DFT Doppler frequency bin as shown in Eq 3.36 to form the total signal power spectrum  $\mathbf{S}$ .  $\mathbf{J}_{(\frac{m}{2} \times n)}$  is a unit matrix of all ones.

$$\mathbf{S} = \mathbf{P} - [\mathbf{M}\mathbf{J}_{(\frac{m}{2} \times n)}]^\top \in \mathbb{R}^{n \times \frac{m}{2}} \quad (3.36)$$

Finally, form  $\mathbf{E}$  in each Doppler frequency bin using Eq 3.37

$$\mathbf{E} = \mathbf{S}(\mathbf{M})^{-1} \quad (3.37)$$

Each row of the  $\mathbf{E}_{(n \times \frac{m}{2})}$  represents a Doppler spectrum at a range given by Eq 3.31 and each column represents a spectral bin in the Doppler bandwidth defined by  $B_d = f_p/2$  with frequency resolution  $\delta f = f_p/m$ . Extract signals of interest by finding elements of  $\mathbf{E}$  within the expected bandwidth of drifting meteor trails which exceed a threshold value. The rows at which  $\mathbf{E}$  exceeds the threshold will correspond to the rows of  $\tilde{\mathbf{V}}_q$  that contain the time-series of the complex-valued voltage signals which are stored to the GPC disk for later analysis such as performing a least squares fit to a decaying sinusoid as shown in Figure 3.2. The threshold SNR is set to 10 [dB], and the rows surrounding those which exceed the detection threshold indicated by the white boxes in Figures 3.26 and 3.27 are also saved to preserve the noise context. At this point, stored echoes could be processed by more computationally intensive and advanced analysis techniques such as the time-frequency discriminator described in [79].

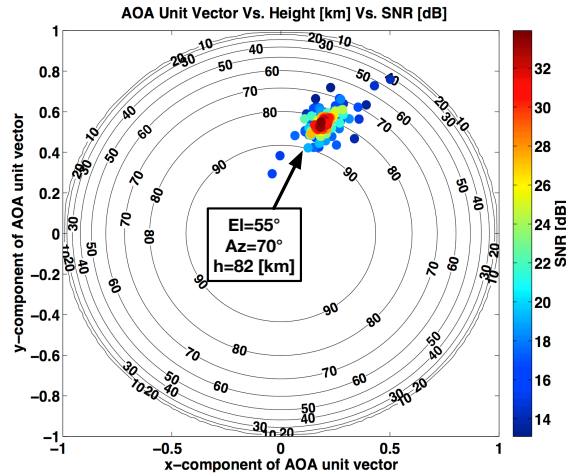


Figure 3.24: Instantaneous AOA solutions are computed from the phase of each pulse of an echo similar the one shown in Figure 3.2 and plotted vs. height. Each solution (pulse) is color-coded to indicate SNR. A clear point cloud is observed near 82 [km]. A weighted least-squares fit to a set decaying sinusoids like those in row 2 of Figure 3.2 will provide the phase offsets used to determine the most likely AOA.

The I/Q demodulation stage is slightly de-tuned to place an echo with zero Doppler at  $f_b = 1/4T_{IPP}$  in the STFT spectrum taken over time (128 pulses) at an identical range gate. Placing zero Doppler at  $f_b = 1/4T_{IPP}$  in the Doppler spectrum prevents DC signal components from influencing the detection. When power within the Doppler spectrum exceeds a threshold, the range-specific time-series is flagged and saved for further analysis. Note that at the Adelaide forward-scatter site, the ground-propagating transmit pulse is clearly observed at the expected inter-station distance of 86 [km]. In the top panel, an attenuated transmit pulse (an RF switch is opened during transmit) is observed at a radar range of 0 [km].

Figures 3.24 and 3.25 show the instantaneous phase observations from two specular meteor echoes. The interferometric solutions were found using the course  $0.5\lambda$  ‘short-baseline’ phase offsets and calibration values. Figure 3.25 is especially interesting as it shows a time-dependent phase drift, behavior not captured in the classical theory of specular meteor trail scatter.

This section has described the system details and development of the CoSRad transceiver. CoSRad is more than a software receiver, rather it comprises a complete phase coherent digital radar system, including a pulse control engine and software defined signal processing chain. CoSRad enables rapidly deployable meteor

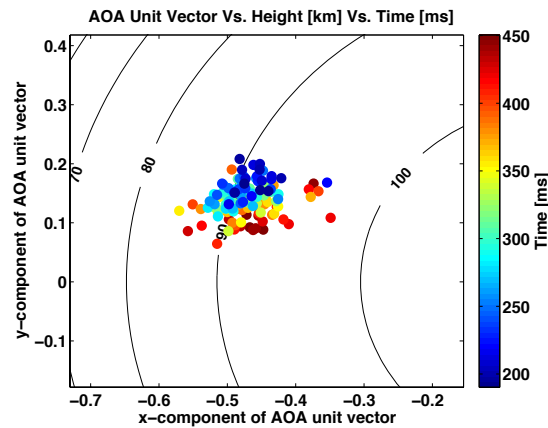


Figure 3.25: Instantaneous AOA solutions of a high-SNR echo color-coded by time. This surprising result shows a change in the location of the trail's scattering center. The traditional analytical model of meteor trail scatter does not capture this behavior which is present in a significant portion ( $> 10\%$ ) of all CoSRad meteor trail observations.

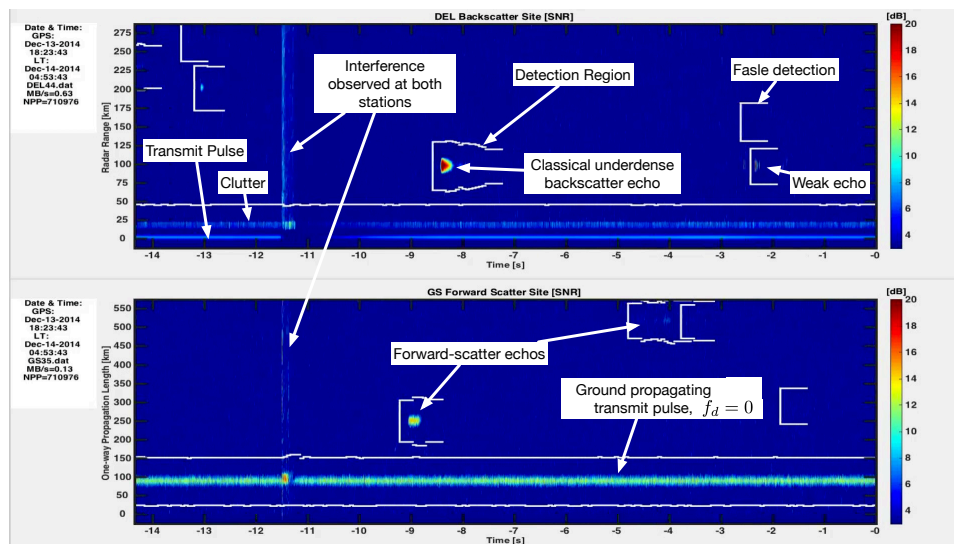


Figure 3.26: Interesting features are identified in a segment of visualized radar data taken during the Geminids meteor shower at 4:53AM on 14 Dec 2014, Adelaide time. The Delamere monostatic site is shown in the top panel and the Adelaide multistatic receiver is on the bottom. At the DEL monostatic site the attenuated transmit pulse is observed at 0 [km] in range followed by clutter probably resulting from the hilly landscape surrounding the DEL transmit site. Bands of interference are observed across all ranges at both sites. The ground-propagating transmit pulse with the expected Doppler frequency of  $f_d = 0$  [Hz] is observed at the expected range of 86 [km] at the ADL forward-scatter site (see Figure 3.18). Observation of the transmit pulse at both the forward and backscatter sites enables the quantification of Doppler error due to oscillator phase mismatches as shown in Figure 3.17.

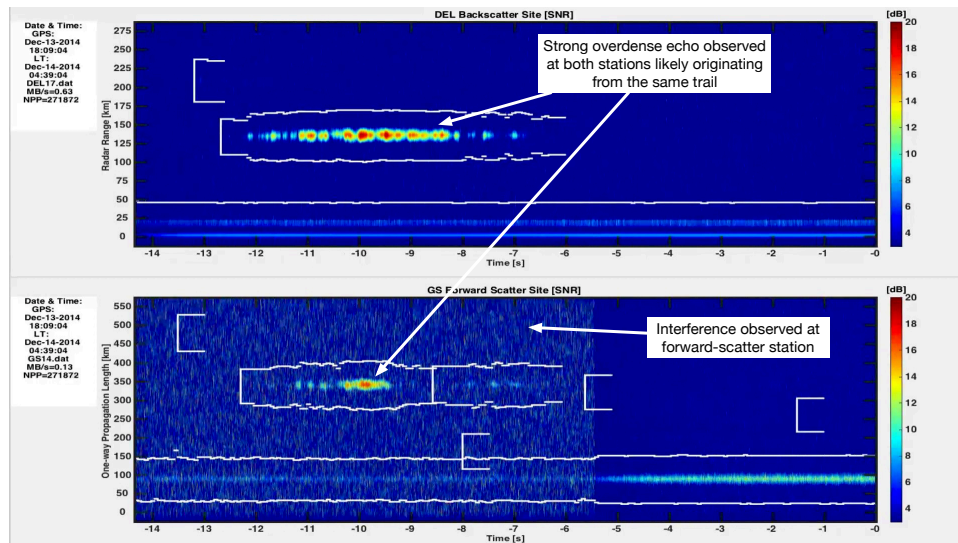


Figure 3.27: A strong echo is observed at both sites at 4:39AM on 14 Dec 2014 Adelaide time, likely originating from the same trail. The echo is embedded in a large band of interference at the forward-scatter site, reducing the SNR. The detector outlined in Section 3.6.1 is sensitive to signals which are coherent across time at the same range, and performs well even with degraded SNR. Most echoes observed under the multistatic wind radar configuration originate from different trails, so this is an unusual observation. Upon termination of the interfering signal at  $\sim -5.5$  [s], a period of SNR recovery is observed on the transmit ground pulse as the estimate of the environmental noise level on each channel ( $\sigma_k$ ) is determined using a running average.

wind radar in both the traditional monostatic and new multistatic architectures. After the application of anti-alias filtering and gain, CoSRad directly samples the antenna feeds of a interferometric array and observes Doppler-shifted specular RF scatter from meteor trails. CoSRad's phase-coherent architecture enables the measurement of the forward-scatter Doppler signal, a key technical requirement enabling the multistatic meteor wind radar. The full system description presented in this paper should help the radar remote sensing community understand how CoSRad could be integrated into existing systems, and also showcase the benefits of software defined, geographically distributed radar systems. Our first results show the success of our prototype MMWR deployment, and lay the groundwork for more substantial MMWR installations. We encourage future remote sensing radar engineers and scientist to draw from work done with CoSRad and implement large-scale multistatic deployments.

## Chapter 4

### Meteor Radar Interferometry And Measurement Precision

“You cannot teach a man anything; you can only help him find it within himself.” – Galileo Galilei

#### 4.1 Introduction

Meteor radar interferometry concerns the problem of spatially locating a specular radar echo from a meteor trail in 3-dimensional space. This problem has almost exclusively been approached using Jones technique where the real-valued phases of a radar echo are measured between the elements of an antenna array like that shown in Figure 4.1 [74]. The phase measurements are then additively combined and used to solve for the direction cosines of the range vector  $\mathbf{R}$  (see Eq 4.1). This approach suffers from a number of drawbacks. The Jones-style solutions are based on an imprecise  $d = 0.5\lambda$  initial estimate of the direction cosines  $(\theta_x, \theta_y)$  [63] which significantly degrades the local solution quality for lower SNR echoes as can be seen in Figure 4.6. Furthermore, the direction cosines have historically been cast as a function of real-valued phase measurements, greatly complicating the mathematics in finding an optimal solution. Finally, almost no attention has been given to determining the precision of the fundamental specular meteor radar measurements of  $(\theta_x, \theta_y, D, f_d$  and  $R)$ . Without knowledge of the fundamental instrument precision, variations in the derived geophysical wind parameters cannot be confidently attributed to actual physical

variability. This chapter presents an elegant complex-plane solution to the meteor wind radar interferometry problem, and formulates the statistical measurement precision based on the fundamental voltage-level CoSRad measurements.

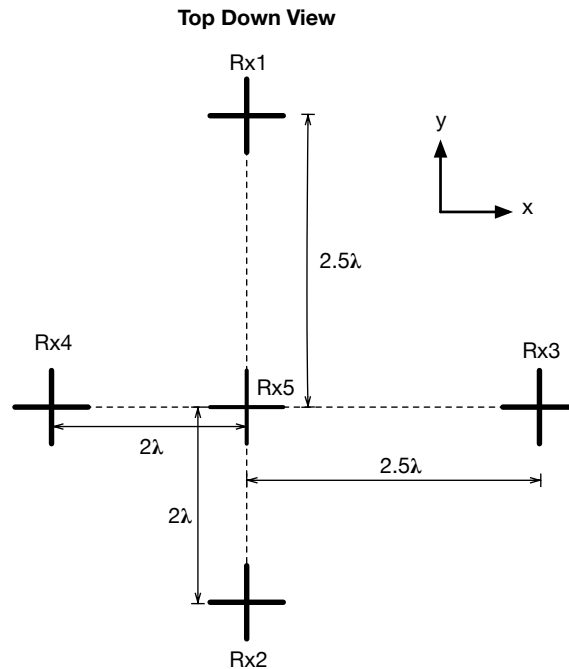


Figure 4.1: Layout of the classical Jones interferometer. Phase differences of a received echo between the antennas along the two baselines (Rx1-Rx2 and Rx3-Rx4) are used to determine of the angle-of-arrival of a specular meteor radar echo.

We can define the angle-of-arrival coordinates of a specular meteor radar echo impinging on a Jones array in terms of the cosine angles of the unit vector pointing in the direction of the trail as shown in Eq 4.1.  $\mathbf{R} = [r_x, r_y, r_z]$  are the cartesian coordinates describing the location of the trail with respect to the array,  $e_x$  and  $e_y$  are the cartesian basis unit vectors aligned with the axis of the array and  $[\theta_x, \theta_y, \theta_z]$  are the direction cosines [124] describing the projection of  $\mathbf{R}$  onto the plane of the array.  $R = |\mathbf{R}|$  is the scalar range measured by the receiver with variance  $\sigma_R^2$ .

$$\begin{aligned}
\theta_x &= \frac{\mathbf{R} \cdot \mathbf{e}_x}{|\mathbf{R}|} \\
\theta_y &= \frac{\mathbf{R} \cdot \mathbf{e}_y}{|\mathbf{R}|} \\
\theta_z &= \sqrt{1 - \theta_x^2 - \theta_y^2} \\
R &= |\mathbf{R}|
\end{aligned} \tag{4.1}$$

The solution to the problem of meteor radar interferometry and the associated measurement uncertainty are closely linked, and the mathematics used for their description are related such that the two topics should be discussed simultaneously. Scientific formulations often present ‘top-down’ **deductive** analysis, where a theory describing a generalized set of observations is presented and the reader is left to apply the theory to a specifically encountered problem. This Chapter takes the somewhat opposite approach of **inductive** analysis which examines the specific details of a single instance of a problem which is assumed to fall under a larger generalized theory. Details of the Jones array meteor radar interferometry problem are presented, and the reader is invited to explore the chapter references for a generalization of the concepts.

A qualitative familiarization with the more intuitive problem of beamforming is helpful when considering the interferometry problem as the two are closely related via antenna reciprocity. Pointing the main lobe of a phased transmit array consisting of a set of spatially distributed antennas in some desired direction involves changing the phase delays associated with each channel of the transmitting array. If the transmitting array were configured according to Figure 4.1, we could simply plug  $\theta_x$  and  $\theta_y$  describing the desired beam direction into Eq 4.9 and apply the resulting phase offsets to each antenna of the array. Note that the phase wrapping terms  $p_k$  are included when  $\mathbf{A}\mathbf{x}$  is evaluated.

The problem of interferometry is the opposite of the beamforming problem. An EM wave impinging on a spatially distributed set of antennas produces a set of measured phase offsets  $\phi_k$ . Now, we must invert (i.e. solve) Eq 4.9 to estimate the direction cosines  $\hat{\theta}_x$  and  $\hat{\theta}_y$  describing the wave’s angle-of-arrival (AOA). Note that when  $d_k > 0.5\lambda$ , the number of phase wraps  $p_k$  cannot be directly determined. Therefore, Eq 4.9

has a set of possible solutions corresponding to the integer-valued set of  $p_k$  which is defined by the array geometry  $\mathbf{d}$  and  $\gamma$ . If we assume  $p_k$  is unknown, as is the case when considering a spatially sparse ( $d_k > 0.5\lambda$ ) Jones array configuration, then Eq 4.9 is no longer elegantly solved using linear techniques.

A primary assumption of statistical uncertainty estimation is that the noise observed on each antenna is a realization of an independent Gaussian random variable, each with a probability density function described by  $\mathcal{N}(0, \sigma_k^2)$ . The question has been posed: If all the antennas are spatially located in the same general region (as is the case with the array in Figure 4.1), do they observe a correlated noise environment and therefore violate the primary assumption? The key lies in developing an appreciation between the temporal and spatial coherence of a signal. Consider a wave having some small bandwidth originating from a single source in space, such as from a single antenna. The generated wavefield is then observed in time at some other point in space, such as by an antenna connected to a sampling receiver. The wavefield generated by the source is coherent in time because the value of future samples can be deterministically predicted based on the past samples. The wavefield is also coherent in space because its value is deterministically calculated at any spatial point around the source. Imagine 2 or 3 sources generating a deterministic wavefield which is sampled in time and space, where the net wavefield is the superposition of the wavefield generated at each individual source. Now imagine that each source is slowly changing location with a random velocity such that the Doppler effect is small. The temporal determinism is maintained because the superposition of the wavefield at any point in space will oscillate at the wavefield frequency, but our ability to predict the spatial structure of the wavefield now requires knowledge of the source locations, which we do not have. In the limit, imagine an infinite collection of sources each having a small random velocity relative to the observer. Environmental noise is generated by such a model. A wavefield generated by an infinite number of moving sources will have temporal coherence at each unique point in space, but our ability to predict the structure of the wavefield between any two spatial locations larger than the antenna dimensions becomes impossible. The spatial superposition of the wavefield only has temporal determinism over spatial dimensions on the order of the wavelength under consideration (the Fourier transform of an infinite spatial dimension is a single point). Any observations of this wavefield over the spatial dimensions larger than the observing antenna are

independent and uncorrelated. For this reason, the noise observed at each spatially distributed antenna in the spatially sparse Jones array is accurately modeled as an independent random variable.

## 4.2 Specular Meteor Trail Signal Model

The classical specular meteor trail signal model comprises two parts. An exponential rise in power during the trail formation, and an exponential decay as the assumed underdense trail diffuses into the neutral atmosphere. This process is described by the classical specular meteor radar Equation 2.1 in Chapter 2. The interferometry problem as it is posed here fits the received radar echo to the classical underdense meteor trail signal in a least-squares sense. The output of the CoSRad signal processing chain described in Chapter 3.5 by Eq 3.30 is represented by  $\tilde{\mathbf{V}}_{\mathbf{q}}$ . A specular meteor radar echo may be present along the  $m$ -dimension rows (along time) of  $\tilde{\mathbf{V}}_{\mathbf{q}}$  (see Figure 3.12). Assuming an underdense meteor trail, the decaying portion of the radar return at a range  $R$  related to sample number  $n$  (see Eq 3.31) is observed at the output of the CoSRad signal processing chain as Eq 4.14. The echo is assumed to be observed on all channels (antennas)  $k$  in Figure 4.1. Here, the amplitude of a radar echo on a specific channel  $k$  is represented as  $A_k$  as opposed to the signifying the envelope the radar transmit pulse as was done in Chapter 3.

$$\tilde{\mathbf{V}}_{\mathbf{q}}(n, m, k) = A_k e^{j(2\pi f_a t[m] + \phi_k)} e^{-D_a t[m]} + w_k(t[m]) \quad (4.2)$$

$$\text{where } t[m] = \frac{m}{f_p} \text{ and } m = 0, 1, \dots, M - 1 \quad (4.3)$$

$$\text{and } k = 1 \dots 5 \quad (4.4)$$

The sample number  $n$  can be obtained from the range  $R$  using Eq 3.31 from Chapter 3. The noise term  $w_k(t[m])$  is described by the Gaussian probability distribution  $w_k(t[m]) \in \mathcal{N}(0, \sigma_k^2)$ . The exponential decay coefficient  $D_a$  in Eq 4.2 is related to the physical diffusion  $D$  coefficient through Eq 4.5.

$$D = \frac{D_a \lambda^2}{16\pi^2} [m^2 s^{-1}] \quad (4.5)$$

Throughout this chapter, the following definitions are used. Quantities with a ‘hat’ signify estimates of true parameters, whereas ‘primed’ quantities signify candidate parameters.

- $k$  : Refers to a channel or antenna in Figure 4.1
- $m$  : Refers to a radar pulse number (see Figure 3.12)
- $A_k$  : Amplitude of the specular meteor radar echo on a channel  $k$  where  $k = [1..5]$ . See row 2 of Figure 3.2 or 4.5
- $f_d$  : Doppler frequency of the specular meteor radar echo
- $D_a$  : Exponential decay coefficient. The decay coefficient is related to the physical diffusion coefficient through Eq 4.5 assuming a monostatic observation.
- $D$  : Physical diffusion coefficient of Eq 2.1b [ $m^2 s^{-1}$ ]
- $\phi_k$  : Phase of the specular echo radar return on each channel  $k$
- $\theta_x$  : Direction cosine of  $\mathbf{R}$  in the  $e_x$  direction.
- $\theta_y$  : Direction cosine of  $\mathbf{R}$  in the  $e_y$  direction.
- $\boldsymbol{\beta}$  : Vector containing the true parameters of the observed signal in Eq 4.14
- $\boldsymbol{\beta}'$  : Vector containing a set of candidate signal model parameters in Eq 4.17
- $\hat{\boldsymbol{\beta}}$  : Vector containing the least squares estimates of the signal model parameters
- $\hat{A}_k$  : Estimate of the amplitude of the observed specular meteor radar echo on a channel  $k$  where  $k = [1..5]$

- $\hat{f}_d$ : Estimate of the observed doppler frequency in Eq 4.14.
- $\hat{D}_a$ : Estimate of the observed decay coefficient in Eq 4.14.
- $\hat{D}$ : Estimate of the observed physical diffusion coefficient
- $\hat{\phi}_k$  : Estimate of the observed phase of the specular echo radar return on each channel  $k$
- $\hat{\theta}_x$  : Estimate of  $\theta_x$
- $\hat{\theta}_y$  : Estimate of  $\theta_y$
- $f_p$  : pulse repetition frequency of the radar pulses
- $t$  : The independent exogenous variable time
- $t_o$  : Beginning of the meteor trail echo in time
- $M$ : Total duration of the meteor trail echo in number of radar pulses
- $t_M$  : Total duration of the meteor trail echo in time
- $\Phi$  : Matrix containing the time-series voltage data observed by CoSRad according to Eq. 4.14
- $\Omega$  : Matrix containing the time-series voltage signal model described by Eq. 4.18.
- $\mathbf{d}$  : Vector containing the distances between each antenna with respect to antenna 5
- $\gamma$  : Vector containing angular position between each antenna with respect to antenna 5
- $\kappa$  : Angular wavenumber.  $\kappa = 2\pi/\lambda$
- $\lambda$  : Radar carrier frequency wavelength.  $\lambda = c/f_o$
- $\mathbf{J}$  : Jacobin of the specular meteor echo signal model  $\Omega$
- $\mathbf{J}_s$  : Jacobin of the spherical coordinate transformation of Eq 4.27.
- $\Sigma$  : Covariance matrix of  $\hat{\beta}$

- $\Sigma_d$  : Submatrix of  $\Sigma$  containing the covariances of the direction cosines and range
- $\Sigma_s$  : Covariance of the echo's spatial location in spherical coordinates
- $\alpha_k$  : Phase biases on each receiver channel  $k$
- $w(t)$  : Additive Gaussian noise term of Eq 4.16 described by the probability distribution  $\mathcal{N}(0, \sigma_k^2)$
- $\sigma_k^2$  : Variance of the observed real-valued noise on each channel  $k$
- $\Psi_x$  : Angle-of-arrival of a wave along the  $e_x$  direction
- $\Psi_y$  : Angle-of-arrival of a wave along the  $e_y$  direction
- $\eta_x$  : Phase relationship between  $\alpha_3$  and  $\alpha_4$
- $\eta_y$  : Phase relationship between  $\alpha_1$  and  $\alpha_2$

Equation 4.14 is known as the observable, and it represents a specular meteor trail echo embedded in the complex-valued voltages produced at the output of the CoSRad signal processing chain of Eq 3.30 and is denoted  $\Phi$ . The columns of  $\Phi$  are populated by the explicit real and imaginary parts of the voltage observations with a functional form given by Eq 4.14 as shown in Eq 4.6.

$$\Phi = \tilde{\mathbf{V}}_{\mathbf{q}}(n, [0 : M-1], k) = [\mathbb{R}(\Phi_k) \mathbb{I}(\Phi_k)] = \begin{bmatrix} \mathbb{R}(\Phi_1(t_o, \boldsymbol{\beta})) & \mathbb{I}(\Phi_1(t_o, \boldsymbol{\beta})) & \dots & \mathbb{R}(\Phi_5(t_o, \boldsymbol{\beta})) & \mathbb{I}(\Phi_5(t_o, \boldsymbol{\beta})) \\ \vdots & \vdots & & \vdots & \vdots \\ \mathbb{R}(\Phi_1(t_m, \boldsymbol{\beta})) & \mathbb{I}(\Phi_1(t_m, \boldsymbol{\beta})) & \dots & \mathbb{R}(\Phi_5(t_m, \boldsymbol{\beta})) & \mathbb{I}(\Phi_5(t_m, \boldsymbol{\beta})) \end{bmatrix} \quad (4.6)$$

The complete 10 element parameter vector is given by Eq 4.7.

$$\boldsymbol{\beta} = [A_1 \ A_2 \ A_3 \ A_4 \ A_5 \ f_d \ D \ \phi_5 \ \theta_x \ \theta_y] \quad (4.7)$$

The goal of the interferometry and uncertainty estimation problem is determining a set of parameters  $\hat{\beta}$  which best describe the voltage observations  $\Phi(\beta, t)$  under the known antenna geometry of Figure 4.1 in addition to assessing the quality of the estimated parameters. A number of techniques exist for finding reasonable values of  $\hat{\beta}$  which describe the observations, however, we will focus on the technique of nonlinear least squares because it provides a direct estimate of the measurement uncertainty, interpreted as a statistical probability. Think of this problem as finding a set of parameters  $\hat{\beta}$  which will reproduce the observations  $\Phi(\beta, t)$  in addition to providing a measure of the precision of the estimated parameters. The observations  $\Phi$  are assumed to have been produced under the physical process governing radar scatter from classical underdense specular meteor trails [95] described in Chapter 2. The first goal of this chapter is finding parameter estimates  $\hat{\beta}$  which represent the ‘true’ physical parameters  $\beta$  in some optimal way. This will require the formulation of a model representing the observed signal  $\Phi(\beta, t)$  as a function of all the parameters in Eq 4.7, including the direction cosines  $\theta_x$  and  $\theta_y$ .

### 4.3 Classical Meteor Radar Interferometry

The fundamental equation used to determine the angle of  $\mathbf{R}$  with respect to to the axis connecting two antennas spaced at a distance  $d$  in one dimension is given by Eq 4.8 where  $\phi$  is the phase measured between the two antennas. Therefore, the direction cosine representing the projection of  $\mathbf{R}$  onto the antenna baseline is given by  $\theta_x = \frac{\phi\lambda}{2\pi d}$ . The direction cosine in the  $e_z$  direction is given by Eq 4.1.

$$\Psi = \cos^{-1} \left( \frac{\phi\lambda}{2\pi d} \right) \quad (4.8)$$

Eq 4.8 can be extended into two dimensions using an arbitrary set of antennas set on a common plane under the antenna geometry described by  $\mathbf{d}$  and  $\gamma$  using Eq 4.9 [131]. This system of equations describes the direction cosines in  $(\theta_x, \theta_y)$  as a function of the phase offsets between each set of antennas in Figure 4.1.

$$\begin{bmatrix} \Delta\phi_{15} + 2\pi p_1 \\ \Delta\phi_{25} + 2\pi p_2 \\ \Delta\phi_{35} + 2\pi p_3 \\ \Delta\phi_{45} + 2\pi p_4 \end{bmatrix} = \begin{bmatrix} -\kappa d_1 \cos(\gamma_1) & -\kappa d_1 \sin(\gamma_1) \\ -\kappa d_2 \cos(\gamma_2) & -\kappa d_2 \sin(\gamma_2) \\ -\kappa d_3 \cos(\gamma_3) & -\kappa d_3 \sin(\gamma_3) \\ -\kappa d_4 \cos(\gamma_4) & -\kappa d_4 \sin(\gamma_4) \end{bmatrix} \begin{bmatrix} \theta_x \\ \theta_y \end{bmatrix} = \mathbf{A}\mathbf{x} \text{ where } p_k \in \mathbb{Z} \quad (4.9)$$

Eq 4.9 is compactly written in matrix form as Eq 4.10. Eq 4.10 is the classical interferometry equation as applied to the Jones style array. Eq 4.10 can be solved in a linear least squares sense for various integer values of  $p_k$  because an ensemble of solutions exist (as implied by Eq 4.8) depending on the antenna geometry encoded in the coefficient matrix  $\mathbf{A}$ . If the phase wrapping constants  $p_k$  are known, the solution to Eq 4.9 becomes either a simple matrix inversion in the case of one set of phase offsets, or a linear least squares optimization problem  $(\mathbf{A}^\top \mathbf{A}) \hat{\boldsymbol{\beta}} = \mathbf{A}^\top \boldsymbol{\Phi}$  when multiple phase measurements are observed over the course of a single echo as is the case with echoes observed by CoSRad.

$$\Delta\phi_{k5} + 2\pi p_k = \mathbf{A}\mathbf{x} \quad (4.10)$$

Where the phase differences are determined by Eq 4.11.

$$\begin{bmatrix} \Delta\phi_{15} \\ \Delta\phi_{25} \\ \Delta\phi_{35} \\ \Delta\phi_{45} \end{bmatrix} = \begin{bmatrix} \phi_1 - \phi_5 \\ \phi_2 - \phi_5 \\ \phi_3 - \phi_5 \\ \phi_4 - \phi_5 \end{bmatrix} \quad (4.11)$$

Eq 4.10 will have multiple solutions at various multiples of  $2\pi$  assuming the antenna spacing depicted in Figure 4.1. This is the real-valued form of the interferometry problem still widely in use today for determining directional cosine solutions [63]. One modern paper describing a rudimentary multistatic system makes us

of the classical interferometry technique [90]. The classical interferometry solution approach has apparently formed the basis for the modern body of literature exploring gravity wave observations with meteor radar [56], and suffers from a number of somber drawbacks. As is outlined in [63, 138, 131] Equation 4.9 requires solving for values of  $p_k$  by summing the phase offsets between the sets of antennas along each baseline, thereby synthesizing the unambiguous phase as would be observed by an antenna placed at  $0.5\lambda$  (assuming a single plane wave is impinging upon the array). The phase delays between the outer sets of antennas form a precise, but ambiguous direction cosine solution corresponding to  $4.5\lambda$ . Values of  $p_k$  are chosen that minimize the difference between the unambiguous ‘short-baseline’  $0.5\lambda$  solution and the ensemble of  $4.5\lambda$  ‘long-baseline’ ambiguous solutions. This inelegant approach requires a convoluted scheme of back-substitution based on the imprecise  $0.5\lambda$  estimate. A questionable assumption is made that the  $4.5\lambda$  ambiguous solution which most closely matches the  $0.5\lambda$  unambiguous solution is the ‘true’ solution. In fact, the simulation of Figure 4.6 shows that even for relatively high SNR echoes ( $>13$  dB), the  $0.5\lambda$  solution for the direction cosines may significantly deviate from the true value, even with no system phase biases ( $\alpha_k = 0$ ). See chapter 5.3 in Kang’s doctoral dissertation [78] for additional details on AOA estimation accuracy using the traditional techniques.

#### 4.4 Complex Plane Meteor Radar Interferometry

Here I will present the complex-plane formulation of the classical meteor radar interferometry problem. Recast Eq. 4.9 on the complex plane by taking the complex exponential of the terms. Working in the complex plane has two primary and related advantages. First, it enables the straightforward mathematical determination of the best-fit parameters. When put in terms of complex exponentials, the parameter space of  $\beta'$  described by Eq 4.18 becomes a smooth, differentiable continuous function (see Figure 4.4) which permits the use of gradient-following numerical solution methods such as the trust-region algorithm [103]. Secondly, because the first derivatives of the residual matrix with respect to the model parameters continuously exist over the parameter space, the Jacobian matrix is numerically calculated which enables determination of the

best-fit model parameter uncertainties (variances). Begin the complex-plane meteor radar interferometry problem by taking the complex exponential of Eq 4.9 as shown in Eq 4.12.

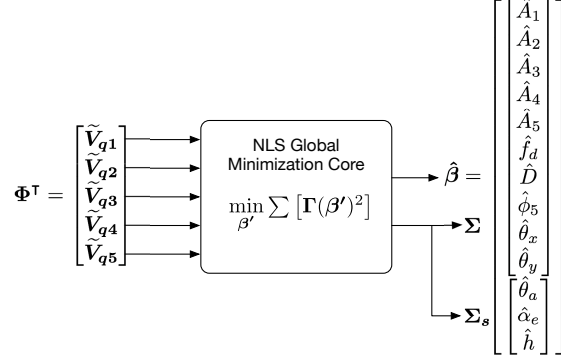


Figure 4.2: Schematic depiction of the nonlinear least squares (NLS) minimization core described in this Chapter. The minimization core accepts a time-series of voltage-level CoSRad observations  $\Phi$  (row 2 of Figure 3.2 or 4.5) and outputs parameter estimates  $\hat{\beta}$  of the specular meteor trail signal model  $\Omega$  along with their associated covariances  $\Sigma$  by globally minimizing the objective function of Eq 4.19 by evaluating Eq 4.21 using iterative gradient methods.

$$e^{j(\phi_k - \phi_5 + 2\pi p_k)} = e^{j\phi_k} e^{-j\phi_5} e^{j2\pi p_k} = e^{j(-\kappa d_k \theta_x \cos \gamma_k - \kappa d_k \theta_y \sin \gamma_k)} \quad (4.12)$$

Solve for the complex phase  $e^{j\phi_k}$  and realize that  $e^{j2\pi p_k} = 1 + 0j$ . This gives an expression for the phase at each channel with respect to channel 5 as a function of the direction cosines  $\theta_x$  and  $\theta_y$  given by Eq 4.13.

$$e^{j\phi_k} = e^{j(-\kappa d_k \theta_x \cos \gamma_k - \kappa d_k \theta_y \sin \gamma_k)} e^{j\phi_5} = e^{j\phi_a(\theta_x, \theta_y)} e^{j\phi_5} \quad (4.13)$$

The first term in Eq 4.13 is a function of  $\theta_x$  and  $\theta_y$  and a set of constant geometric terms, therefore  $e^{j\phi_a(\theta_x, \theta_y)} = e^{j(-\kappa d_k \theta_x \cos \gamma_k - \kappa d_k \theta_y \sin \gamma_k)}$ . Equation 4.13 is the complex form of the real-valued interferometry equation 4.9. Given a set of measured phase differences  $\phi_k$ , Eq 4.13 is solved on the complex plane to find the direction cosine terms describing the AOA of the specular meteor echo. The full equation describing the

complex-valued output of the CoSRad pulsed Doppler signal processing chain including the phase differences at each antenna as a function of the direction cosines is written as Eq 4.14.

$$\tilde{\mathbf{V}}_{\mathbf{q}}(n, m, k) = A_k e^{j2\pi f_a t[m]} e^{-D_a t[m]} e^{j\phi_{ak}(\theta_x, \theta_y)} e^{j\phi_5} + w_k(t[m]) \quad (4.14)$$

$$(4.15)$$

Where the observed phase  $\phi_k$  in Eq 4.6 has been equated with the phase as a function of directional cosines with respect to the phase on channel 5:  $\phi_k = \phi_{ak}(\theta_x, \theta_y) + \phi_5$ . The full set of equations and unknowns representing the observed signal as a function of the true (not estimated) signal parameters  $\boldsymbol{\beta}$  is given by Eq 4.16. The notation indicating the explicit dependence of  $t$  on  $m$  has been dropped for convenience.

$$\boldsymbol{\Phi}(\boldsymbol{\beta}, t) = \tilde{\mathbf{V}}_{\mathbf{q}} = \begin{bmatrix} A_1 e^{-D_a t} e^{j2\pi f_a t} e^{j\phi_{a1}(\theta_x, \theta_y)} e^{j\phi_5} \\ A_2 e^{-D_a t} e^{j2\pi f_a t} e^{j\phi_{a2}(\theta_x, \theta_y)} e^{j\phi_5} \\ A_3 e^{-D_a t} e^{j2\pi f_a t} e^{j\phi_{a3}(\theta_x, \theta_y)} e^{j\phi_5} \\ A_4 e^{-D_a t} e^{j2\pi f_a t} e^{j\phi_{a4}(\theta_x, \theta_y)} e^{j\phi_5} \\ A_5 e^{-D_a t} e^{j2\pi f_a t} e^{j\phi_5} \end{bmatrix}^T + \begin{bmatrix} w_1(t) \\ w_2(t) \\ w_3(t) \\ w_4(t) \\ w_5(t) \end{bmatrix}^T \quad (4.16)$$

As stated earlier, the goal of the interferometry problem becomes finding values of  $\boldsymbol{\beta}$  that represent the observed signal  $\boldsymbol{\Phi}$  in some optimal way. To accomplish this, a signal **model** is defined as Eq 4.17 as a function of candidate parameter vectors  $\boldsymbol{\beta}'$ . Values of  $\boldsymbol{\beta}'$  which best reproduce the observations  $\boldsymbol{\Phi}(\boldsymbol{\beta}, t)$  using the signal model  $\boldsymbol{\Omega}(\boldsymbol{\beta}', t)$  is the optimal estimate  $\hat{\boldsymbol{\beta}}$  of  $\boldsymbol{\beta}$ .

$$\mathbf{\Omega}(\boldsymbol{\beta}', t) = \begin{bmatrix} A'_1 e^{-D'_a t} e^{j2\pi f'_d t} e^{j\phi_{a1}(\theta'_x, \theta'_y)} e^{j\phi'_5} \\ A'_2 e^{-D'_a t} e^{j2\pi f'_d t} e^{j\phi_{a2}(\theta'_x, \theta'_y)} e^{j\phi'_5} \\ A'_3 e^{-D'_a t} e^{j2\pi f'_d t} e^{j\phi_{a3}(\theta'_x, \theta'_y)} e^{j\phi'_5} \\ A'_4 e^{-D'_a t} e^{j2\pi f'_d t} e^{j\phi_{a4}(\theta'_x, \theta'_y)} e^{j\phi'_5} \\ A'_5 e^{-D'_a t} e^{j2\pi f'_d t} e^{j\phi'_5} \end{bmatrix}^T \quad (4.17)$$

Eq 4.17 represents a ‘model’ of the observed specular echo from a meteor trail. Note that in the noiseless case,  $w_n(t) = 0$  and  $\mathbf{\Omega}(\hat{\boldsymbol{\beta}}, t) = \mathbf{\Phi}(\boldsymbol{\beta}, t)$ . But of course, electrical noise will always corrupt our desire to find the true parameter values. Now that the signal observations  $\mathbf{\Phi}(\boldsymbol{\beta}, t)$  are represented by an appropriately selected model  $\mathbf{\Omega}(\boldsymbol{\beta}', t)$ , we are in a position to attempt a solution, or to find the values of  $\boldsymbol{\beta}'$  that best represent  $\boldsymbol{\beta}$ .

## 4.5 Finding The Least Squares Estimate of $\boldsymbol{\beta}$

Software packages such as Matlab and IDL offer excellent nonlinear least squares minimization algorithms when the problem is cast in purely real terms. From this point on, the explicit dependence of  $\mathbf{\Omega}$  and  $\mathbf{\Phi}$  on  $\hat{\boldsymbol{\beta}}$ ,  $\boldsymbol{\beta}'$ ,  $\boldsymbol{\beta}$  and  $t$  is occasionally dropped for notational convenience. Rewrite Eq 4.17 as Eq 4.18 so that the  $I$  and  $Q$  (real and imaginary) components of  $\mathbf{\Omega}$  are explicitly expressed along the columns of  $\mathbf{\Omega}$ . Note that the voltage observations  $\tilde{\mathbf{V}}_q(n, [0 : M - 1], k) = \mathbf{\Phi}(\boldsymbol{\beta}, t)$  are already in complex rectangular format at the output of the CoSRad pulsed Doppler signal processor (see Eq 3.29). Eq 4.18 represents a system of  $10M$  equations and 10 candidate parameter values  $\boldsymbol{\beta}'$ . The fact that the number of estimated parameters equals the number of channels is merely a coincidence and a consequence of having five channels (antennas), each observing  $I$  and  $Q$  signal components. We could add additional antennas and still produce valid solutions.

$$\mathbf{\Omega}(\boldsymbol{\beta}', t) = \begin{bmatrix} \mathbb{R} \left( A'_1 e^{-D'_a t} e^{j2\pi f'_d t} e^{j\phi_{a1}(\theta'_x, \theta'_y)} e^{j\phi'_5} \right) \\ \mathbb{I} \left( A'_1 e^{-D'_a t} e^{j2\pi f'_d t} e^{j\phi_{a1}(\theta'_x, \theta'_y)} e^{j\phi'_5} \right) \\ \mathbb{R} \left( A'_2 e^{-D'_a t} e^{j2\pi f'_d t} e^{j\phi_{a2}(\theta'_x, \theta'_y)} e^{j\phi'_5} \right) \\ \mathbb{I} \left( A'_2 e^{-D'_a t} e^{j2\pi f'_d t} e^{j\phi_{a2}(\theta'_x, \theta'_y)} e^{j\phi'_5} \right) \\ \mathbb{R} \left( A'_3 e^{-D'_a t} e^{j2\pi f'_d t} e^{j\phi_{a3}(\theta'_x, \theta'_y)} e^{j\phi'_5} \right) \\ \mathbb{I} \left( A'_3 e^{-D'_a t} e^{j2\pi f'_d t} e^{j\phi_{a3}(\theta'_x, \theta'_y)} e^{j\phi'_5} \right) \\ \mathbb{R} \left( A'_4 e^{-D'_a t} e^{j2\pi f'_d t} e^{j\phi_{a4}(\theta'_x, \theta'_y)} e^{j\phi'_5} \right) \\ \mathbb{I} \left( A'_4 e^{-D'_a t} e^{j2\pi f'_d t} e^{j\phi_{a4}(\theta'_x, \theta'_y)} e^{j\phi'_5} \right) \\ \mathbb{R} \left( A'_5 e^{-D'_a t} e^{j2\pi f'_d t} e^{j\phi'_5} \right) \\ \mathbb{I} \left( A'_5 e^{-D'_a t} e^{j2\pi f'_d t} e^{j\phi'_5} \right) \end{bmatrix}^{\top} \quad (4.18)$$

10 × M

$$\mathbf{\Gamma}(\boldsymbol{\beta}', t) = \begin{bmatrix} f_1(\boldsymbol{\beta}', t) \\ f_2(\boldsymbol{\beta}', t) \\ f_3(\boldsymbol{\beta}', t) \\ f_4(\boldsymbol{\beta}', t) \\ f_5(\boldsymbol{\beta}', t) \\ f_6(\boldsymbol{\beta}', t) \\ f_7(\boldsymbol{\beta}', t) \\ f_8(\boldsymbol{\beta}', t) \\ f_9(\boldsymbol{\beta}', t) \\ f_{10}(\boldsymbol{\beta}', t) \end{bmatrix}^{\top} = \begin{bmatrix} \mathbb{R} [A_1 e^{-D_a t} e^{j2\pi f_d t} e^{j\phi_{a1}(\theta_x, \theta_y)} e^{j\phi_5} + w_1(t)] - \mathbb{R} [A'_1 e^{-D'_a t} e^{j2\pi f'_d t} e^{j\phi_{a1}(\theta'_x, \theta'_y)} e^{j\phi'_5}] \\ \mathbb{I} [A_1 e^{-D_a t} e^{j2\pi f_d t} e^{j\phi_{a1}(\theta_x, \theta_y)} e^{j\phi_5} + w_1(t)] - \mathbb{I} [A'_1 e^{-D'_a t} e^{j2\pi f'_d t} e^{j\phi_{a1}(\theta'_x, \theta'_y)} e^{j\phi'_5}] \\ \mathbb{R} [A_2 e^{-D_a t} e^{j2\pi f_d t} e^{j\phi_{a2}(\theta_x, \theta_y)} e^{j\phi_5} + w_2(t)] - \mathbb{R} [A'_2 e^{-D'_a t} e^{j2\pi f'_d t} e^{j\phi_{a2}(\theta'_x, \theta'_y)} e^{j\phi'_5}] \\ \mathbb{I} [A_2 e^{-D_a t} e^{j2\pi f_d t} e^{j\phi_{a2}(\theta_x, \theta_y)} e^{j\phi_5} + w_2(t)] - \mathbb{I} [A'_2 e^{-D'_a t} e^{j2\pi f'_d t} e^{j\phi_{a2}(\theta'_x, \theta'_y)} e^{j\phi'_5}] \\ \mathbb{R} [A_3 e^{-D_a t} e^{j2\pi f_d t} e^{j\phi_{a3}(\theta_x, \theta_y)} e^{j\phi_5} + w_3(t)] - \mathbb{R} [A'_3 e^{-D'_a t} e^{j2\pi f'_d t} e^{j\phi_{a3}(\theta'_x, \theta'_y)} e^{j\phi'_5}] \\ \mathbb{I} [A_3 e^{-D_a t} e^{j2\pi f_d t} e^{j\phi_{a3}(\theta_x, \theta_y)} e^{j\phi_5} + w_3(t)] - \mathbb{I} [A'_3 e^{-D'_a t} e^{j2\pi f'_d t} e^{j\phi_{a3}(\theta'_x, \theta'_y)} e^{j\phi'_5}] \\ \mathbb{R} [A_4 e^{-D_a t} e^{j2\pi f_d t} e^{j\phi_{a4}(\theta_x, \theta_y)} e^{j\phi_5} + w_4(t)] - \mathbb{R} [A'_4 e^{-D'_a t} e^{j2\pi f'_d t} e^{j\phi_{a4}(\theta'_x, \theta'_y)} e^{j\phi'_5}] \\ \mathbb{I} [A_4 e^{-D_a t} e^{j2\pi f_d t} e^{j\phi_{a4}(\theta_x, \theta_y)} e^{j\phi_5} + w_4(t)] - \mathbb{I} [A'_4 e^{-D'_a t} e^{j2\pi f'_d t} e^{j\phi_{a4}(\theta'_x, \theta'_y)} e^{j\phi'_5}] \\ \mathbb{R} [A_5 e^{-D_a t} e^{j2\pi f_d t} e^{j\phi_5} + w_5(t)] - \mathbb{R} [A'_5 e^{-D'_a t} e^{j2\pi f'_d t} e^{j\phi'_5}] \\ \mathbb{I} [A_5 e^{-D_a t} e^{j2\pi f_d t} e^{j\phi_5} + w_5(t)] - \mathbb{I} [A'_5 e^{-D'_a t} e^{j2\pi f'_d t} e^{j\phi'_5}] \end{bmatrix}^{\top} \quad \sqrt{\mathbf{W}} \quad (4.19)$$

Eqs. 4.16 and 4.18 are vector-valued functions of the explicitly expressed real and imaginary components of the phase differences measured across each antenna of the array. The model  $\mathbf{\Omega}(\boldsymbol{\beta}', t)$  takes candidate parameter vectors of size  $1 \times 10$  and return matrices of size  $M \times 10 \in \mathbb{R}$ . The objective function is now defined

as the difference between the observed signal  $\Phi$  and the model  $\Omega$  evaluated at some candidate parameter vector  $\beta'$  and is explicitly expressed by Eq 4.19.  $\Gamma$  is also known as the residual matrix and is compactly written in Eq 4.20 where the explicit dependence on  $t$  has been dropped from the notation.

$$\Gamma(\beta') = (\Phi - \Omega(\beta'))\sqrt{W} \quad (4.20)$$

The goal of the nonlinear least squares procedure is to minimize the sum of the squares of the objective function  $\Gamma$  over the domain of the candidate input parameters  $\beta'$  as shown in Eq 4.21.  $\hat{\beta}$  is the least squares estimate of the true parameters embedded within  $\Phi$  when Eq 4.21 is minimized over the domain of the candidate model parameters. This is an optimization problem of the nonlinear least squares type.

$$\min_{\beta'} \sum [\Gamma(\beta')^2] \quad (4.21)$$

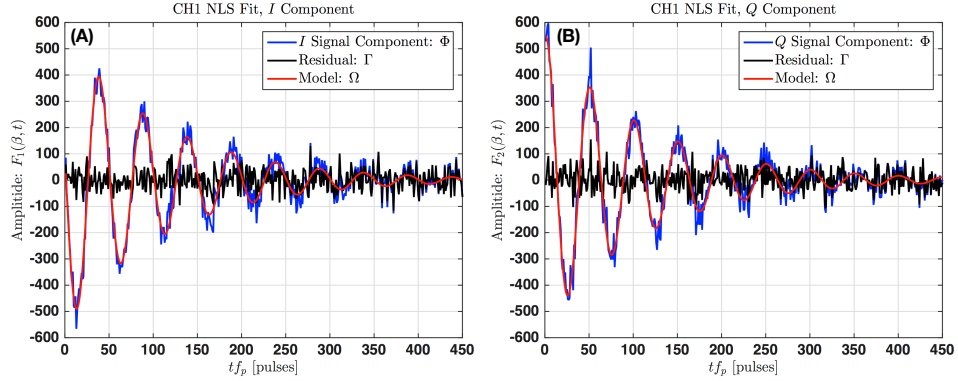


Figure 4.3:  $I$  (A) and  $Q$  (B) components of a simulated meter trail echo.  $D=2 [m^2s^{-1}]$ ,  $f_d=10$  [Hz], SNR=20 [dB]. The best fit parameters  $\hat{\beta}$  for  $\Omega$  were found by evaluating Eq 4.21. The fit is performed on each of the five channels. Only the fit for Channel 1 is shown in this figure.

$W$  is a diagonal matrix of weights representing the inverse variances of the observed noise in each  $I$  and  $Q$  channel as shown in Eq 4.22.  $I$  and  $Q$  are formed digitally with no offsets as discussed in Chapter 3 and shown by Eq 3.26, therefore the variance of each component of the complex-valued signal is half that

of the real-valued signal.  $\mathbf{W}$  gives channels with lower noise variance (and therefore higher SNR) more influence over the estimate of  $\hat{\beta}$ .

$$\mathbf{W} = \begin{bmatrix} \frac{2}{\sigma_1} & & & & & & & & & 0 \\ & \frac{2}{\sigma_1} & & & & & & & & \\ & & \frac{2}{\sigma_2} & & & & & & & \\ & & & \frac{2}{\sigma_2} & & & & & & \\ \vdots & & & & \frac{2}{\sigma_3} & & & & & \vdots \\ & & & & & \frac{2}{\sigma_3} & & & & \\ & & & & & & \frac{2}{\sigma_4} & & & \\ & & & & & & & \frac{2}{\sigma_4} & & \\ & & & & & & & & \frac{2}{\sigma_5} & \\ 0 & & & & & & & & & \frac{2}{\sigma_5} \end{bmatrix}_{10 \times 10} \quad (4.22)$$

Figure 4.4 shows the wrapping structure of the interferometric solutions. Local extrema in the objective function occur at regular intervals along the  $\theta'_x$  and  $\theta'_y$  parameters. This results from the Jones antenna spacing of  $d > 0.5\lambda$ . By inspection of Eq. 4.8, we can see for  $d > 0.5\lambda$ , an ensemble of phase differences  $\Delta\phi$  exist which satisfy any given angle-of-arrival  $\Psi$ . As has been done historically and assuming a monochromatic plane wave impinging on the classical Jones array, the phase differences observed by an antenna spacing of  $d = 0.5\lambda$  in both the  $\mathbf{e}_x$  and  $\mathbf{e}_y$  directions is created by adding the phase differences  $\Delta\phi_{x0.5\lambda} = \Delta\phi_{35} + \Delta\phi_{45}$  and  $\Delta\phi_{y0.5\lambda} = \Delta\phi_{15} + \Delta\phi_{25}$  thereby providing an unambiguous solution to Eq 4.8. Antenna spacing with this additive property was the original motivation behind the Jones-style array because it appears to offer a straightforward unambiguous solution to Eq 4.8.

Philosophically, imagine that all the information needed for an unambiguous determination of the direction cosines is somehow encoded in an antenna geometry which spatially samples the wave at multiples of  $0.5\lambda$ . Indeed, Figure 4.4 demonstrates that a global extrema exists on the surface defined by Eq 4.21 over

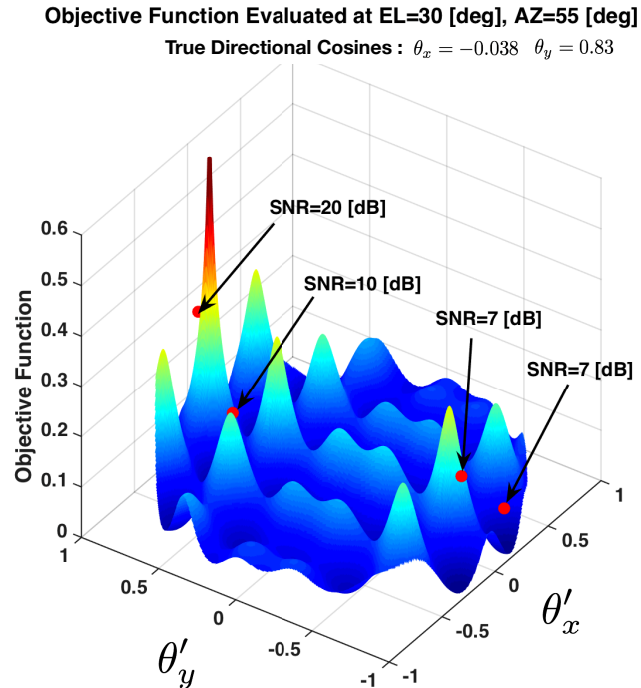


Figure 4.4: Inverse of the objective function (Eq 4.20) evaluated over the domain of  $\theta'_x$  and  $\theta'_y$ . All other parameters in  $\beta'$  are held constant. For this example  $\beta(\theta_x, \theta_y) = (-0.038, 0.83)$ . The inverse of  $\Gamma$  is plotted because the peaks are easier to visualize. The primary peak represents the global minimum of  $\Gamma$ . Initial guesses based on the traditional short-baseline estimation of the direction cosines are also plotted for various SNR values. Using the traditional local solution technique, minimization of 4.20 would produce inaccurate values for  $\hat{\beta}$  under all but the 20 [dB] SNR case.

the domain of the direction cosine parameters  $\theta'_x$  and  $\theta'_y$ . This fact can also be appreciated by calculating the spatial spectrum of the array [78, 71]. Implications of this realization are profound for determining meteor radar interferometric solutions. When cast on the complex plane, global optimization techniques [128] can be used to unambiguously minimize Eq 4.21 thereby estimating  $\beta$  in an optimal least-squares sense. With Matlab, use the constrained 'lsqnonlin()' solver wrapped with the 'multistart()' global optimizer to solve Eq 4.21 using a modern multi-core computer. This approach breaks Eq 4.21 into a grid of regions. The required density of the search grid in the  $\theta'_x$  and  $\theta'_y$  parameter space is defined by the antenna spacing, as can be seen by inspection of Figure 4.4. Upon evaluation of Eq 4.21, the local minimum of each region is determined on a separate processor core (remember that Figure 4.4 is the inverse of Eq 4.20). The regions are then

re-combined and the smallest-valued minima is taken as  $\hat{\beta}$ . In this way, determination of the global minimum is guaranteed over the  $\beta'$  parameter domain. This technique represents the state-of-the-art in meteor radar interferometry. Figure 4.6 shows the striking difference in solution quality between the historical solution technique and the global solution procedure described in this chapter.

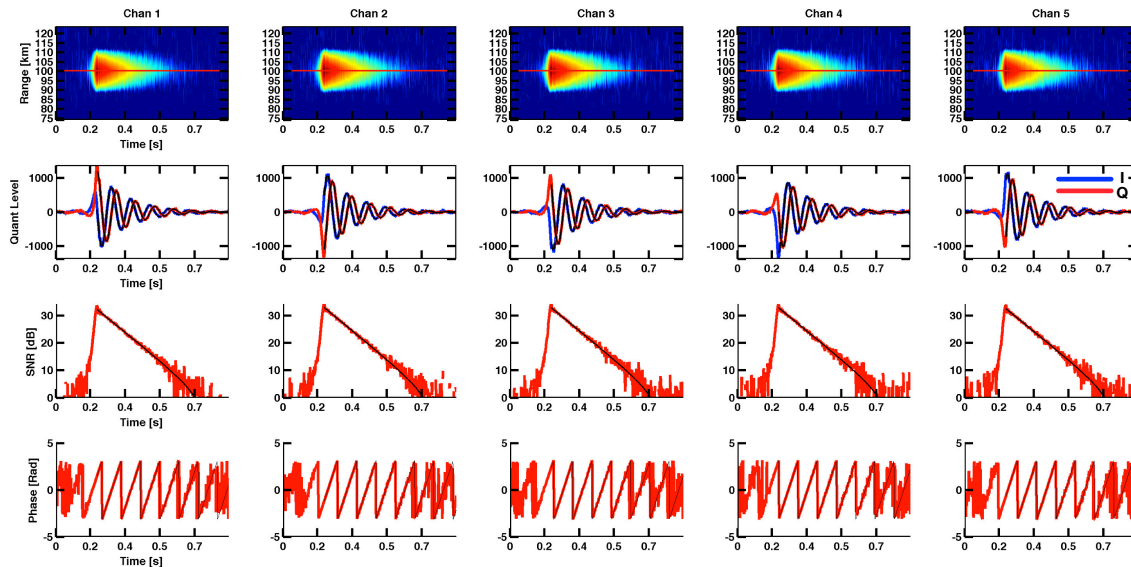


Figure 4.5: Simulated specular backscatter meteor trail echo as observed on the Jones interferometer depicted in Figure 4.1 using the CoSRad radar transceiver at  $f_o = 35.24$  [MHz] at  $f_p = 500$  [Hz]. The echo is simulated by modeling the radar echo at the output of each antenna feed and propagating the received signal through the entire CoSRad receiver chain (including the FPGA filter). The model accounts for all terms involved with classical meteor trail formation including evaluation of the Fresnel integrals of Eq 2.3.  $\hat{\beta}$  is found using Eq 4.21, and the explicit phase differences between each channel of the simulated echo are determined by substituting  $\hat{\theta}_x$  and  $\hat{\theta}_y$  into Eq 4.9. The functional form (defined by Eq 4.18) of the most likely model parameters  $\hat{\beta}$  representing the simulated data is plotted as the black trace in the second row of the figure. The power and phase fits are subsequently derived from the voltage fit.

## 4.6 Statistical Uncertainty

I was surprised to find that the words ‘error’ and ‘uncertainty’ are almost nonexistent in the modern specular meteor radar literature. One modern paper [61] describes the range resolution as 2 [km] (an almost meaningless metric in the context of specular meteor radar assuming a single target) but makes no reference to the height or range uncertainty. In [59], the seasoned investigator claims that meteor radar instrumental errors are the source of the variance his diffusion coefficient observations, but makes no attempt to quantify

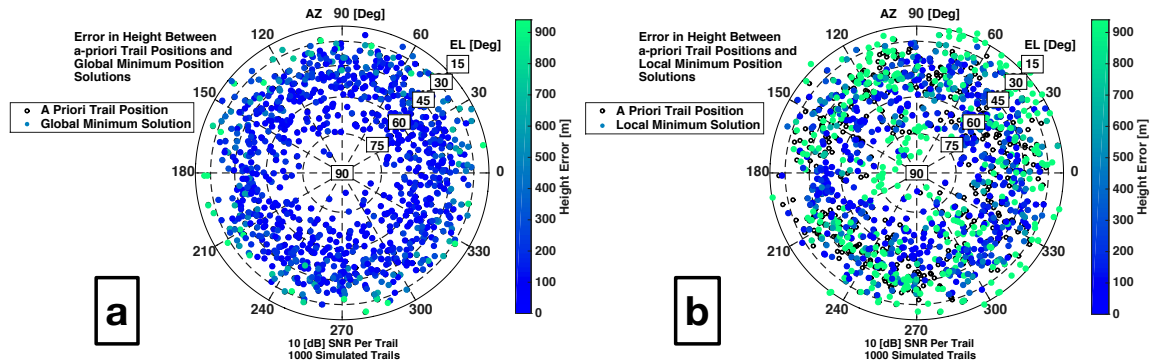


Figure 4.6: 1000 echoes similar to that depicted in Figure 4.5 were generated at 10 [dB SNR] with a uniform azimuthal distribution and a Gaussian height distribution with mean of 92 [km]. The direction cosines were determined using the traditional solution technique (b) and the global complex-plane technique outlined in this chapter (a). The improvement in solution quality is striking and obvious.

or explain such “instrumental errors” which are more accurately described in terms of “instrument precision” and “observational bias.” An instrumental error or bias is generally a constant quantity which is applied to correct the accuracy of a measurement. Instrument uncertainty is the statistically characterized variation in the observation of a given physical parameter. In a recent investigation of mesospheric winds [15], the authors make no mention of the specular meteor radar instrument precision used to derive the wind data. The following analysis provides a framework for quantifying meteor radar measurement precision in the fundamental physical measurement parameters  $\beta$ , and future investigators are invited to incorporate this statistical uncertainty quantification technique into their windfield derivations.

Given a set of voltage observations  $\Phi$  represented by the model  $\Omega$  that are embedded in zero-mean gaussian noise,  $w_k(t) \in \mathcal{N}(0, \sigma_k^2)$ , a least-squares estimate of the most likely parameters  $\hat{\beta}$  representing the true model parameters  $\beta$  is given by Eq 4.21. Because  $\hat{\beta}$  is an estimate of the true model parameters, it too must have a statistical distribution described by some probability density. Determining the parameters of the probability density function describing the variations of  $\hat{\beta}$  due to  $w_k(t)$  is the problem of statistical uncertainty determination and propagation. Said another way, we wish to determine the expected variation in any estimate of the true model parameters  $\beta$  in a rigorous statistical sense by finding the covariance matrix of the parameter estimates shown in Eq 4.23. The diagonal elements of  $\Sigma$  are the estimated parameter

variances  $\sigma_{\hat{\beta}(k)}^2$  and the off-diagonal elements are their covariances. Because the residual matrix  $\mathbf{\Gamma}$  has a normal distribution ( $\mathbf{\Phi}(\boldsymbol{\beta}, t) - \mathbf{\Omega}(\boldsymbol{\beta}, t) = w_k(t) \in \mathcal{N}(0, \sigma_k^2)$ ), the least squares estimate of  $\boldsymbol{\beta}$  is also the maximum likelihood estimate [80].

$$\boldsymbol{\Sigma} = \begin{bmatrix} \sigma_{\hat{\beta}(1)}^2 & \sigma_{\hat{\beta}(1)}\sigma_{\hat{\beta}(2)} & \sigma_{\hat{\beta}(1)}\sigma_{\hat{\beta}(3)} & \cdots & \sigma_{\hat{\beta}(1)}\sigma_{\hat{\beta}(10)} \\ \sigma_{\hat{\beta}(2)}\sigma_{\hat{\beta}(1)} & \sigma_{\hat{\beta}(2)}^2 & \sigma_{\hat{\beta}(2)}\sigma_{\hat{\beta}(3)} & & \\ \sigma_{\hat{\beta}(3)}\sigma_{\hat{\beta}(1)} & \sigma_{\hat{\beta}(3)}\sigma_{\hat{\beta}(2)} & \sigma_{\hat{\beta}(3)}^2 & & \\ \vdots & & & \ddots & \\ \sigma_{\hat{\beta}(10)}\sigma_{\hat{\beta}(1)} & & \cdots & & \sigma_{\hat{\beta}(10)}^2 \end{bmatrix}_{10 \times 10} \quad (4.23)$$

Begin by considering a matrix of the first derivatives of the residual  $\mathbf{\Gamma}(\boldsymbol{\beta}', t)$  with respect to the model parameters  $\boldsymbol{\beta}'$ . This matrix is known as the ‘Jacobian’ and is denoted  $\mathbf{J}$  given by Eq 4.24. Finding  $\hat{\boldsymbol{\beta}}$  does not necessarily require forming the strict analytical representation of  $\mathbf{J}$ , however its numerical form is important for calculating the covariance of the estimated parameters  $\boldsymbol{\Sigma}$ . The size of  $\mathbf{J}$  represents the number of equations vs. the number of unknowns. With a time-series of  $M$  real-valued observations from five antennas, we can form  $10M$  simultaneous equations using Eq 4.19 with the 10 candidate parameters  $\boldsymbol{\beta}'$  defined in Eq 4.7. Notice that  $\mathbf{J}$  represents the first term of a Taylor-series expansion of Eq 4.20 about a set of candidate model parameters  $\boldsymbol{\beta}'$ . The numerical Jacobian is formed by the ‘lsqnonlin()’ Matlab solver to follow the objective function gradients to a global minimum. The numerical Jacobian is used in Eq 4.26 to find parameter covariance  $\boldsymbol{\Sigma}$ . Because  $\mathbf{J}$  is a first-order approximation of Eq 4.20 about  $\boldsymbol{\beta}'(t)$ , the covariance matrix  $\boldsymbol{\Sigma}$  is only valid when the difference between the true parameters  $\boldsymbol{\beta}$  and estimated parameters  $\hat{\boldsymbol{\beta}}$  is small. This also implies that the covariance matrix is only valid at the global minimum of  $\mathbf{\Gamma}$  which is guaranteed when globally evaluating Eq 4.21. The numerical simulations in section 4.7.2 suggest that these requirements are met for nearly all specular meteor trail echoes above 3 [dB]. In this formulation, the Jacobian is scaled by  $\sqrt{\mathbf{W}}$  to simplify the final solution. In practice only the differences between the weights influence the final statistical result, so in the case of closely matched variances ( $\sigma_k$ ) in Eq 4.22, we

may set  $\sqrt{\mathbf{W}} = \mathbf{I}$ .

$$\mathbf{J}(\mathbf{\Gamma}(\boldsymbol{\beta}', t)) = \begin{bmatrix} \left[ \begin{array}{ccc} \frac{\partial f_1(t_1)}{\partial \beta'(1)} & \cdots & \frac{\partial f_1(t_1)}{\partial \beta'(10)} \\ \vdots & \ddots & \vdots \\ \frac{\partial f_1(t_M)}{\partial \beta'(1)} & \cdots & \frac{\partial f_1(t_M)}{\partial \beta'(10)} \end{array} \right] \\ \vdots \\ \left[ \begin{array}{ccc} \frac{\partial f_{10}(t_1)}{\partial \beta'(1)} & \cdots & \frac{\partial f_{10}(t_1)}{\partial \beta'(10)} \\ \vdots & \ddots & \vdots \\ \frac{\partial f_{10}(t_M)}{\partial \beta'(1)} & \cdots & \frac{\partial f_{10}(t_M)}{\partial \beta'(10)} \end{array} \right] \end{bmatrix} \sqrt{\mathbf{W}} \quad (4.24)$$

The Jacobian  $\mathbf{J}$  describes how differences between the residuals and the observations change with respect to the model input parameters when calculated through Eq 4.20. Said another way,  $\mathbf{J}$  describes how  $\mathbf{\Gamma}$  behaves when we ‘shake’ on the candidate model parameters inputs  $\boldsymbol{\beta}'$ . Remember that the goal of this problem is to find the covariance  $\boldsymbol{\Sigma}$  of the estimated parameters  $\hat{\boldsymbol{\beta}}$ , and therefore we desire knowledge of how the least-squares best fit parameter vector  $\hat{\boldsymbol{\beta}}$  behaves when we ‘shake’ on the residual voltages  $\mathbf{\Gamma}$ . This is the essence of the inverse variance problem, and this description suggests the formation of the inverse of  $\mathbf{J}$ .

Define the scalar-valued mean square error  $\epsilon$  as the sum of the squares of the weighted residual matrix  $\mathbf{\Gamma}$  as Eq 4.25 evaluated at some candidate parameter vector  $\boldsymbol{\beta}'$ . The mean square error is a measure of the variance of the residuals [118]. In this formulation, the weights have already been included in the objective function (Eq 4.20).

$$\epsilon = \sum \mathbf{\Gamma}(\boldsymbol{\beta}'(t)) \quad (4.25)$$

Under the assumption of a Gaussian distribution of the errors between the model  $\boldsymbol{\Omega}$  and the observa-

tions  $\Phi$  defined as  $\Gamma$  in Eq 4.20, the covariance of the input parameters has the amazingly simple solution given by Eq 4.26. As with Eq 4.25, the weighting matrix has been included in the scaling of  $\mathbf{J}$ . Eq 4.26 is the covariance of the model parameters  $\Sigma$  which describes the statistical uncertainty (precision) of the estimated parameters  $\hat{\beta}$  assuming the model  $\Omega$ .

$$\Sigma = \frac{\epsilon (\mathbf{J}^T \mathbf{J})^{-1}}{a - b} = \frac{\epsilon (\mathbf{J}^T \mathbf{J})^{-1}}{M10 - 10} \quad (4.26)$$

Where  $a$  is the number of simultaneous equations which equals the number of rows of  $\mathbf{J}$ , and  $b$  is the number of parameters in  $\hat{\beta}$ . Some caveats apply when applying Eq 4.26. The casual investigator may be tempted to include additional signal parameters in  $\hat{\beta}$  such as the explicit phase estimate for each channel  $\hat{\phi}_k$ . In this case, the rows of  $\mathbf{J}$  become linearly dependent because the phase estimates are a linear combination of the direction cosines (Eq 4.9) and  $\mathbf{J}$  becomes rank deficient. When  $\mathbf{J}$  becomes rank deficient,  $\mathbf{J}^T \mathbf{J}$  is ill-conditioned and non-invertible. Therefore, Eq 4.26 only applies when  $\text{rank}(\mathbf{J}) = \text{length}(\hat{\beta})$ . The 'lsqnonlin()' solver in Matlab used to evaluate Eq 4.21 can provide the numerically evaluated Jacobian  $\mathbf{J}(\hat{\beta})$  and the residual matrix  $\Gamma(\hat{\beta})$  for direct use in Eqs 4.25 and 4.26. Providing an analytical Jacobian will improve the 'lsqnonlin()' solution time by a factor of 2.

After estimating the direction cosines using Eq 4.21, estimates the echo location in the spherical coordinates of azimuth  $\hat{\theta}_a$ , elevation  $\hat{\alpha}_e$  and height  $\hat{h}$  are determined using Eq 4.27 where the radial coordinate is the radar range estimate  $\hat{R}$ .

$$\mathbf{f}_s(\theta_x, \theta_y, R) = \begin{bmatrix} f_{s1}(\theta_x, \theta_y) \\ f_{s2}(\theta_x, \theta_y) \\ f_{s3}(\theta_x, \theta_y, R) \end{bmatrix} = \begin{bmatrix} \theta_a \\ \alpha_e \\ h \end{bmatrix} = \begin{bmatrix} \tan^{-1}\left(\frac{\theta_y}{\theta_x}\right) \\ \cos^{-1}\left(\theta_x \sqrt{\frac{\theta_y^2}{\theta_x^2} + 1}\right) \\ R \sqrt{1 - \theta_x^2 - \theta_y^2} \end{bmatrix} \quad (4.27)$$

The statistical uncertainties in the directional cosine coordinates and range are transformed into

uncertainties in the spherical coordinates described in Eq 4.27 by the widely practiced generalized uncertainty propagation technique of Eq 4.30 [104]. First form the Jacobian of Eq 4.27 as shown in Eq 4.28. This task is well-suited for computer algebra systems such as the symbolic toolbox or muPad in Matlab. Make use of the functions ‘jacobian()’ and ‘matlabFunction()’ to generate a suitable error propagation Jacobian  $\mathbf{J}_s$  for implementation of this technique. Most computer algebra systems manipulate complex-valued symbols by default, therefore, care should be taken when symbolically computing the real-valued derivatives of Eq 4.28.

$$\mathbf{J}_s = \begin{bmatrix} \frac{\partial f_{s1}}{\partial \theta_x} & \frac{\partial f_{s1}}{\partial \theta_y} & \frac{\partial f_{s1}}{\partial R} \\ \frac{\partial f_{s2}}{\partial \theta_x} & \frac{\partial f_{s2}}{\partial \theta_y} & \frac{\partial f_{s2}}{\partial R} \\ \frac{\partial f_{s3}}{\partial \theta_x} & \frac{\partial f_{s3}}{\partial \theta_y} & \frac{\partial f_{s3}}{\partial R} \end{bmatrix} = \begin{bmatrix} \frac{\partial f_{s1}}{\partial \theta_x} & \frac{\partial f_{s1}}{\partial \theta_y} & 0 \\ \frac{\partial f_{s2}}{\partial \theta_x} & \frac{\partial f_{s2}}{\partial \theta_y} & 0 \\ \frac{\partial f_{s3}}{\partial \theta_x} & \frac{\partial f_{s3}}{\partial \theta_y} & \frac{\partial f_{s3}}{\partial R} \end{bmatrix} \quad (4.28)$$

Note that for propagation of variance, (as opposed to finding the variance via inverse methods as was done in Eq 4.26), the Jacobian need not be full rank. This allows us to determine the variance of any derived parameters, even if they happen to have linear dependence. The statistical uncertainties from the estimated parameters of  $\hat{\theta}_x$ ,  $\hat{\theta}_y$  and  $\hat{R}$  are propagated into uncertainties in the derived parameters of Eq 4.27 using Eq 4.30

$$\begin{aligned} \Sigma_d &= \begin{bmatrix} \sigma_{\hat{\beta}(9)}^2 & \sigma_{\hat{\beta}(9)}\sigma_{\hat{\beta}(10)} & \sigma_{\hat{\beta}(9)}\sigma_{\hat{R}} \\ \sigma_{\hat{\beta}(10)}\sigma_{\hat{\beta}(9)} & \sigma_{\hat{\beta}(10)}^2 & \sigma_{\hat{\beta}(10)}\sigma_{\hat{R}} \\ \sigma_{\hat{R}}\sigma_{\hat{\beta}(9)} & \sigma_{\hat{R}}\sigma_{\hat{\beta}(10)} & \sigma_{\hat{R}}^2 \end{bmatrix} = \begin{bmatrix} \sigma_{\hat{\theta}_x}^2 & \sigma_{\hat{\theta}_x}\sigma_{\hat{\theta}_y} & \sigma_{\hat{\theta}_x}\sigma_{\hat{R}} \\ \sigma_{\hat{\theta}_y}\sigma_{\hat{\theta}_x} & \sigma_{\hat{\theta}_y}^2 & \sigma_{\hat{\theta}_y}\sigma_{\hat{R}} \\ \sigma_{\hat{R}}\sigma_{\hat{\theta}_x} & \sigma_{\hat{R}}\sigma_{\hat{\theta}_y} & \sigma_{\hat{R}}^2 \end{bmatrix} \\ &= \begin{bmatrix} \sigma_{\hat{\theta}_x}^2 & \sigma_{\hat{\theta}_x}\sigma_{\hat{\theta}_y} & 0 \\ \sigma_{\hat{\theta}_y}\sigma_{\hat{\theta}_x} & \sigma_{\hat{\theta}_y}^2 & 0 \\ 0 & 0 & \sigma_{\hat{R}}^2 \end{bmatrix} \end{aligned} \quad (4.29)$$

A submatrix of  $\Sigma$  is formed as Eq 4.29. The covariance of the range estimate with respect to the direction cosines is also assumed small. This makes intuitive sense as the radar’s range measurement should

not depend on the arrival angle of the echo.

$$\Sigma_s = \begin{bmatrix} \sigma_{\theta_a}^2 & \sigma_{\theta_a}\sigma_{\alpha_e} & \sigma_{\theta_a}\sigma_h \\ \sigma_{\theta_e}\sigma_{\alpha_a} & \sigma_{\alpha_e}^2 & \sigma_{\alpha_e}\sigma_h \\ \sigma_h\sigma_{\theta_a} & \sigma_h\sigma_{\alpha_e} & \sigma_h^2 \end{bmatrix} = \mathbf{J}_s \Sigma_d \mathbf{J}_s^\top \quad (4.30)$$

As was the case with Eq 4.24, notice that Eq 4.28 comprises the first non-constant terms of a Taylor series expansion of  $\mathbf{f}_s$ . One caveat of the first-order error propagation approach is that the estimated parameters  $\hat{\boldsymbol{\beta}}$  must not lie too far from the true parameters  $\boldsymbol{\beta}$ . In other words, if the total error between the estimated and true parameters is too large,  $\mathbf{J}_s$  is no longer a good approximation for how the covariance matrix  $\Sigma$  maps onto the covariance  $\Sigma_s$  of the derived parameters. The simulation results in Section 4.7.2 suggest that echoes above 3 [dB] in SNR provide adequately precise solutions for application of Eq 4.30.

### 4.6.1 Multistatic Wind Vector Retrieval

The notation regarding multistatic wind vector retrieval differs throughout the literature, and various papers suffer from infuriating math errors and inadequately detailed explanations. This section is based on a modern paper describing IAP's MMARIA system [122], where I have attempted to unify the notation and provide detailed explanations of the applicable equations and their origins in the radar literature. I have also cast the equations in terms of the directly measured parameters of Doppler frequency and meteor trail position. Wind retrieval results based on an unpublished technique currently in development at IAP are presented in Figure 4.7. The SVD inversion of Figure 4.7 does not currently account for the fundamental precision estimation described in Section 4.6. Integrating meteor wind radar instrument precision into IAP's SVD inversion technique is currently an active research topic. The coherent wind structures above 100 [km] suggest that Earth's geomagnetic field does not dramatically bias the high-altitude wind measurements (see Chapter 2.2), however, geomagnetic effects on high-altitude winds such as those shown in Figure 4.7 is also an active research topic. An independent wind retrieval technique based on unpublished inverse methods formulated by Prof. David Hysell of Cornell University is currently under development with the goal of providing an independent retrieval for comparison to Dr. Strober's current iterative SVD technique.

After obtaining of an ensemble of meteor trail position and Doppler measurements  $i$  at each receiving station of a networked multistatic radar, with each measurement having an associated  $\Sigma_i$ ,  $\Sigma_{d_i}$  and  $\hat{\beta}_i$ , an estimate of the vector field  $\hat{\mathbf{u}}(\mathbf{r}_i)$  best representing the true windfield at some desired height and time resolution defined by the window of  $i$  is determined by evaluating Eq 4.35 [122]. The wind is represented by the vector quantity  $\mathbf{u}'(\mathbf{r}_i) = [u'_i, v'_i, w'_i]$  within some chosen height and time window. In the general case, an arbitrary set of windfield vectors estimates  $\hat{\mathbf{u}}(\mathbf{r}_i)$  are generated over some spatial and temporal window defined by  $i$  (see Figure 1.3). In the monostatic case,  $\mathbf{r}_i$  is the location of the estimated windfield vector  $\hat{\mathbf{u}}$  within some height bin and time window. In the multistatic case,  $\mathbf{r}_i$  represents the locations of each estimated windfield vector, forming a vector field estimate of the true windfield. Under arbitrary network geometry, the Doppler shift observed at any receiver location is a function of the Bragg vector magnitude  $k_{Bi}$ . The

quantity  $\mathbf{m}_i$  is defined as a unit vector that points from the receiving station to the trail. The observed Doppler shift for any given trail is represented as the dot product between the wind vector  $\mathbf{u}(\mathbf{r}_i)$  and the magnitude of the Bragg vector as shown in Eq 4.31 [22, 122].

$$f_{di} = [\mathbf{u}(\mathbf{r}_i) \cdot \mathbf{m}_i] \frac{k_{Bi}}{2\pi} \quad (4.31)$$

The Bragg vector magnitude in Eq 4.31 is given by Eq 4.32

$$k_{Bi} = \frac{2\pi}{\lambda_{Bi}} \quad (4.32)$$

where the Bragg wavelength associated with each trail observation is given by Eq 4.33 and  $\phi$  is the specular scattering angle given by Figure 2.1.  $\lambda$  is the radar wavelength  $\lambda = c/f_o$ .

$$\lambda_{Bi} = \frac{\lambda}{2 \cos \phi} \quad (4.33)$$

In the case zero specular scattering angle ( $\phi = 0$ ) the trail is observed by a receiver collocated with the transmitter and the Bragg wavelength becomes  $\lambda_{Bi} = \lambda/2$ . Eq 4.31 then reduces to Eq 4.34 which relates the measured Doppler frequency  $f_{di}$  to the wind vector  $\mathbf{u}(\mathbf{r}_i)$  and meteor trail location  $\mathbf{m}_i$ . Eq 4.34 is easily rearranged to produce the radial velocity measurement  $v_i$  using a monostatic radar under the assumption of  $\phi = 0$ .

$$f_{di} = [\mathbf{u}(\mathbf{r}_i) \cdot \mathbf{m}_i] \frac{2}{\lambda} \rightarrow v_i = [\mathbf{u}(\mathbf{r}_i) \cdot \mathbf{m}_i] = \frac{f_{di}\lambda}{2} \quad (4.34)$$

As was done in Section 4.4 for determine the fundamental signal parameters, Eq 4.31 is used to estimate the vector windfield  $\hat{\mathbf{u}}(\mathbf{r}_i)$  by minimizing the quantity  $([\mathbf{u}'(\mathbf{r}_i) \cdot \mathbf{m}_i] k_{Bi} - 2\pi f_{di})^2$  as shown in Eq 4.35

$$\min_{\mathbf{u}'(\mathbf{r}_i)} \sum_i ([\mathbf{u}'(\mathbf{r}_i) \cdot \mathbf{m}_i] k_{Bi} - 2\pi f_{di})^2 \quad (4.35)$$

In the monostatic case where the specular scattering angle is zero, Eq 4.35 reduces to Eq 4.36 [56]. The vertical wind component is typically assumed small compared to the horizontal components such that  $w'_i = 0$ . The quantity  $\mathbf{u}'(\mathbf{r}_i) \cdot \mathbf{m}_i$  represents the projection of a candidate wind vector  $\mathbf{u}'(\mathbf{r}_i)$  in the direction of the trail, which is equal to the measured radial neutral wind velocity assuming the trail shares the motion of the neutral windfield. Therefore,  $v_i = \mathbf{u}'(\mathbf{r}_i) \cdot \mathbf{m}_i$ . To find the best-fit monostatic wind vector  $\hat{\mathbf{u}}(\mathbf{r}_i)$  in some height and time window, minimize the quantity  $(\mathbf{u}'(\mathbf{r}_i) \cdot \mathbf{m}_i - v_i)^2$  over a set of candidate wind vectors  $\mathbf{u}'(\mathbf{r}_i)$  as implied by Eq 4.34 and shown in Eq 4.36.

$$\min_{\mathbf{u}'(\mathbf{r}_i)} \sum_i [\mathbf{u}'(\mathbf{r}_i) \cdot \mathbf{m}_i - v_i]^2 \quad (4.36)$$

If we include the Doppler and directional cosine measurement precision terms, Eq 4.35 becomes the problem shown in Eq 4.37 where  $\Sigma_a$  is found via Choleski Decomposition of the non-diagonal covariance of the Doppler and directional cosine measurements for each trail of the ensemble  $i$ . How the precision in the directional cosine terms is represented in  $\Sigma_a$  is currently an active area of research at IAP. Finding values of  $\hat{\mathbf{u}}$  along with the estimated vector windfield precision which best represents the vector windfield observations under the known measurement parameter precision is a nontrivial generalized least squares optimization problem well suited as a future dissertation topic, and represents the future of inverse-variance meteor wind radar statistical signal processing. Finding solutions to Eq 4.37 is currently an active research topic among the atmospheric physics community and at IAP. As of this writing, positions are available for investigators

who wish to attempt a solution.

$$\min_{\mathbf{u}'(\mathbf{r}_i)} \sum_i [(\mathbf{u}'(\mathbf{r}_i) \cdot \mathbf{m}_i) k_{Bi} - 2\pi f_{di}]^T (\Sigma_d^I)^{-1} \Sigma_a^{-1} [(\mathbf{u}'(\mathbf{r}_i) \cdot \mathbf{m}_i) k_{Bi} - 2\pi f_{di}] \quad (4.37)$$

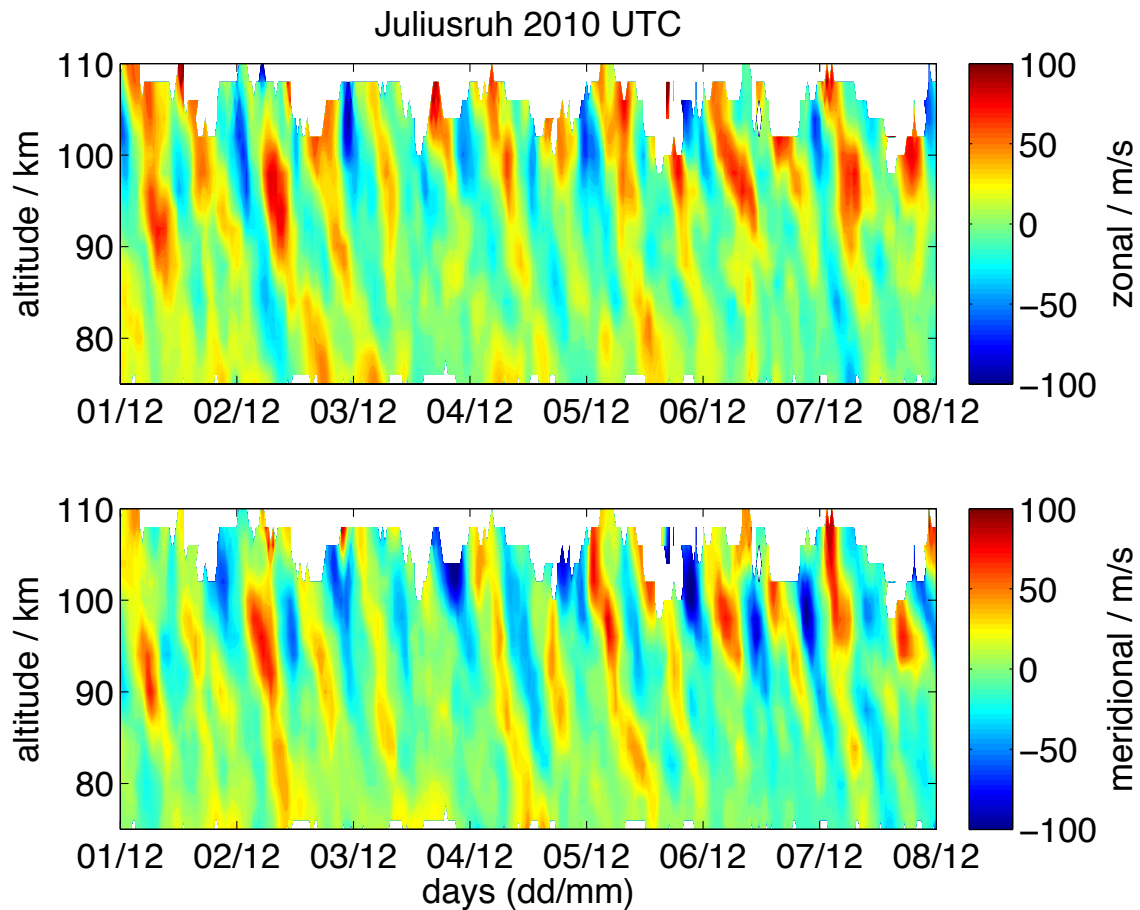


Figure 4.7: Example of Zonal and Meridional winds from the Juliusruh specular meteor radar [115] provided by [Strober, G] of IAP in 2015. The winds were calculated using advanced inversion techniques applied to raw specular meteor radar data from 2010. This currently unpublished approach uses an iterative singular value decomposition (SVD) technique developed at IAP and applied to Eq 4.36 to find best-fit winds. Dr. Strober’s description of the wind inversion technique is given in Appendix A.

## 4.7 Forward Model and Simulation Results

Validation of the statistical uncertainty and error propagation technique outlined in Section 4.6 required the creation of a sophisticated instrument forward model. Simulated CoSRad observations of specular meteor trail echoes are generated with statistical spatial distributions and distributions in the true parameters  $\beta$  assuming some noise environment. The simulated voltage-level echoes like the one shown in Figure 4.3 are placed in the columns of  $\Phi$ . After  $\hat{\beta}$  and  $\Sigma$  are determined, the true (known) a-priori parameter values  $\beta$  are compared with the best fit parameters  $\hat{\beta}$ . The solution core only uses knowledge of the true parameters to loosely bound the ‘lsqnonlin()’ solver in  $D'_a$  and  $f'_d$  for decreased computation time, but this simulation optimization is not necessary to replicate the presented results. Simulating the phase delays associated with an arbitrary antenna geometry is greatly simplified through use of the Matlab Phased Array Toolbox. The function ‘collectPlaneWave()’ proved especially convenient in creating the array forward-model.

### 4.7.1 Forward Model Range Estimation

The radar range uncertainty has been set at  $\sigma_{\hat{R}} = 176$  [m] corresponding to the uncertainty of the approximate propagation path length (the absolute range determination ability) associated with one CoSRad sample when configured for typical meteor radar applications (see Chapter 3 and Figure 3.9). This simplification is a reasonable but not entirely accurate representation of reality. When observing echoes with even moderate SNR (>10 dB), the variance in the sample number corresponding to the range of maximum power from the output of the matched filter (Chapter 3, Eq 3.28) rapidly approaches zero. This phenomenon results from using a simple arithmetic average weighted by the SNR to estimate the sample number corresponding to maximum power and subsequently range (see Chapter 3.6.1). For proper range estimation, a signal model representing the output of the matched filter defined by the shape of the transmit pulse (a square in the case of the CoSRad observations such as that shown in Figure 3.26) should be fit to the output of the matched filter using a least squares technique similar to that described in Section 4.5. For the

purposes of this investigation, setting a constant range variance does not significantly effect the estimated precision results as it essentially sets a lower-bound on the height uncertainty estimate for high SNR echoes at high elevation angles (see Figure 4.9). Figure 4.12 shows the cumulative distribution functions of the error distributions of Figures 4.10 and 4.11 and strongly suggest that the estimated parameters are unbiased, and that the estimated uncertainties are realized from the Gaussian distribution. The estimates are consistent over SNR and across the parameter space of  $\beta$ . This uncertainty estimation technique represents the current state-of-the-art in specular meteor radar parameter and uncertainty estimation.

#### 4.7.2 Uncertainty Estimation Performance

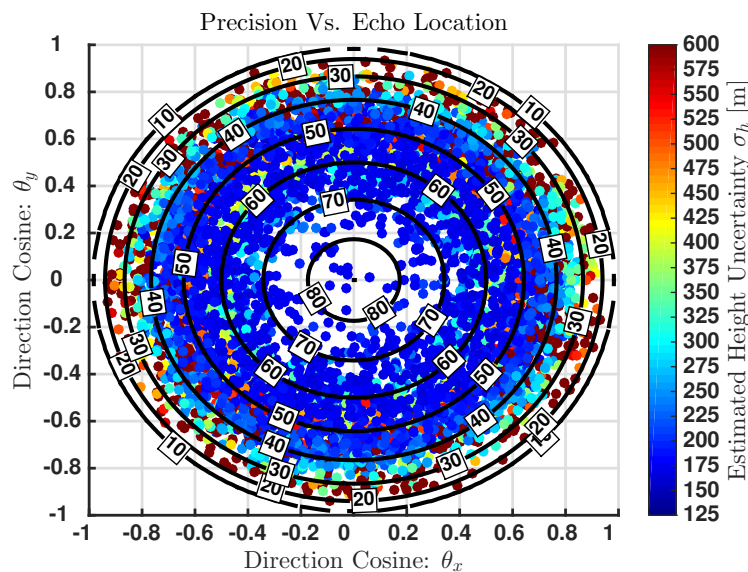


Figure 4.8: Qualitative depiction of 6000 simulated echoes, generated with a uniform azimuthal distribution. The simulated echoes are uncorrelated in time and height and therefore do not represent a geophysically realistic windfield. The elevation angle contours are labeled in [deg]. Each echo is color-coded to indicate the estimated height uncertainty  $\sigma_h$  from Eq 4.30. Note that echoes may have a larger estimated uncertainty than the maximum colorbar limit of 600 [m].

Figure 4.8 provides a qualitative depiction of the simulated echo spatial distribution along with the estimated uncertainty distribution, and clearly shows that an increase in estimated uncertainty is correlated with decreasing in elevation angle. All uncertainty estimates are statistical in nature, therefore an echo coincidentally having a low true error may have a large estimated uncertainty, and an echo with a larger true

error could be estimated with an uncertainty falling outside the first standard deviation of the estimator. Echoes with a true error falling outside the second ( $2\sigma_h$ ) standard deviation in height estimation should become increasingly unlikely, so we would expect to see very few echoes having large true errors with a small uncertainty, which is indeed the case. Figure 4.8 does not succinctly describe the magnitude of the estimated errors. For this, turn to Figures 4.9, 4.10, 4.11 and 4.12. As expected, the estimated uncertainties tracks the true errors and decreases with increasing SNR. Furthermore, the estimated parameters and uncertainties appear to be unbiased and consistent over all values of SNR, which is corroborated by Figure 4.12.

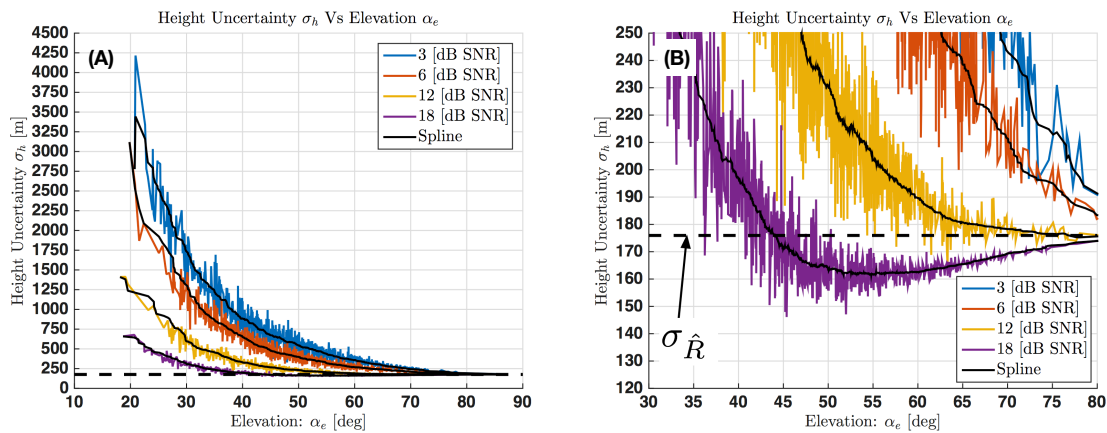


Figure 4.9: Height uncertainty is plotted as a function of elevation angle. Uncertainty is maximized at low SNR and at low elevation angles. The height uncertainty approaches the range uncertainty  $\sigma_{\hat{R}}$  for higher elevation angles as expected. Interestingly, panel (B) shows that for high SNR echoes at mid-elevation angles, the height uncertainty is driven by  $\sigma_{\hat{R}}$ . For SNR=18 [dB SNR], the height uncertainty actually drops below  $\sigma_{\hat{R}}$  resulting from the projection of  $\sigma_{\hat{R}}$  onto  $h$ .

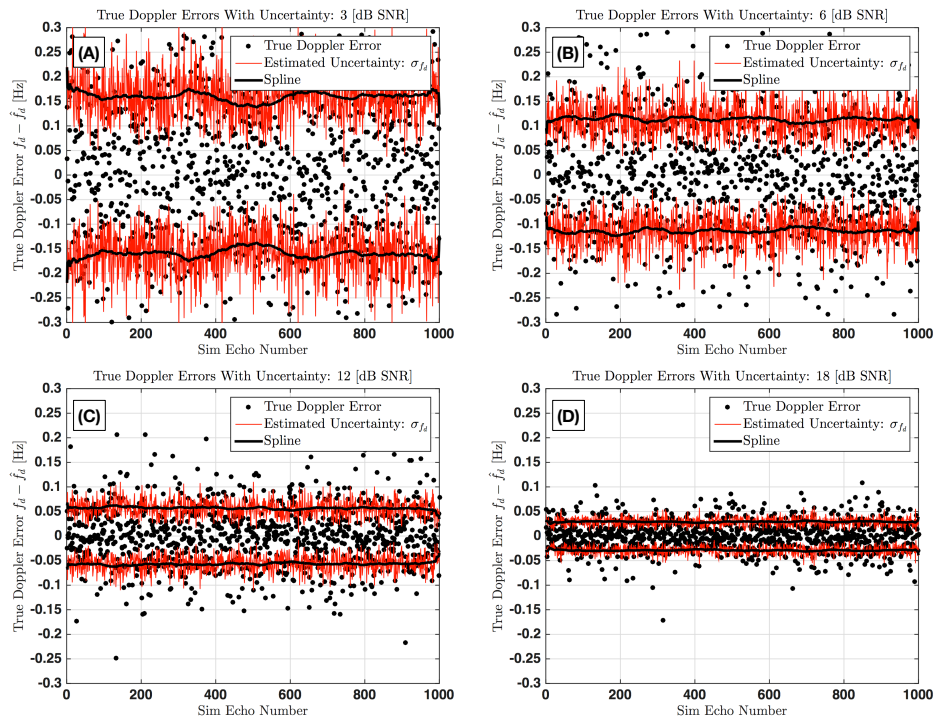


Figure 4.10: Comparison of 4000 echoes with random Doppler velocities  $f_d \in \mathcal{N}(0, 10)$  [Hz] and diffusion coefficients  $D \in \mathcal{N}(5, 2)$  [ $\text{m}^2 \text{s}^{-1}$ ] with their estimated uncertainties and true errors. Echoes are generated at four different SNR levels with the spatial distribution shown in Figure 4.8. Estimates of the true model parameters  $\hat{\beta}$  and their associated parameter uncertainties  $\Sigma$  for each simulated echo are determined using the global solution technique of Section 4.4. Both the estimated Doppler uncertainty  $\sigma_{f_d}$  and the known a-priori Doppler error ( $f_d - \hat{f}_d$ ) are plotted. A smoothing spline function is fit to the uncertainty estimates representing the average of the estimated uncertainties.

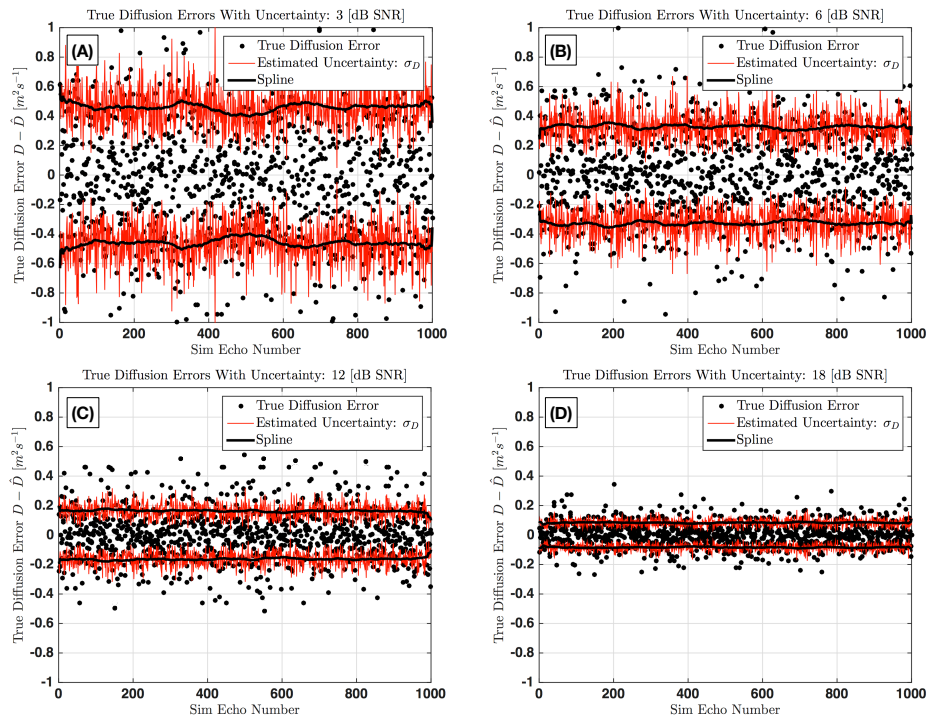


Figure 4.11: Comparison of 4000 echoes with random Doppler velocities  $f_d \in \mathcal{N}(0, 10)$  [Hz] and diffusion coefficients  $D \in \mathcal{N}(5, 2)$  [m<sup>2</sup> s<sup>-1</sup>] with their estimated uncertainties and true errors. Echoes are generated at four different SNR levels with the spatial distribution shown in Figure 4.8. Estimates of the true model parameters  $\hat{\beta}$  and associated parameter uncertainties  $\Sigma$  for each simulated echo are determined using the global solution technique of Section 4.4. Both the estimated diffusion uncertainty  $\sigma_D$  and the known a-priori diffusion error ( $D - \hat{D}$ ) are plotted. A smoothing spline function is fit to the uncertainty estimates representing the average of the estimated uncertainties.

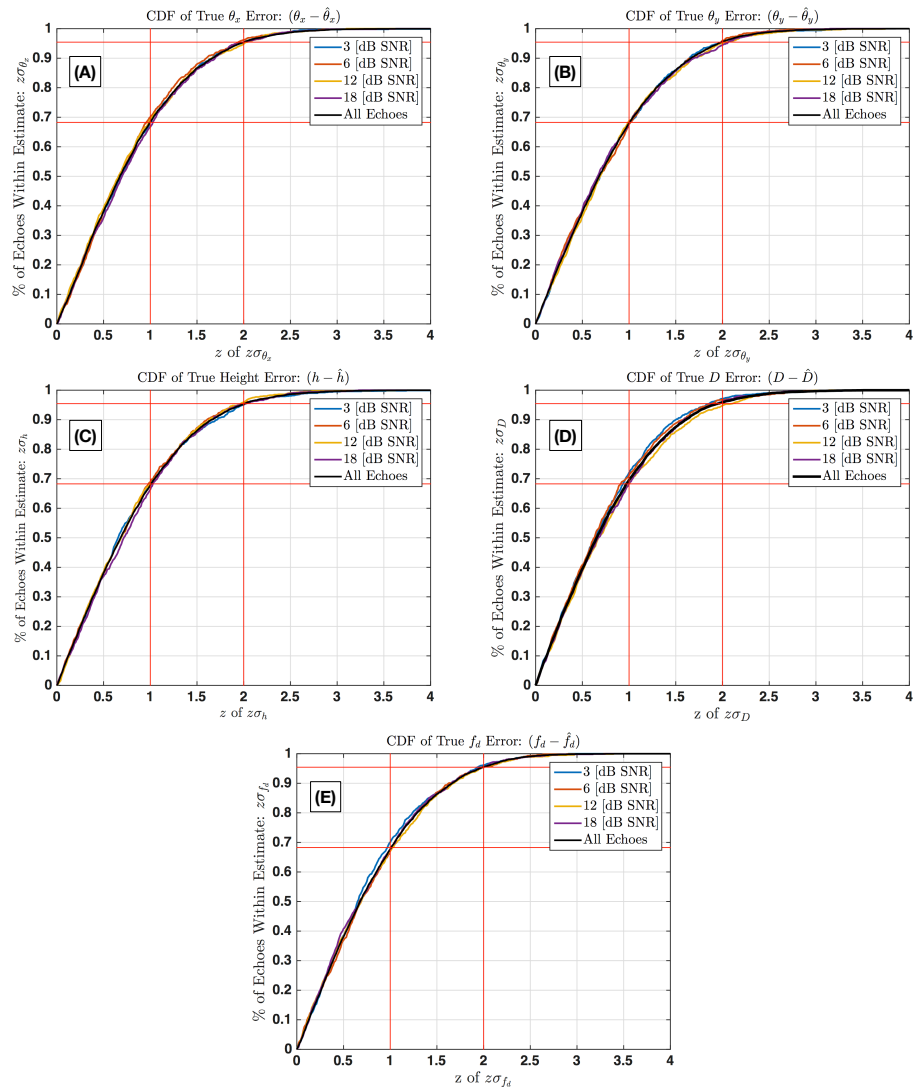


Figure 4.12: CDFs of the true a-priori parameter error compared to the estimated parameter uncertainty. All 4000 echoes of Figures 4.10 and 4.11 are included along with an additional 2000 echoes having a constant Doppler  $f_d = 10$  [Hz], and normally distributed SNR  $\in \mathcal{N}(13, 4)$  [dB SNR] with a uniform azimuthal distribution. The first and second standard deviations of the Gaussian CDF are also plotted. The CDFs of the estimated uncertainties closely track those expected from the Gaussian distribution.

## 4.8 Complex Plane Phase Calibration

Yet another point of contention in the meteor radar community concerns the phase calibration of the antenna array. Various calibration techniques have been attempting for array phase calibration of remote sensing radar systems including the use of radio stars [20] or radio beacons [131]. More recently, all-sky optical cameras have been used to validate the radar interferometric solutions from bright visible meteor trails [90]. The radio star and optical all-sky camera array calibration approaches show promise in addition to the technique presented here. A comprehensive specular meteor radar phase calibration strategy would probably combine elements of all three strategies. In Sections 4.3 and 4.6 the phase at the output of each receiver channel was assumed to be a perfect time-delayed reproduction of the phase observed on each antenna. No systemic phase biases between the five receiver channels were included in the analysis. With real specular meteor radar systems, phase biases exist between true phase of the observed signal at the antennas, and the output of the receiver. The meteor radar literature is somewhat sparse on the topic of phase calibration. One paper by Holdsworth [64] describes a rudimentary version of the maximization technique outlined in this section using real-value phases, complicating the implementation. The paper also suffers from at least one math error in equation 19. During efforts to produce reasonable results using the CoSRad data acquired at the Jones array located in Delemare, South Australia (see Figure 3.18), Prof. Jorge Chau (currently serving as the director of the radar group at the Institute for Atmospheric Physics located in Khlungsborn, Germany), made available a page of notes formulating Holdsworth's technique on the complex plane, thereby simplifying the implementation. Prof. Chau's original notes are shown in Figure A.1 of Appendix A. While mathematically correct, Prof. Chau's notes proved to be an implementation challenge as they were intended for his own personal analysis of Holdsworth's technique. The goal of this section is to combine elements from Holdsworth's technique and Prof. Chau's mathematical formulation into a clear calibration procedure for application to SDR-based specular meteor radar systems. The approach outlined in this chapter only directly applies to the Jones antenna configuration; however, it can guide a clever radar engineer in applying the technique to other antenna configurations.

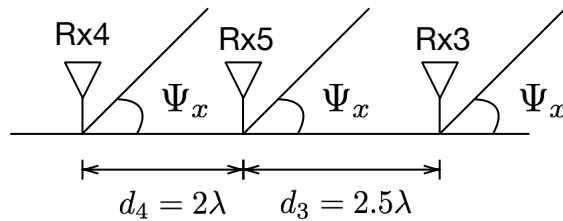


Figure 4.13: A plane wave intersects the array of Figure 4.1 along the  $e_x$  direction at an elevation angle  $\Psi_x$ . The geometry and mathematical formulation is identical in the  $e_y$  direction but with a different incidence angle  $\Psi_y$ .

Eq 4.38 now includes a phase bias term  $\alpha_k$  as part of the observed signal originally given by Eq 4.16.

$$\Phi(\boldsymbol{\beta}, t) = \begin{bmatrix} A_1 e^{-Dt} e^{j2\pi f_d t} e^{j\phi_{a1}(\theta_x, \theta_y)} e^{j\phi_5} e^{j\alpha_1} \\ A_2 e^{-Dt} e^{j2\pi f_d t} e^{j\phi_{a2}(\theta_x, \theta_y)} e^{j\phi_5} e^{j\alpha_2} \\ A_3 e^{-Dt} e^{j2\pi f_d t} e^{j\phi_{a3}(\theta_x, \theta_y)} e^{j\phi_5} e^{j\alpha_3} \\ A_4 e^{-Dt} e^{j2\pi f_d t} e^{j\phi_{a4}(\theta_x, \theta_y)} e^{j\phi_5} e^{j\alpha_4} \\ A_5 e^{-Dt} e^{j2\pi f_d t} e^{j\phi_5} e^{j\alpha_5} \end{bmatrix}^T + \begin{bmatrix} w_1(t) \\ w_2(t) \\ w_3(t) \\ w_4(t) \\ w_5(t) \end{bmatrix}^T \quad (4.38)$$

The problem of phase calibration is determination of the assumed constant phase bias values  $\alpha_k$ . The values of  $\alpha_k$  which compensate for the (assumed) fixed phase biases present on each channel of a CoSRad-based digital meteor radar system comprise the ‘phase calibration values’. As was done in Section 4.3, the phases are referenced to channel 5 such that  $\alpha_5 = 0$  and  $e^{j\alpha_5} = 1 + 0j$ . Begin by writing the phases observed at the output of the receiver on each antenna in Figure 4.13 with respect to channel 5. Eq 4.39 represents the phase delays observed at the output of the CoSRad receiver assuming a monochromatic plane wave originating from a single target impinging on the antenna array as a function of  $\Psi_x$ . This assumption is valid under most specular meteor radar conditions as observing more than one trail at the same range at the same time is unlikely.

$$\begin{aligned}
e^{j\phi_3} &= e^{j(\kappa d_3 \cos(\Psi_x) + \alpha_3)} \\
e^{j\phi_4} &= e^{j(\kappa d_4 \cos(\Psi_x) + \alpha_4)}
\end{aligned} \tag{4.39}$$

Next form the product of the complex-valued phase observations as shown in Eq 4.40 which describes the unambiguous phase at two antennas spaced at  $d = \lambda/2$  assuming a single target.

$$\begin{aligned}
e^{j\phi_3} e^{j\phi_4} &= e^{j(\kappa d_3 \cos(\Psi_x) + \alpha_3)} e^{j(\kappa d_4 \cos(\alpha_3 + \alpha_4))} \\
&= e^{jk(d_3 + d_4) \cos(\Psi_x) + j(\alpha_3 + \alpha_4)}
\end{aligned} \tag{4.40}$$

The goal of determining  $\alpha_3$  and  $\alpha_4$  given Eq 4.40 requires a mathematical relationship which is independent of  $\Psi_x$ . Because the values of  $\alpha_3$  and  $\alpha_4$  are assumed unknown (the system is uncalibrated), any values of  $\Psi_x$  and  $\Psi_y$  measured between the antennas originating from a specular meteor trail echo will will produce an inaccurate estimate of the direction cosines  $(\hat{\theta}_x, \hat{\theta}_y)$  by evaluation of Eq 4.21. However, determining a phase relationship between  $\alpha_3$  and  $\alpha_4$  which is independent of  $\Psi_x$  is possible. Write Eq 4.40 and either expression of Eq 4.39 as a function of  $\Psi_x$ .

$$e^{j\kappa \cos \Psi_x} = \left[ e^{j\phi_3} e^{j\phi_4} e^{-j(\alpha_3 + \alpha_4)} \right]^{\frac{1}{d_3 + d_4}} \tag{4.41}$$

$$e^{j\kappa \cos \Psi_x} = \left[ e^{j\phi_3} e^{-j(\alpha_3 + \alpha_4)} \right]^{\frac{1}{d_3}} \tag{4.42}$$

Equate Eq 4.41 and 4.42 and move all the constant terms to one side, and set the variable terms equal to  $\eta_x$  as shown in Eq 4.44. The mathematics are identical in the  $e_y$  direction and reference to both phase relationships is denoted by  $\boldsymbol{\eta} = [\eta_x \ \eta_y]$ .

$$\left[ e^{j\phi_3} e^{j\phi_4} e^{-j(\alpha_3+\alpha_4)} \right]^{\frac{1}{d_3+d_4}} = \left[ e^{j\phi_3} e^{-j(\alpha_3+\alpha_4)} \right]^{\frac{1}{d_3}} \rightarrow \quad (4.43)$$

$$\left[ e^{j\phi_3} \right]^{\frac{-d_4}{d_3+d_4}} \left[ e^{j\phi_4} \right]^{\frac{d_3}{d_3+d_4}} = e^{j\frac{-\phi_3 d_4}{d_3+d_4}} e^{j\frac{\phi_4 d_3}{d_3+d_4}} = e^{j\left[\frac{(\alpha_3+\alpha_4)d_3}{d_3+d_4} - \alpha_3\right]} = e^{j\eta_x} \quad (4.44)$$

Eq 4.44 represents the phase relationship between antennas Rx3 ( $\phi_3$ ) and Rx4 ( $\phi_4$ ) as  $\eta_x$ , which is a function of the phase biases  $\alpha_3$  and  $\alpha_4$  and the constant antenna geometry terms. In principle, a single high-SNR echo could be used to determine a value for  $\eta_x$  by plugging the measured quantities for  $e^{j\phi_3}$  and  $e^{j\phi_4}$  into Eq 4.44. Because Eq 4.44 is based on the imprecise  $d = \lambda/2$  summation of  $\phi_3 + \phi_4 = e^{j\phi_3} e^{j\phi_4}$ ,  $\eta_x$  becomes a noisy quantity as small variations between the measured phases on the left hand side of Eq 4.44 will cause large deviations of  $\eta_x$  from its expected value, therefore, we must resort to building a statistical picture for the determination of  $\eta_x$ . Figure 4.16 shows the histograms of  $\eta_x$  and  $\eta_y$  calculated for each uncalibrated echo in Figure 4.15. Values for  $\eta_x$  and  $\eta_y$  are determined by fitting a Gaussian PDF to the distributions.

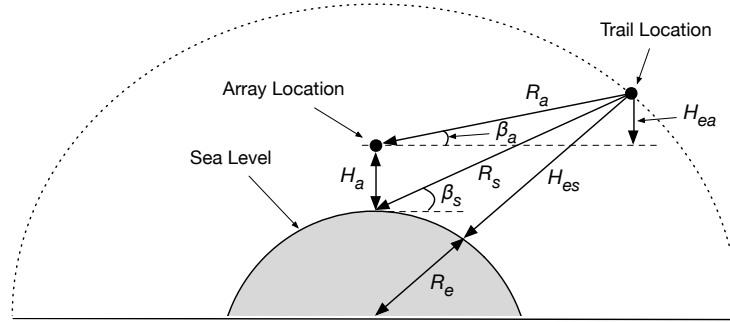


Figure 4.14: When calculating a meteor trail height for use in the calibration procedure, geometric biasing terms should be taken into account such as Earth's curvature and the height of the array above sea level  $H_a$ . For radars located on 2.7 [km] of Antarctic ice at the South Pole [87], the array height correction term is crucial for obtaining accurate results. Geometric correction factors are also discussed in [62] and [86].

To demonstrate the complex plane phase calibration technique, the set of known phase delays in Eq 4.45 were applied to the  $I$  and  $Q$  components of 5000 simulated echoes between 8-13 [dB SNR]:  $\Phi_u = \Phi e^{j\alpha_k}$  where  $\Phi_u$  is the set of uncalibrated observations depicted in Figure 4.15.

$$\alpha_{ka} = \begin{bmatrix} -223 \\ 66 \\ -78 \\ 182 \\ 0 \end{bmatrix}^{\circ} \quad (4.45)$$

The histogram of  $\eta$  produced using Eq. 4.44 is then used to find  $\hat{\eta}$  for the total population of uncalibrated echoes  $\Phi_u$ . Figure 4.16 shows the histograms of  $\eta_x$  and  $\eta_y$  with the mean values  $\hat{\eta}$  identified. Notice that  $\eta_x$  and  $\eta_y$  are real-valued radians, and therefore wrap between  $[\pi : -\pi]$ . Care must be taken when finding  $\hat{\eta}$  of the wrapped distribution in Figure 4.16.  $\hat{\eta}$  represents the phase relationships between the antennas along each baseline independent of  $\Psi$  and  $\alpha_k$ .

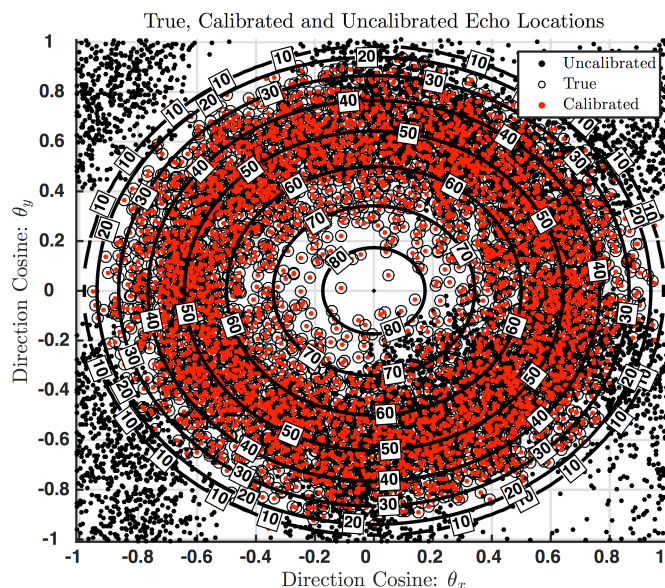


Figure 4.15: The set of known phase delays  $\alpha_k$  in Eq 4.45 are applied to a set of simulated echoes to create the uncalibrated set  $\Phi_u$ . After application of the calibration procedure, the phase calibration estimates  $\hat{\alpha}_k$  are applied to the uncalibrated set and the location of each echo is re-calculated. The resulting calibrated set of echoes are seen to have good agreement with the a-priori ‘true’ echo locations.

After determination of  $\hat{\eta}$  using Eq 4.44 applied to a large population of observations as shown in Figure 4.16, we are in a position to estimate the antenna phase bias terms  $\alpha_3$  and  $\alpha_4$  (or  $\alpha_1$  and  $\alpha_2$  in the

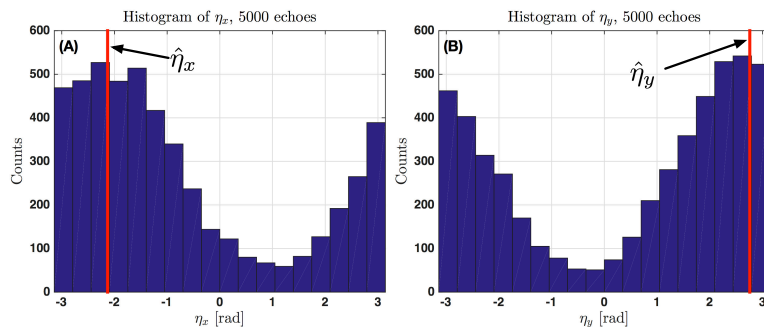


Figure 4.16: Histograms of the phase relationships  $\eta_x$  and  $\eta_y$  between the antennas along both the  $e_x$  and  $e_y$  baselines. Reference to the mean values of both histograms is denoted by  $\hat{\boldsymbol{\eta}} = [\hat{\eta}_x \hat{\eta}_y]$ . A clear peak is identified in  $\boldsymbol{\eta}$  along both baselines and is used in Eqs 4.46 and 4.47 to create the calibration map of Figure 4.17. For accurate determination of  $\hat{\boldsymbol{\eta}}$ , a Gaussian distribution is fit to the histograms, carefully taking into account the observed phase wrapping behavior.

$e_y$  direction). The phase bias estimates  $\hat{\alpha}_k$  are found by what I have termed the ‘Maximization Technique’. The concept is rather straightforward: the best estimated phase biases should result in the maximization of the number of meteor trail detections originating from the meteoric ablation zone of 80-110 [km] in height. Said another way, there should exist a set of phase bias correction terms  $\hat{\alpha}_k$  that when applied to  $\Phi_u$  will maximize the total number of ‘valid’ height determinations  $h$  calculated using Eqs 4.21 and then 4.27.

Finding  $\hat{\alpha}_k$  need not necessitate an exhaustive search over the entire five channel  $\alpha'_k$  parameter space because the problem has been decomposed into two dimensions through Eq 4.44. To see this fact, expand terms and rewrite Eq 4.44 such that  $\alpha'_3$  is the independent variable as shown in Eq 4.46. The phase bias  $\alpha'_2$  as a function of  $\alpha'_1$  in the  $e_y$  direction is also written as Eq 4.47.

$$e^{j\alpha'_4} = f_x(\alpha'_3) = e^{j\eta_x} e^{j\eta_x \frac{d_4}{d_3}} e^{j \frac{\alpha'_3 d_4}{d_3}} \quad (4.46)$$

$$e^{j\alpha'_2} = f_y(\alpha'_1) = e^{j\eta_y} e^{j\eta_y \frac{d_2}{d_1}} e^{j \frac{\alpha'_1 d_2}{d_1}} \quad (4.47)$$

To determine  $\hat{\alpha}_k$ , evaluate Eqs 4.46 and 4.47 over the  $(\alpha'_1, \alpha'_3)$  domain of  $[0 : 10\pi]$ . The domain of  $(\alpha'_1, \alpha'_3)$  is found by noting that both equalities  $e^{j\alpha'_2} = e^{j \frac{\alpha'_1 d_2}{d_1}}$  and  $e^{j\alpha'_4} = e^{j \frac{\alpha'_3 d_4}{d_3}}$  hold at multiples of

$10\pi$ . For each set of candidate phase offsets  $\alpha'_k$ , the height of each echo in the population  $\Phi_u$  is calculated and the number of echoes found within  $\pm 10$  [km] of the simulated height mean of 92 [km] are plotted as a percentage of the total number of 5000 simulated echoes in Figure 4.17. This approach of maximizing the total number of echoes observed within the meteor zone does contain one subtle source of error: the meteor trail height distribution may become artificially narrowed. A more sophisticated approach might include elements of Maximum Likelihood estimation where the number of echoes within a given height distribution is maximized over  $\alpha'_k$ . In either approach, an assumed model for the meteor trail height distribution is required. If the assumed model does not accurately represent geophysical reality, then observations made under the estimated bias terms  $\hat{\alpha}_k$  will contain errors present in the geophysical height distribution model. This calibration technique could be tightly integrated with the complex-plane interferometry of Section 4.4 to create a system which provides continuously updated values of  $\hat{\alpha}_k$  with the changing external environmental factors which affect  $\alpha_k$ .

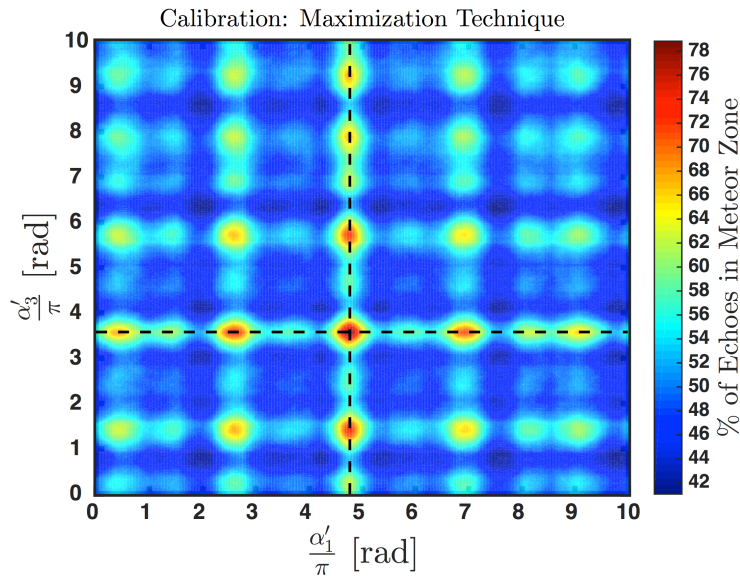


Figure 4.17:  $\alpha'_1$  and  $\alpha'_3$  are swept over the domain of  $[0 : 10\pi]$ . Each set of candidate phase offsets  $\alpha'_k$  are applied to the set of uncalibrated observations  $\Phi_u$  and the height of each echo is subsequently calculated. The number of echoes falling within  $\pm 10$  [km] of the simulated height mean of 92 [km] are plotted as a percentage of the total number of 5000 simulated echoes. A clear peak is observed at  $(\alpha'_1, \alpha'_3) = (4.76\pi, 3.57\pi)$  which closely matches the a-priori phase bias  $\alpha_{ka} = [-223 \ 66 \ -78 \ 182 \ 0]^\circ$  though Eqs 4.46 and 4.47

The phase calibration procedure outlined in this section is unlikely to consistently produce calibration

values within  $5^\circ$  of the true values, and therefore we can expect this figure to represent a lower bound on the height errors due to phase biases. Figure 4.18 shows the effect of a  $5^\circ$  constant phase bias applied to the various channels. Investigators have shown reluctance to reveal the variance in their meteor radar system bias values, but anecdotal evidence suggests the standard deviation of  $\alpha_k$  to be on the order of  $\pm 10^\circ$ . This does not necessarily imply that the estimated phase biases deviate from their true values by  $\pm 10^\circ$  as many time-dependent factors may effect the phase biases including system and environmental temperatures, component age and even ground moisture content. The phase calibration technique could be tightly integrated with the complex-plane interferometry solutions to provide continuously updated phase calibration values during system operation.

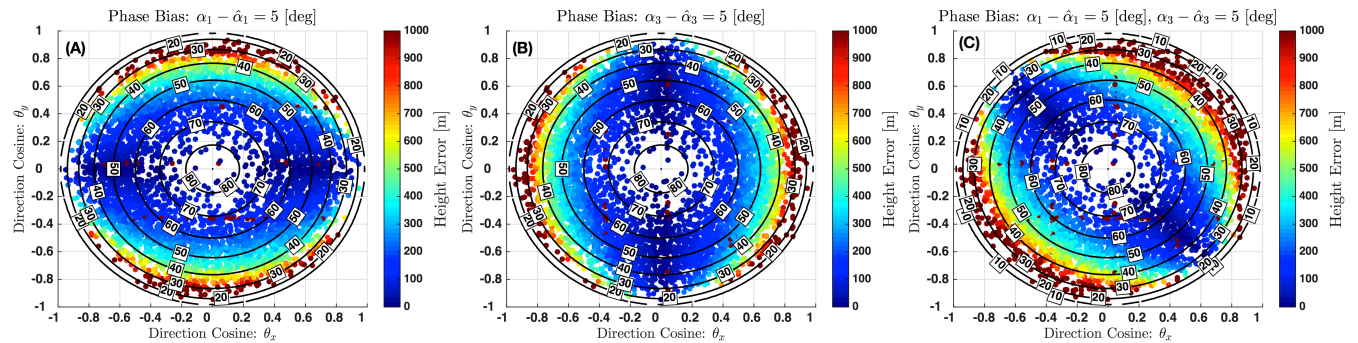


Figure 4.18: A depiction of how a  $5^\circ$  constant phase bias applied to channels Rx1 (A), Rx3 (B) and both Rx1 and Rx3 (C) effect the echo height determination. Contours of constant elevation angle are indicated in [deg]. Interestingly, the height determination biases remain asymmetric in panel (C).

## Chapter 5

### Overview and Future Work

The work presented in this dissertation represents the current state-of-the-art in specular meteor radar instrumentation, modeling of specular meteor trail scattering, interferometry solutions and uncertainty estimation. Chapter 2 first summarized the classical meteor trail scattering equations and then presented two modern theories of trail diffusion. Tinin's technique for modeling the tempo-spatial structure of the ground illumination pattern is refined and applied to the observation of a meteor shower. Two experiments are proposed to provide experimental evidence for Dimant and Oppenheim's modern trail diffusion theory and Tinin's specular scattering formulation. Chapter 3 presents technical details of the Colorado Software Radar (CoSRad), an innovative software-defined radar remote sensing transceiver system. Observational results are presented which showcase CoSRad's ability for extensive reconfigurability, and the technical descriptions can guide future radar remote sensing engineers in understanding how the CoSRad architecture could be applied to solve new remote radar sensing problems. First of their kind long-baseline software-defined specular meteor trail observations are presented in Figures 3.26 and 3.27. The dissertation material crescendos in Chapter 4 with the presentation of a new and elegant technique for solving the specular meteor radar interferometry problem on the complex plane. One consequence of the nonlinear least squares minimization technique is the calculation of the parameter covariance matrix described in Section 4.6, which represents the first statistically rigorous measurement uncertainties placed on the fundamental meteor radar observational parameters of Eq 4.7. Finally, Holdsworth's specular meteor radar array calibration technique

is combined with Prof. Chau's unpublished complex plane formulation shown in Appendix A to produce a straightforward statistical calibration implantation. Each Chapter is summarized below and a number of dissertation-level topics are suggested for future investigators.

(1) Numerical modeling of the ground illumination pattern generated by specular scatter of radar pulses from meteor trails with arbitrary receiver/transmitter geometry motivates the development and deployment of multistatic specular meteor radar. The numerical framework used to generate the ground illumination patterns presented in Chapter 2 is well suited for inclusion of Dimant and Oppenheim's [26] particle-in-cell (PIC) meteor trail electron density model [28]. This proposed extension to my work could reveal new tempo-spatial structures in the ground illumination pattern such as those observed in Figure 2.21 and provide new experimental insight when observing specular meter trail echoes under the modern diffusion theory.

New experimental observations based Oppenheim's work combined with my implementation of Tinin's GIP technique [126] will guide future investigators in designing experiments to provide evidence in support of Dimant and Oppenheim's theory. One such experiment is proposed whereby a known meteor stream is observed using a CoSRad-based multistatic array. Another possible line of future investigation involves observation of the 'critical time' when the character of meteor trail diffusion instantaneously transitions from anisotropic to isotropic. Similar to the work done in providing evidence of Dimant's diffusion using nonspecular echoes [102], correlating the critical time with the time of day would provide compelling evidence from the perspective of specular echoes. Integrating Dimant and Oppenheim's electron density model [28] into Tinin's formulation for the ground illumination pattern, observation and time-of-day correlation of the diffusion critical time, and multistatic meteor stream observations are dissertation-level extensions to this work. Future investigators are also encouraged to explore the potential of a new dust accelerator facility at the University of Colorado [119] which shows some promise in producing laboratory plasmas analogous to those generated by ablating meteors.

(2) A universal software-defined radar transceiver, the Colorado Software Radar (CoSRad) has shown the fundamental viability of the multistatic specular meteor radar measurement technique. First-of-their-kind long-baseline specular meteor trail observations are presented in Chapter 3. CoSRad is designed for integration with most existing specular meteor radar systems, as shown by the deployment history of Table 3.3. CoSRad comprises a direct-sampling data acquisition system including a complete radar timing engine and a software-defined multistatic pulsed Doppler radar. Future investigators are encouraged to use the software-defined radar transceiver system architecture described in this dissertation for application to their own multistatic specular meteor wind radar deployments.

CoSRad has observed a time-dependent drift in Doppler frequency as shown in Figure 3.25. This geophysical observation could be incorporated into the meteor trail specular scatter signal model of Eq 4.2 as an additional complex-exponential term describing a slowly-changing time-dependent phase. Recently, the commercially available Nutaq software-defined transceiver systems have become available [137]. Nutaq-based systems are well suited to host the next iteration of CoSRad. Porting the CoSRad software radar into a Nutaq transceiver platform and deploying a CW pseudorandom multistatic specular wind radar network [133, 122] in addition to providing a geophysical explanation of the observed time-dependent phase drift of Figure 3.25 both represent dissertation-level extensions to this work.

(3) The problem of meteor radar interferometry and statistical uncertainty is elegantly solved by casing the relevant equations onto the complex plane and performing a global solution search using a nonlinear least squares (NLS) iterative minimization technique. All 10 fundamental specular meteor radar signal parameters of Eq 4.7 are estimated by minimizing a single objective function, producing a numerically evaluated Jacobian matrix at the global NLS minimum. Statical signal processing techniques are borrowed from the field of satellite orbit determination [116], and the full-rank numerical Jacobian is inverted to generate a parameter covariance matrix which is forward-propagated to find the statistical uncertainties in direction cosine, height, Doppler and physical diffusion coefficient.

The statistical uncertainties are shown to be consistent over the entire estimated parameter space including SNR as is clearly shown in Figure 4.12. This achievement represents an important advance in specular meteor radar interferometric solutions and instrument precision analysis, and lays the groundwork for solving the inverse-variance problem associated with fitting a vector windfield to the multistatic specular radar observations enabled by CoSRad and described by Eq 4.37. This extension to the interferometry solution and precision formulation of Chapter 4 is a dissertation-level project with currently active funding.

Acknowledgements: This work was funded through NSF grants ANT0538672, ATM0449985, OISE1415056, OIA1444241. International development was also supported through the JIREP program at the Jicamarca Radio Observatory under NSF-AGS0905448. SAMMER deployment was supported by Dr. Janches under NSF-OISE0824742. Support for the LFMCW project came from Dr. Williams' CIRES Innovative Research Program grant designed to stimulate a creative research environment within CIRES and to encourage synergy between disciplines and research colleagues. The author would also like to thank and acknowledge Mr. Brian Fuller and Mr. Adrian Murphy from Genesis Software for their support in the prototype Multistatic Meteor Wind Radar deployment to Delamere and Adelaide Australia and Prof. Chau for his guidance in formulating the complex-plane solutions of Chapter 4.

## Bibliography

- [1] E Appleton. Progress in radio communication. Nature, 135:745–747, 1935.
- [2] E Appleton and R Naismith. Some measurements of upper-atmospheric ionisation. Proceedings of the Royal Society of London, 137:36–61, 1932.
- [3] E Appleton and R Naismith. The radio detection of meteor trails and allied phenomena. Proceedings of the Physical Society of London, 59(333):461–473, 1947.
- [4] Multiple Authors. Recommendation itu-r p.372 radio noise. Electronic Publication, 2015.
- [5] S Avery. The meteor radar as a tool for upper atmosphere research. Advances in Space Research, 10(10):193–200, 1990.
- [6] J Baggaley. The determination of the initial radii of meteor trains. Monthly Notices of the Royal Astronomical Society, 147:231–243, 1970.
- [7] J Baggaley, G Bennett, I Steel, and D Taylor. The advanced meteor orbit radar facility: Amor. Quarterly Journal of the Royal Astronomical Society, 35:293–320, 1994.
- [8] J Baker, M Ruohoniemi, A Ribeiro, L Clausen, R Greenwald, N Frissell, and K Sterne. SuperDARN ionospheric space weather. Aerospace and Electronic Systems Magazine, IEEE, 26(10):30–34, 2011.
- [9] A Ballinger, P Chilson, R Palmer, and N Mitchell. On the validity of the ambipolar diffusion assumption in the polar mesopause region. Annales Geophysicae, 26(11):3439–3443, 2008.
- [10] W Bennett. Spectra of quantized signals. Bell System Technical Journal, 27(3):446–472, 1948.
- [11] D Bilitza. International Reference Ionosphere 2000. Radio Science, 36(2), 2001.
- [12] Dieter Bilitza, Lee-Anne McKinnell, Bodo Reinisch, and Tim Fuller-Rowell. The international reference ionosphere today and in the future. Journal of Geodesy, 85(12):909–920, November 2011.
- [13] P Blackett and A Lovell. Radio echoes and cosmic ray showers. Proceedings of The Royal Society of London, pages 183–186, 1941.
- [14] R Buder. The Invention That Changed the World: How a Small Group of Radar Pioneers Won the Second World War and Launched a Technological Revolution. Simon & Schuster, 1996.
- [15] R Buriti, W Hocking, P Batista, and A Medeiros. Observations of equatorial mesospheric winds over cariri (7.4°s) by a meteor radar and comparison with existing models. Annales Geophysicae, pages 485–497, 2008.

- [16] Cedar: the new dimension. strategic vision for the national science foundation program on coupling, energetics and dynamics of atmospheric regions, 2011.
- [17] Z Cepelcha, J Borovicka, W Elford, D Revelle, R Hawkes, V Porubcan, and M Simek. Meteor phenomena and bodies. Space Science Reviews, 84:327–471, 1998.
- [18] M Cervera, D Holdsworth, I Reid, and M Tsutsumi. Meteor radar response function: Application to the interpretation of meteor backscatter at medium frequency. Journal of Geophysical Research-Space Physics, 109, 2004.
- [19] G Cevolani, G Bortolotti, C Franceschi, G Grassi, G Trivellone, A Hajduk, and S Kingsley. The bologna-lecce forward scatter radar experiment: Preliminary results. Planetary and Space Science, 43(6), 1995.
- [20] J Chau, T Renkwitz, G Stober, and R Latteck. MAARSY multiple receiver phase calibration using radio sources. Journal of Atmospheric and Solar-Terrestrial Physics, 118:55–63, October 2014.
- [21] J Davies and C Ellyett. The Diffraction of Radio Waves From Meteor Trails and the Measurement of Meteor Velocities. Philosophical Magazine, 40(305), 1949.
- [22] R de Elía and I Zawadzki. Optimal Layout of a Bistatic Radar Network. Journal of Atmospheric and Oceanic Technology, 18:1184–1194, 2001.
- [23] S. de la Pena, S. Avery, J. Avery, E. Lau, and D. Janches. Wind measurements of MLT region using the Platteville, CO MEDAC 50 MHz meteor radar. Journal of Atmospheric and Solar-Terrestrial Physics, 67(13):1211–1215, 2005.
- [24] N Deegan, R Fitzpatrick, and G Forti. Study of Meteor Wind Measurement Techniques. Smithsonian Astrophysical Observatory, 1970.
- [25] Y Dimant and M Oppenheim. Meteor generated plasma columns in E-region ionosphere: fields and diffusion. arXiv:physics/0512103, December 2005.
- [26] Y Dimant and M Oppenheim. Meteor trail diffusion: 2. Analytical theory. Journal of Geophysical Research, 2006.
- [27] Y Dimant and M Oppenheim. Meteor trail diffusion and fields: 1. Simulations. Journal of Geophysical Research, 2006.
- [28] Y Dimant and M Oppenheim. First 3-d simulations of meteor plasma dynamics and turbulence. Geophysical Research Letters, feb 2015.
- [29] Distributed Arrays of Small Instruments for Solar-Terrestrial Research: Report of a Workshop, 2011.
- [30] M E Dyrland, C M Hall, F J Mulligan, and M Tsutsumi. Improved estimates for neutral air temperatures at 90 km and 78 N using satellite and meteor radar data. Radio Science, 45, 2010.
- [31] L Dyrud, M Oppenheim, S Close, and S Hunt. Interpretation of Nonspecular Radar Meteor Tails. Geophysical Research Letters, 29(21), 2002.
- [32] T Eckersley. Analysis of the effect of scattering in radio transmission. Journal of the Institution of Electrical Engineers, 86(522):548–563, 1940.
- [33] T Eckersley and F Farmer. Short Period Fluctuations in the Characteristics of Wireless Echoes From the Ionosphere. Proceedings of the Royal Society of London, 184:196–217, 1945.
- [34] W Elford. Radar observations of meteor trails, and their interpretation using Fresnel holography: a new tool in meteor science. Atmospheric Chemistry and Physics, 4:911–921, 2004.

- [35] VR Eshleman. The Theoretical Length Distribution of Ionized Meteor Trails. Journal of Atmospheric and Terrestrial Physics, 10(2):57–72, 1957.
- [36] VR Eshleman and L Manning. Radio communication by scattering from meteoric ionization. Proceedings of the IRE, pages 530–536, 1952.
- [37] D Farley. Theory of equatorial electrojet plasma waves: new developments and current status. Journal of Atmospheric and Terrestrial Physics, 47(8-10):729–744, August 1985.
- [38] J Forbes, N Makarov, and Y Portnyagin. First results from the meteor radar at South Pole: A large 12-hour oscillation with zonal wavenumber one. Geophysical Research Letters, 22(23):3247–3250, 1995.
- [39] S J Franke, X Chu, A Z Liu, and W K Hocking. Comparison of meteor radar and Na Doppler lidar measurements of winds in the mesopause region above Maui, Hawaii. Journal of Geophysical Research: Atmospheres, 110(D9), 2005.
- [40] D Fritts, D Janches, H Limura, W Hocking, N Mitchell, R Stockwell, B Fuller, B Vandeppeer, J Hormaechea, C Brumini, and H Levato. Southern argentina agile meteor radar: System design and initial measurements of large-scale winds and tides. Journal of Geophysical Research, 115, 2010.
- [41] F Galindo and M Kuyeng. Improved e-region electron density and meridional wind measurements over jicamarca using multi-static configurations. CEDAR Conference Poster, 2008.
- [42] D Galligan, G Thomas, and J Baggaley. On the relationship between meteor height and ambipolar diffusion. Journal of Atmospheric and Solar-Terrestrial Physics, 66(11):899–906, 2004.
- [43] M Geller, S Bowhill, and G Hess. A description of the University of Illinois meteor radar system and some first results. Journal of Atmospheric and Solar-Terrestrial Physics, 39:15–24, 1977.
- [44] G Groves. A theory for determining upper-atmosphere winds from radio observations on meteor trails. Journal of Atmospheric and Terrestrial Physics, 16:344–356, 1959.
- [45] A Gruzdev and G Brasseur. Long-term changes in the mesosphere calculated by a two-dimensional model. Journal of Geophysical Research, 2005.
- [46] T Grydeland, F Lind, P Erickson, and J Holt. Software radar signal processing. Annales Geophysicae, 23(1):109–121, 2005.
- [47] T Grydeland, FD Lind, PJ Erickson, and JM Holt. Software Radar signal processing. Annales geophysicae, 23(1):109–121, 2005.
- [48] L Guo and G Lehman. First meteor radar observations of tidal oscillations over Jicamarca (11.95 ° S, 76.87 ° W). Annales Geophysicae, 27:2575–2583, 2009.
- [49] D Gurnett and A Bhattacharjee. Introduction to Plasma Physics With Space and Laboratory Applications. Cambridge University Press, 2005.
- [50] F Hasebe, T Tsuda, T Nakamura, and M D Burrage. Validation of HRDI MLT winds with meteor radars. Annales Geophysicae, 15(9):1142–1157, 1997.
- [51] Tim Hentschel. Sample Rate Conversion in Software Configurable Radios. Artech House Publishers, 2002.
- [52] N Herlofson. Plasma resonance in ionospheric irregularities. Arkiv for Fysik, 3:247–297, 1951.
- [53] J Hey and G Stewart. Radar Observations of Meteors. Proceedings of the Physical Society of London, pages 858–883, 1947.
- [54] G Hill. The Benefits of Undersampling. Electronic Design, 42(14), 1994.

- [55] C Hines and P Forsyth. The forward-scattering of radio waves from overdense meteor trails. Canadian Journal of Physics, 35, 1957.
- [56] W Hocking. A new approach to momentum flux determinations using SKiYMET meteor radars. Annales Geophysicae, 23(7):2433–2439, October 2005.
- [57] W Hocking, W Elford, B Candy, and B Briggs. First results with the Adelaide VHF radar: spaced antenna studies of tropospheric winds. Journal of Atmospheric and Solar-Terrestrial Physics, 49(4):353–366, 1987.
- [58] W Hocking, B Fuller, and B Vandeppeer. Real-time determination of meteor-related parameters utilizing modern digital technology. Journal of Atmospheric and Solar-Terrestrial Physics, 63(2-3):155–169, January 2001.
- [59] W Hocking, T Thayaparan, and J Jones. Meteor decay times and their use in determining a diagnostic mesospheric temperature-pressure parameter: methodology and one year of data. Geophysical Research Letters, 24(23):2977–2980, 1997.
- [60] W. K. Hocking. A review of Mesosphere–Stratosphere–Troposphere (MST) radar developments and studies, circa 1997–2008. Journal of Atmospheric and Solar-Terrestrial Physics, 73(9):848–882, June 2011.
- [61] P Hoffmann, W Singer, D Keuer, and W Hocking. Latitudinal and longitudinal variability of mesospheric winds and temperatures during stratospheric warming events. Journal of Atmospheric Physics, pages 2355–2366, 2007.
- [62] D Holdsworth. Buckland Park all-sky interferometric meteor radar. Radio Science, 39(5), 2004.
- [63] D Holdsworth. Angle of arrival estimation for all-sky interferometric meteor radar systems. Radio Science, 40(6), December 2005.
- [64] D Holdsworth, M Tsutsumi, I Reid, T Nakamura, and T Tsuda. Interferometric meteor radar phase calibration using meteor echoes. Radio Science, 39(5), 2004.
- [65] D Hysell, J Chau, and M Milla. The Jicamarca phased-array radar. 2013 IEEE International Symposium on Phased Array Systems & Technology, pages 669–675, 2013.
- [66] D Hysell, F Rodrigues, J Chau, and J Huba. Full profile incoherent scatter analysis at Jicamarca. Annales Geophysicae, February 2008.
- [67] Marcos Inoñán. The new Jicamarca acquisition radar system and its first applications for the study of the equatorial ionosphere. CEDAR Conference Poster, 2011.
- [68] C Jacobi. 6 year mean prevailing winds and tides measured by VHF meteor radar over Collm (51.3 degrees N, 13.0 degrees E). Journal of Atmospheric and Solar-Terrestrial Physics, 78-79:8–18, April 2012.
- [69] D Janches, S Close, J Hormaechea, N Swarnalingam, A Murphy, D O’Connor, B Vandeppeer, B Fuller, D Fritts, and C Brunini. the southern Argentina agile meteor radar orbital system (SAAMER-OS): an initial sporadic meteoroid orbital survey in the southern sky. The Astrophysical Journal, 809(1):36, 2015.
- [70] D Janches, W Hocking, S Pifko, J Hormaechea, D Fritts, C Brunini, R Michell, and M Samara. Interferometric meteor head echo observations using the southern argentina agile meteor radar. Journal of Geophysical Research: Space Physics, pages 1–19, 2014.
- [71] D Johnson and D Dudgeon. Array Signal Processing. Prentice Hall, 1993.

- [72] J Jones. On the decay of underdense radio meteor echoes. Monthly Notices of the Royal Astronomical Society, 173:637–648, 1975.
- [73] J. Jones. Oblique-scatter of radio waves from meteor trains: Full-wave calculations. Planetary and Space Science, 1991.
- [74] J. Jones, A Webster, and W Hocking. An improved interferometer design for use with meteor radars. Radio Science, 33(1):55–65, 1998.
- [75] W Jones. Theory of diffusion of meteor trains in the geomagnetic field. Planetary and Space Science, 39(9):1283–1288, 1991.
- [76] W Jones and J Jones. Oblique Scattering of Radio-Waves From Meteor Trains - Theory. Planetary and Space Science, 38(1):55–66, 1990.
- [77] T Kaiser and R Closs. Theory of Radio Reflections From Meteor Trails 1. Philosophical Magazine, 43(336):1–32, 1952.
- [78] C Kang. Meteor Radar Signal Processing and Error Analysis. PhD thesis, University of Colorado, 2008.
- [79] C Kang and S Palo. A time-frequency method for detecting VHF underdense meteor signals. Radio Science, 42, 2007.
- [80] M Kay. Fundamentals of Statistical Signal Processing. Prentice Hall, 1993.
- [81] W Kester. Add noise dither to blow out ADC's dynamic range. Electronic Design, 1999.
- [82] J Kraus. Radio Astronomy. McGraw-Hill Inc., 1966.
- [83] E Kudek and S Bhattacharyya. A new approach in incoherent scatter F region E x B drift measurements at Jicamarca. Journal of Geophysical Research, 104, December 1999.
- [84] K Kumar. Temperature profiles in the MLT region using radar-meteor trail decay times: Comparison with TIMED/SABER observations. Geophysical Research Letters, 34(16), August 2007.
- [85] M Larsen. Winds and shears in the mesosphere and lower thermosphere: Results from four decades of chemical release wind measurements. Journal of Geophysical Research-Space Physics, 107, 2002.
- [86] E Lau, S Avery, J Avery, D Janches, S Palo, R Schafer, and A Makarov. Statistical characterization of the meteor trail distribution at the South Pole as seen by a VHF interferometric meteor radar. Radio Science, 41(4), 2006.
- [87] E Lau, S Avery, J Avery, S Palo, and N Makarov. Tidal analysis of meridional winds at the south pole using a vhf interferometric meteor radar. Journal of Geophysical Research-Atmospheres, 111, 2006.
- [88] A Lovell. Meteors, comets and meteoric ionization. Reports on Progress in Physics, 11:389–444, 1948.
- [89] A Lovell and J Clegg. Characteristics of Radio Echoes from Meteor Trails: I. The Intensity of the Radio Reflections and Electron Density in the Trails. Proceedings of the Physical Society. Section B, 60(5):491–498, January 1948.
- [90] W Madkour, M Yamamoto, Y Kakinami, and S Mizumoto. A low cost meteor observation system using radio forward scattering and the interferometry technique. Experimental Astronomy, 2015.
- [91] L Manning, O Villard, and A Peterson. Meteoric echo study of upper atmosphere winds. Proceedings of the Institute of Radio Engineers, 38(8):877–883, 1950.
- [92] H Marsh, T Bennett, J Baggaley, J Fraser, and E Plank. Measuring meridional mesospheric winds with the AMOR meteor radar. Journal of Atmospheric and Solar-Terrestrial Physics, 62(13):1129–1133, 2000.

- [93] J Mathews. Radio science issues surrounding HF/VHF/UHF radar meteor studies. Journal of Atmospheric and Solar-Terrestrial Physics, 66:285–299, 2004.
- [94] J Mathews and J Urbina. Multi-static, common volume radar observations of meteors at Jicamarca. Geophysical Research Letters, 34, 2007.
- [95] D McKinley. Meteor Science and Engineering. McGraw-Hill, 1961.
- [96] N Mitchell and C Beldon. Gravity waves in the mesopause region observed by meteor radar: 1. a simple measurement technique. Journal of Atmospheric and Solar-Terrestrial Physics, 2009.
- [97] HG Müller. Atmospheric tides in the meteor zone. Planetary and Space Science, 1966.
- [98] Edmond Murad and Iwan Williams. Meteors in the Earth's Atmosphere. Cambridge University Press, 2002.
- [99] H Nagaoka. Effect of meteors on radio transmission. Reports on Radio Research of Japan, 2:49–53, 1932.
- [100] V Nechitailenko. Modern problems of meteor wind interpretation. Journal of Atmospheric and Terrestrial Physics, 53(6-7):653–661, 1991.
- [101] K Nishimura, E Gotoh, and T Sato. Fine scale 3D wind field observation with a multistatic equatorial atmosphere radar. Journal of the Meteorological Society of Japan, 84A:227–238, July 2006.
- [102] M Oppenheim, G Sugar, E Bass, and Y Dimant. Day to night variation in meteor trail measurements: Evidence for a new theory of plasma trail evolution. Geophysical Research Letters, 35, 2008.
- [103] Y Pei and D Zhu. A trust-region algorithm combining line search filter technique for nonlinear constrained optimization. International Journal of Computer Mathematics, 91, 2014.
- [104] M Peralta. Propagation of Errors: How to Mathematically Predict Measurement Errors. CreateSpace Independent Publishing Platform, 2012.
- [105] WM Pickering and CD Watkins. Ambipolar diffusion and motion of ion clouds in the earth's magnetic field. Planetary and Space Science, 1969.
- [106] JA Pierce. Abnormal ionization in the E region of the ionosphere. Proceedings of the Institute of Radio Engineers, 26(7):892–908, 1938.
- [107] M Poulter and J Baggaley. Radiowave Scattering From Meteoric Ionization. Journal of Atmospheric and Terrestrial Physics, 39(7):757–768, 1977.
- [108] M Poulter and J Baggaley. The applications of radio-wave scattering theory to radio-meteor observations. Planet and Space Science, 26:969–977, January 1978.
- [109] JPM Prentice, ACB Lovell, and CJ Banwell. Radio Echo Observations of Meteors. Monthly Notices of the Royal Astronomical Society, 107(2):155–163, 1947.
- [110] Schunk R and Nagy A. Ionospheres: Physics, Plasma Physics and Chemistry. Cambridge University Press, 2009.
- [111] J Reed. Software Radio: A Modern Approach to Radio Engineering. Prentice Hall, 2002.
- [112] E Remsberg. On the observed changes in upper stratospheric and mesospheric temperatures from UARS HALOE. Annales geophysicae, 26(5):1287–1297, 2008.
- [113] D Robertson and D Liddy. Measurements of winds in the upper atmosphere by means of drifting meteor trails I. Journal of Atmospheric and Solar-Terrestrial Physics, 1953.

- [114] RG Roper. Winds from the Atlanta (34 N, 84 W) radio meteor wind facility. Journal of Atmospheric and Terrestrial Physics, 40(8):891–894, 1978.
- [115] C Schult, G Stober, D Keuer, and W. Singer. Radar observations of the Maribo fireball over Juliusruh: revised trajectory and meteoroid mass estimation. Monthly Notices of the Royal Astronomical Society, 450(2):1460–1464, April 2015.
- [116] B Schutz, B Tapley, and G Born. Statistical Orbit Determination. Academic Press, 2004.
- [117] R Seal, J Urbina, M Sulzer, N Aponte, and S Gonzalez. Design and implementation of a multi-purpose radar controller using open-source tools. Radar Conference, 2008. RADAR'08. IEEE, pages 1–4, 2008.
- [118] G Seber and C Wild. Nonlinear Regression. Wiley-Interscience, 2005.
- [119] A Shu, A Collette, K Drake, E Grün, M Horányi, S Kempf, A Mocker, T Munsat, P Northway, R Srama, Z Sternovsky, and E Thomas. 3 MV hypervelocity dust accelerator at the Colorado Center for Lunar Dust and Atmospheric Studies. Review of Scientific Instruments, 83(7):075108, July 2012.
- [120] AM Skellett. The ionizing effects of meteors. Proceedings of the Institute of Radio Engineers, 23(2):132–149, 1935.
- [121] DI Steel and WG Elford. The height distribution of radio meteors: comparison of observations at different frequencies on the basis of standard echo theory. Journal of Atmospheric and Terrestrial Physics, 53(5):409–417, 1991.
- [122] G Stober and J Chau. A multistatic and multifrequency novel approach for specular meteor radars to improve wind measurements in the MLT region. Radio Science, 50(5), 2015.
- [123] GR Sugar. Radio propagation by reflection from meteor trails. In Proceedings of the IEEE, pages 116–136, 1964.
- [124] K Tang. Mathematical Methods for Engineers and Scientists 2. Springer, 2007.
- [125] M Tinin and B Kim. Wave scattering by a strongly elongated irregularity. Radiophysics and quantum electronics, 47(12):947–954, 2004.
- [126] M Tinin and B Kim. Modeling of the space–time structure of radio scattering from meteor trail. Journal of Atmospheric and Solar-Terrestrial Physics, 68(9):977–988, June 2006.
- [127] J Tsui. Special Design Topics in Digital Wideband Receivers. Artech House, 2010.
- [128] Ugray, Zsolt, L Lasdon, John C, Plummer, F Glover, J Kelly, and R Mart. Scatter Search and Local NLP Solvers: A Multistart Framework for Global Optimization. INFORMS Journal on Computing, 19:328–340, 2007.
- [129] T Valentic. New approaches to meteor radar data processing. PhD thesis, University of Colorado, 1996.
- [130] TA Valentic, JP Avery, SK Avery, MA Cervera, WG Elford, RA Vincent, and IM Reid. A comparison of meteor radar systems at Buckland Park. Radio Science, 31(6):1313–1329, 1996.
- [131] Valentic, C and Avery P. Self-survey calibration of meteor radar antenna arrays. IEEE Transactions on Geoscience and Remote Sensing, 35, May 1997.
- [132] RG Vaughan, NL Scott, and DR White. The Theory of Bandpass Sampling. IEEE Transactions on Signal Processing, 39(9):1973–1984, 1991.
- [133] J Viernen, J Chau, N Pfeffer, M Clahsen, and G Strober. Coded continuous wave meteor radar. Atmospheric Measurement Techniques, 2015.

- [134] A Westman, G Wannberg, and A Pellinen-Wannberg. Meteor head echo altitude distributions and the height cutoff effect studied with the EISCAT HPLA UHF and VHF radars. Annales geophysicae, 22(5):1575–1584, 2004.
- [135] C Williams, L Bianco, P Johnston, D Law, S Palo, and C Vaudrin. Developing a lower boundary layer radar for renewable energy research. CIRES Innovative Research Project Poster, November 2012.
- [136] CR Williams. Inexpensive FM-CW Radar for Boundary-Layer Precipitation Studies. Geoscience and Remote Sensing Letters, IEEE, 8:1031–1035, 2011.
- [137] NuRAN Wireless. Nutaq software defined radios. <http://www.nutaq.com>.
- [138] JP Younger, IM Reid, and RA Vincent. Mutual coupling of antennas in a meteor radar interferometer. Radio Science, 48(2):118–121, 2013.
- [139] JP Younger, IM Reid, RA Vincent, and DA Holdsworth. Modeling and observing the effect of aerosols on meteor radar measurements of the atmosphere. Geophysical Research Letters, 35(15), 2008.
- [140] P Zigo. Observability function of the Bologna-Modra forward scatter system. Contributions of the Astronomical Observatory Skalnaté Pleso, 38(1):61–69, 2008.

## Appendix A

### Supplemental Wind Computation and Array Calibration Details

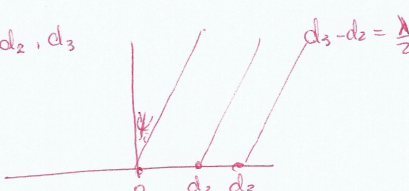
Dr. Strober's description of Figure 4.7 is listed below:

"The zonal and meridional wind was computed applying a singular value decomposition fit to solve for the coefficients putting the constrain that the vertical velocity  $w$  is almost zero. After the first initial guess I additionally apply constrains to get an optimized solution regarding the smoothness in time and the vertical coordinate. After computing the wind field for 24 hours I use a smoothness matrix to estimate the temporal gradient between neighbor points (vertical and time) and use this information in the next SVD inversion. Typically after 3-5 steps I get a stable and well-behaved solution for the winds. In contrast to the zeroth order Tikhonov regularization, there is no amplitude decrease/leakage due to the truncating of some singular values. However, both approaches provide very good wind estimates for the horizontal wind components."

Kborn. 14.03.2015

Meteor phase calibration

Meteor location  $\psi_i$   
 For three antennas in "x" direction  $0, d_2, d_3$   
 without phase delays:  
 $P_{2i} = e^{jk d_2 \sin \psi_i}$   
 $P_{3i} = e^{jk d_3 \sin \psi_i}$



With phase delays  $\alpha_2, \alpha_3$   
 $P_{2i}' = e^{jk d_2 \sin \psi_i + \alpha_2}$  (1);  $P_{3i}' = e^{jk d_3 \sin \psi_i + \alpha_3}$  (2)

Since  $d_3 - d_2 = \frac{1}{2} \lambda$ , lets use  $P_{3i}' P_{2i}'^* \rightarrow$  i.e.  $\phi_{3i} - \phi_{2i}$   
 $P_{3i}' P_{2i}'^* = e^{jk(d_3 - d_2) \sin \psi_i + \Delta \alpha}$  (3) where  $\Delta \alpha = \alpha_3 - \alpha_2$ .

From (3)  $e^{jk \sin \psi_i} = \left( P_{3i}' P_{2i}'^* e^{-j \Delta \alpha} \right)^{\frac{1}{k(d_3 - d_2) \sin \psi_i}}$  (4)  
 From (2)  $e^{jk \sin \psi_i} = \left( P_{3i}' e^{-j \alpha_3} \right)^{\frac{1}{k d_3 \sin \psi_i}}$  (5)

Then  $P_{3i}'^{\left( \frac{d_2}{d_3 - d_2} \right)} P_{2i}'^* \frac{d_3}{d_3 - d_2} P_{3i}' = e^{j \Delta \alpha \frac{d_3}{d_3 - d_2}} e^{-j \alpha_3}$

$P_{3i}'^{\frac{d_2}{d_3 - d_2}} P_{2i}'^* \frac{d_3}{d_3 - d_2} = e^{j \delta}$

$\alpha_3 = \delta \frac{(d_3 - d_2)}{d_2} + \alpha_2 \frac{d_3}{d_2}$

where  $\delta = \frac{+d_2 \alpha_3}{d_3 - d_2} = \frac{d_3}{d_3 - d_2} \alpha_2$

Find  $\delta$  from histogram of  $P_{3i}'^{\frac{d_2}{d_3 - d_2}} P_{2i}'^* \frac{d_3}{d_3 - d_2}$

---

Figure A.1: Prof. Jorge Chau's original complex-plane phase calibration notes for specular meteor radar utilizing the Jones antenna configuration. These notes were made available via a personal communication with Prof. Chau. The formulations in Chapter 4.8 were based on these notes in combination with the real-valued formulation of [64]. In Chapter 4.8, I have substituted  $\eta$  for  $\gamma$  used in this formulation.